The interior of planets as characterised by their magnetic fields : the Jovian and Martian cases

Shivangi Sharan

COLLEGE DOCTORAL PAYS DE LA LOIRE
ED MATIERE,MOLECULES MATERIAUX ET GEOSCIENCES

Nantes Université

THÈSE DE DOCTORAT DE

NANTES UNIVERSITÉ

ÉCOLE DOCTORALE N° 596
Matière, Molécules, Matériaux et Géosciences
Spécialité : Sciences de la Terre et des Planètes

Par

Shivangi SHARAN

Sur l'utilisation du champ magnétique pour caractériser l'intérieur des planètes : les cas de Jupiter et de Mars

The interior of planets as characterised by their magnetic fields : the Jovian and Martian cases

Thèse présentée et soutenue à Nantes, le 30/01/2023
Unité de recherche : Laboratoire de Planétologie et Géosciences, Nantes Université, CNRS UMR 6112, Nantes, France

Rapporteurs avant soutenance :

Maria Alexandra Pais	Assistant Professor, Physics Department, University of Coimbra
Annick Chauvin	Professeure, Géosciences Rennes, Université de Rennes

Composition du Jury :

Président :

Olivier Grasset	Professeur, Laboratoire de Planétologie et Géosciences, Nantes Université

Examinateurs :

Mioara Mandea	Physicienne, Conseil National des Astronomes et Physiciens, Centre National d'Études Spatiale
Pascal Tarits	Professeur, Laboratoire Géosciences Océan, Université Bretagne Occidentale
Maria Alexandra Pais	Assistant Professor, Physics Department, University of Coimbra
Michele Dougherty	Professor, Department of Physics, Imperial College London

Directeur de thèse :

Benoit Langlais	Directeur de Recherche CNRS, Laboratoire de Planétologie et Géosciences, Nantes Université

Co-directeur de thèse :

Erwan Thébault	Directeur de Recherche CNRS, Laboratoire de Magmas et Volcans, Université Clermont Auvergne
Olivier Verhoeven	Maître de Conférences, Laboratoire de Planétologie et Géosciences, Nantes Université

Acknowledgements

My deepest gratitude to the three strangers who decided to adopt, raise and educate a random student they met on the internet three years ago. Thank you Benoit for your support and advice in everything I do, be it professional or personal. As a foreigner, I would have been lost without your guidance. Thank you Erwan for clearing all my doubts with the utmost patience. Thank you Olivier for your ever constant help and encouragements.

The next set of thank yous' is for all my colleagues who made my stay in Nantes easier. Thank you Hagay for breaking down all complex problems to understandable concepts. Thank you Diana for taking care of all my petty to huge troubles since I first arrived. Thank you Mioara and Pascal for your guidance throughout my PhD. Thank you Alexandra, Annick, Michele and Olivier for taking the time to be a part of my thesis. To my french officemates for making me feel comfortable by always opting for english- thank you Marine, Marion and Maëva. To all the people of LPG who always had a smile on their faces irrespective of the weather Nantes threw at us- a big Thank you.

No matter how good the working environment is, we always need friends to hang around with. You all have been a constant support throughout my journey. Big shoutout to the family I built here- this place would have been very lonely without you guys. Thank you to my chefs- Sneha, Frank, Chung, Carolina, Victor. Thank you to my walking french translators- Sitraka, Justine, Mary, Ronan. Thank you to my foodies who always said yes to impromptu dinner plans- Rodney, Alessandra, Kota, Luis, Chimira, Pinar.

Finally, to my family. I would not be doing anything in life if I did not have my parents and my sister standing like a pillar beside me, forever supporting and cheering. Thank you for being there for me always. To my friends back home who are as important to me- thank you for picking up my calls whenever I needed it.

Last and also the least, a small note of thanks to the pandemic for giving me the liberty of working from my bed even on the weekdays.

Abstract

This research work entails studying the magnetic field of planets, typically Mars and Jupiter, and deciphering information about the interior structure from them. There are internal and external sources of magnetic field around a planet which can be modelled using Spherical Harmonics (SH). The internal sources are dominantly the currents in the dynamo and crust. The crustal fields are constant in time while the dynamo fields undergo variations. These changes in field are termed as secular variations (SV). The external fields are time-varying and are produced from the interaction of the planet with solar phenomena like the solar winds and interplanetary magnetic fields. The externally inducing fields generate an internally induced field due to electromagnetic induction. In this work, we concentrate on the internal magnetic field to decipher information about the interior properties of the two planets. For Jupiter, we work with the internal dynamo field while for Mars, we work with the internally induced fields.

Jupiter has the largest planetary magnetic field in the Solar System. The field is produced in the dynamo due to convection in the conducting liquid metallic hydrogen and undergoes changes over time. We use magnetic measurements across 5 years from the latest satellite Juno to model the internal field and the SV up to SH degrees 16 and 8 respectively. Using the model, we derive important results for the planet. The dynamo is generated at a depth of 0.83 times the radius of the planet. The SV is dominated by advective movements and varies at a rate of about 0.6% per year. The radial field maps at the surface and dynamo radius show two prominent features- a positive field patch in the north and an intense negative patch near the equator. The SV maps display both zonal and non-zonal features.

Mars currently does not possess a core field. It has a static crustal field and a transient field of external and internal origins. For this study, we use data across 7 years each from two satellites, Mars Global Surveyor (MGS) and Mars Atmosphere and Volatile Evolution (MAVEN) to observe the time-varying fields. Analysis of the fields from both satellites, which are of the order of 10^2 nT, display a 27 days trend corresponding to the rotation of the Sun. This can be utilized to obtain a magnetic index on Mars. The transient field models obtained up to SH degree 3 display a peculiarity as the magnitude of the induced fields are not always lower than the inducing fields. We proceed to use these models to try to obtain information about the conductivity of the interior by estimating probability distribution functions using Bayesian inversion.

Résumé

Introduction Générale

Pour comprendre le passé, le présent et l'avenir de notre planète ainsi que de l'ensemble du système solaire, il est nécessaire de connaître son origine et son évolution. Cela passe par l'étude de l'intérieur des planètes et de la façon dont il a pu changer ou évoluer au fil du temps. Pour la Terre, le moyen le plus efficace pour étudier sa structure interne est l'observation sismique. Cependant, ce n'est pas applicable pour toutes les planètes et d'autres méthodes sont nécessaires. L'étude des champs magnétiques est l'une d'entre elles, car elle permet de comprendre certaines propriétés de l'intérieur.

Les champs magnétiques observés autour des planètes contiennent des informations sur leurs différentes sources. Ces sources sont soit internes, soit externes à la planète. Les données magnétiques obtenues à partir de magnétomètres en surface ou à bord de satellites en orbite peuvent être utilisées pour développer des modèles. Pour estimer ces modèles, l'approche la plus commune est l'utilisation de fonctions en harmoniques sphériques (SH) qui consistent en une modélisation des champs magnétiques autour d'une planète (en dehors des sources) en fonction d'un potentiel magnétique. Les harmoniques sphériques sont définies en termes de degré et d'ordre, qui correspondent à des échelles spatiales différentes particulières.

Les sources magnétiques peuvent être classées, de manière générale, comme provenant de 4 régions différentes. La source interne primaire est associée aux courants dans la région de la dynamo. Les courants de dynamo sont dus à la convection dans un liquide conducteur en rotation. Cela génère un champ global et de haute intensité qui peuvent aimanter certains éléments de surface comme des minéraux. Il en résulte une aimantation de la croûte, appelée le champ crustal. Bien que les champs générés par la croûte soient statiques dans le temps, le champ généré par la dynamo subit des changements. Les variations de ce champ dans le temps sont appelées variation séculaire (SV). La troisième source est constituée par les courants générés à l'extérieur de la planète. L'interaction de la planète et de son champ avec des phénomènes solaires, tels que les vents solaires ou le plasma d'autres corps dans le voisinage de la planète, génère des champs magnétiques d'origine externe. Ces champs peuvent générer à leur tour des courants dans la croûte et le manteau par induction électromagnétique, ce qui forme un champ interne induit par l'extérieur.

La modélisation par des SH permet de séparer le champ magnétique en fonction de

ses sources qui sont soit internes, soit externes à la planète. Les modèles générés sont utiles pour comprendre les planètes et leurs propriétés, en particulier par l'analyse de certaines quantités statistiques et par les cartes développées à l'aide de ces modèles. Les propriétés telles que la profondeur de génération du champ et la conductivité électriques des sources induites peuvent être déterminées. Une quantité statistique importante qui peut être déterminée à l'aide des modèles est appelée le spectre de puissance. Il indique l'énergie du champ à un degré SH particulier.

Dans ces travaux de doctorat, deux planètes sont étudiées : Mars et Jupiter. Alors que Jupiter est une géante gazeuse, Mars est une planète tellurique. Une géante gazeuse est principalement composée de gaz alors qu'une planète tellurique possède des éléments rocheux en son sein. Malgré le fait que l'intérieur de ces planètes soit différent, les propriétés de leurs sources magnétiques sont probablement similaires. Ceci permet d'extrapoler les connaissances du champ magnétique terrestre aux autres planètes.

Le champ magnétique de Jupiter

Jupiter est la plus grande planète du système solaire avec un rayon de 71 492 km (1 R_J). C'est la cinquième planète. Elle met environ 10 heures pour faire une rotation complète sur elle-même, et il lui faut presque 12 ans pour faire une révolution autour du Soleil. Elle a été visitée par diverses missions de survol de satellites. En revanche, il n'y a eu que deux missions d'orbiteurs, à savoir Galileo et Juno. D'après les études théoriques et les observations par satellite, Jupiter est composée d'un noyau petit mais dense qui s'étend dans un noyau dilué jusqu'à 0,5-0,6 R_J. La couche suivante est composée d'hydrogène métallique à haute conductivité et riche en hélium. La couche la plus superficielle est constituée d'hydrogène moléculaire qui s'étend dans l'atmosphère de la planète. La conductivité de cette couche et de l'hélium présent est comparativement plus faible que dans la précédente.

Le champ magnétique interne de Jupiter est généré par une dynamo auto-entretenue. Cette dynamo est due à des courants de convection dans l'hydrogène métallique et conducteur. Jupiter génère le plus grand champ planétaire du système solaire. Les satellites ont mesuré une forte intensité du champ magnétique même à de grandes distances de la surface. L'axe du champ magnétique jovien forme un angle d'environ 10° avec l'axe de rotation. Cette inclinaison et la rotation rapide de la planète ont un effet important sur ses satellites naturels. L'environnement de plasma et le système de courants externes autour de la planète ont également des intensités élevées qui s'étendent jusqu'à ses lunes. En raison de l'absence de couche solide et de courants conducteurs près de la surface, Jupiter ne possède pas de champs crustaux ou induits. Ainsi, son champ peut être divisé en un champ interne généré par une dynamo et un champ externe interagissant avec la planète.

Pour modéliser ces deux sources, les données du dernier satellite Juno sont utilisées. La sonde spatiale Juno a été lancée en août 2011 et est entrée dans l'orbite de Jupiter en juillet 2016. Elle fournit des données magnétiques depuis lors. Les orbites de Juno

sont très elliptiques, l'apoapse atteignant plus de 100 R_J. Le périapse descend jusqu'à 2500 km au-dessus de la surface. L'orbite du satellite est optimisée de telle sorte que l'on obtienne une couverture globale de la planète. Pour cette étude, les données sur 5 ans, d'août 2016 à novembre 2021, en dessous de 300 000 km, sont utilisées.

Avant de commencer l'inversion des données réelles de Juno, une analyse synthétique est réalisée à partir d'un modèle géomagnétique. L'objectif est de tester la robustesse de l'inversion et de vérifier si les données peuvent être utilisées pour modéliser les variations temporelles du champ. Le modèle CHAOS-7.11 est utilisé pour prédire les valeurs du champ magnétique aux emplacements de l'orbite de Juno. Cependant, comme l'intensité et la forme des spectres de puissance de Jupiter et de la Terre sont différentes, les modèles de champ jovien pré-existants sont utilisés pour mettre à l'échelle le modèle géomagnétique. Le champ est prédit à l'aide du modèle terrestre et à l'emplacement des mesures Juno. Ces données synthétiques sont ensuite inversées pour récupérer le modèle. Le modèle SH obtenu à partir des emplacements de Juno correspond très étroitement au modèle original redimensionné. Cela confirme que l'inversion est robuste et que les variations temporelles peuvent être estimées simultanément avec le champ interne.

En utilisant les résultats des tests synthétiques, un modèle de champ interne jusqu'au degré 20 et un modèle SV jusqu'au degré 8 sont calculés. Les données à basses altitudes sont utilisées pour modéliser le champ externe jusqu'au degré 2. En raison de la distribution des données du satellite, il existe des champs non résolus dans l'hémisphère sud, ce qui entraîne un aliasing spectral. Par conséquent, le modèle interne est tronqué au degré 16. Grâce au modèle obtenu, le rayon de la dynamo, les temps de corrélation ainsi que l'interprétation des cartes radial sur les mouvements au sommet de la dynamo sont déterminés.

Le rayon de la dynamo est estimé en utilisant le spectre de puissance de deux sous-familles appelées famille non-zonale et famille quadrupole. Ceci permet de déterminer la profondeur de la génération de la dynamo à 0.83 R_J. La variation séculaire observées correspond à un changement d'environ 2,9% sur 5 ans, ce qui indique la nécessité de modéliser simultanément le champ et le SV. En utilisant les spectres du champ principal et du SV simultanément, les échelles temporelles où le champ devient non corrélé sont déterminés. La valeur la plus élevée est de 2471 ans pour le terme dipôle et la valeur la plus basse de 45 ans est obtenue pour le degré 7. Le changement de champ est attribué de manière dominante au mouvement d'advection du fluide. Enfin, les cartes de champ radial à la surface et dans le rayon de la dynamo sont examinées ce qui a permis de déterminer que les variations ont des motifs à la fois zonaux et non zonaux.

Le champ magnétique de Mars

En ce qui concerne Mars, c'est une planète tellurique avec une structure composée d'un noyau, d'un manteau et d'une croûte. Son rayon correspond à la moitié de celui de la Terre, mais sa période orbitale est deux fois plus longue. Il y a ou il y a eu beaucoup de missions vers Mars, notamment des survols, des orbiteurs et des atterrisseurs. De

nombreuses informations sur la structure interne de la planète proviennent de la récente mission InSight, qui est la première à avoir déposer un sismomètre à sa surface. L'intérieur de Mars contient des éléments légers, tels que des silicates, plus que ce qui est observé sur Terre. La croûte a une épaisseur comprise entre 25 et 75 km, suivie d'un manteau jusqu'à une profondeur d'environ 1800 km.

Parmi les orbiteurs autour de la planète, qui assurent une couverture spatiale globale, seuls deux satellites, Mars Global Surveyor (MGS) et Mars Atmosphere and Volatile Evolution (MAVEN), sont équipés de magnétomètres et fournissent des mesures de champ magnétique. Celles-ci ont révélé que la planète ne possède actuellement aucune dynamo, mais qu'elle possède de puissants champs crustaux. Cependant, ces champs, qui sont d'un ordre de grandeur supérieur à celui observé sur Terre aux altitudes du satellite, indiquent la présence d'une dynamo passée. De plus, les résultats de la mission InSight indiquent que les valeurs à la surface sont encore plus intenses que celles prédites depuis l'orbite. Mars possède également des champs externes complexes dus à l'interaction avec le vent solaire et les champs magnétiques interplanétaires. Ils forment une onde de choc et un environnement de plasma avec des géométries variables en fonction des interactions locales avec les champs crustaux.

Les champs externes induisent une réponse interne due à la présence de matériaux conducteurs dans la croûte et le manteau. Dans ce travail, les données de MGS et MAVEN sont utilisées pour modéliser les champs magnétiques, en particulier les champs transitoires.. Les configurations orbitales de ces deux satellites sont très différentes dans l'espace. MGS a été lancé en novembre 1996 et a fourni des données jusqu'en 2006. MAVEN a été lancé en novembre 2013 et transmet encore des données à l'heure actuelle. Alors que l'orbite finale de MGS était quasi circulaire, MAVEN tourne autour de la planète sur une orbite elliptique qui varie avec l'heure locale. L'utilisation des données des deux satellites permet d'observer le champ à différentes altitudes. Les données de l'orbite quasi circulaire varient entre 350 et 450 km d'altitude. Comme l'orbite est quasi circulaire, il est plus facile d'observer les données de MGS du côté jour et du côté nuit pour comprendre les différences entre elles. Les données de l'orbite elliptique varient entre 100 km et plus de 6000 km. Un compromis entre la couverture et l'altitude est fait et seules les données en dessous de 1000 km sont utilisées.

La première étape de la modélisation du champ transitoire consiste à supprimer les champs statiques intégrés dans les observations. Pour cela, un modèle de champ crustal existant est utilisé pour prédire les valeurs à l'emplacement de nos mesures satellitairees et les soustraire des données. Les champs résiduels qui en résultent sont beaucoup plus faibles en magnitude et montrent une certaine relation avec les champs magnétiques interplanétaires. Ils indiquent un cycle de 27 jours, lié à la rotation du Soleil sur lui même, qui peut être utilisé pour développer des indices magnétiques. Ces indices sont utiles pour distinguer les périodes d'activité externe des périodes calmes sur la planète. Les SH sont utilisées pour modéliser les champs transitoires induits par l'extérieur à l'intérieur observés dans les données résiduelles. Des modèles sont calculés chaque jour pour observer les séries temporelles. Contrairement à la Terre, la magnitude des champs

inducteurs externes à Mars n'est pas toujours supérieure à la magnitude des champs induits internes dans les modèles que nous calculons.

Les champs induits permettent de comprendre la conductivité de l'intérieur. L'inversion bayésienne est utilisée pour obtenir un profil de conductivité 1-D du manteau à partir des modèles en utilisant certaines données définies a priori pour différents paramètres. Les valeurs des paramètres correspondent aux couches à l'intérieur de la planète et la conductivité est estimée pour chacune d'entre elles en utilisant une probabilité gaussienne. Les valeurs sont calculées à l'aide d'une fonction de transfert Q, qui représente le rapport entre les parties induites et inductrices dans le domaine fréquentiel. Nous utilisons les séries temporelles de degré 1 et d'ordre 0 sont pour notre inversion. La valeur maximum pour avoir un conducteur pur pour Q, en utilisant le terme zonal du dipôle, est de 0,5, ce qui résulte du fait que les champs inducteurs sont, au moins, deux fois plus importants que les champs induits. Ceci est différent de ce que nous obtenons avec nos modèles variant dans le temps. Des résultats synthétiques fournissent une bonne estimation de la conductivité mais les données réelles fournissent des résultats différents. En effet, l'inversion des données semble robuste mais la séparation des champs internes et externes pour les champs transitoires est difficile à réaliser sur Mars avec les vraies données. Par conséquent, l'interprétation de la fonction de densité de probabilité pour obtenir une valeur de conductivité fiable pour l'intérieur reste ambiguë.

Conclusion Générale

La dernière partie de cette thèse aborde les travaux futurs qui pourront être réalisés dans le prolongement du présent travail. Les défis rencontrés lors du traitement des données ou de la modélisation, ainsi que la façon de les surmonter avec différentes techniques ou différentes données, sont également discutés. Pour Jupiter, l'étape suivante consisterait à établir des cartes montrant l'écoulement du fluide conducteur au sommet de la dynamo. En complément, les données de la mission prolongée Juno et de la future mission JUICE permettraient de mieux comprendre le champ magnétique et ses variations. Pour Mars, l'accent serait mis sur une meilleure séparation des champs internes et externes variant dans le temps. Une façon d'y parvenir pourrait être le développement d'indices magnétiques. Un autre moyen pourrait être de comprendre les magnétosphères locales et de les utiliser pour la séparation. Différentes techniques de modélisation pour l'inversion de la conductivité peuvent également être utilisées. On peut soit utiliser une modélisation en 3-D, soit modéliser en tenant compte de la susceptibilité magnétique de chaque couche. Enfin, une comparaison avec la Terre serait utile pour comprendre les similitudes ainsi que les différences entre les différentes planètes.

Table of Contents

The Martian Case

List of Figures

List of Tables

Introduction

1. General Introduction and Background

The mystery that the universe is can only be solved if we figure out its origin and evolution over time. In order to understand the expanding space around us, we can start by looking at our small neighborhood. One very tiny part of the universe comprises our Solar System. Understanding the interior of the planetary bodies of the Solar System will bring us one step closer to comprehending the big picture.

The easiest way to understand the interior of anything is to look or travel deep inside it. However, the maximum humans have been able to drill on Earth is only about 12 km deep. This makes one look for alternative methods to estimate what constitutes the Earth or any other planet. One such method would entail collecting and studying the samples obtained from the interior. The physical and chemical parameters like temperature or constituents of rocks as well as simulations based on these parameters can give a fair idea. However, these techniques rely on availability of the samples and are more useful for localised studies. Another way would be to use scientific equipment that measure certain parameters. For a global overview of the planet that probes the deep interior, a dense network of instruments covering the entire planet and their simultaneous observations are highly efficient. Some of the best methods which attain this are seismic observations, gravity and magnetic field measurements.

On Earth, seismological studies have by far provided the most accurate results. Seismic waves travel with different velocities through different layers that have different properties. This gives an insight as to what the layers inside the planet are and what the depth of each of these layers are (Gutenberg 2016). The next best results have been derived from gravity and magnetic measurements. The gravity measurements at different locations give an estimate of its variation with depth and latitude. These observations offer an indication about the shape, density and distribution of mass anomalies on the planet (e.g., Heiskanen and Meinesz 1958).

The magnetic measurements and the models obtained from them provide another way to comprehend the interior processes. One of the earliest uses of the Earth's magnetic field was for navigation using compasses. Today, the study of the field is used for a lot of purposes depending on its origin. The most important is to get information about the core and the dynamic processes happening inside it. It is also useful in computing the electrical conductivity distributions of the interior. Our understanding of the planetary

bodies has greatly enhanced thanks to the several approaches and observations.

Unsurprisingly, the maximum we know about a planet is our own. From these indirect ways of deciphering the interior, we have obtained both local and global models describing the Earth. To name a few properties, we know about the numerous layers present inside (Figure 1.1), their composition as well as their temperature. For instance, we know from seismic observations that there are four layers inside the Earth that extend to a radius of about 6371 km. The deepest layer is called the inner core which is solid while the next layer, the outer core, is liquid. The core is composed primarily of iron-nickel alloys with more than 80% iron and has extremely high temperatures. Above it lies the large mantle which is rich in minerals, mainly silicates. The temperature starts decreasing gradually in the mantle. The final layer of the mantle is called the asthenosphere on which sits the topmost thinnest rocky layer which is the lithosphere.

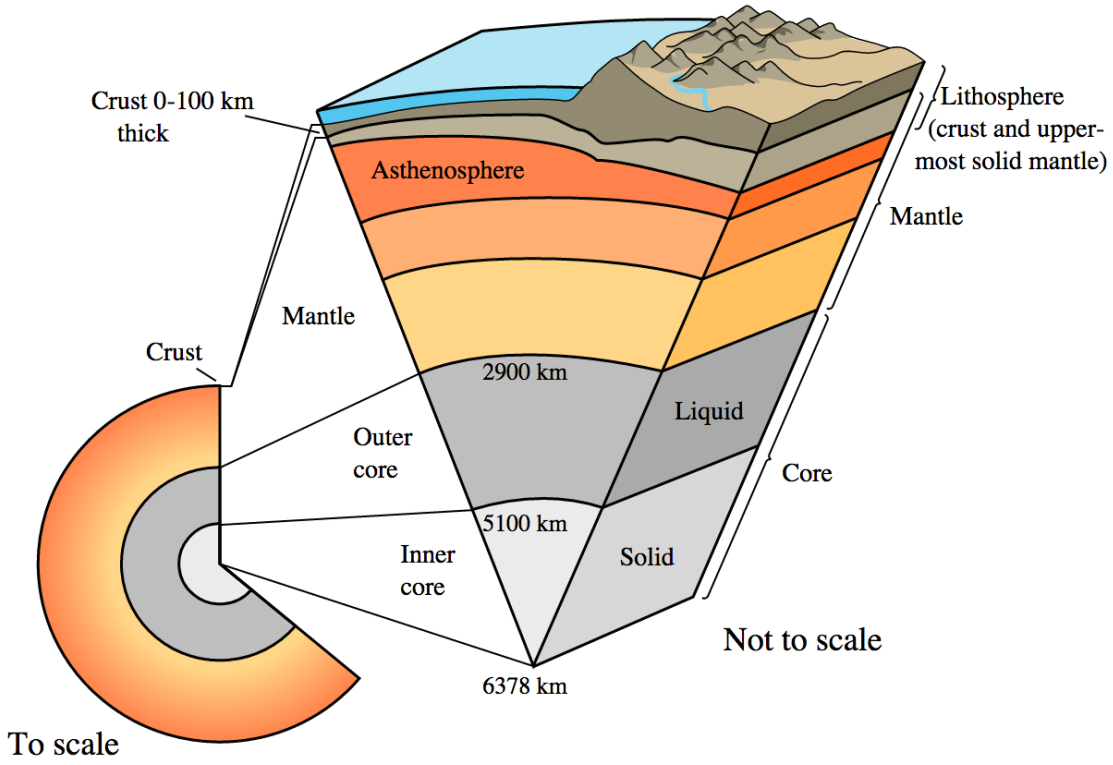

Figure 1.1: Cutaway views showing the internal structure of the Earth in terms of the layers present and their chemical state. The radius is assumed to be near 6371 km. The crust is roughly up to a depth of 100 km, the mantle to 2900 km while the core is at the centre. The liquid outer core is responsible for the generation of the core field. Credit: USGS

Unfortunately, we do not have the means to look as closely at other planetary bodies. Hence, we apply the theories and hypotheses that work on Earth to other planets that exhibit similar behaviour in order to better understand them. At present, we have several types of observations available for them. In this thesis, we use the magnetic field measurements in an attempt to characterise what the interior of planets, specifically, Jupiter and

Mars look like. For this reason, we first start by looking at the magnetic field of Earth, its sources and observations. The conventionally used unit for magnetic measurements is nano-Tesla (nT).

1.1 The Geomagnetic Field

Field Sources

The magnetic field of Earth, called the geomagnetic field, is primarily generated by a self sustaining dynamo, which requires an electrically-conducting fluid and an energy source that drives the convection within a spherical shell in rotation. This is termed as the core or main field as it originates in the liquid outer core for Earth. Convection in the conducting metallic iron produces the field. The core field is very intense and extends to large radii outside the planet (Stevenson 1983). It constitutes more than 90% of the geomagnetic field observed at the surface. The main field is dominantly dipolar, thus creating field lines that resemble those around a bar magnet (Figure 1.2). The field at the surface near the equator is about 30,000 nT and 60,000 nT near the poles (Mandea and Korte 2010). The magnetic axis of the dipole field is not aligned with the rotation axis of Earth. Currently, there is a tilt of about 12° between them.

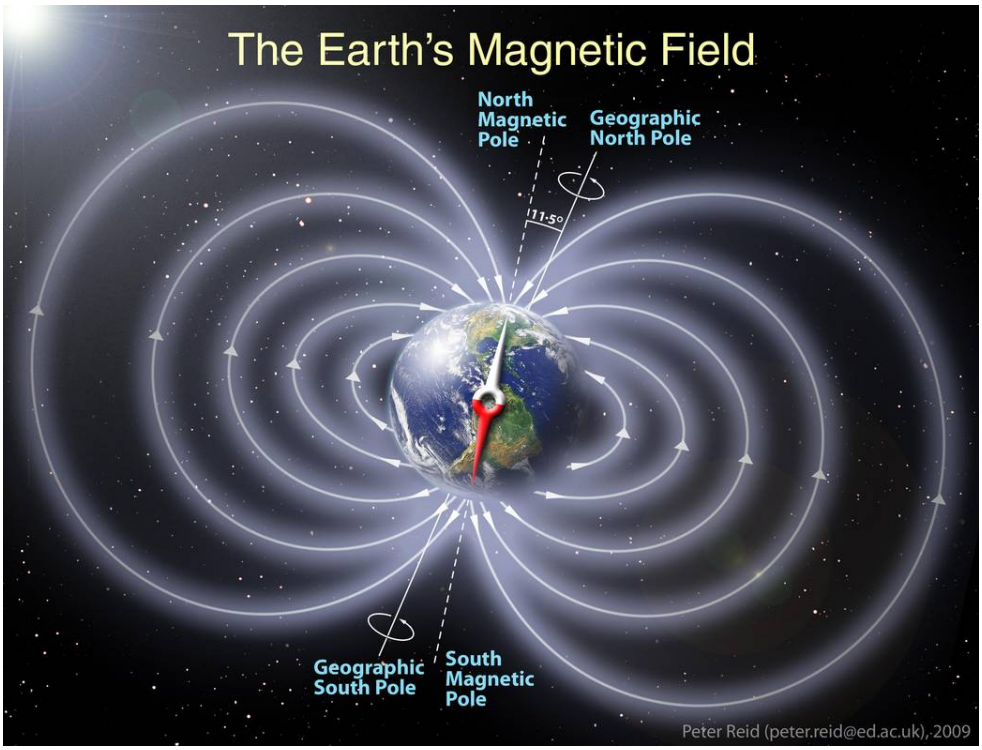

Figure 1.2: Depiction of the magnetic field lines generated by the core field of Earth. The axis of the magnetic field is tilted with respect to the Earth's rotation axis by 11.5°. Credit: Peter Reid, SCI-FUN

The core field can magnetise the rocks that contain magnetic material which are present on the crust. This creates crustal or remanent fields that are static. The magnitude of the crustal fields on average lies between $10-10^2$ nT. Most often, they are formed when magma cools down and solidifies below a certain temperature called the Curie temperature. The ambient temperatures at the surface allow the rocks and seafloors to sustain permanent magnetisation. The remanent magnetisation can thus give information about the core fields that magnetised it in the past, based on the polarity and magnitude it retains. The study of such records is called paleomagnetism. An important process of the geodynamo is revealed from this. The paleomagnetic records show evidence of different polarities leading us to discover that the geomagnetic field undergoes reversals, i.e., the north and south poles flip at some intervals of times. Although the rate of reversal is irregular, they can occur anywhere between a few thousand years to about millions of years, with the last reversal taking place more than 0.78 million years ago (Constable and Korte 2006). Since the sources of both the core and crustal fields are inside the planet, they constitute the internal magnetic field sources.

Another source for the internal field is a consequence of the field that is generated external to the planet. The main field extends far away from the planet's surface and interacts with the outer environments, like the solar winds, the interplanetary magnetic fields and the plasma around the planetary body to generate external current systems. The higher is the intensity of the internal magnetic field, the larger is the magnetosphere of the planet. The magnetosphere is the surrounding magnetic environment of a planet (Figure 1.3). Its shape resembles that of a teardrop since it constantly reacts with charged particles coming from the Sun. The limit of the magnetosphere that interacts foremost with these incoming particles forms the bow shock. The rear end that extends longer is called the magnetotail. The interaction and movement in the magnetosphere forms another source for the magnetic field, producing the so-called external magnetic fields (Baumjohann and Nakamura 2007), which are transient in nature. They have magnitudes lower than about 10^2 nT. Since the planet is conducting as a whole and the time-varying external sources are outside this body, the latter can induce currents inside the planet through electromagnetic induction. The field is dependent on the conductivity in the interior. This creates an additional source for the internal fields and is termed as the externally induced internal fields.

The geomagnetic field is not static in nature but undergoes changes over time. The changes take place over time scales ranging across seconds to years (Mandea and Purucker 2005). The source for the rapid changes is the time-varying external current systems. There are many quantities called magnetic indices defined in order to understand the transient sources. The indices provide a value for the variations in field observed over short time scales. The fields and the indices are heavily dependent on the solar activity. The other source for the variations is the main field. The changes observed in this field are most probably related to the movement of the conducting liquid. The temporal variations over a year or more are termed as the secular variation (SV) of the field. The SV at the surface is of the order of about 200 nT/yr.

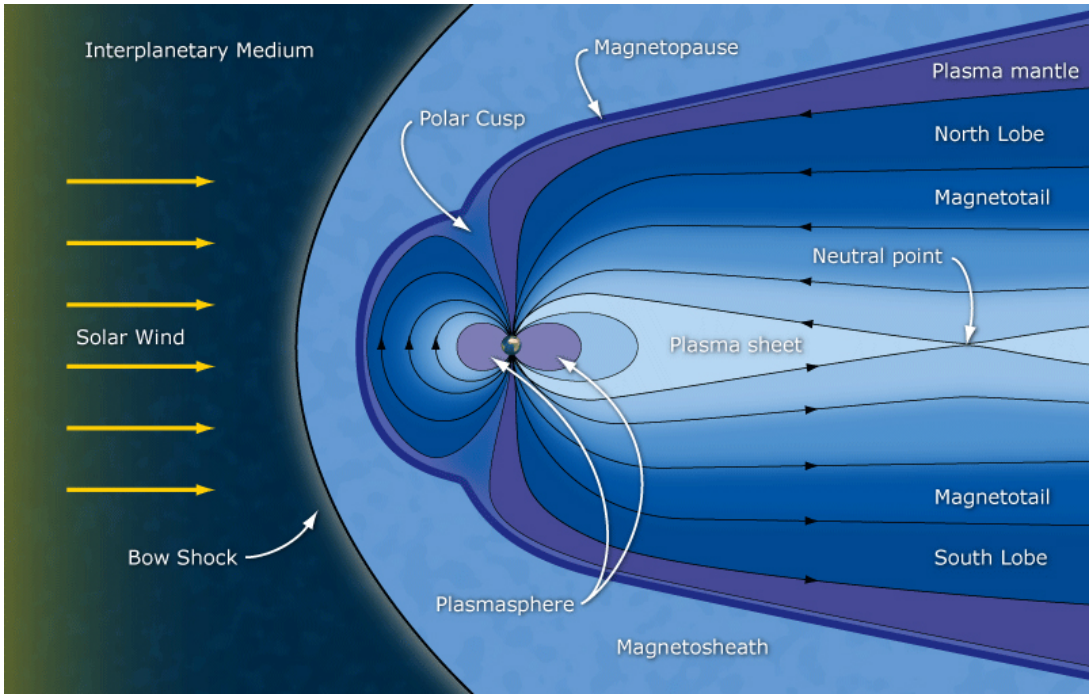

Figure 1.3: The magnetic environment around a planet (here, Earth). The yellow lines represent the solar winds emitted by the Sun while the blue and violet regions depict the various layers of the magnetosphere. Credit: ESA/C. T. Russel

Field Observations

Our extensive knowledge about the geomagnetic field and its sources is a result of the magnetic observations that have been available for centuries using different methods. The earliest geomagnetic measurements made were of angles like declination and inclination (Hulot et al. 2010). Declination is the angle between the true north and magnetic north; whereas inclination is the dip of the magnetic vector below the horizontal plane. The observations were made on land as well as on sea by naval ships for navigation purposes. During the 1800s, a proper network of magnetic observatories started to develop. Currently, there are over 100 ground observatories spread over the planet that constantly measure the magnetic field. The list and data from these are available on the International Real-time Magnetic Observatory Network (INTERMAGNET). These observatories are especially useful for observing the time variations and obtaining the magnetic indices since they are stationary and undergo no spatial variations. However, the same reason is also its drawback. The map of current observatories is displayed in Figure 1.4, which shows the lack of homogeneity in terms of their distribution over the planet. A similar issue arises from using only paleomagnetic records. They are useful for studying the crustal field and the ancient core field, but another method was needed to better map the current global field. This provided the motivation to develop satellites for the sake of acquiring a spatial coverage of the entire planet.

Over the years, there have been many satellite missions providing magnetic data. Starting in the 1960s, the first satellite providing scalar measurements was POGO. Even

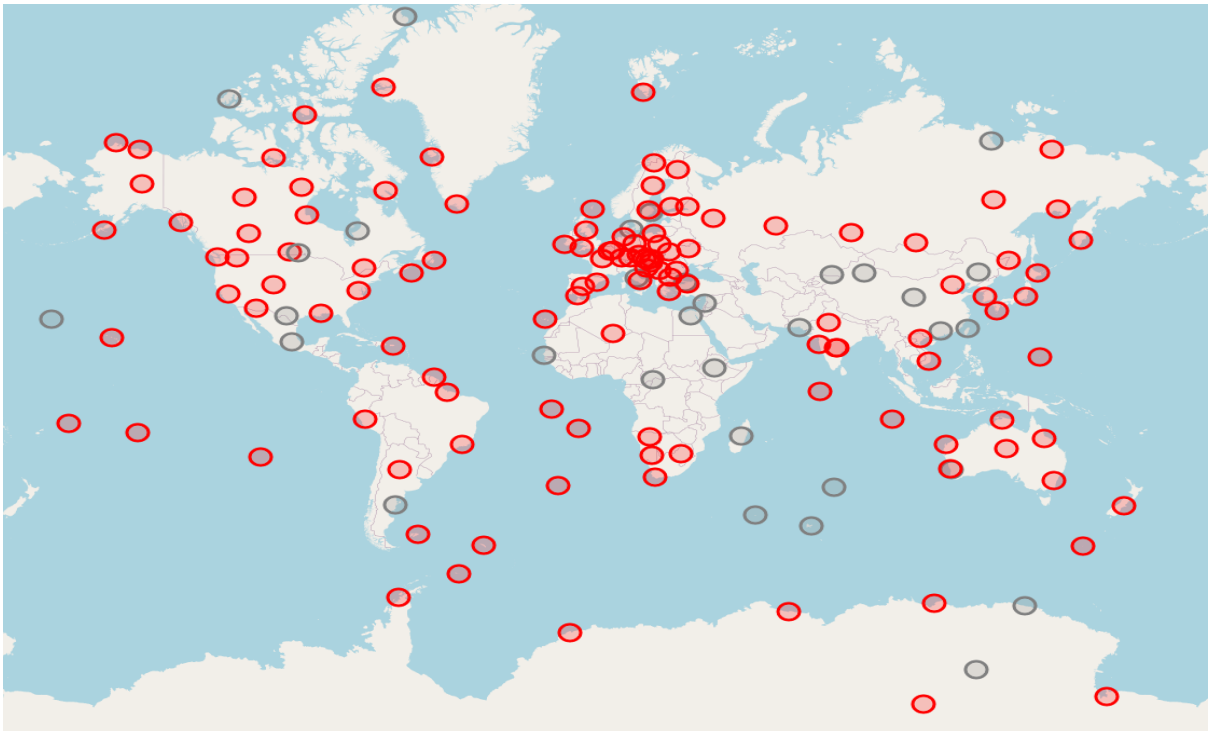

Figure 1.4: The map of magnetic observatories spread over Earth's surface. The red circles denote the active observatories whose data are available while the grey circles denote the observatories with status closed as on the INTERMAGNET website. Credit: INTERMAGNET

though the satellite attained a homogeneous coverage below 800 km, the field was not well resolved by only intensity information (Backus 1970). Almost a decade later, MAGSAT provided the first vector satellite measurements (e.g., Langel et al. 1980). The satellite operated for less than a year in a low altitude near-polar orbit and mapped well the core field. Next, after nearly two decades, the satellite Ørsted was launched (e.g., Olsen 2002). It was in a polar orbit providing data between 640 and 880 km altitudes for more than 15 years. The improved data set was used to model the main field and the SV. The relatively higher altitudes allowed the satellite to measure the rapid changes in the external fields. These measurements were followed by the CHAMP and SAC-C satellites data. Together, they provided continuous observations over different altitudes (e.g., Maus et al. 2006; Sabaka et al. 2015). This enabled to understand the fields from all the different sources and the changes over the years. Presently, two low Earth orbiting missions-CryoSat-2 and Swarm provide continuous magnetic data. The main purpose of CryoSat-2 was not magnetic observations (Olsen et al. 2020). However, it contains magnetometers whose data are regularly used complementary to other satellites, especially Swarm. The Swarm mission consists of 3 satellites and was launched in 2013. The mission delivers simultaneous high resolution data for the geomagnetic field that are regularly used to estimate magnetic models (e.g., Friis-Christensen et al. 2006; Thébault et al. 2016). The configuration of the 3 satellites provides efficient separation of the internal and external fields.

The observation and understanding of the geomagnetic field gives us an idea about the sources of the field. Figure 1.5 displays the internal and external sources. In summary, we have-
- the dynamo field in the deep interior due to convection in a conducting liquid,
- the induced field in the regions above it due to time-varying currents and the electrical properties of the interior,
- the crustal field at the surface due to magnetisation of rocks by the core field, and
- the external field that stems from particle interaction in space.

We now try to use our comprehension about the magnetic field and extend it to other planets. The next section discusses our current knowledge about the magnetism of the different bodies in the Solar System.

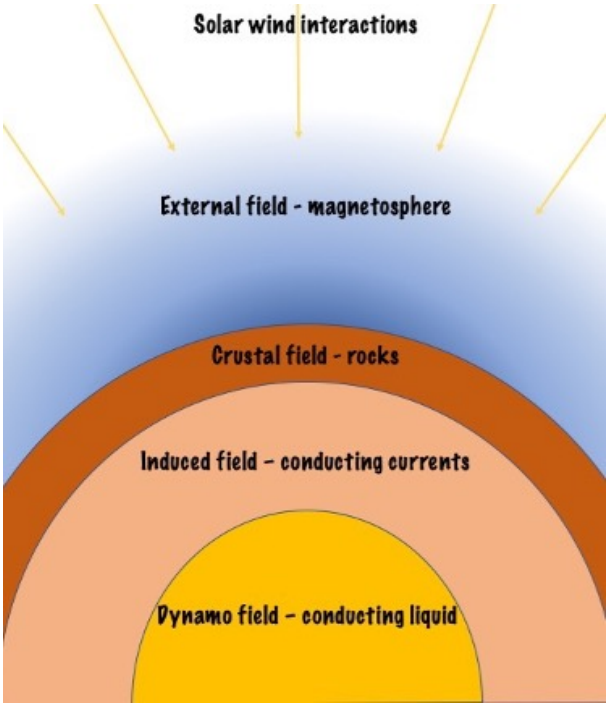

Figure 1.5: The planetary magnetic field sources. The core or dynamo field is generated by convection in a conducting liquid in rotation. The crustal field is associated with the magnetised minerals in the uppermost layer. The external field is produced by the currents in the magnetosphere which produces an induced field in the interior of planets depending on its electrical conductivity.

1.2 Planetary Magnetic Field

Most of our magnetic field observations for other planets come from satellites orbiting around them. For Mars and Moon, we also have or had magnetometers present on the surface as well as geological samples. While magnetometers and samples provide local measurements, the orbiting satellites have different configurations in space, establishing a global view of the planet. The data obtained are used to model the field that provide

information about the planet's interior. In addition, an indirect measurement of the magnetic field comes from radio emissions.

The planets in our Solar System are broadly categorised as either Terrestrial (Earth-like) or Gaseous (Jupiter-like) (Stevenson 2003). Terrestrial planets have a solid surface while gaseous planets are primarily composed of gases. But even though planets are characterised in two categories, their magnetic fields are similar to each other in terms of the sources and the generation of field. In particular, the core field is produced due to different materials in the interior for the terrestrial and gaseous planets but their characteristics are broadly similar. The majority of the field is due to the main field generated by convection in a conducting fluid. Although not all planets generate fields from all the 4 major sources, Figure 1.6 compares the magnetic field of the different planets with respect to the Earth's. In particular, the gaseous planets do not have a tangible surface and hence produce no crustal fields. On the other hand, almost all planets experience external fields due to the interaction with solar particles but the resulting induced fields are dependent on their interior. In addition to the planets, some moons also have their own or induced magnetic fields. In the following, we present a brief review of the current knowledge of each planet and some of their moons.

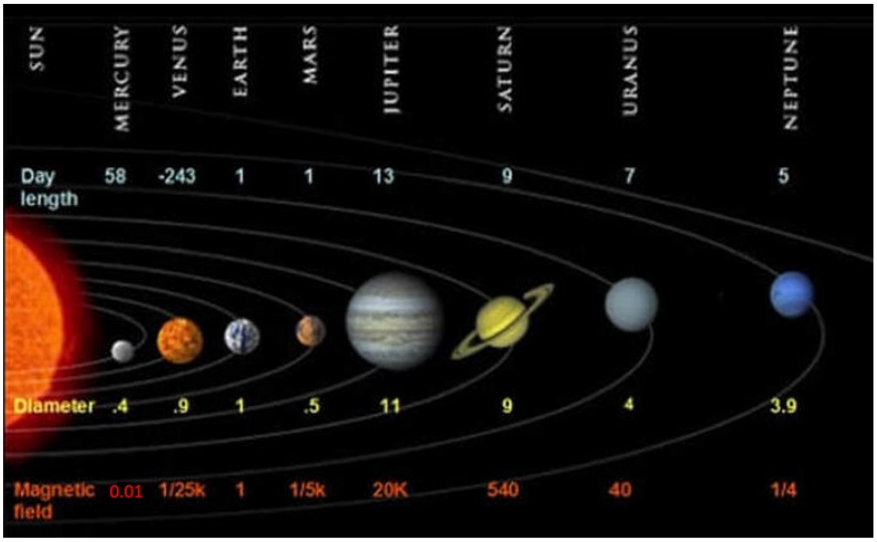

Figure 1.6: The planets in the solar system with their rotation period in days and diameter and strength of magnetic field as compared to Earth. Credit: Modified from NASA/S. Hanmer

Mercury

The smallest and first planet from the Sun is Mercury. It has a radius of about 2440 km and takes around 88 days to make one revolution. The first satellite to visit the

planet was Mariner 10 which revealed that its interior comprised of a core, mantle and crust (Breuer et al. 2007). Being much smaller in size, the presence of a dynamic (at present) magnetic field was not expected on the planet. However, the magnetometers onboard Mariner 10 and the next mission Messenger almost 30 years later measured the magnetic field of Mercury, albeit very weak. The observations and models derived from them tell us that it has a relatively weak dipole field, i.e., about two orders of magnitude lower than that observed on Earth (e.g., Ness et al. 1975; Anderson et al. 2011). The angle between the magnetic and rotation axes is less than 3° and the magnetic equator is about 400 km north of the geographic equator at the surface (Thébault et al. 2018). Due to the close proximity of the planet to the Sun, the external fields observed are strong. Analysis of the time-varying fields measured by Messenger reveal that the mantle electrical conductivity is up to 1 S/m and the core size is near 2060 ± 22 km (Wardinski et al. 2019). Mercury's field is dominantly axisymmetric but there are traces of non-axisymmetric core field near the high northern latitudes which are consistent with a stratified layer above the core (Wardinski et al. 2021). No SV has been detected so far on the planet. However, the data distribution and hence the observations of Messenger are biased towards the northern hemisphere. The results from the recently launched mission BepiColombo would overcome this and could provide further constraints about the field around the planet.

Venus

Venus is the second planet from the Sun and is considered Earth's twin because of their similarities in size and mass (Svedhem et al. 2007). One year comprises about 224 days on the planet. There have been many space missions targeted to study Venus at low and high altitudes, with some of them including a magnetometer. All these missions observed a well developed bow shock and ionosphere (Russell et al. 1979). The Pioneer Venus and Venus Express orbiter missions confirmed that the planet does not have a dynamo but it possesses an induced magnetosphere. The magnetotail of Venus resembles that of Earth in terms of plasma interaction with the field (Zhang et al. 2012). But despite being Earth's twin, it lacks a dynamo possibly due to non-convecting completely fluid or, contrarily, frozen core (Stevenson et al. 1983). However, there are currently many new missions under development for Venus like DAVINCI, VERITAS and EnVision, which might help bring some clues in order to better understand the absence of magnetic field.

Moon

Moon can also be considered as a terrestrial body given that its internal composition is similar to these planets. We know since a few decades from the Apollo and satellite missions that Moon does have crustal fields, although not intense. The generation of it however has many different theories, some of them being an iron core dynamo or an ancient magnetised core (Dyal et al. 1974). Magnetic field models using data from orbiters and landing sites display crustal field anomalies and simple external field geometries (e.g.,

Purucker 2008; Ravat et al. 2020). Electrical conductivity profiles of the upper and mid mantle estimated from orbiter data match those calculated from the Apollo landing sites. They constrain the conductivity to a maximum value of 0.1 S/m for depths ranging between 300 to 900 km below surface (Mittelholz et al. 2021).

Mars

Mars is the last of the terrestrial planets with a core, mantle and crust structure. Its radius is half the Earth's but its orbit period is double. There have been a plethora of missions to Mars which includes flybys, orbiters and landers. Out of the orbiters around the planet that provide a global spatial coverage and continuous data over years, there are only two satellites, namely MGS and MAVEN, that carried magnetometers. Additionally, the lander InSight also measures the field from its location near the equator. These revealed that the planet currently possesses no dynamo but has strong crustal fields (e.g., Acuna et al. 1998; Langlais et al. 2004), similar to the Moon. Interaction with the solar wind and the interplanetary magnetic fields forming a bow shock and plasma environment are also observed (Winterhalter et al. 2004). The magnetic data from the two orbiters are observed and used to model the remanent crustal fields. The fields, which are one order of magnitude higher than that observed on Earth at satellite altitudes, indicate the presence of a past dynamo (e.g., Acuña et al. 1999). The results from the InSight lander indicate that the values at the surface are even more intense. More about the interior of Mars and details about its magnetic field exploration are discussed in Chapter 6.

Jupiter

Jupiter is the first giant planet from the Sun. It is also the largest planet in the Solar System with its radius exceeding 10 times that of the Earth. Jupiter has a rotation period of about 10 hours and takes almost 12 years to make one revolution. It has been visited by various satellites flybys and gravity assists. There have been only two orbiter missions, Galileo and Juno, for the planet till now. All these satellites measured high intensity of magnetic field even at large distances from the surface (e.g., Smith et al. 1974; Connerney et al. 2018). Jupiter generates the highest planetary field with its magnetic axis at an angle of about 10° from the rotation axis. This inclination and the fast rotation of the planet has a significant effect on its natural satellites that is discussed below (Jia et al. 2010). The plasma environment and the external current system around the planet also has high intensities that extends up to its moons. The upcoming JUICE orbiter mission will provide more information about Jupiter's magnetosphere and its interaction with the Jovian satellites. The dominant internal field of Jupiter is termed as the dynamo field rather than the core field since the core is supposedly not the layer that generates this field. The interior of Jupiter and its magnetic field are discussed in detail in Chapter 3.

Saturn

The next planet is Saturn, with its radius just about 10,000 km smaller than Jupiter but its magnetic field about 100 times weaker. There have not been many flyby or orbiter missions to Saturn. Most of the information about the planet and its environment comes from its only orbiter Cassini, of the Cassini-Huygens mission, that was in orbit for over 10 years. The field of Saturn is similar to that of Mercury in terms of its axial symmetry. The dipole field axis is extremely aligned with the rotation axis and the magnetic equator is about 2000 km above the geographic equator (Burton et al. 2009). The axisymmetry makes it difficult to calculate its rotation rate. Similar to Jupiter, the external field system of Saturn is strong and affects its satellites. The magnetic data results suggest that the planet has a complex dynamo, with a primary deep and secondary shallower dynamo, that generates the magnetic field (Dougherty et al. 2018).

Moons of Jupiter and Saturn

The Galileon and Saturnian moons, like our Moon, have time-varying internally inducing fields. In particular, Jupiter's moons Ganymede, Europa and Callisto show large magnetic field intensities. The largest moon of our Solar System, Ganymede, even has its own magnetic field, very likely from a dynamo (Kivelson et al. 1996). Europa and Callisto show induced magnetic fields due to the periodically varying magnetic environment around them. The intensity of the induced fields indicates conductivity close to the surface that is best explained by subsurface oceans of salty liquid water (Khurana et al. 1998). Saturn's moons Titan and Enceladus, similar to Jupiter's Io are embedded in strong plasma environments. It is difficult to understand the fields observed at Titan due to its thick atmosphere (Saur et al. 2010). For Enceladus, the interaction of the plasma with atmospheric plume near the south pole generates the magnetic field (Dougherty et al. 2006).

Uranus and Neptune

The least studied and the most inaccessible planets of our Solar System, due to their large distances, are Uranus and Neptune. They are about 4 times the size of Earth but have very weak magnetic fields. Their fields are considered very different from the other two giant planets, but similar to each other in terms of strength and geometry. The rotation and magnetic axes are at angles larger than 40° and there is possibly nondipole dominance of the field (e.g., Ruzmaikin and Starchenko 1991; Holme and Bloxham 1996). Out of the many speculations, the reason for this is mostly attributed to a dynamo operating in a thin conductive convecting shell.

1.3 Thesis Overview

The focus of this thesis lies on understanding and interpreting the magnetic fields observed around Mars and Jupiter. We will now turn our attention to these two planets to study in-depth about them. We start off by a comparison with Earth in terms of position and other physical properties. We show them in Table 1.1 with the values in absolute numbers and relative to Earth.

Table 1.1: Comparison between the absolute and relative values of the physical properties of Earth, Mars and Jupiter. The unit for absolute values are provided in the first column while the relative values are subject to Earth.

	EARTH	**MARS**		**JUPITER**	
		absolute	relative	absolute	relative
Distance from Sun (A.U.)	1	1.52	1.52	5.20	5.20
Diameter (km)	12,742	6,787	0.53	142,984	11.21
Mass (10^{24} kg)	5.97	0.642	0.11	1,898	317.80
Density (kg/m^3)	5,514	3,934	0.71	1,326	0.24
Gravity (m/s^2)	9.8	3.7	0.38	23.1	2.36
Rotation Period (hours)	23.9	24.6	1.03	9.9	0.42
Day Length (hours)	24	24.7	1.03	9.9	0.41
Perihelion (10^6 km)	147.1	206.7	1.41	740.6	5.04
Aphelion (10^6 km)	152.1	249.3	1.64	816.4	5.37
Orbit Period (days)	365.2	687	1.88	4,331	11.9
Orbit Velocity (km/s)	29.8	24.1	0.81	13.1	0.44
Orbit Inclination (degrees)	0	1.8	-	1.3	-
Orbit Eccentricity (degrees)	0.01	0.09	5.60	0.05	2.93

Currently, one satellite around Mars and Jupiter each provides continuous magnetic field measurements from orbit. The 3 Swarm satellites provide the same for Earth. They give high resolution data for all the three planets. Table 1.2 compares the sources of the field for Earth, Mars and Jupiter as are known from our present knowledge. The external fields are observed on all the three planets. The inducing fields due to the external fields are however not yet observed on Jupiter. But they are observed on Jupiter's moons due to the external currents system. The crustal fields are also not observed on Jupiter. It is a gas planet and lacks a surface, in the proper sense of the word. We refer to the layer at the planet's radius as its surface instead. Earth and Jupiter both currently have a dynamo that generates the intrinsic field. A very important feature of the dynamo is its SV. Since Mars has no current dynamo, no SV can be estimated for it.

Table 1.2: Comparison between the present magnetic field sources of Earth, Mars and Jupiter.

	EARTH	**MARS**	**JUPITER**
Dynamo Field	Yes	No	Yes
Crustal Field	Yes	Yes	No
External Field	Yes	Yes	Yes
Internally Induced Field	Yes	Yes	Unknown

There are many questions that can arise from magnetic field observations and models. The obvious ones would be regarding the internal and external sources and how they affect the planet. The dynamo and its processes as well as time variations, the electrical conductivity of the minerals present in the deep interior, changes in the rotation rates and magnetic axes are just some of these questions. In this thesis, we attempt to answer the questions related to Jupiter and Mars using the information we extrapolate from our knowledge about Earth.

For Jupiter, we focus ourselves to understand the depth of the dynamo and the SV processes.
1) How deep is the magnetic field of Jupiter generated?
2) Are there any time variations in the field?
3) What is the morphology of the time variations of this field?

For Mars, we analyse and discuss the time-varying fields and how they can infer the internal conductivity.
1) Are the external fields around Mars significant?
2) What are the characteristics of this field?
3) How do they influence the Martian interior?

To answer these questions, we make use of models. The magnetic fields around the planets can be modelled according to their sources. They can then be used to obtain and predict information about their internal structure. Here, we will use Spherical Harmonics (SH) to estimate the models from the observations. The next chapter explains in detail the SH modelling and the results that can be extracted from the model.

This thesis is divided into two parts. The first part describes the magnetic processes in Jupiter and its internal field as the focus for understanding its dynamo and evolution. The second part concentrates on Mars and the ability of its time-varying fields to sound the mantle structure and conductivity. Both the parts contain three chapters each.

In Part I, Chapter 3 deals with the introduction and exploration of the Jovian magnetic field and the advantages of modelling using the magnetic data from Juno. Chapter 4 provides the details about the model obtained using SH for the Jovian field. Chapter

5 discusses the results obtained and the implications for the dynamo.

In Part II, Chapter 6 details the exploration of the Martian magnetic field using MGS and MAVEN and the differences between the two satellites. The crustal field removal and external field modelling is the focus of Chapter 7. The inversion technique of the Bayesian approach and the conductivity profiles are discussed in Chapter 8.

In a short and final part, the last chapter provides a brief conclusion and perspectives for future work for both planets.

2. Spherical Harmonic Analysis and Modelling

An inverse problem consists of estimating unknown parameters that are related by some theory to known values, mostly measurements. In planetary physics, we generally have no direct access to the physically relevant parameters at the desired locations but measure their effects outside the source region. Magnetic field can be generated by a large variety of electromagnetic phenomena and these sources occur on almost all spatial and temporal scales. The exact separation of the sources, a prerequisite for inferring planetary processes, is in magnetism one of the most challenging problems. A way to tackle the issue is to rely first on assumptions regarding the sources and then to describe them with mathematical functions in order to reproduce the measurements. The preliminary steps require the definition of a basis of complete (orthogonal) mathematical functions and a numerical inverse operation to estimate the coefficients of the mathematical description. These coefficients, or models, can be used to interpolate or extrapolate measurements at our desired locations.

2.1 Mathematical Description

We assume that measurements are acquired in regions free of electric currents. In reality, this assumption is not true for all measurements, especially in places where the spacecraft crosses electrically conducting sheets that are directly exposed to the solar wind. Hence, we always carry out a selection of the measurements (quiet measurements, spatially restricted to source free regions, etc.) to ensure the statistical conformity of this hypothesis.

From Maxwell's equations in a source free location, i.e., in the absence of any currents, we have (Langel and Hinze 1998)-

$$\nabla \cdot \mathbf{B} = 0 \tag{2.1}$$

$$\nabla \times \mathbf{B} = 0 \tag{2.2}$$

where, $\mathbf{B}$ is the vector magnetic field. Since the curl of a gradient is zero, the magnetic field can be expressed as the gradient of a magnetic scalar potential V as-

$$\mathbf{B} = -\nabla V \tag{2.3}$$

Using Equations (2.1) and (2.3), potential V satisfies the Laplace Equation-

$$\nabla^2 V = 0 \tag{2.4}$$

In spherical coordinates where r, θ and ϕ are the radius, co-latitude and longitude respectively, Equation (2.4) becomes-

$$\frac{1}{r^2}\frac{\partial}{\partial r}\left(r^2\frac{\partial V}{\partial r}\right) + \frac{1}{r^2\sin\theta}\frac{\partial}{\partial\theta}\left(\sin\theta\frac{\partial V}{\partial\theta}\right) + \frac{1}{r^2\sin^2\theta}\left(\frac{\partial^2 V}{\partial\phi^2}\right) = 0 \tag{2.5}$$

The solution of this equation for the potential, for internal (V_{int}) and external (V_{ext}) sources, is expressed in terms of an infinite series of Spherical Harmonics (SH) functions as (Gauss 1839)-

$$\begin{aligned} V(r,\theta,\phi,t) &= V_{int}(r,\theta,\phi,t) + V_{ext}(r,\theta,\phi,t) \\ &= a\sum_{n=1}^{\infty}\sum_{m=0}^{n}\left\{\left(\frac{a}{r}\right)^{n+1}\left(g_n^m(t)\cos m\phi + h_n^m(t)\sin m\phi\right)P_n^m\big(\cos\theta\big)\right\} \\ &+ a\sum_{n=1}^{\infty}\sum_{m=0}^{n}\left\{\left(\frac{r}{a}\right)^{n}\left(q_n^m(t)\cos m\phi + s_n^m(t)\sin m\phi\right)P_n^m\big(\cos\theta\big)\right\} \end{aligned} \tag{2.6}$$

where t is the time and a is the reference radius of the planet. The parameters of the series expansion $g_n^m(t)$ and $h_n^m(t)$ are the time-dependent internal field Gauss coefficients of degree n and order m while $q_n^m(t)$ and $s_n^m(t)$ are the external field coefficients, conventionally given in the units of nT. The $P_{n,m}(cos\theta)$ are associated Legendre functions (Ferrers 1877) and P_n^m are the Schmidt quasi-normalised associated Legendre functions (Schmidt 1917), defined as-

$$P_n^m(\cos\theta) = \begin{cases} P_{n,m}(\cos\theta) & \text{for m} = 0 \\ \\ \sqrt{2\frac{(n-m)!}{(n+m)!}}P_{n,m}(\cos\theta) & \text{for m} > 0 \end{cases} \tag{2.7}$$

where,

$$P_{n,m}(\cos\theta) = \frac{1}{2^n.n!}\left(1-\cos^2\theta\right)^{m/2}\left(\frac{d}{d\cos\theta}\right)^{n+m}(\cos^2\theta - 1)^n \tag{2.8}$$

The three vector components of the magnetic field in the radial, southward and eastward horizontal directions (B_r, B_θ and B_ϕ) are calculated from the negative gradient of the potential in spherical coordinate system as-

$$B_r = -\frac{\partial V}{\partial r}, \quad B_\theta = -\frac{1}{r}\frac{\partial V}{\partial\theta}, \quad B_\phi = -\frac{1}{r\sin\theta}\frac{\partial V}{\partial\phi} \tag{2.9}$$

SH have very interesting properties. They offer the most compact solution in spherical coordinates and they converge evenly over the sphere so that the resolution does not depend on the geographical position. Moreover, they offer a possibility to carry out a first order separation of the magnetic sources with respect to the reference radius $r = a$.

For example, if all the magnetic sources are confined within the sphere of radius a, the field must vanish at infinity and coefficients $q_n^m(t)$ and $s_n^m(t)$ become zero (Chapman and Bartels 1940).

The hypothesis can be further elaborated if we take into account the time changes of the magnetic field. For short time variations, for example, over a day, we can simply monitor the changes from one period to another assuming the field remains constant over a given period. But for longer time variations, we need to model them simultaneously with the field. Since we are mostly interested in describing the magnetic field deep inside the planet generated by a dynamo process, we assume that the spatial variations of these signals are mostly large scale and that their time variations are secular, i.e., ranging from months to years. In order to characterise the SV, magnetic field measurements should be available over at least a few years. The SV is the first derivative of the magnetic field with respect to time and, if enough accurate measurements are available, many more quantities such as secular acceleration (second time derivative) and higher order derivatives can be accessible. There are various methods for parameterising the time $\mathbf{t}$ and therefore for modelling the SV. The most versatile technique is to rely on piecewise polynomials such as B-Splines separated by knots at which continuity between the different pieces are ensured. B-Splines are convenient because they allow us to test the maximum time resolution and derivative accessible given a set of measurements. The time complexity can be tuned by simply modifying the spline order. Formally, a time series such as $g_n^m(t)$ for example, represented with i knots over the full time span and to order k can be expanded in splines $S_{i,k}$ such as-

$$g_n^m(t) = \sum_i \alpha_i S_{i,k} \tag{2.10}$$

For a spline order $k = 0$ with say, three knots, $i = 1 : 3$ at times t_1, t_2, and t_3, the coefficient $g_n^m(t) = \alpha_1$ in the interval $[t_1, t_2]$ and $g_n^m(t) = \alpha_2$ in the interval $[t_2, t_3]$. However, by continuity conditions at t_2, the Gauss coefficient has to be constant over the full time span. This is the static representation of the internal main field assuming no SV. For estimating a first order SV, we must work with at least splines of order 1 that will be piecewise linear in the intervals $[t_1, t_2]$ and $[t_2, t_3]$. Splines of higher orders will represent the time variations as being piecewise cubic, quadratic etc. However, we already see that increasing the complexity of the temporal variation implies involving a significant number of additional coefficients α_i for a given $g_n^m(t)$, which adds to the practical difficulty when dealing with a finite dataset of magnetic field measurements with geographical and temporal gaps. When we have all our coefficients defined, we can use it to understand the magnetic field.

2.2 Power Spectra and Model Terminologies

SH possess several important properties. These functions are orthogonal in the sense of the scalar product on a sphere. As a result, if measurements are perfect, infinite and

distributed over a sphere at a constant time t_0, we can formally estimate the parameters by a mathematical inverse problem. Let $V(\mathbf{r}')$ be the magnetic potential generated at radius $\mathbf{r}'$ fully known on a closed spherical surface
$\partial\Omega' : \{r', 0 \leq \theta' \leq \pi, 0 \leq \phi' \leq 2\pi\}$ and $d\partial\Omega' = r'^2 \sin\theta' d\theta' d\phi'$
and the SH $\beta_n^m = e^{im\phi} P_n^m(\cos\theta)$. Then, it can be shown that-

$$g_n^m(t_0) = \mathrm{Re}\left\{ \frac{1}{a \left\|\beta_n^m\right\|_{\partial\Omega}^2} \oint_{\partial\Omega'} V(\mathbf{r}', t_0) \left(\frac{r'}{a}\right)^{n+1} \beta_n^m(\theta', \phi') d\partial\Omega' \right\}, \tag{2.11}$$

$$h_n^m(t_0) = \mathrm{Im}\left\{ \frac{1}{a \left\|\beta_n^m\right\|_{\partial\Omega}^2} \oint_{\partial\Omega'} V(\mathbf{r}', t_0) \left(\frac{r'}{a}\right)^{n+1} \beta_n^m(\theta', \phi') d\partial\Omega' \right\}, \tag{2.12}$$

Similarly for q_n^m and s_n^m in Equation 2.6. This demonstrates that each coefficient is mathematically independent of all other coefficients but also independent of the radius r provided $V(\mathbf{r}')$ (respectively the magnetic field) is known on a closed surface. This property allows us to represent the magnetic field at any radius and in particular at the planet's surface or its core boundary, assuming there are no sources present in between. The same orthogonality property allows to calculate a magnetic spectrum, i.e. a quantity relating the energy of the signal to the wave number n, the SH degree where, in addition, it can be shown that (Backus et al. 1996)-

$$\lambda_n(r) \simeq \frac{2\pi r}{\sqrt{n(n+1)}} \approx \frac{2\pi r}{n + \frac{1}{2}}, \tag{2.13}$$

where $\lambda_n(r)$ is the characteristic spatial (horizontal) length scale corresponding to degree n at radius r. The Lowes-Mauersberger spectrum represents the magnetic field power spectrum per SH degree (Mauersberger 1956; Lowes 1974). For a given time, and at a given radius r, it can be defined as-

$$\mathcal{R}_n = (n+1)\left(\frac{a}{r}\right)^{(2n+4)} \sum_{m=0}^{n} [(g_n^m)^2 + (h_n^m)^2] \tag{2.14}$$

at SH degree n. Similarly, for the SV, where $\dot{g}_n^m$ and $\dot{h}_n^m$ are the SV Gauss coefficients, it can be defined as-

$$\mathcal{S}_n = (n+1)\left(\frac{a}{r}\right)^{(2n+4)} \sum_{m=0}^{n} [(\dot{g}_n^m)^2 + (\dot{h}_n^m)^2] \tag{2.15}$$

An example of the power spectrum is shown in Figure 2.1. It displays the main field spectrum of the geomagnetic field at the surface and the spectrum extrapolated to the core-mantle boundary (CMB). An important observation from this is the apparent break in the Earth's field near SH degree 13-14. The interpretation for this was that the core field dominates until degree 13 and the crustal fields dominate from degree 15.

Instead of the full spectrum calculated for all terms of a particular degree, partial spectra using restricted ensembles of parameters can also be defined. Most often, these conditions are defined using the degree and/or order of the model. The $m = 0$ terms

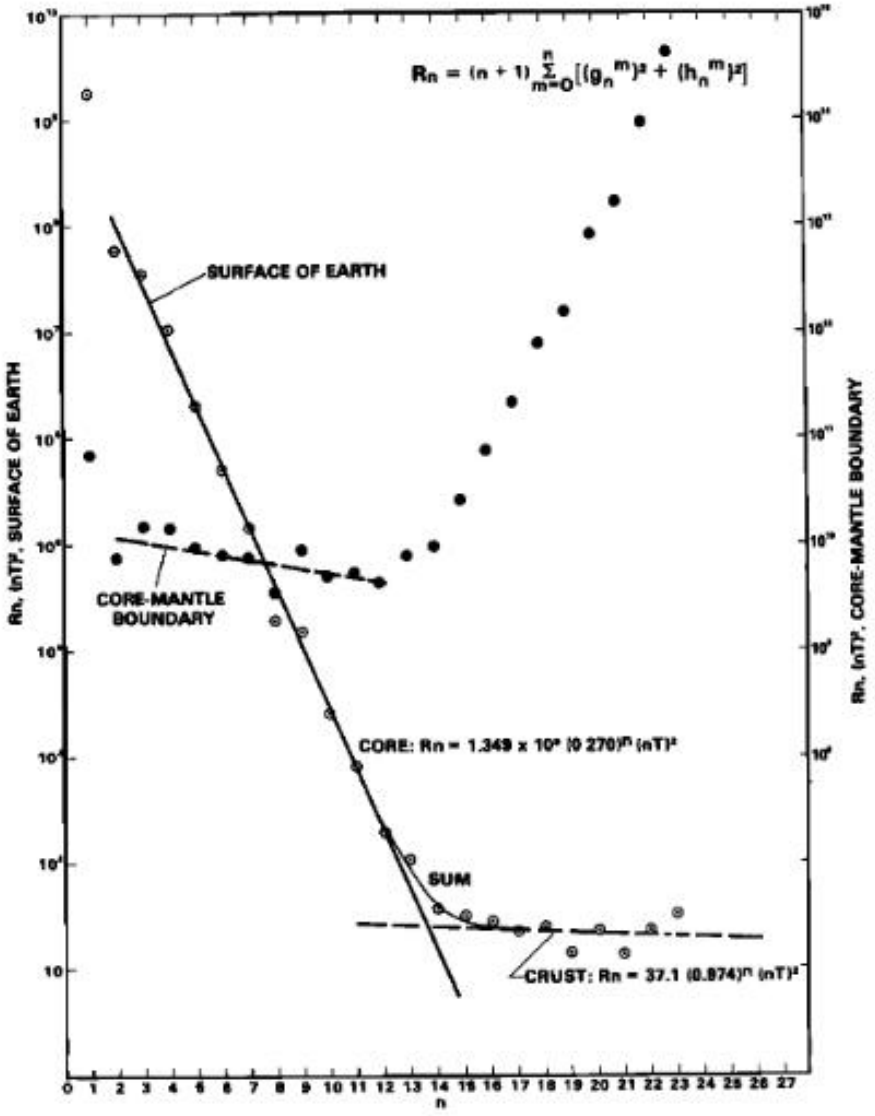

Figure 2.1: The power spectrum for the geomagnetic field from Langel and Estes (1982). The curves are fit to the surface results and extrapolated to the CMB.

are called the zonal terms or family that represent latitudinal bands on the sphere while the non-zonal ($m \neq 0$) terms indicate longitudinal bands. The zonal terms have no longitudinal (ϕ) component. The $n = |m|$ terms are called the sectoral terms while all the other terms are called the tesseral terms. Degree and order 0 term does not exist since there is no magnetic monopole. The degree 1 coefficients are the dipole terms, degree 2 are the quadrupole terms, degree 3 are octupole and so on. However, this should not be confused with the dipole and quadrupole families, which consist of coefficients corresponding to $n + m$ odd and even terms respectively (McFadden et al. 1988).

Figure 2.2 displays a visual presentation of SH using the example of the axial dipole term and the degree 4 coefficients. The inverse problem that is solved to obtain the model is discussed in the next section.

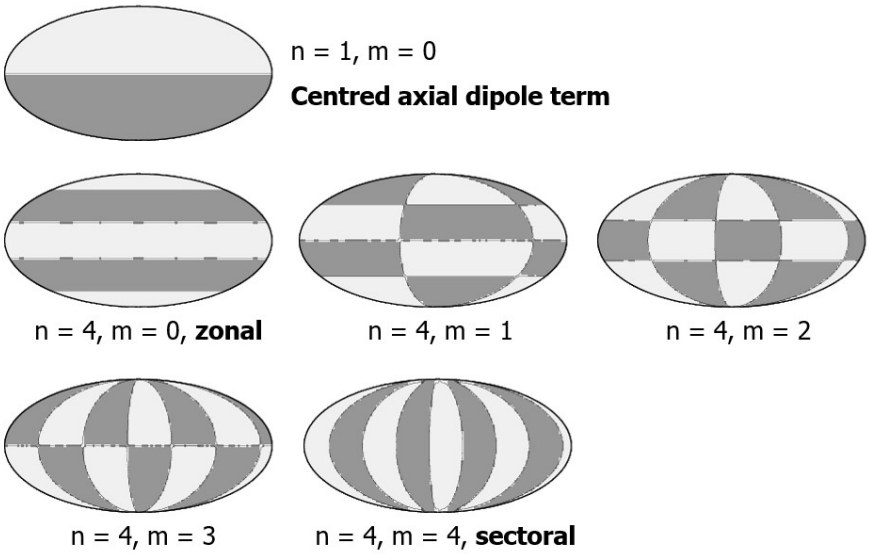

Figure 2.2: Visual representation of the SH degree 1 order 0 and SH degree 4 terms. The zonal terms are the m=0 terms, the n=|m| terms are called the sectoral terms while the other terms are referred as tesseral terms. Credit: B. Langlais

2.3 Solving for the coefficients

The mathematical definitions defined above require estimating reliably the Gauss coefficients at all degrees n and orders m, which represent an infinite ensemble (since the series is infinite). In practice, there is a need to truncate the series to a maximum degree expansion N (Gubbins 1983; Holme and Bloxham 1996). Numerically, when the number of measurements and their distribution differ from the ideal case, the mathematical inverse problem in Equation (2.11) can be approximated using linear algebra. As the Equation (2.6) is linear, the problem can be modelled by a system of linear equations. Let γ be the vector field components and $\mathbf{A}$ the design matrix with the SH. The Gauss coefficients to be estimated are represented by the vector m. The magnetic field measurements are therefore linked to the Gauss coefficients by-

$$\gamma = \mathbf{A}m + \mathbf{e} \tag{2.16}$$

where e is the vector of measurement errors (or misfits between the observations γ and the predictions of the field by the estimated model $\mathbf{A}m$).

The linear inverse problem is conveniently solved using a standard least squares method seeking to minimize the square norm (L2-norm) between the model and the measurements-

$$\Theta^2 = \|\gamma - \mathbf{A}m\|^2 \tag{2.17}$$

or, including a priori data error as a covariance matrix $\mathbf{C}_e$, it is-

$$\Theta^2 = (\gamma - \mathbf{A}m)^T \mathbf{C}_e^{-1} (\gamma - \mathbf{A}m). \tag{2.18}$$

The functional Θ^2 is minimized by taking the derivative of m-

$$\frac{\partial \Theta}{\partial \mathbf{m}} = 0. \tag{2.19}$$

If the inverse problem is overdetermined; i.e, when the number of measurements γ is larger than the number of parameters m, the solution $\widetilde{m}$ can be estimated by-

$$\widetilde{m} = (\mathbf{A}^T \mathbf{C}_e^{-1} \mathbf{A})^{-1} \mathbf{A}^T \mathbf{C}_e^{-1} \gamma \tag{2.20}$$

In the ideal case where enough measurements are available on a closed spherical surface, and for an isotropic and uncorrelated error where $\mathbf{C}_e^{-1}$ is diagonal and constant, $\mathbf{C}_e^{-1} = \sigma^2 \mathbf{I}$, the matrix $(\mathbf{A}^T \mathbf{C}_e^{-1} \mathbf{A})^{-1} = \sigma^2 (\mathbf{A}^T \mathbf{A})^{-1}$ is fully diagonal and invertible by virtue of SH. In practice, this is rarely the case, particularly for highly elliptic satellite missions, because of data selection rejecting measurements that do not comply with the source free assumption, and because of the time parameterization that introduces covariances between the parameters. To deal with such numerical issues, the symmetric and positive matrix $(\mathbf{A}^T \mathbf{C}_e^{-1} \mathbf{A})$ is decomposed by Singular Value Decomposition (SVD) (Lanczos 1950)-

$$\mathbf{A}^T \mathbf{C}_e^{-1} \mathbf{A} = \mathbf{U} \mathbf{S} \mathbf{U}^T, \tag{2.21}$$

where, $\mathbf{U}$ is the matrix of eigenvectors and $\mathbf{S}$ is the diagonal matrix of eigenvalues. The inverse matrix becomes-

$$\left(\mathbf{A}^T \mathbf{C}_e^{-1} \mathbf{A}\right)^{-1} = \mathbf{U}^T \mathbf{S}^{-1} \mathbf{U}, \tag{2.22}$$

where it is seen that the inversion depends on the numerical values of the diagonal elements in $\mathbf{S}$. The conditioning number, given by the ratio of the maximum to minimum eigenvalue should be as low as possible for a model. In the case of close-to-zero eigenvalue, the solution is solved using the pseudoinverse, or Moore–Penrose inverse ${}^{+}\mathbf{S}^{-1}$ and the inverse problem finally is-

$$\widetilde{m} = (\mathbf{U}^{T+} \mathbf{S}^{-1} \mathbf{U})^{-1} \mathbf{A}^T \mathbf{W} \gamma \tag{2.23}$$

where, for more generality, we also introduce $\mathbf{W}$ instead of $\mathbf{C}_e^{-1}$ to allow the possibility to perform a weighted least-squares inverse problem. This option is important if there are many more data in specific regions, for example near the poles as compared to the equator, in order to minimize biased solutions towards the concentration of data. Weights can be distributed according to the geographical distribution but also using other techniques relying on iterative statistics and error estimates. One such common technique is using Huber weighting distribution (Huber 1996), which is an iterative method designed to minimize the leverage of outliers using a hybrid error distribution between Laplacian and Gaussian (Olsen 2002; Thébault et al. 2015).

The effect of the Moore–Penrose inverse is estimated with the resolution matrix $\mathbf{R}$ indicating which parameters are constrained by the measurements and which are strongly regularized by the truncated SVD-

$$\mathbf{R} = (\mathbf{U}^{T+} \mathbf{S}^{-1} \mathbf{U})^{-1} \mathbf{A}^T \mathbf{W} \mathbf{A}. \tag{2.24}$$

When the matrix $\mathbf{R}$ is an identity matrix, all parameters are constrained by the measurements. The efficiency of the inverse problem can be checked in the spatial and time domains by computing maps of residuals but also using standard statistical estimates. The misfit residuals between the observations γ and the model predictions $\widetilde{\gamma}$ for N_d number of observations and N_p parameters is defined as-

$$\sigma = \sqrt{\frac{1}{N_d - N_p} \sum_{i=1}^{N_p} (\gamma - \widetilde{\gamma})^2} \tag{2.25}$$

This is the a posteriori standard deviation of the data error. Next, the bias b can be estimated by simply computing the mean residuals-

$$b = \frac{1}{N_p} \sum_{i=1}^{N_p} (\gamma - \widetilde{\gamma}) \tag{2.26}$$

When the measurements are fit to their error and if the mathematical model is a good approximation, the bias should be close to 0. The correlation coefficient r between the input and the predicted measurements is another indicator to check for systematic bias. Denoting the observations as γ and the predictions by $\widetilde{\gamma}$ and their means by $\overline{\gamma}$ and $\overline{\widetilde{\gamma}}$ respectively, the correlation coefficient r is-

$$r = \frac{\sum_{i=1}^{N_d} (\gamma_i - \overline{\gamma})(\widetilde{\gamma}_i - \overline{\widetilde{\gamma}})}{\sqrt{\sum_{i=1}^{N_d} (\gamma_i - \overline{\gamma})^2} \sqrt{\sum_{i=1}^{N_d} (\widetilde{\gamma}_i - \overline{\widetilde{\gamma}})^2}} \tag{2.27}$$

Finally, the model coefficients are provided with their covariance error matrix using the data standard error estimate (Equation 2.25)-

$$\mathbf{C}_g = \sigma^2 (\mathbf{U}^{T+} \mathbf{S}^{-1} \mathbf{U})^{-1} \tag{2.28}$$

The Jovian Case

3. Jovian Exploration

Jupiter is the largest planet in the solar system with an equatorial radius of 71,492 km (1 R_J) at a distance of about 5.2 AU from the Sun. This chapter starts with a brief review of the current knowledge about the Jovian interior, dynamics and its magnetic field. We then present the various spacecrafts that visited Jupiter and discuss some of the magnetic field models obtained from them, in particular, using Juno.

3.1 The Interior and Dynamics

In the absence of data, we expand the theories of currently understandable objects to the desired target objects. And, in the absence of abundant data, models are extremely useful. The accepted models are those that best fit the constraints demonstrated by the measurements. For Jupiter, the theories state that it is gaseous and the composition is similar to that of the Sun. The interior is primarily composed of hydrogen and also helium (e.g., Wildt 1938; Demarcus 1958). The first constraints for subsequent models were provided by radius and gravitational harmonics using satellite missions data (e.g., Campbell and Synnott 1985; Hubbard and Marley 1989). Gradually, more constraints were added like the mass fractions of hydrogen and helium (Guillot et al. 1997). The different theories and models and their evolving knowledge from new data give us a good estimate of the present interior structure of the planet.

Interior Structure

The interior of Jupiter can be described as a core surrounded by fluid envelops. The core can be assumed to be dense and made up of ice and rocks while the envelopes consist primarily of liquid metallic and molecular hydrogen layers along with helium (Guillot 1999, 2005). Even though the size of the core is unknown, it should be small but with very high densities and temperatures. Its mass must be less than 10 Earth masses. Above the core, the envelops contain heavy elements along with the different phases of hydrogen. The exact reason for the phase change of hydrogen inside Jupiter is uncertain. Due to the high pressure inside the planet, hydrogen exists in a highly conductive metallic form. On the other hand, the outer layers are at lower temperatures and pressures, and hydrogen exists in molecular form here. The boundary between the metallic and molecular hydrogen is not a properly defined one but is a gradual transition

with the inner envelop being more helium rich than the outer layer. The transition layer was assumed to be narrow due to helium being insoluble in metallic hydrogen at low pressures. However, demixing temperatures might rise with pressure and increase the thickness of this layer (Pfaffenzeller et al. 1995). The molecular hydrogen extends up to the atmosphere, and the 1 bar pressure layer is assumed to be the surface.

Simulations and laboratory measurements have tried to study and understand the transition layer. First-principles simulations by Morales et al. (2013) suggested that the phase change in hydrogen first undergoes a liquid-liquid transition between molecular and atomic liquid. The molecular dissociation in liquid hydrogen through this transition occurs at high pressures and below critical temperatures of about 1500 K. An experimental study by Brygoo et al. (2021) attempted to estimate the thickness of the transition. They placed the hydrogen-helium demixing layer between the depths of 0.68 and 0.84 R_J. To mimic the Jovian interiors, they used pre-compressed hydrogen-helium samples in diamond-anvil cells and shock compressed them using laser pulses. They estimated that 15% of the radius is affected by the phase separation.

Recent studies, mostly using Juno gravity data, put some more constraints on the interior model of Jupiter. The gravity field of Jupiter is not hemispherically symmetric but displays a north-south asymmetry (Iess et al. 2018). This means that there are components corresponding to atmospheric and internal dynamics due to the flows at the interior in addition to solid body rotation. Hence, the gravity fields can be linked to atmospheric flows or winds and, the interior. The zonal winds can be understood using the odd zonal harmonics of the gravity fields while the even gravitational harmonics can be used to constrain the planet's radial density profile. The zonal winds are winds that flow east-west along a constant latitude. The gravity values can be inverted to obtain a wind field. Using a vertical decay profile, Kaspi et al. (2018) showed that the zonal winds decay in amplitude as they go deeper. They dissipate at a depth of about 3000 km below the surface. This corresponds to about 0.95 R_J. On the other hand, from the even harmonics, Jupiter's density profile has been used to describe a dilute core. Wahl et al. (2017) suggested an extended dilute core from 0.3 to 0.5 R_J due to the heavy materials getting dissolved in the metallic hydrogen. They used numerical simulations of the hydrogen-helium mixtures and compared the results to Juno's gravity measurements. The measurements were best explained by the simulations using a dilute core. Militzer et al. (2022) considered their dilute core up to 0.63 R_J to match their model to the gravity harmonics observed by Juno measurements. In addition, they assumed an ab initio equation of state and a wind model. The dilute core includes a stably stratified layer where the abundance of heavy elements decrease.

For a comparison of how different interior models of Jupiter evolved with time, Figure 3.1 displays the models of Guillot (1999), Wahl et al. (2017) and Brygoo et al. (2021).

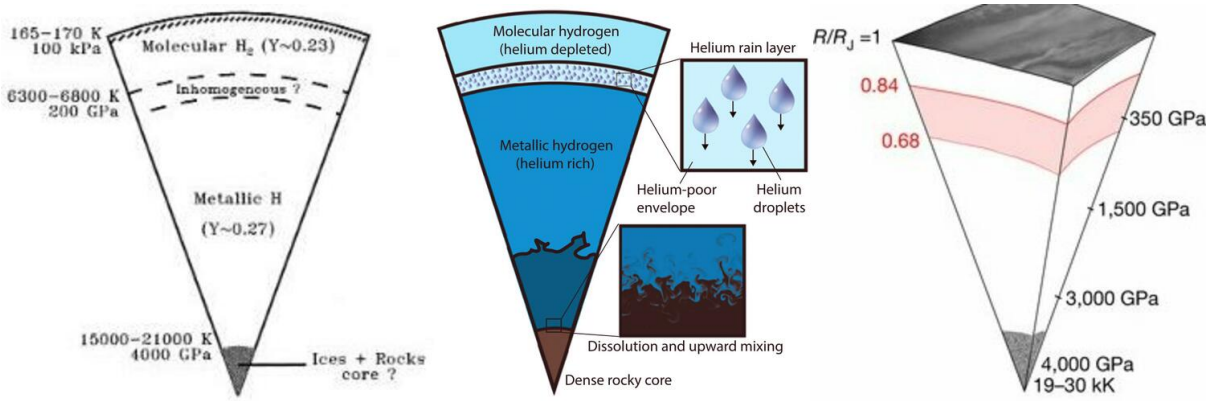

Figure 3.1: The constraints on the interior of Jupiter as defined in Guillot (1999), Wahl et al. (2017) and Brygoo et al. (2021) respectively. The Y in the first figure represents the helium mass mixing ratio.

Dynamics

The rotation rate of Jupiter is about 9 hours 55 minutes but the gases rotate differently at different latitudes (Hubbard 1982). The zonal winds have maximum amplitude at the equator. The atmospheric rotation at the poles is similar to that of the deep interior and is much slower than that at the equator. The rapid rotation and winds of the planet forms a large vortex on the visible surface, called the Great Red Spot. It is located at the latitude 22.5° south of the equator with speeds exceeding 100 m/s (Marcus 1993).

The movements of the fluids inside Jupiter transport heat by convection and the very high temperatures and pressures inside the planet renders it electrically conducting (Jones 2011). The dependence of the electrical conductivity in the interior to different concentrations of helium is insignificant (French et al. 2012). Therefore, assuming constant helium fraction values in the outer and inner layers, ab initio simulations show that the conductivity essentially dies down in the nonmetallic regions. Hence, the source of Jupiter's dynamo is the convection in the conductive liquid metallic hydrogen that produces predominantly dipolar fields.

Jupiter's dynamo also generates high intensity non-dipole fields. Numerical simulation models tried to replicate dynamo reversals similar to the geomagnetic field, but there is no observational proof available to match them (Jones 2014). The depth of the dynamo from numerical simulations is hinted being very close to the surface and suggests a stable stratification layer (e.g., Duarte et al. 2018; Tsang and Jones 2020; Gastine and Wicht 2021). Wicht et al. (2019) studied the decaying electrical conductivity with depth using these models and predicted the flow in this decay region to be diffusive. Wicht and Gastine (2020) proposed a two-stage dynamo action- a deep dynamo with high conductivity produces the dipole dominated dynamo while a shallow dynamo operates where the conductivity is lower. The recent model of Militzer et al. (2022) also assumes a two stage dynamo, each followed by a stably stratified layer. However, while the metallic hydrogen layer is part of the deep dynamo in Wicht and Gastine (2020), the layer is the source of

secondary dynamo in the model of Militzer et al. (2022). It would be interesting to see and compare the results we obtain about the dynamo using magnetic field measurements.

3.2 Magnetic Observations

Though most of our present knowledge about the magnetism of Jupiter derives from observations and models from satellite data, the first measurements were obtained through radio emissions. In early 1955, radio emissions were detected that were concluded to have come from Jupiter (Burke and Franklin 1955). However, it was only after a few years that this and other subsequent emissions were understood to be evidences of magnetic field (e.g., Warwick 1964, 1967). The accepted explanation for the source were particles trapped in the Jovian magnetosphere. Inferences about the magnetic field were made using the observations. From the polarization of the emission, the dipole moment was found to be parallel to the rotation axis, which meant a north-south magnetic axis for Jupiter. This was opposite to that observed on Earth. Additionally, variations in the radiation (or radio emissions) suggested that the magnetic axis was titled at about 9° to the rotation axis (Morris and Berge 1962). Assuming that the radio sources had a constant period, the mean rotation rate was estimated to be 9 hours 55 minutes 29.37 seconds with error of about a second (Douglas and Smith 1963). Next, Jupiter's magnetic field was measured in-situ through magnetometers onboard various flyby and orbiting satellite missions, which largely confirmed these indirect conclusions.

3.2.1 Before Juno

The 1970s proved a crucial and exciting time for the Jovian exploration in space. Four space probes carrying magnetometers returned data, measured from around the planet, using which magnetic models were derived. The observations made by the flybys of the Pioneer 10 and 11 satellites in 1973 and 1974 respectively provided the first estimates of the magnetic field. Together, the two satellites provided measurements from radial distances ranging between 1.6 to about 175 R_J. The field measured at closest distances was near 10^5 nT while the higher altitude measurements suggested presence of high thermal plasma and current sheets around the planet (Smith et al. 1974; Van Allen et al. 1974; Smith et al. 1975). These measurements were used to model the internal and external fields. The next visits were by the flybys of Voyager 1 and 2 in 1979. Voyager 1 had a slightly higher periapsis of about 4.9 R_J and Voyager 2 observed data from beyond 10 R_J. Perturbation fields due to Jupiter's interaction with its satellites were observed (Ness et al. 1979a,b; Connerney et al. 1982).

The perturbed fields are best described by modelling the azimuthal current system aligned with the magnetic equatorial plane as a magnetodisk. The magnetodisk is the region surrounding Jupiter which comprises charged particles and plasma (Connerney et al. 1981; Khurana 1992). The SH modelling did not work with these satellite trajectories in Jupiter's magnetosphere since there were no measurements in source free locations.

Instead, a model describing a thin disc is used to represent it. The parameters used to define the models are mostly the inner and outer radius of the disc and its thickness. A current density constant and the angles of the current system are also defined. The external field models extend to more than 30 R_J beyond the surface. At a distance of 15 R_J, the magnetodisk measurements are comparable to the internal fields.

The next magnetic flyby data came from the Ulysses probe more than a decade later in 1992 at the closest approach of about 6 R_J. The dipole term and magnetodisk currents values required to fit the data to the models using this satellite were a little lower than the previous models, but still similar to the values obtained by the other spacecrafts. None of the satellites showed any evidence of SV (Balogh et al. 1992; Connerney et al. 1996; Dougherty et al. 1996). Ulysses made another flyby around Jupiter in 2004, but from very large distances. The results from all these flybys were consistent with those observed from the emissions. The dipole tilt was estimated anywhere between 9 and 11 degrees with the rotation axis while the dipole moment was in the range of 4x10^5 nT. Magnetic models up to degree 3 were reliably estimated. Two other missions, Cassini-Huygens and New Horizons made flybys around Jupiter but did not provide any magnetic measurements.

The first orbiting satellite around the planet, Galileo, was launched in October 1989 (Russell 2012). It was also the first satellite to orbit an outer planet and provided measurements around Jupiter and its moons from 1995 to 2003. Including the initial and final orbits, it made 36 passes around Jupiter including flybys to Ganymede, Callisto, Europa, Io and Amalthea. Galileo was in an elliptical orbit that acquired data at mostly low latitudes and high altitudes. It was designed to understand the Jovian system that includes the planet and its vast magnetosphere but also its natural satellites. Galileo made important observations for Jupiter's moons. It discovered the intrinsic magnetic field around Ganymede (Kivelson et al. 1996) and induced fields attributing to subsurface oceans for Europa and Callisto (Khurana et al. 1998). The data across 8 years presented the opportunity to detect possible time variations. However, the spatial coverage of the orbiting satellite was not very suitable to model a global SV using its data alone (Yu et al. 2010).

Since a SV model was difficult to obtain using only Galileo measurements, Ridley and Holme (2016) estimated a model using magnetic observations from all satellites that visited Jupiter. The data used was spread over three decades, albeit inhomogeneously (Figure 3.2). There were no data available near to the poles or the high-latitudes above 50°. In order to minimise external fields, measurements used were below 12 R_J. But even the lowest altitude data were at radial distances of about 1.75 R_J. Most of the selected data were at high altitudes and from the Galileo mission. For the external field corrections, each orbit was modelled using a magnetodisk model. Two SH models were computed using regularisation of minimum norm- Jupiter constant field (JCF) and Jupiter secular variation (JSV). The JCF model assumed observations with no time variations and had only main field coefficients while the JSV model accounted for field change and co-estimated the SV with the main field. They used three levels of damping

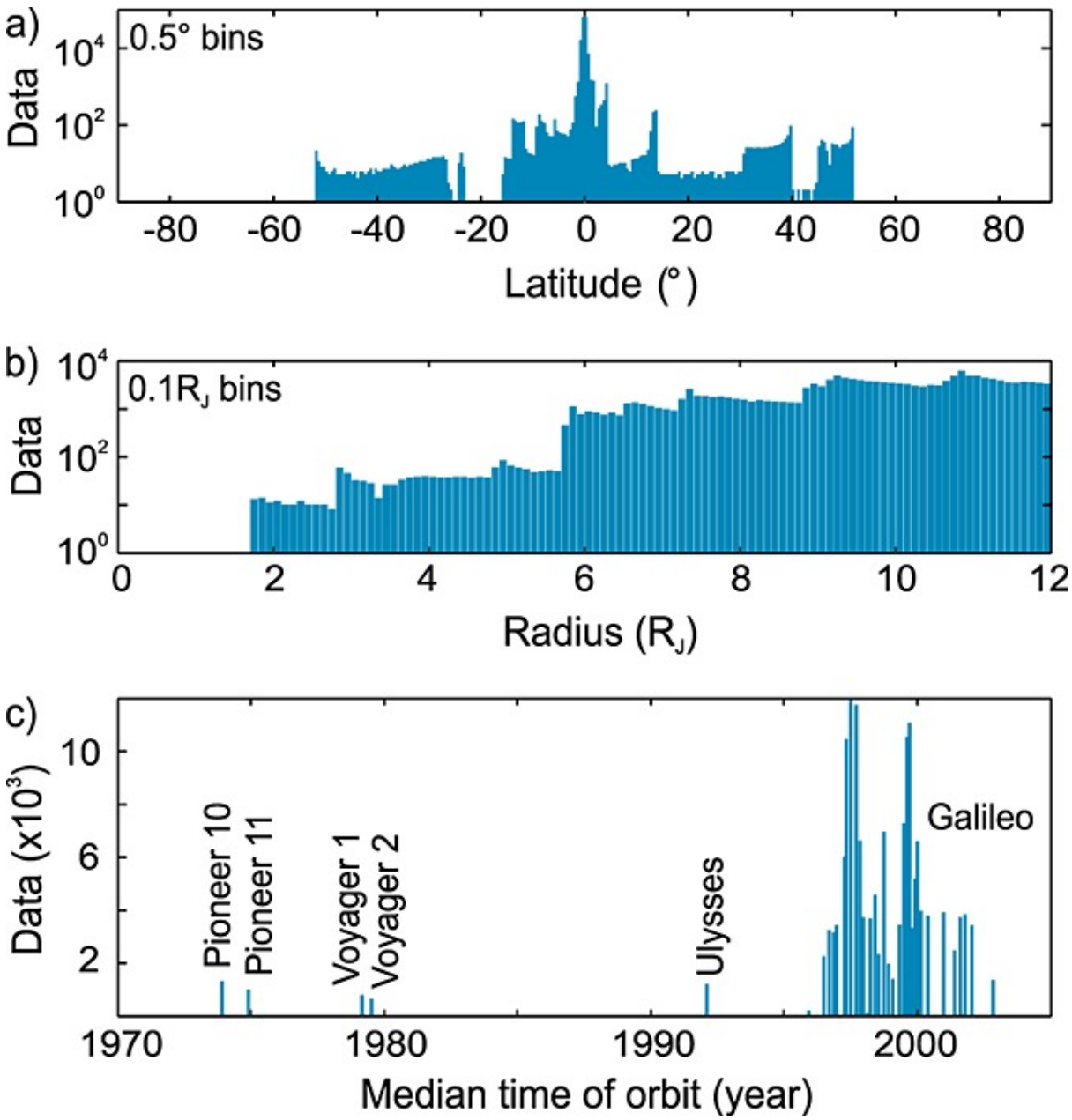

Figure 3.2: Distribution of the used data set from Ridley and Holme (2016) for their magnetic field modelling with respect to (a) latitude, (b) radial distance from Jupiter and (c) time.

for smoothing their models. The intermediate damping model was preferred. The JSV model was considered better because of its lower residuals and greater smoothness. Table 3.1 displays the degree 1 terms for this magnetic model. The power spectrum at the surface for the SV was noted highest for the quadrupole term after which it decreased with degree. The model to data misfits for near planet measurements ranged between 400 to 800 nT for the three vector components. The maximum field intensity, as well as the change in the field intensity over the data interval, observed using the model was in the northern hemisphere with magnitudes 1.7x10^6 nT and 1.11x10^5 nT respectively. They assumed two values of the dynamo radius at 0.85 and 0.90 R_J to map the field

and SV. They indicated possibilities of reversed polar flux patches that are related to tangential cylinders as is the case for the geomagnetic and hermean field (Olson and Aurnou 1999; Wardinski et al. 2021). Both their models were constructed up to degree 7 but they considered their main field model to be reliable up to degree 5 and their SV model reliable only up to degree 2.

What was needed for better modelling of both the main field and the SV was data improvement in terms of coverage. None of these satellites provided data near the poles or the surface. This was overcome by the recent Juno mission.

3.2.2 Juno

Juno space probe was launched on August 5th, 2011 and entered Jupiter's orbit in July 2016 (Bolton et al. 2017). The scientific goals of Juno includes understanding the origin and interior of Jupiter as well as its atmosphere. The spacecraft weights 3625 kg and is powered by three solar arrays of length 9 m each. It carries 8 scientific instruments which includes particle detectors, radiometers and a camera among others. The detectors and spectrometers provide a fair idea about the atmosphere while the interior structure can be understood using the gravitational and magnetic measurements. The two fluxgate magnetometers are located on one of the three solar arrays and measure the vector magnetic field (Figure 3.3).

Juno is the first satellite with a polar orbit around the planet. Its trajectory is highly elliptical with one complete orbit taking about 53 days until orbit 34 and about 43 days after. The orbit apoapsis exceeds 100 times Jupiter's radius while the periapsis is near 2500 km above surface (or, radius 1.03 R_J). The orbits were designed such that the satellite covers the entire planet. The first few orbits were placed 90° apart and the subsequent orbits reduce the longitudinal spacing by half to obtain data from the gaps left previously. Juno has completed 38 orbits and data are available for all except the second. Currently, the orbits are separated less than 11° apart in longitude. The consecutive periapsis shift northward one degree in latitude starting from the equator. The variation of the periapsis with respect to longitude, latitude and altitude for all 38 orbits are shown in Figure 3.4. An orbit change occurred between perijove 34 and 35 to reduce the orbit period of Juno. This resulted in the longitudes of the periapsis of these orbits to be similar, as opposed to the almost constant longitudinal spacing before.

The magnetic measurements observed by the satellite have already been used to propose recent models of the Jovian field. Connerney et al. (2018) provided an internal field model up to degree 10 using the first 9 orbits. The external fields were treated using magnetodisk models. Data was available for 8 orbits that were separated 45° apart in longitude. The model was estimated up to degree 20 but determined well only up to degree 10. The dynamo radius was estimated at 0.85 R_J using the main field spectrum from degrees 2 to 10. An updated external magnetodisk field model using Juno's first 24 orbits was also made available (Connerney et al. 2020). The internal field was fixed using the above discussed internal field model up to degree 10. The best fit to the magneto-

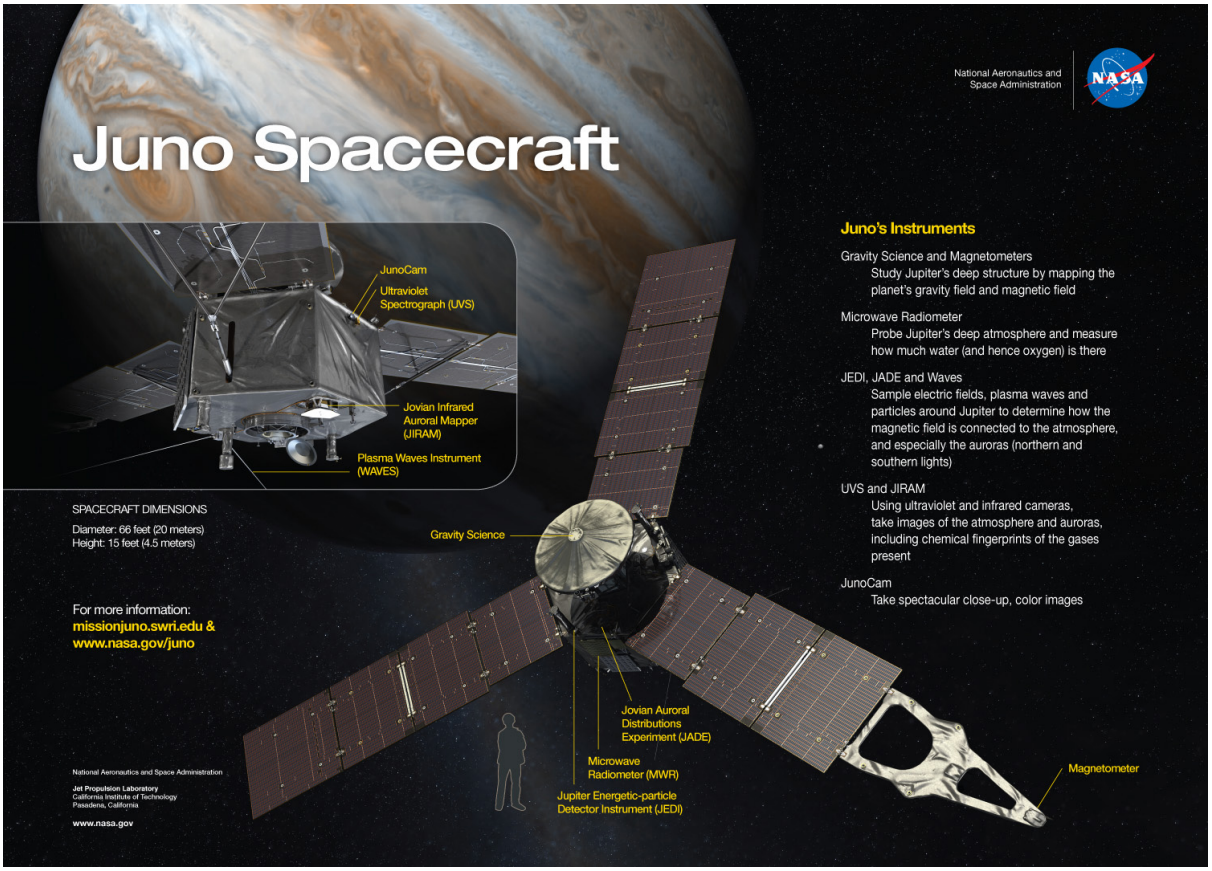

Figure 3.3: The instruments onboard the Juno spacecraft. The scientific payload includes a gravity science system, microwave radiometer, plasma and energetic particle detectors, spectrometers, stellar reference unit and a color imager. The two magnetometers are located at the end of one of the three solar panels. Source: NASA

spheric current model came from inner and outer radius of 7.8 and 51.4 R_J respectively. A similar magnetodisk model also using the first 24 orbits and the degree 10 internal model was provided by Wang et al. (2021). They stated that fields between 10 and 50 R_J were governed by the magnetodisk model while solar winds control the shape above this region. The data below 10 R_J is dominated by the dynamo field. The initial internal field model was later updated by Connerney et al. (2022). They calculated a static model up to degree 30 for internal and degree 1 for external, using the first 33 orbits. Their model was estimated up to degree 30 but was well resolved until degree 13 though they stated that some information could be retained until degree 18. They used near planet data within 2.5 R_J to obtain a normalised model. They determined the dynamo radius at 0.806 R_J using a straight line fit to the power spectrum from degrees 3 to 17. The degree 1 coefficients for both the internal models are displayed in Table 3.1 while the radial surface field map from the latter model is displayed in Figure 3.5. The two internal field models were subtracted to provide evidences of temporal changes in the field, especially near the equator.

Additionally, Moore et al. (2018) suggested SV to be of the order of 10^4 nT/year with the field displaying hemispheric dichotomy. The non-dipole field is confined to the

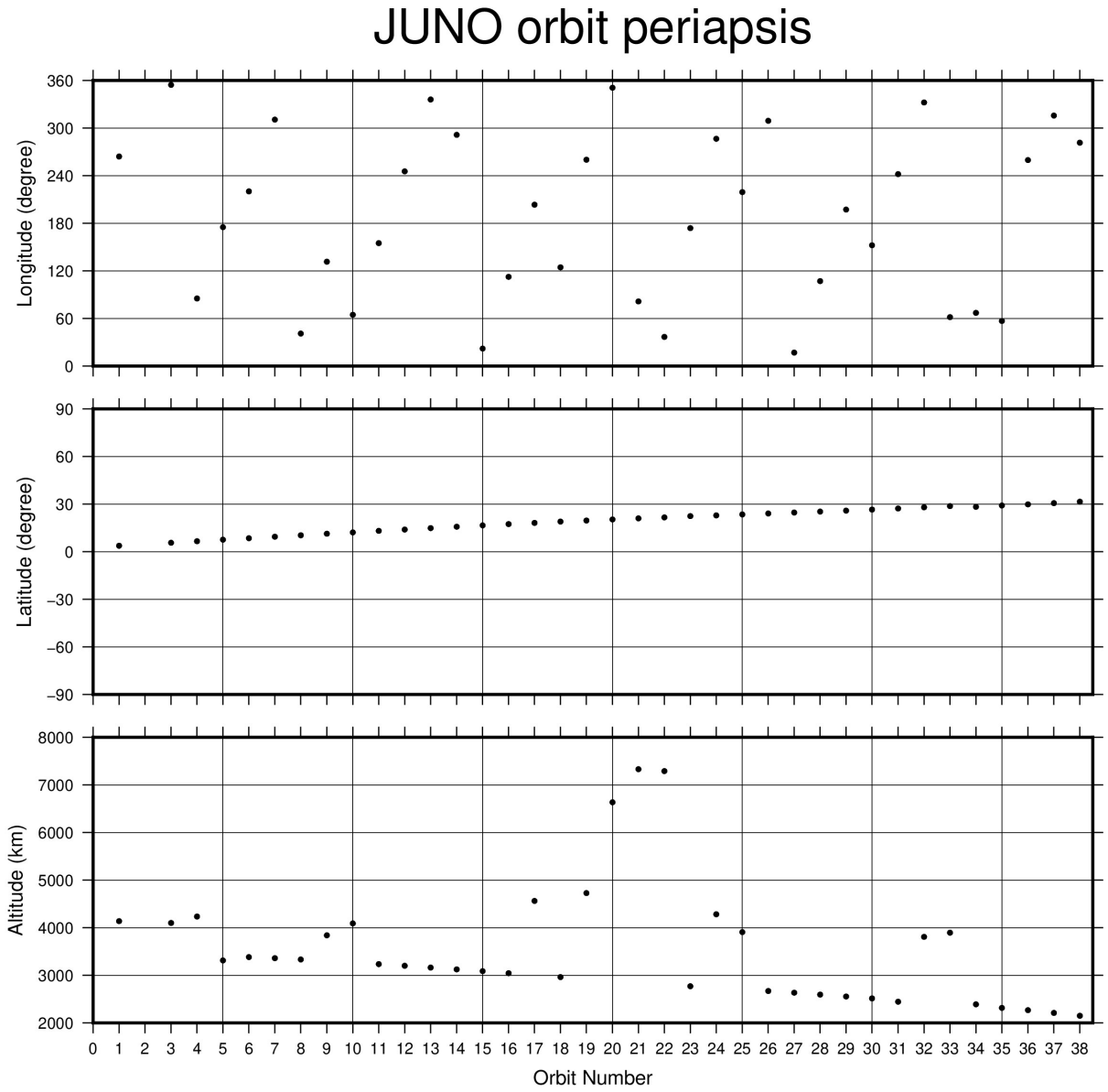

Figure 3.4: The periapsis variation with respect to longitude, latitude and altitude for the first 38 Juno orbits. Data is not available for orbit number 2.

northern hemisphere while the southern displays mostly dipole fields, possibly due to radial variations. Moore et al. (2019) estimated the field change over a 45-year time span which revealed temporal change of an intense magnetic flux patch near the equator. They explained the cause of the SV to be advection due to zonal winds. This would result in the axial dipole changing more slowly than the other components. Dietrich et al. (2021) argued about advection being the sole driver of the SV. Their preferred zonal wind model extends deeper and has large amplitudes that do not match SV based only on advective flows. Bloxham et al. (2022) suggested both advection and diffusion as sources with flows associated with magnetoconvection and surface zonal wind penetration. They inverted the main field along with a latitude dependent zonal drift of the field and noticed two prominent SV regions. The patch near the equator was consistent with previous results

while another was observed in the northern hemisphere. The radial SV on the surface from their model is displayed in Figure 3.6. None of the existing models based on Juno data attempted to model the global temporal variation of the field with the main field simultaneously.

Table 3.1: Degree 1 terms (g_0^1, g_1^1 and h_1^1) for the Jovian magnetic field models by Ridley and Holme (2016), Connerney et al. (2018) and Connerney et al. (2022).

Terms	Ridley and Holme (2016)	Connerney et al. (2018)	Connerney et al. (2022)
g_0^1 (nT)	409620.37	410244.70	410993.40
g_1^1 (nT)	-68257.07	-71498.30	-71305.90
h_1^1 (nT)	23845.92	21330.50	20958.40

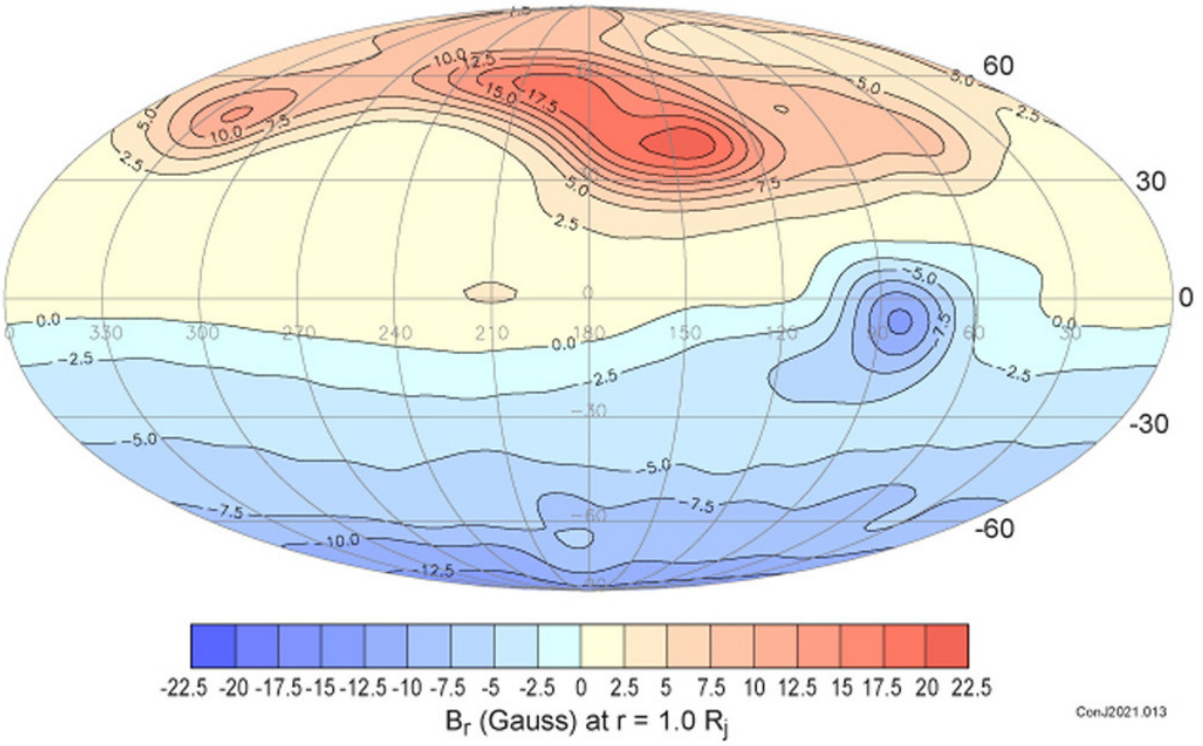

Figure 3.5: Contours of the radial magnetic field in Gauss (1 G = 10^5 nT) at the surface of Jupiter in Mollweide projection from Connerney et al. (2022). Contour intervals are chosen to span 7-9 contour levels in the northern hemisphere.

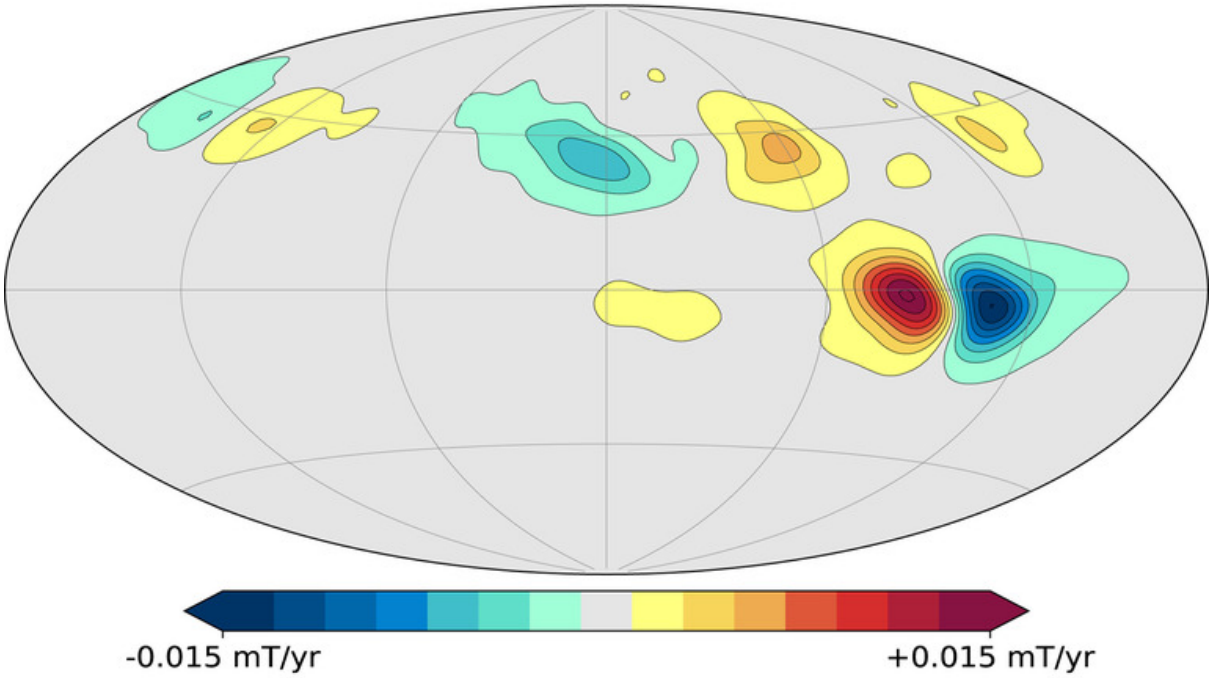

Figure 3.6: Secular variation of the radial component of the field (1 mT = 10^6 nT) at the surface from Bloxham et al. (2022).

4. Internal Field Model

This chapter applies the SH analysis discussed in Chapter 2 on the Juno observations for synthetic and real field data inversion. We start with the discussion of the Juno data used in this study. Our aim is to choose data suitable for modelling the internal dynamo field. For synthetic inversion, we make use of a geomagnetic model to predict values at Juno locations. We then invert the results to obtain a model and compare it to the original model used. The results for the synthetic model as well as some comparison tests performed on it are discussed. We then use our understanding about the data and inversion on the real field measurements to estimate an internal field and SV model.

4.1 Description of the Data

In this work, we use Juno data to estimate a SH model. Magnetic field measurements acquired by Juno are available under two versions for sampling rates of up to 64 samples per second. The version 1 data provides measurements across the entire orbit, whereas the version 2 data gives only near planet measurements from the orbit, denoted as perijove hereafter. Both version 1 and 2 data are available in three Cartesian coordinate systems - Planetocentric, Sun-State and Payload. Since planetocentric system is body-fixed, it is the most appropriate to study the internal field.

To estimate our magnetic field model, we use the version 2 one-second data from the first 38 perijoves. The satellite went into safe mode during its second orbit providing no data for perijove 2. A spacecraft maneuver to align one of the instruments onboard was performed before perijove 19. This resulted in some spurious oscillations for this perijove and hence we remove it. In order to minimize external field contributions and to increase the signal to noise ratio of high internal magnetic field harmonics, we select measurements near the planet's surface, i.e., data below an arbitrarily chosen altitude of 300,000 km (or, radius $\sim$5.2 R_J). The vector data range from August 2016 to November 2021 giving 870,593 data locations, that are plotted in Figure 4.1. Minimum measured field intensity is about 3000 nT at the maximum altitudes while the maximum intensity reaches above 10^6 nT.

The field defined in the Planetocentric coordinate system are defined in Cartesian coordinates using x, y and z orthogonal axes. In this system, the x axis is on the equatorial plane of the body (in direction of prime meridian), the z axis lies along the rotation axis (positive in direction of positive angular momentum) and the y axis is

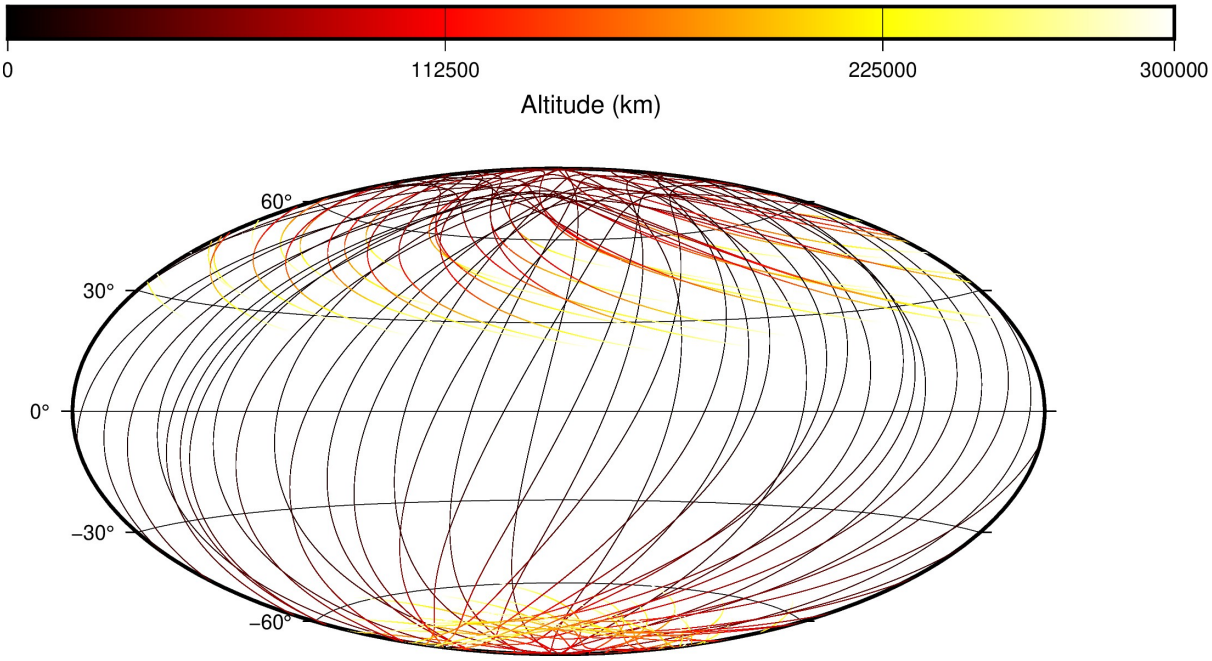

Figure 4.1: The data distribution for the first 38 Juno perijoves. The colors denote the altitude of the spacecraft above the surface of Jupiter. The map is centered at 180° longitude.

perpendicular to both the x and z axes.

For SH modelling, Spherical coordinates are used. It uses r, θ and ϕ as coordinates, which denote the field in the radial, co-latitudinal and longitudinal directions respectively. For converting the Cartesian coordinates to Spherical coordinates, we use -

Radius of spacecraft (in km)

$$r = \sqrt{x^2 + y^2 + z^2} \tag{4.1}$$

Co-latitude (90 - latitude, in degrees)

$$\theta = \tan^{-1}\left(\frac{\sqrt{x^2 + y^2}}{z}\right) \tag{4.2}$$

Longitude (in degrees)

$$\phi = \tan^{-1}\left(\frac{y}{x}\right) \tag{4.3}$$

For converting the field in Cartesian coordinates to Spherical coordinates -

$$B_r = B_z \cos\theta + \left(B_x \cos\phi + B_y \sin\phi\right) \sin\theta \tag{4.4}$$

$$B_\theta = -B_z \sin\theta + \left(B_x \cos\phi + B_y \sin\phi\right) \cos\theta \tag{4.5}$$

$$B_\phi = -B_x \sin\phi + B_y \cos\phi \tag{4.6}$$

4.2 Inversion of Synthetic Data

In order to test the efficiency of the method to solve the inverse problem for model determination and the ability of Juno data distribution to detect time variations in the field, synthetic analyses are required. Here, we use the vector magnetic field predictions at the actual Juno locations and epochs using the latest geomagnetic field model CHAOS-7.11 (Finlay et al. 2020). CHAOS-7.11 is a time-dependent model based on magnetic field observations collected by low-Earth orbiting satellites and ground observatories between years 1999 and 2022. It is expanded to SH degree $N_{int} = 20$ for both the internal field and its time variation using order 6 B-splines (De Boor 2001) with a 6-month knot separation.

The first step is to confirm if we can directly compare the magnetic models of Earth and Jupiter or if we need some extra parameters. From magnetic observations, we know that Jupiter's field is more than 20 times that of the Earth. From existing Jovian magnetic models, we can make a comparison with the geomagnetic model. For models of the Earth, it is widely known that the core field energy dominates only up to degrees 12 or 13. Beyond this, the internal crustal field is dominant. Taking the power spectrum of the CHAOS-7.11 model (Figure 4.2) over all degrees, the main field lies in the ranges of about 10 to 10^{10} nT^2. The SV spectrum is of the orders of 10^{-4} to 10^4 $(\mathrm{nT/yr})^2$. The main field displays maximum power for the dipole and decreases with degree. The SV energy also decreases with degree but displays maximum for the quadrupole term. On the other hand, for Jupiter, there is no crustal field and hence no contribution from it would be apparent in the internal field spectrum. Using the model by Connerney et al. (2022) as reference (Figure 4.2), we see that the main field energy ranges between 10^7 and 10^{12} nT^2 up to degree 20. The variation with degree is similar to that observed for Earth. We do not know yet how the SV spectrum for Jupiter varies with degree or its strength. Ridley and Holme (2016) provided a Jovian SV model but it was only reliably defined till degree 2. Hence, we do not depend on it for our comparison.

The strength and shape of Earth's and Jupiter's external magnetic fields are also significantly different. On Earth, their geometry is assumed to be large scale and modelled using data from observatories and satellites. The SH allows an effective method to separate the external sources from the internal. The solar wind interactions are the main driving force of the external fields. On the Sun-side, the magnetosphere is less than 10 times the Earth's radius. The magnetosphere of Jupiter extends much further. It can be divided into three zones- inner, middle and outer (e.g., Connerney et al. 2020; Wang et al. 2021). The current sheets and plasma emitted by its moon, in particular Io plays a major role in constituting the environment. The plasma is confined near the Jovian magnetic equator, mainly in the inner and middle magnetosphere and hence modelled as a magnetodisk. The magnetodisk models start near radius 7 R_J and extend beyond 50 R_J. Below the inner radius, the dominant field is the one generated by the dynamo.

The comparison of the internal and external fields between the two planets brings us to the conclusion that a direct comparison between models of Earth and Jupiter is not feasible. To overcome this for the internal field, we use a scaling technique. We scale the

geomagnetic coefficients to get the strength and shape of the Jovian model for the internal field. For the SV, the new coefficients provide an amplified strength but we maintain its shape. For proper external field correction, we use measurements below the inner radius of the magnetodisk. Especially for data in the equatorial plane, we use values that are very close to the surface ($< 2\ R_J$). This allows us to ignore the need to exclusively correct for any external field contamination in the measurements. The contribution of the current systems at low altitudes is very small. At these altitudes, we can assume a small SH degree would be sufficient to account for any external effect that could have leaked into the internal field.

4.2.1 Initial Model

In a first step towards building a realistic synthetic data set, we estimate by standard least-squares the power law of Jupiter's magnetic field model. We use the full model available up to degree 30 after completion of the Juno prime mission (Connerney et al. 2022) to re-scale the geomagnetic model. For the CHAOS model, we use coefficients at the central epoch of the Juno data. We estimate two power laws in order to account for the different internal field sources contributing to the model. Indeed, a distinct change of slope occurs around SH degree 13 which indicates that the field from the core dominates from SH degrees 1 to 13, while the field from the crust dominates from SH degree 14 (Langel and Estes 1982). For each part of the power spectrum we use the power law difference of the geomagnetic model with Jupiter's model to re-scale the CHAOS internal field model. In addition, we impose that the power spectrum of the re-scaled SV keeps the same slope as the original CHAOS model since we are unaware of its shape and strength for Jupiter. We also notice that without this precaution, the synthetic SV power spectrum diverges at the assumed dynamo radius of Jupiter (0.81 R_J from Connerney et al. (2022)). The power laws of the initial spectra as well as the power spectra of the re-scaled CHAOS main field model, following now the general trend of the model by Connerney et al. (2022), and its SV are displayed in Figure 4.2.

Using the rescaled model coefficients, we estimate the field at the Juno time and locations. This automatically amplifies the field strength for the synthetic geomagnetic data. The rescaling of the CHAOS model allows us to incorporate the a priori information provided with Juno data. In the database, each measurement is given with a precision index corresponding to the magnetometer operating range and an instrumental noise. The uncertainties are defined for six different operating ranges and vary with the strength of the ambient magnetic field (Connerney et al. 2017). The maximum and minimum ranges are defined as 0.05 and 25 nT for field values ranging between 1 and 10^6 nT per axis. An intrinsic noise level less than 1 nT is defined for the instrument. Each synthetic observation we build is therefore associated with a weight (with a minimum weight of 1 nT) and we further add a Gaussian random noise of 25 nT, the upper bound of the instrument error, to each vector measurement.

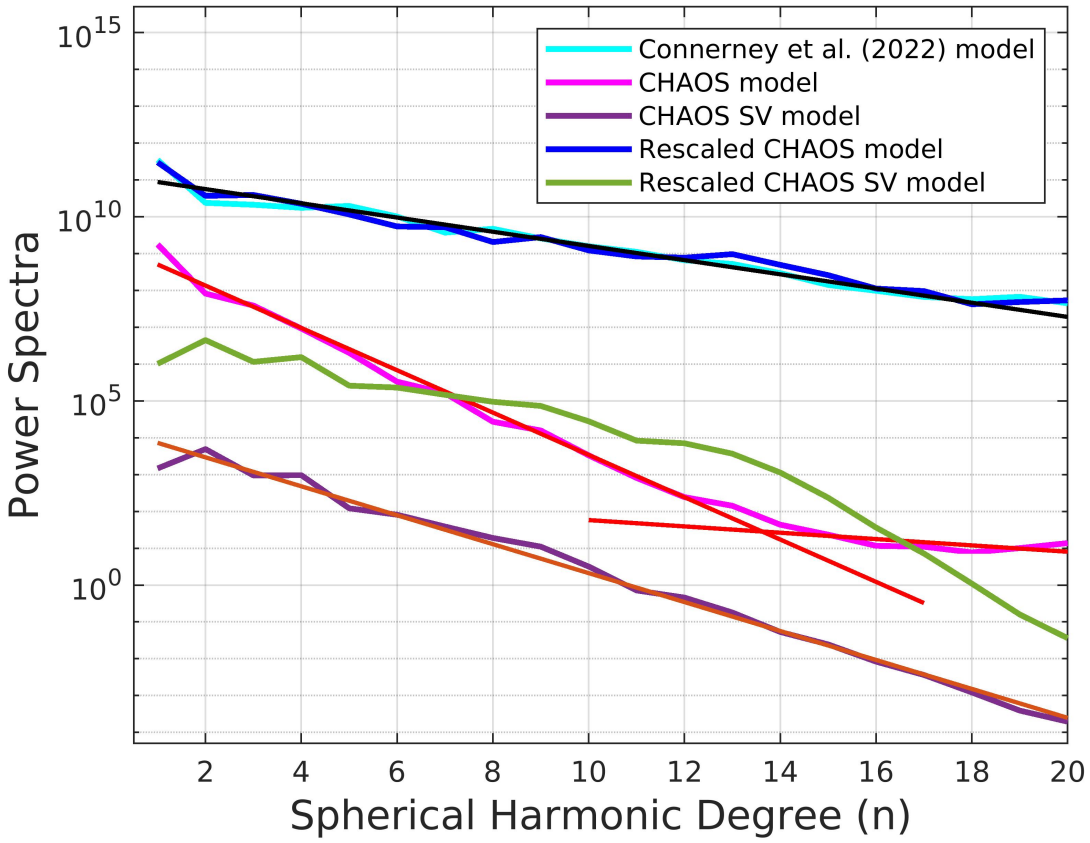

Figure 4.2: The scaling of coefficients for synthetic analysis. The initial power spectrum of the CHAOS-7.11 main field model (magenta), its SV (purple) and the spectrum of Connerney et al. (2022) main field (cyan). The red, orange and black straight lines are the power law rules estimated by least-squares fits for these models respectively. The power laws for the CHAOS main field model (red lines) are different from degrees 1 to 13 and from degrees 14 to 20. The new rescaled CHAOS-7.11 main field and SV models are shown in blue and green respectively. The units for main field are nT^2 and $(\mathrm{nT/year})^2$ for SV spectra.

4.2.2 Synthetic Results

We then set up the parameterization of the inverse problem. Similar to our test model, we derive the internal static field up to SH degree $N_{int} = 20$. The synthetic data contains a significant amount of rapid SV, secular acceleration, and contributions of higher time derivatives, including some geomagnetic jerks, which are sudden changes in the second time derivative of the Earth's magnetic field (e.g., Aubert and Finlay 2019). For this reason, an order 6 B-splines is required to model the time variations. But the maximum resolution of the internal time variation of our model is imposed by the time interval and the spatial coverage between Juno's polar orbits. In addition, the amount of data available for Jupiter is much less than that for Earth over similar time periods. Hence, we choose to parameterize the time variation with splines of order 2 and for SH degrees

1 to 10 only. We estimate a static external field up to SH degree 2.

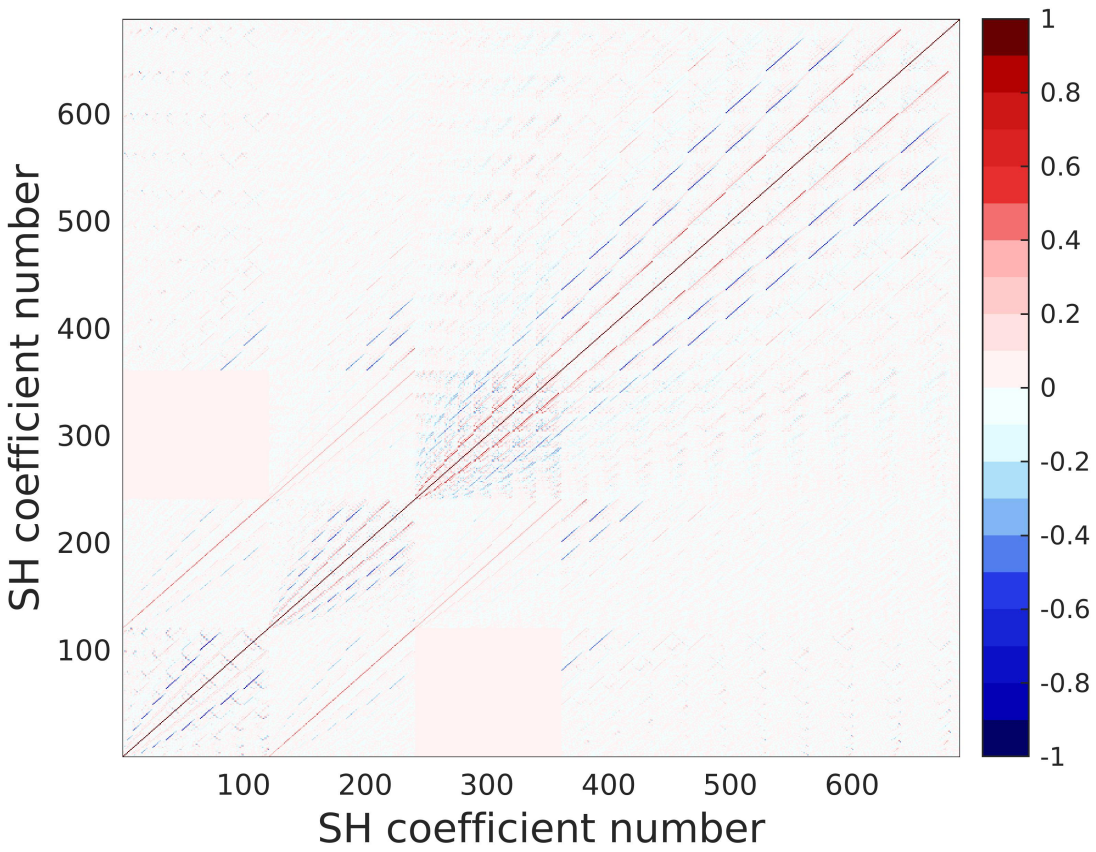

Figure 4.3: The covariance matrix for the model using synthetic data set. It displays a well conditioned inverse problem with some correlations due to the use of splines method.

The 688 coefficients are then estimated by weighted least-squares and the inversion is performed with a SVD algorithm. Inverting coefficients using SVD offers the possibility to solve the problem with a truncated SVD technique if needed later for the inversion of real data. The examination of the covariance matrix (Figure 4.3) indicates that we are not dealing with an ill-conditioned inverse problem that would require an explicit regularization. The first 240 coefficients represent the 2 spline knots while the next 440 coefficients from 241 up to 680 contains the main field with the embedded spline coefficients of the last knot. The covariance is ideally a diagonal matrix but we expect some correlation between the coefficients due to the splines, as is visible from the figure.

4.3 Comparison of Initial and Synthetic Models

The results of a synthetic inversion can be assessed using several criteria (Thébault et al. 2015; Alken et al. 2021). We use some of these criteria to analyse the rescaled input coefficients with the synthetic case output coefficients. The reference model is the initial rescaled CHAOS-7.11 model at the central epoch of the Juno data used while the

synthetic model is the model estimated by the inversion.

4.3.1 Sensitivity Matrix

The sensitivity matrix allows to assess the quality of the model. For this, we first determine the difference between the coefficients of the reference and synthetic models. We then normalise them using the mean amplitude of the reference model at the particular degree. Assuming i and j for the synthetic and reference models respectively, we have-

$$S(n,m) = \begin{cases} 100 \dfrac{{}_ig_n^m - {}_jg_n^m}{\sqrt{\dfrac{1}{(n+1)(2n+1)} \sum_{m=0}^{n} [({}_jg_n^m)^2 + ({}_jh_n^m)^2]}} & \text{for m} \geq 0 \\ 100 \dfrac{{}_ih_n^m - {}_jh_n^m}{\sqrt{\dfrac{1}{(n+1)(2n+1)} \sum_{m=0}^{n} [({}_jg_n^m)^2 + ({}_jh_n^m)^2]}} & \text{for m} < 0 \end{cases} \tag{4.7}$$

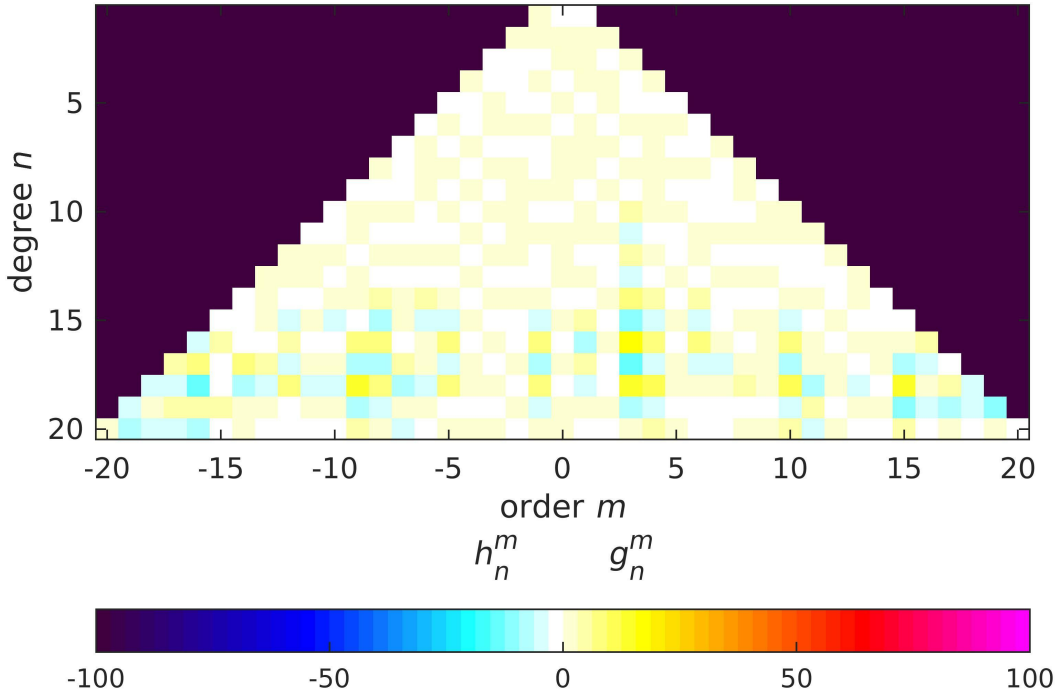

Figure 4.4: The sensitivity matrix for each degree and order of the main field coefficients as seen between the reference and synthetic models.

Figures 4.4 and 4.5 displays the sensitivity matrix for the main field and SV respectively. The main field matrix displays that the coefficients are very well resolved up to degree 15-16. The higher degree terms are not that well resolved comparatively. For the SV, the matrix displays differences from degree 8. The reason for this could be the orbit configuration of Juno. Figure 4.6 shows the altitude versus latitude graph for the used data. We note that with increasing orbit number, the satellite goes lower in altitude in

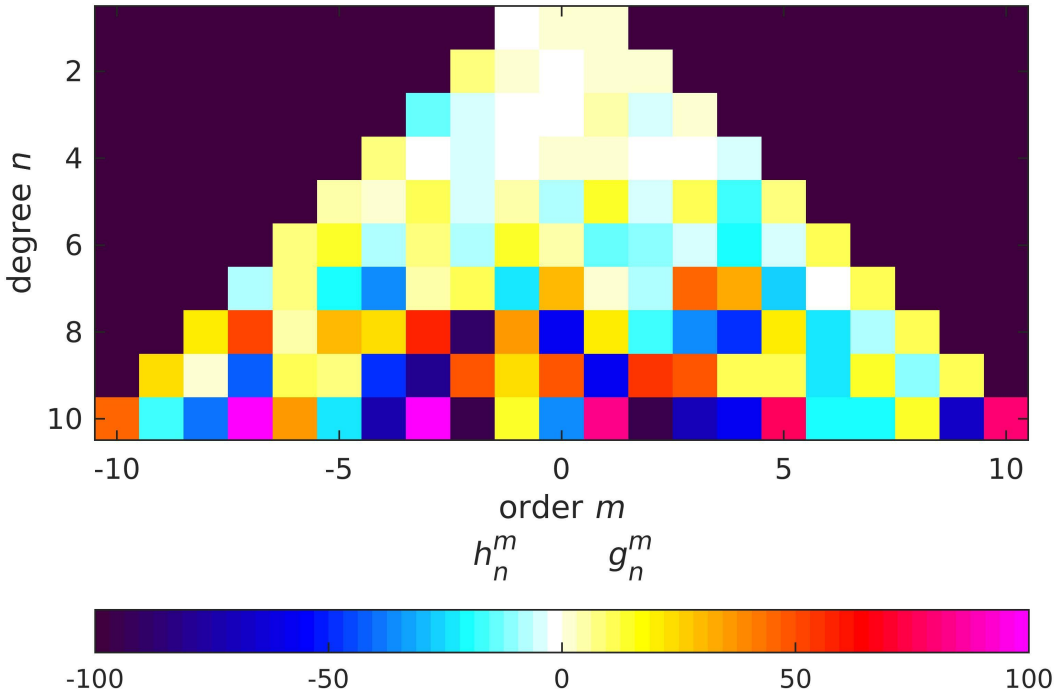

Figure 4.5: The sensitivity matrix for each degree and order of the SV coefficients as seen between the reference and synthetic models.

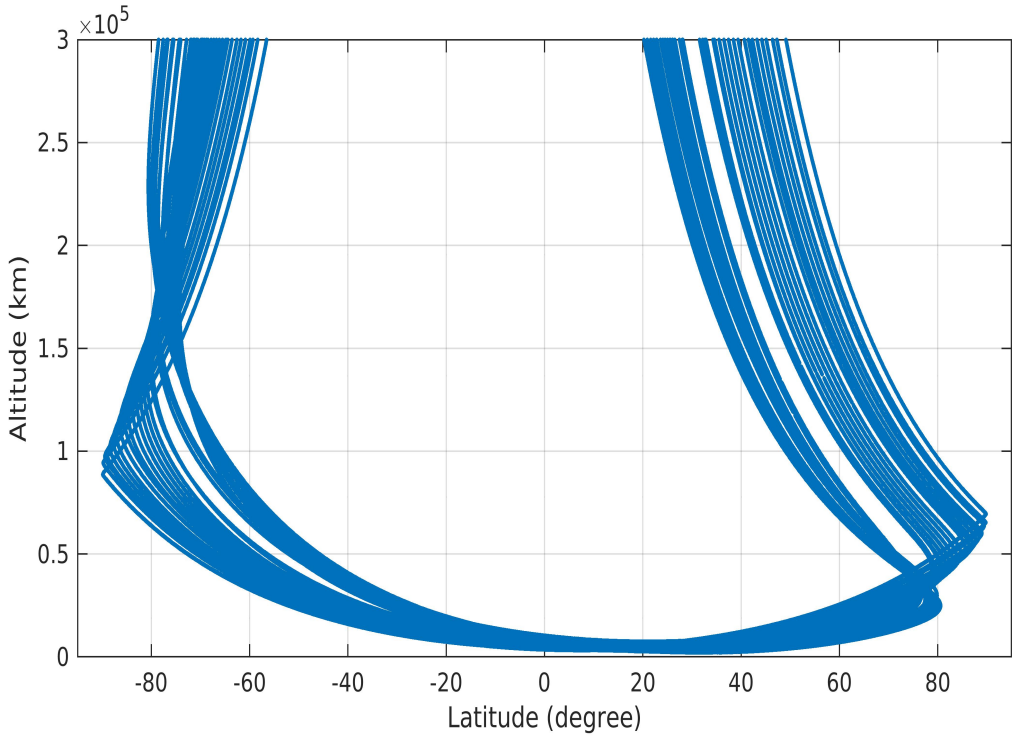

Figure 4.6: The altitude versus latitude of the data observations for the first 38 Juno perijoves.

the northern hemisphere while increasing the size of a gap at similar latitude ranges over the southern hemispheres. In particular, the region near the poles above latitudes 60° in the north has more data below some 100,000 km compared to the same region in the south. This can result in some small scale features corresponding to the higher degree terms being less resolved. Additionally, the sensitivity matrix for the SV is affected by the synthetic data which contains much higher time variations for the geomagnetic field.

4.3.2 Power Spectra and Correlation

The next two analyses are done using the power spectra of the two models and their correlation. For the correlation between two models, we have-

$$r(n,m) = \frac{\sum_{m=0}^{n} ({}_i g_n^m \, {}_j g_n^m + {}_i h_n^m \, {}_j h_n^m)}{\sqrt{\left(\sum_{m=0}^{n} [({}_i g_n^m)^2 + ({}_i h_n^m)^2]\right)\left(\sum_{m=0}^{n} [({}_j g_n^m)^2 + ({}_j h_n^m)^2]\right)}} \tag{4.8}$$

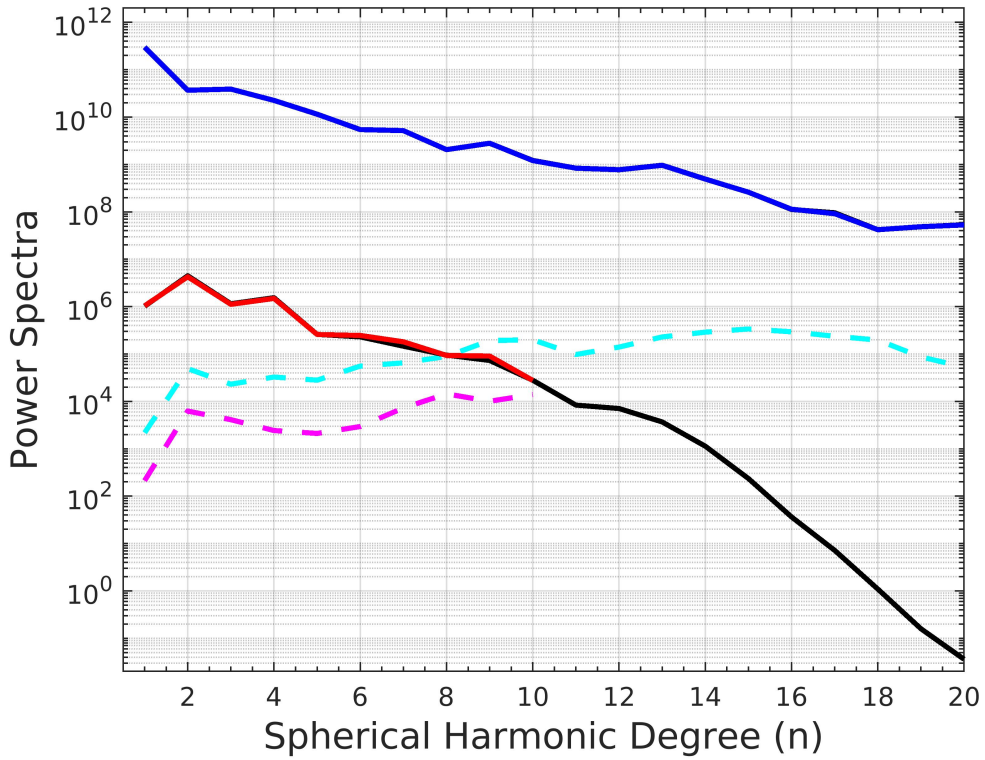

Figure 4.7: The power spectrum of the main field (blue) and SV (red) of the synthetic and reference (black) models at the Jovian surface. Also displayed are the power spectra of the difference between the two model coefficients for the main field (cyan) and the SV (magenta). The units for the main field is nT^2 and for the SV is $(\mathrm{nT/year})^2$.

Figure 4.7 shows the power spectrum of the reference and estimated model for the main field and SV. The figure also displays the power spectrum of the difference between

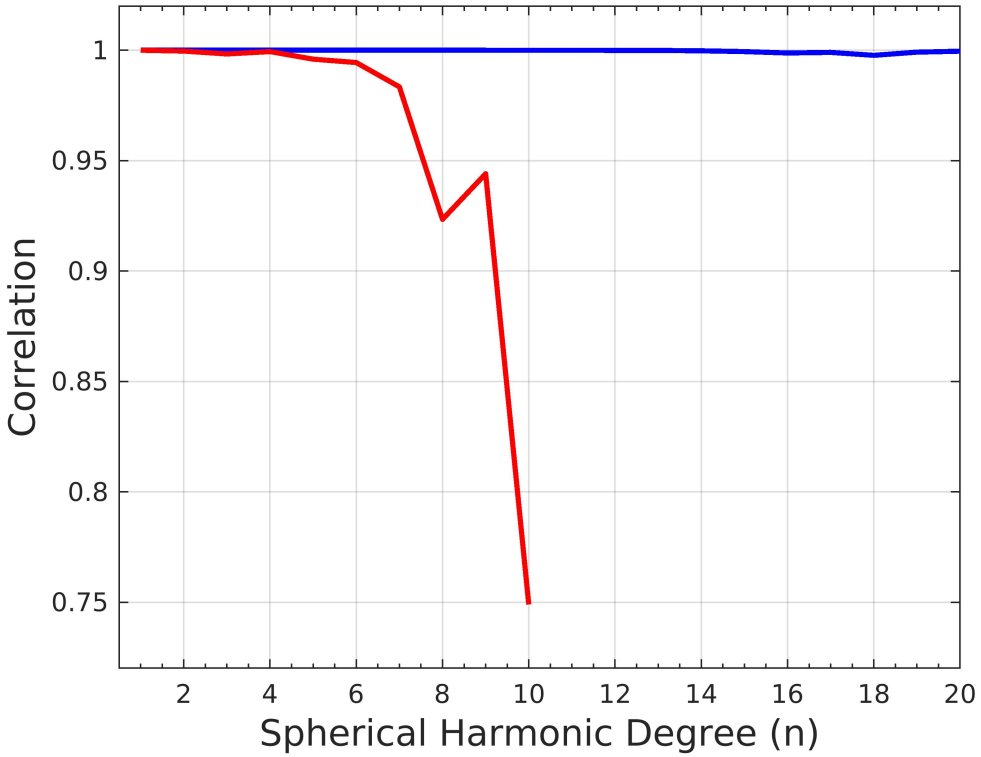

Figure 4.8: The spherical harmonic correlation between the reference and synthetic models for the main field (blue) and the SV (red).

the model coefficients. The spectrum of the main field of the estimated model almost mimics that of the reference model. The difference is less than 10^6 nT^2 which is almost half the exponent value of the actual spectra. Similar results are obtained for the SV. The difference of the SV spectra follows the shape of the difference of the main field till degree 8. The correlation for the SV also fluctuates beyond degree 8 as shown in Figure 4.8. The increase in correlation for the SV at degree 9 and the subsequent decrease after could be a sign of energy leakage. As discussed before, the geomagnetic data contains a lot of time variations which were possible to not have been accounted for in the estimated model. The power spectra of the main field for both models correlate better than 0.99 over all degrees.

4.3.3 Residuals

Our final assessment is done through residual maps of both the main field and the SV. Figure 4.9 shows the radial field maps from the synthetic model and the difference between the reference and synthetic models at 0.81 R_J (the assumed dynamo radius of the Connerney et al. (2022) model which was used for scaling). The differences are shown both in the same color scale as the field and SV, and in a saturated scale to better observe them. We observe significant differences between the models in the southern hemisphere, in particular near the pole for both the field and SV. The localised residuals there are

about an order of magnitude lower. They indicate the presence of a small power leakage that is amplified at the dynamo radius, especially for the SV. The main field difference shows small scale features confined mainly between 90° and 240° longitudes above 50° latitudes. The SV differences in the southern hemisphere are spread over all longitudes above similar latitudes. The reasonings for the high residuals at these regions are similar to our discussion for the sensitivity matrix. The orbits create a gap in the southern hemisphere which restricts us to properly model the field there. Moreover, the synthetic data contains much more variations than is resolved for in the inversion.

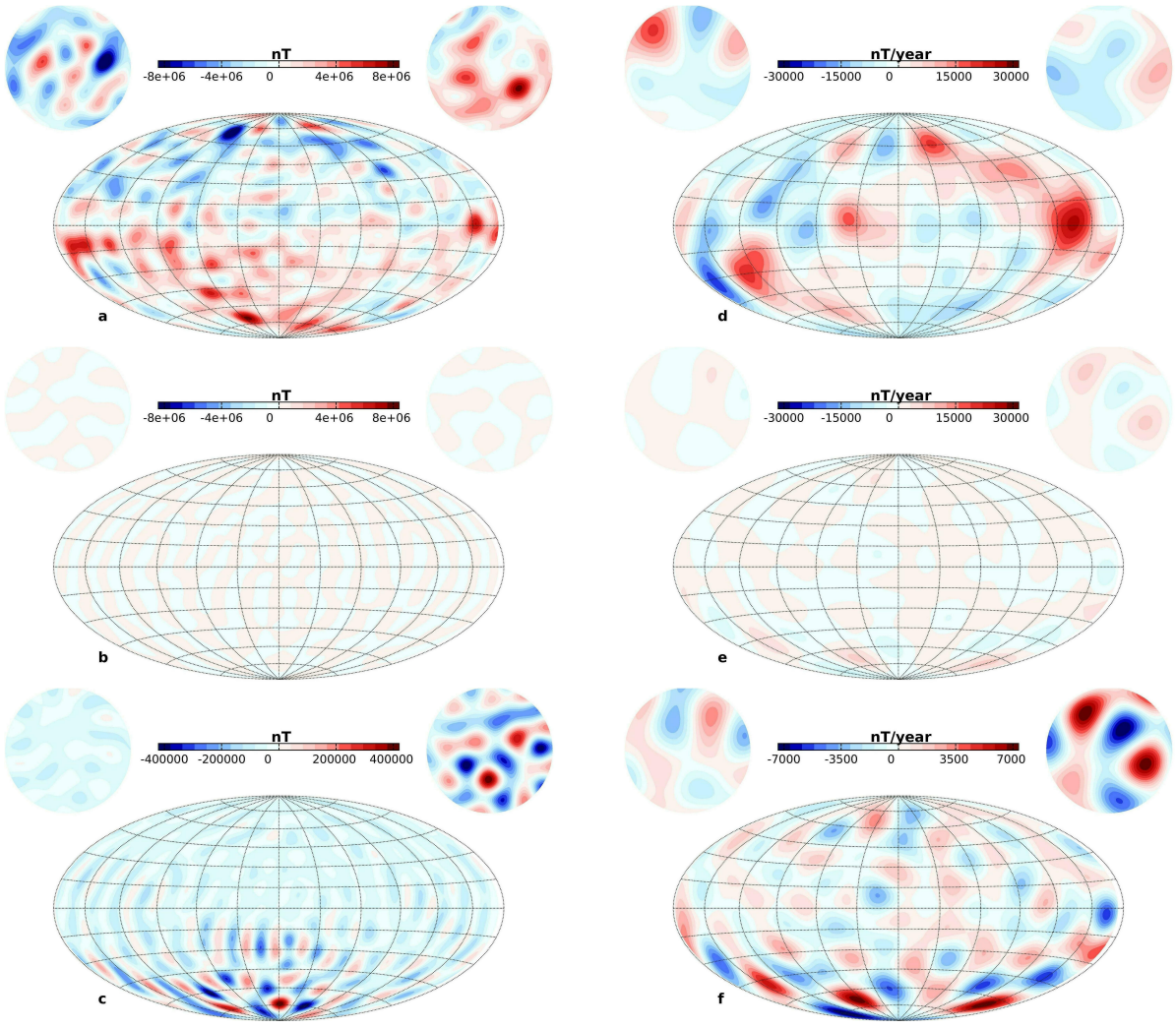

Figure 4.9: The radial field of the synthetic model (**a**), the difference of the radial field between the reference and synthetic models with the same color scale (**b**) and with a saturated color scale (**c**). The radial SV of the synthetic model (**d**), the difference of the radial SV between the reference and synthetic models with the same color scale (**e**) and with a saturated color scale (**f**). The maps are centered at 180° longitude and plotted at 0.81 R_J. The small maps on the left of each display the north pole while the right displays the south pole.

4.4 Inversion of Real Data

The synthetic inversion and tests performed using the geomagnetic model allows us to robustly assess the inversion process. Using the deductions made from them, we can now efficiently calculate the model using the real data. The synthetic results prove that Juno orbits can robustly model the internal field to degree 20 and the time variations till at least degree 8. Similar to our synthetic analysis, we assume that a degree 2 external field model would be sufficient to account for the currents present outside the planet at low altitudes.

For modelling the temporal variations of the internal field, we use B-splines of order 2. We use three knots, at the beginning, middle and final epochs of the measurements where spacing is about 2.62 years. To calculate the SH coefficients, we apply a weighted least-squares inversion approach based on the SVD algorithm. The weights used are the same as before, defined in nT by the instrument error and intrinsic noise for each Juno data location. The conditioning number obtained from the inversion is about $4\text{x}10^5$ which is quite large. We suspect that power is leaking from some unresolved small and rapid spatial scales. This prompts us to apply the truncated SVD approach. In this case, we ignore the values for which the normalised eigenvalues are lower than 10^{-4}. This leads us to reject 30 out of the 608 eigenvalues in the weighted least-squares inversion. From Equation (2.21), we know that the S matrix consists of the eigenvalues. Figure 4.10 displays the values with respect to the number of coefficients. In order to distinguish between the normal and abnormal values clearly, we show the inverse of the eigenvalues instead. After the removal of the abnormal values, the conditioning number now changes to a much acceptable value of $9\text{x}10^3$. We also calculate a model without any time variations to further test the need to model the SV. The inversion parameters are kept the same otherwise. Here, we reject 27 eigenvalues out of the 448 determined.

4.4.1 Model Statistics

For the models calculated with and without SV, we estimate for each a posteriori standard error on the coefficients from the covariance matrix and the inversion misfit for the three vector components. The covariance is similar to the synthetic test showing almost no correlation between the coefficients. We concentrate more on the residuals to indicate the necessity of modelling the SV. The inversion algorithm misfits for each vector component for both models are given in Table 4.1. The misfit difference between these two cases supports the fact that a statistically significant and global SV is present in the measurements. The modelling of the SV along with the main field improves data fit better than increasing field complexity.

We also draw a comparison of our results to the main field model estimated by Connerney et al. (2022). The Figure 4.11 and Table 4.2 show the intensity root mean square differences between Juno's dataset and predictions for all the three models, considering different truncation degrees for each model. The external field coefficients for all three

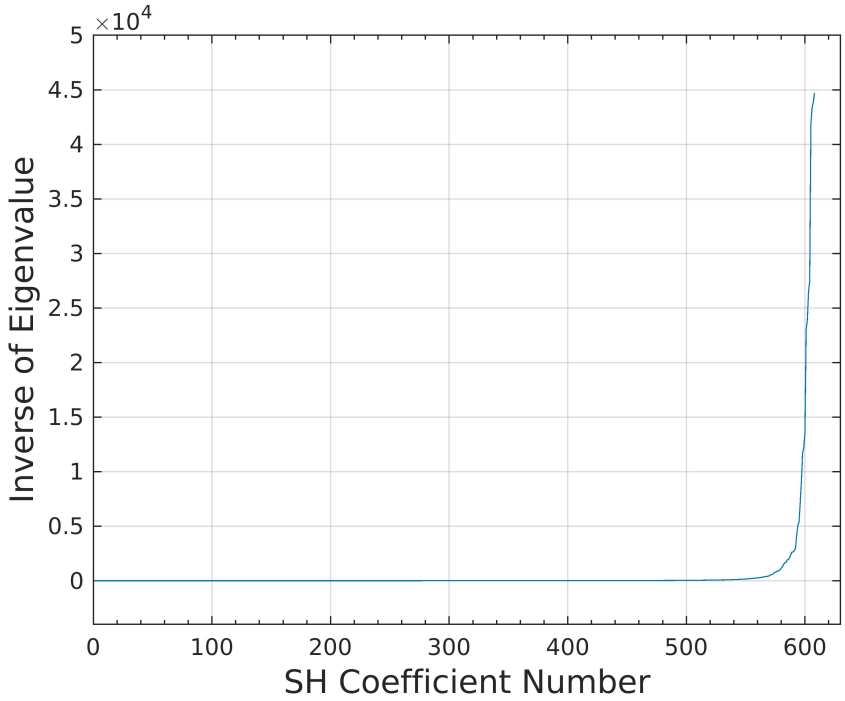

Figure 4.10: The inverse of eigenvalues as a function of the number of coefficients.

Table 4.1: Inversion algorithm misfits (in nT) for models without and with secular variation (N_{int} = 20 and 8 for the main field and SV respectively).

Model	B_r	B_θ	B_ϕ	**B**
without SV	416.49	351.36	422.28	398.16
with SV	227.23	245.81	256.93	244.12

models were set to their respective maximum degrees for each internal field truncation degree. The initial root mean square of the Juno data used is 147,378 nT. The misfits for the model by Connerney et al. (2022) in Table 4.2 is shown up to degree 20 only for comparison between the three models. All the three models show very similar misfit values till degree 16. The slight variations could be attributed to the computation process of the residuals. This implies that all three models are well resolved until then. The residuals of the model by Connerney et al. (2022) does not drop at the truncation degree. Instead, it gradually lowers as it is a normalised model aimed at improving the fit. However, the maximum reliable degree for their model is 13 which can be extended till 18. For our two models estimated with and without the SV, the residuals reach a plateau at degree 16 and drops down at degrees 19 and 20. The final residuals are lower for the model with SV.

Finally, we look at the energy spectra for our model at the surface in Figure 4.12 with their error bars. An error is calculated for each of the coefficient during inversion. We calculate different spectra for the model by adding random combinations of the error to

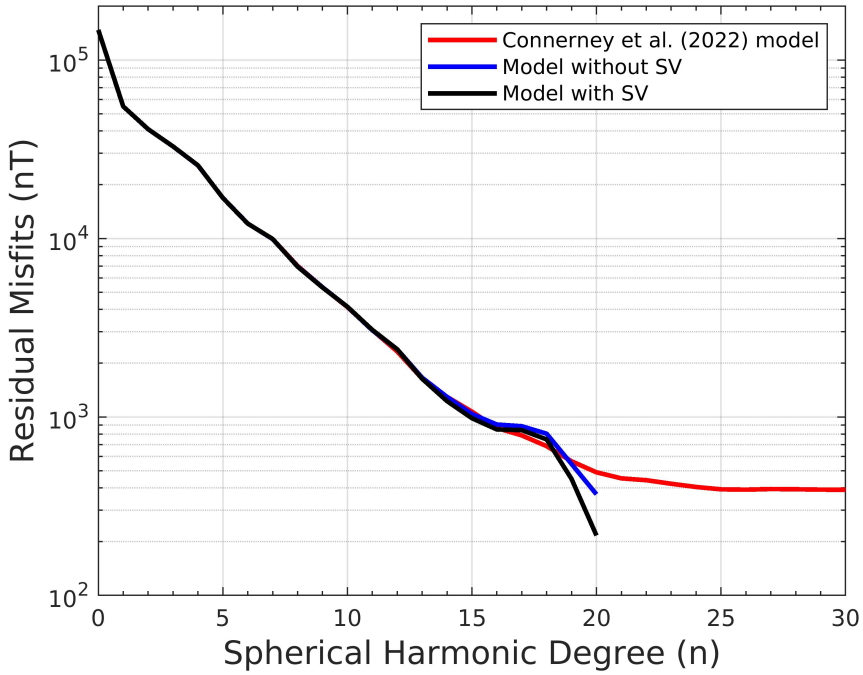

Figure 4.11: The residual misfits plotted as a function of the SH degree for the model by Connerney et al. (2022) (red), a model without SV (blue) and the estimated model (black).

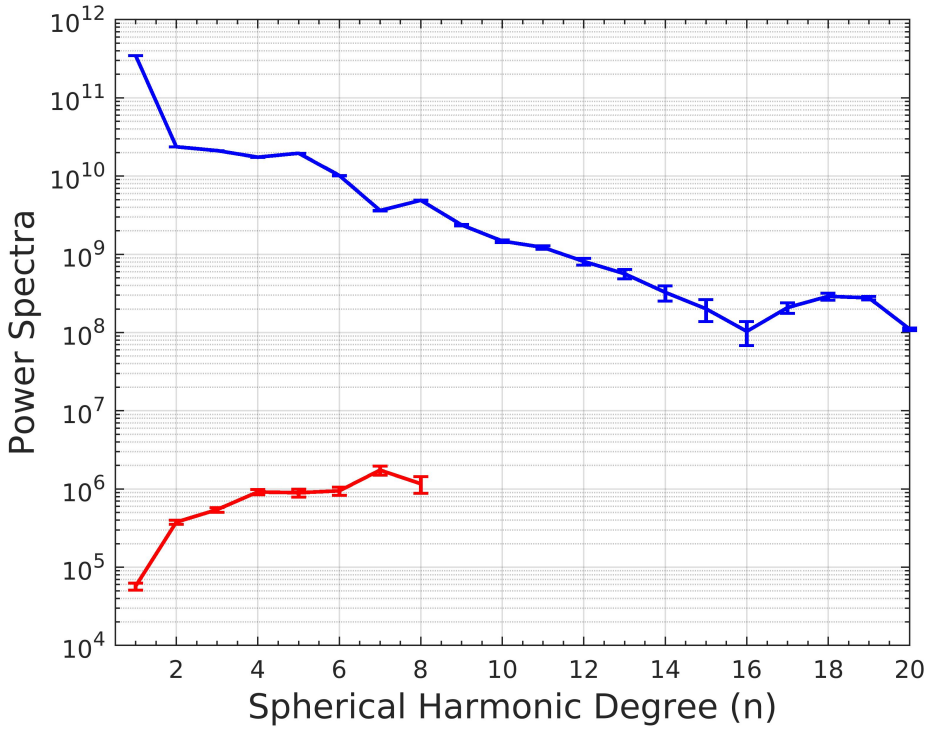

Figure 4.12: The power spectra with error bars for the main field (shown in blue, units - nT^2) and SV (shown in red, units - $(nT/year)^2$) of the model at the surface.

Table 4.2: Intensity misfits (in nT) for varying internal truncation degrees (N_{int} = 20) and maximum external degrees (N_{ext} = 2 for the model with and without SV and N_{ext} = 1 for the model by Connerney et al. (2022)) for the difference between Juno dataset used and predictions made by the models.

Degree	Model with SV	Model with no SV	Model of Connerney et al. (2022)
1	54918.22	54910.79	54921.49
2	40965.35	40944.44	40962.45
3	32774.92	32765.38	32779.05
4	25694.01	25654.39	25659.61
5	16873.81	16883.52	16880.58
6	12108.84	12119.48	12119.81
7	9936.47	9915.68	9924.40
8	6952.41	6971.59	7019.45
9	5313.38	5331.17	5329.63
10	4145.55	4140.90	4124.86
11	3075.17	3057.77	3068.82
12	2393.88	2393.60	2326.88
13	1636.26	1658.99	1639.06
14	1225.91	1294.98	1295.46
15	983.24	1038.41	1070.40
16	850.60	906.58	866.32
17	843.35	886.95	787.98
18	747.68	805.23	685.84
19	449.28	544.65	564.37
20	216.59	368.36	489.35

the coefficients. The error bars shown in the figure are the standard deviation over the generated spectra. The SV spectrum of the geomagnetic field decreases with degree at the surface. However, for Jupiter, we observe an increase with degree. The main field model remains stable until degree 16 after which there is an increase of power observed till $n = 18$. This probably arises because of the spectral aliasing of the remaining signal in the measurements. As was observed in the synthetic analysis, the less amount of data available near the south pole can contribute to it. The synthetic sensitivity matrix also displayed good results till degree 16. There is a possibility that it is a consequence of the truncated SVD approach used which can dampen some terms. Moreover, the residuals

for our model match well those of the normalised model of Connerney et al. (2022) until degree 16. Therefore, we truncate the final model to $N_{int} = 16$.

4.4.2 Final Model

The final model is established by truncating the model till degree 16. The radial field and SV maps calculated at the surface from the model are displayed in Figure 4.13. The field is of the order of 10^6 nT. There is a large positive flux in the northern hemisphere and an intense negative patch near the equator called the Great Blue Spot. The maximum SV is observed for the radial field with the value 10,480 nT/year at the surface. This corresponds to a 2.9% change over the course of the five years of the dataset used, compared to the 1.8% change over a similar duration for the Earth's magnetic field. As for the Earth's, the SV should not be ignored when modelling the magnetic field over periods exceeding a few years or even less.

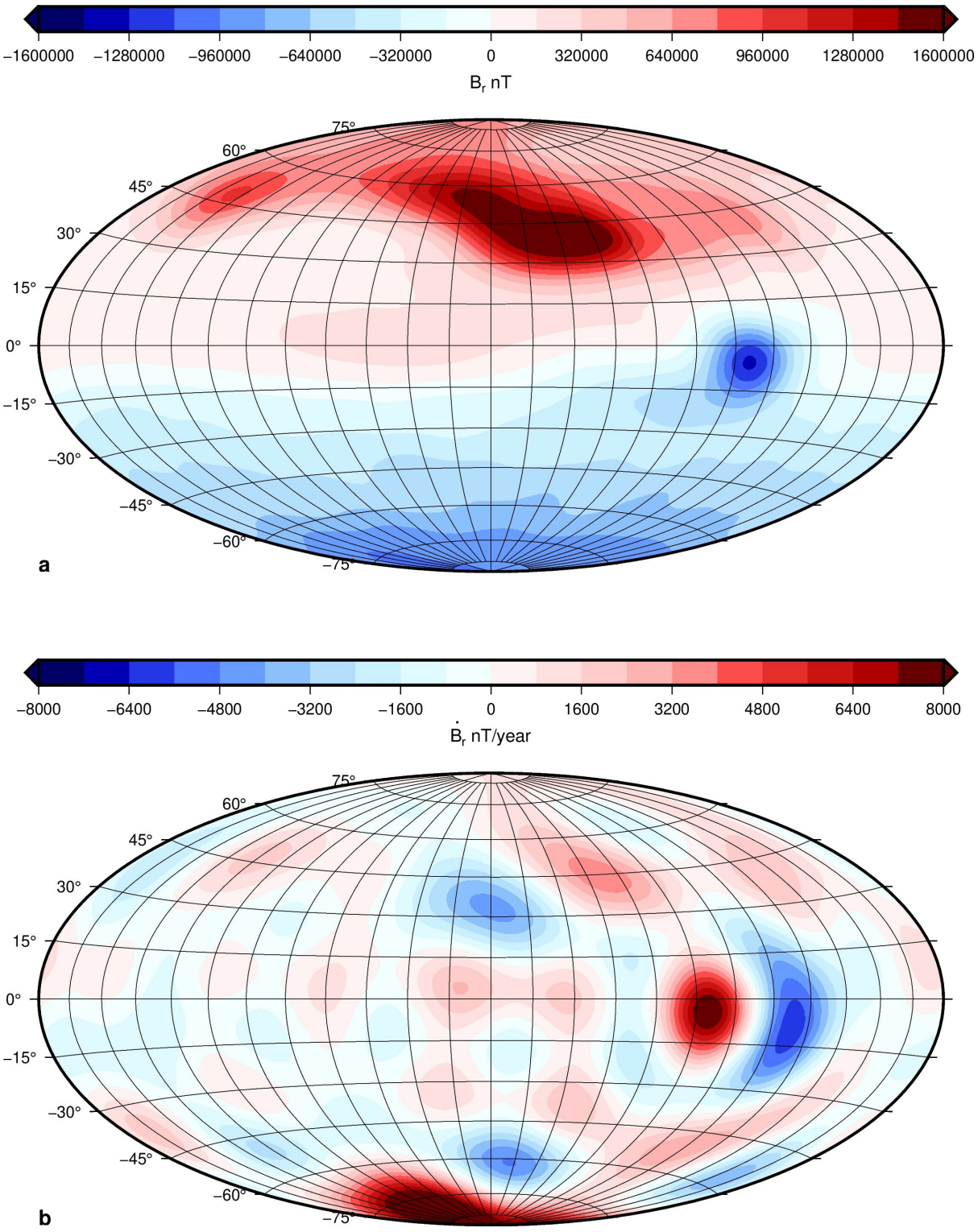

Figure 4.13: The (**a**) radial field and (**b**) its SV at Jupiter's surface. The maps are centered at 180° longitude.

5. Implications for the Interior

Our aim is to understand the interior of Jupiter using the internal magnetic field and SV model. Through quantitative analysis of the model, the interior properties can be deciphered. The first part of this chapter focuses on the statistical analyses using the model. They can constrain the depth of the dynamo as well as the morphology of the field change with time. The second part discusses the maps constructed from the models that can be used to infer information about the dynamo field and its implications for the interior.

5.1 Statistical Analysis of the Model

Some statistical properties of the model can be obtained using the power spectra of the main field and the SV, separately as well as combined. For Jupiter, we focus on calculating the depth of dynamo generation using the main field spectrum. The combined main field and SV spectra are used to obtain information about the field flow inside the planet.

5.1.1 Dynamo Radius Estimation

We know that for Earth, the field spectrum (Lowes 1966) can be steadily interpreted in terms of magnetic source location. There is an apparent slope break near degree 13 that distinguishes between the energy from the core and the crustal field components, respectively. Ignoring the dipole term, the spectrum becomes almost flat when downward extrapolated to the CMB for the core part, while it shows an almost null slope at the surface for higher degrees. This property has been observed for a long time and has been suggested to provide a crude estimate of the core radius on other planets where seismological measurements are not available. It is known as the white noise hypothesis - immediately outside the dynamo region, the part of the magnetic spectrum associated with the dynamo is assumed flat, and the depth to the dynamo can thus be approximately estimated (Lowes 1974). However some terms (mostly n=1 and n=2) have to be ignored in order for this approximation to match the radius of the Earth's core (Cain et al. 1989; Voorhies 2004). This method was used by Connerney et al. (2018) and Connerney et al. (2022) for estimating the radius for the Jovian dynamo from their magnetic models. While Connerney et al. (2018) omitted the degree 1 term and placed the radius at 0.85 R_J,

Connerney et al. (2022) omitted both degree 1 and 2 terms and estimated a value of 0.81 R_J. Similarly, Tsang and Jones (2020) performed several numerical dynamo simulations for the Jovian field to estimate the radius using the spectra. They presented radii between 0.82 and 0.87 R_J for many different limiting degrees.

This crude estimation of determining the dynamo radius can be refined by using alternative expressions of the power spectrum. Langlais et al. (2014) defined two expressions, first using the non-zonal terms and second using the quadrupole family. The two sub-families show flat spectra independent of degree n at radius r, interpreted as the CMB for Earth. The non-zonal spectrum has a null slope due to the assumed randomness of the terms. The time-averaged paleomagnetic models imply axisymmetric geomagnetic field in the long term. The non-axisymmetric part or the non-zonal terms cancel out and can thus be assumed random. On the other hand, the flatness of the quadrupole family spectrum is explained by the dominance of rotational effects in the dynamo process. The flow in the interior is arranged in axial columns that are symmetric with respect to the equator. This induces a dominantly anti-symmetric field or dipole family field on the CMB while the symmetric or quadrupole family part can be assumed random. The two spectra can be defined as-

$$\mathcal{R}_n^{nz}(r) = (n+1)\left(\frac{a}{r}\right)^{(2n+4)} \sum_{m=1}^{n} [(g_n^m)^2 + (h_n^m)^2] \tag{5.1}$$

$$\mathcal{R}_n^{qf}(r) = (n+1)\left(\frac{a}{r}\right)^{(2n+4)} \sum_{m=0,\ n+m\ even}^{n} [(g_n^m)^2 + (h_n^m)^2] \tag{5.2}$$

The power spectra and their linear fits for the geomagnetic field model CHAOS-7.11 are shown in Figure 5.1 in blue at the CMB. The black lines display the linear best fit for the spectra. The first panel shows the full spectrum from degrees 1 to 13 and its slope as well as the slope after omitting the dipole term. The next two panels display the non-zonal and quadrupole families spectra and their best linear fits. Comparing the slopes obtained for all four cases, we determine that the partial spectra exhibit a closer-to-zero slope as compared to the full spectrum. The values for dynamo radius calculated from the spectra, i.e., looking for a null slope, using degrees 1 to 13 and 2 to 13 are 3257.32 km and 3388.02 km respectively. The radius estimated from the non-zonal and quadrupole families are 3480.78 km and 3489.06 km respectively. The value from the non-zonal spectrum matches best the seismological value for the CMB of Earth taken as 3481.7 km. The next best match comes from the quadrupole family. Hence, we use these two sub families to estimate the dynamo radius of Jupiter using our model (Figure 5.1).

We estimate the dynamo radius for varying truncation degrees of the main field model N_{int} seeking in a minimum least-squares sense the depth at which the power spectra from the non-zonal and quadrupole families of coefficients are statistically flat. We use the model till degree 20, i.e., we consider the omitted terms as well in order to further test our choice of truncating the model at degree 16. The values for the different degrees for the two families are shown in Table 5.1. The error bars on the estimated dynamo radius

decrease up to truncation degree $N_{int} = 16$ for both families (Figure 5.2). It is also the truncation degree for which the maximum likelihood estimates from the non-zonal and quadrupole families of power spectra coincide. This supports our choice of truncating the present model to the maximum degree 16.

For truncation degree 16, the maximum likelihood value from the non-zonal spectrum is equal to 0.831 R_J and that from the quadrupole family is equal to 0.829 R_J. We use their mean and combine their standard errors to provide a single estimate of $0.830 \pm 0.022 R_J$. R_{sf} is used hereafter to define the dynamo radius or more precisely, the bottom of the source free region.

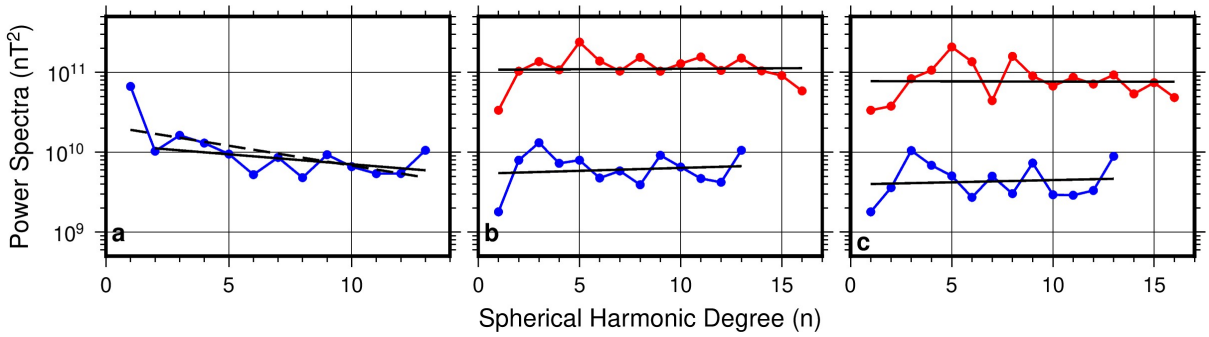

Figure 5.1: (**a**) Geomagnetic power spectrum of CHAOS-7.11 model at the CMB with linear regression from n=1-13 (black dashed line, slope = -0.0497) and 2-13 (black line, slope = -0.0250). (**b**) The non-zonal spectra with linear regression (black line) for the geomagnetic model (blue, slope = 0.0074) at CMB and for our model (red, slope = 0.0012) at the estimated dynamo radius R_{sf}. (**c**) The quadrupole family spectra with linear regression (black line) for the geomagnetic field (blue, slope = 0.0056) at CMB and for our model (red, slope = -0.0005) at the estimated dynamo radius R_{sf}. The slopes are not exactly zero in the figure because the spectra are plotted at the CMB value for Earth and mean radius R_{sf} for Jupiter instead of the radius obtained for the particular spectrum.

Given our dynamo radius, we can now look at the full power spectra of the main field and SV at both the surface and R_{sf}. Adding to the spectra figure at the surface from the last chapter, we show the spectra at R_{sf} with the error bars in Figure 5.3 for our final model. The main field spectrum at the dynamo radius is shown up to the model truncation degree 16 only. As on Earth, the spectra at both radii display a maximum for the dipole term and mostly decreases with degree. The SV spectra increases with degree at both the surface and the dynamo radius. The small scale features display more power than the large scale dipole or quadrupole terms.

5.1.2 Secular Variation Timescales

The ratio of the power spectra of the main field $\mathcal{R}_n$ to the SV $\mathcal{S}_n$ is used to establish a quantity τ as a function of degree n, which is known as the correlation time or the SV timescale. The SV timescale gives a measure of how long it takes for the field of a

Table 5.1: Dynamo radius values (in R_J) for Non-zonal and Quadrupole Families with varying truncation degrees.

Degree	Non-Zonal	Quadrupole
10	0.861	0.862
11	0.859	0.855
12	0.851	0.847
13	0.850	0.845
14	0.844	0.837
15	0.839	0.835
16	0.831	0.829
17	0.837	0.833
18	0.847	0.841
19	0.856	0.848
20	0.858	0.853

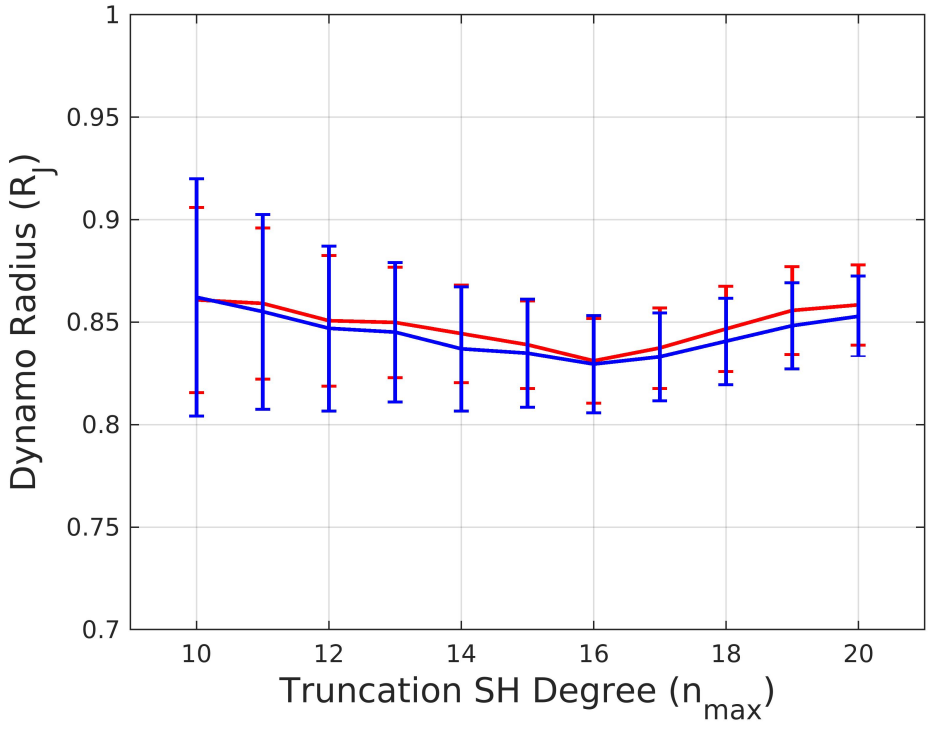

Figure 5.2: The dynamo radius estimates with their error bars calculated using the non-zonal (red) and quadrupole (blue) terms at different truncation degrees using the estimated model.

particular degree to get reorganized, or become uncorrelated to its former state at that degree (e.g., Hulot and Le Mouël 1994; Christensen and Tilgner 2004; Amit et al. 2018).

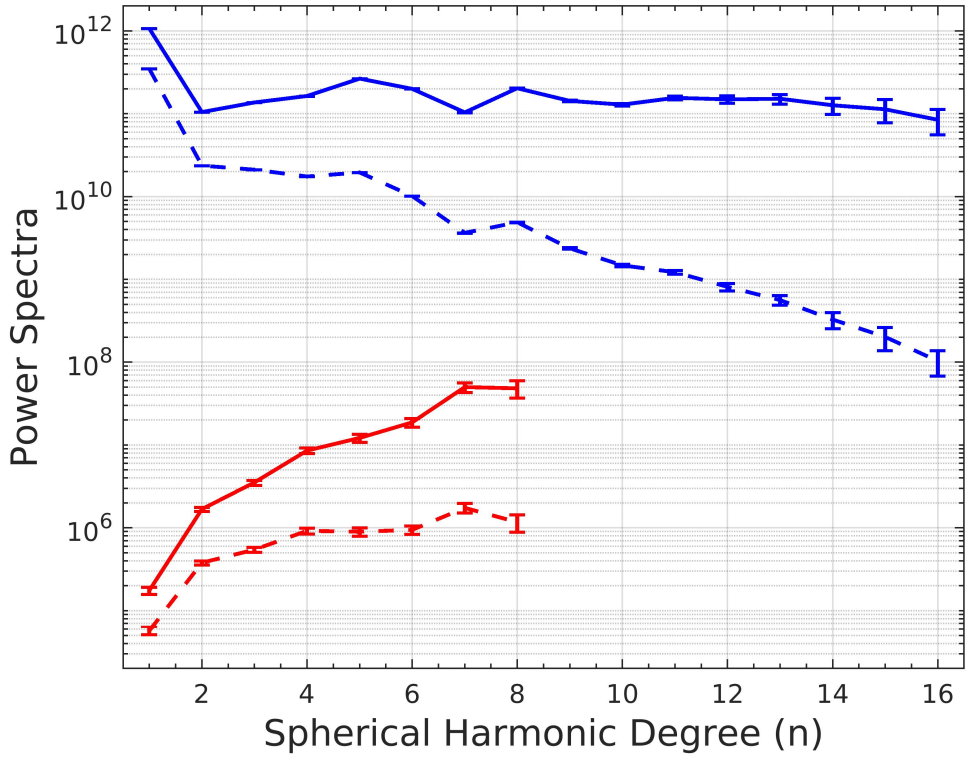

Figure 5.3: The power spectra with error bars for the main field (shown in blue, units - nT^2) and SV (shown in red, units - $(nT/year)^2$) of the model at the surface (dashed line) and at R_{sf} (solid line).

They are independent of depth and can be expressed as-

$$\tau_n = \sqrt{\frac{\mathcal{R}_n}{\mathcal{S}_n}} \tag{5.3}$$

From our knowledge about the Earth, the change in the geomagnetic field is one of the consequences of the field flow in the interior by two methods, namely advection and diffusion (Holme and Olsen 2006; Christensen et al. 2012). A quantity called the magnetic Reynolds number is defined as the relative ratio of the effects of advection to diffusion.

The radial component of field B_r is continuous through the CMB and the induction equation governing the change in this component over time can be expressed as-

$$\frac{\partial B_r}{\partial t} = -\boldsymbol{\nabla}_H \cdot (\boldsymbol{u} B_r) + \frac{\eta}{R_{sf}} \nabla^2 (r B_r) \tag{5.4}$$

where, the first term on the right hand side denotes advection and the second term denotes diffusion. $\boldsymbol{\nabla}_H$ is the horizontal gradient, $\boldsymbol{u}$ is the velocity of the fluid at the top of dynamo and η is the magnetic diffusivity. From scaling analysis, a power law in relation to the SV timescales τ can be defined to find whether SV is advective or diffusive. The theory states that the τ is inversely proportional to the degree for advective SV while it is inversely proportional to the square of the degree for diffusive SV. In other words, the

slope of the best fit line would be -1 for pure advective SV and -2 for pure diffusive SV. The dipole term behaves differently and so we omit this term while scaling (Amit and Olson 2010; Christensen et al. 2012).

Geomagnetic field models and numerical dynamo simulations indicate that the non-dipole SV timescales are inversely proportional to the SH degree. We calculate the correlation times for the CHAOS-7.11 model and the slope of its best linear fit to the non-dipole terms in blue in Figure 5.4. The correlation time for the geomagnetic dipole (τ_1) is 1100 years while the lowest value we obtain is 23 years for degree 12. The best linear fit slope for the non dipole terms in the log-log scale is -1.12 with a standard deviation of 0.15 which indicates advective SV.

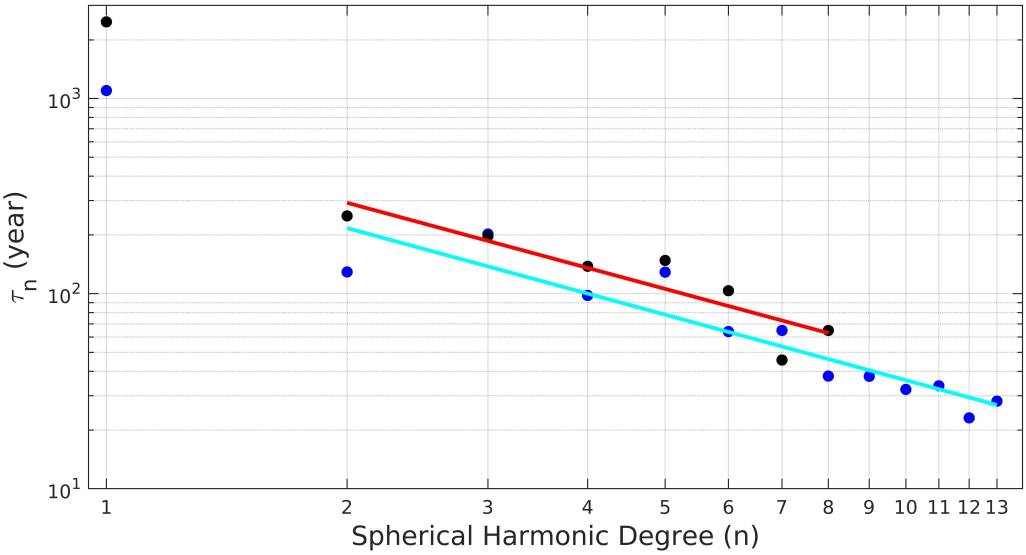

Figure 5.4: The SV timescales of the geomagnetic model CHAOS-7.11 (blue dots) and the estimated Jupiter model (black dots). The cyan and red lines are the linear best fits to the non-dipole parts for Earth and Jupiter respectively.

Using the power spectra of the field and the SV model we estimated, we determine the SV timescales for Jupiter, shown in Figure 5.4 in black. The correlation time for the dipole (τ_1) is 2471 years while the lowest value is 46 years for degree 7. Both Earth and Jupiter demonstrate similar order for the dipole as well as non-dipole terms. The best linear fit slope for $n = 2 - 8$ is -1.11 with a standard deviation of 0.23. A slope of -1 is within one standard deviation while a -2 slope is well outside two standard deviations. This suggests from the scaling laws that the field change is dominated by advective effects, similar to Earth. The similarity with the geodynamo also suggests a comparable Reynolds number of about 1000.

5.2 Field Maps from the Model

We now look at many different maps of the field and the SV at the estimated dynamo radius and try to interpret it to get some information about the field and flow at the interior. The field is of the order of 10^6 nT which consists of both dipole and non-dipole contributions. In order to compare their strengths, we can split the field into the two parts at R_{sf}. The radial dipole and non-dipole fields are shown in Figure 5.5. The non-dipole field is almost 5 times greater than the dipole field when comparing their respective maximum intensities. The magnetic north of the dipole axis of Jupiter is in the northern hemisphere. This is opposite to what is observed on Earth. The intense positive flux in the northern hemisphere and the Great Blue Spot are both visible in the non-dipole field. We have no information related to the existence of dynamo reversals of Jupiter from the data.

5.2.1 Non-dipole Field

In particular, we study the non-dipole field and compare it to the dipole field. Christensen et al. (2010) used four quantitative criteria for Earth-like dynamo models using field at the CMB. Table 5.2 displays the values for our model and CHAOS-7.11 model at two different degrees and the standard geomagnetic value. The standard Earth values are adopted from Christensen et al. (2010). The maximum degree N for which the quantities are calculated is assumed 8 but we also calculate the ratio for our whole model, i.e., up to degree 16 and display the field at this degree in Figure 5.6. For reference, CHAOS-7.11 values are also shown both for degree 8 and up to the core field represented till degree 13. However, we discuss and compare only the degree 8 values in the text. The R_{sf} value for Earth is the CMB value.

The first quantity is relative axial dipole power, defined as the ratio between the axial dipole (AD) and the remaining non-axial dipole (NAD) field-

$$\frac{AD}{NAD} = \frac{P_1^0}{P_1^1 + \sum_{n=2}^{N} \left(\frac{a}{R_{sf}}\right)^{(2n-2)} \sum_{m=0}^{n} P_n^m} \tag{5.5}$$

where,

$$P_n^m = (n+1)[(g_n^m)^2 + (h_n^m)^2] \tag{5.6}$$

For the geodynamo, although the value is decreasing with time, the standard value is taken to be 1.4, while the present day value is 0.93. For Jupiter, the relative axial dipole power is 0.85, indicating that Jupiter's dynamo is either less dipolar or comparable to Earth's (Figures 5.6a and 5.6b). The higher is the power of the axial dipole, the more antisymmetric the radial component is with respect to the equator.

For the symmetry of the non-dipole field, it is divided into even/odd and zonal/non-zonal components. The even components are symmetric with respect to the equator while the odd components describe the anti-symmetry of the non-dipole field. This can be

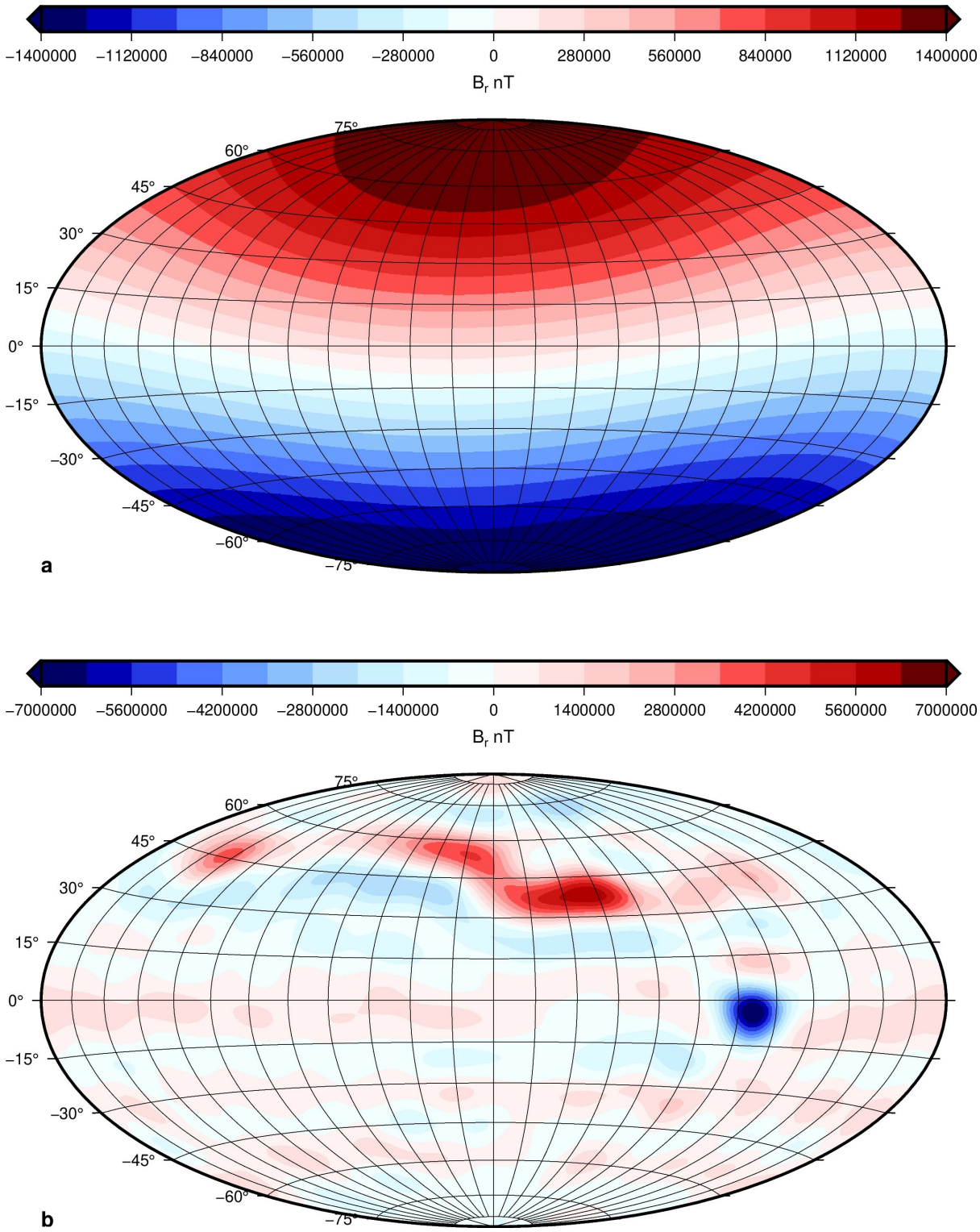

Figure 5.5: The radial dipole (top) and non-dipole (bottom) fields at R_{sf}. The map is centered at 180° longitude.

understood by the odd-even ratio (Equation (5.7)). On the other hand, the axisymmetry is defined by the zonal to non-zonal ratio (Equation (5.8)). They are defined as-

$$\frac{O}{E} = \frac{(n+1)\left(\frac{a}{R_{sf}}\right)^{(2n+4)} \sum_{m=0,\ n+m\ odd}^{N} [(g_n^m)^2 + (h_n^m)^2]}{(n+1)\left(\frac{a}{R_{sf}}\right)^{(2n+4)} \sum_{m=0,\ n+m\ even}^{N} [(g_n^m)^2 + (h_n^m)^2]} \tag{5.7}$$

$$\frac{Z}{NZ} = \frac{(n+1)\left(\frac{a}{R_{sf}}\right)^{(2n+4)} \sum_{m=0,\ n=0}^{N} [(g_n^m)^2 + (h_n^m)^2]}{(n+1)\left(\frac{a}{R_{sf}}\right)^{(2n+4)} \sum_{m=0,\ n\neq 0}^{N} [(g_n^m)^2 + (h_n^m)^2]} \tag{5.8}$$

A random equipartitioned non-dipole field ratio would give an equatorial anti-symmetry of 0.83 since there are more even-valued terms. Similarly, a random equipartitioned field Z/NZ ratio is 0.10 since the number of non-zonal terms are much higher. The O/E value for Earth has not been varying much while the Z/NZ ratio has been slightly increasing with time. The equatorial anti-symmetry for present day Earth is 0.84 and its standard value is 1.0, whereas our model provides a value of 0.52. Thus, Jupiter's non-dipole field is comparatively more symmetric with respect to the equator (Figures 5.6c and 5.6d). The zonal to non-zonal ratio for present day Earth is 0.33 and the standard value is 0.15, while for our model the value is 0.20. Comparing to the standard value, it indicates a stronger zonal contribution for Jupiter (Figures 5.6e and 5.6f).

Lastly, we observe the flux concentration value as a parameter for geodynamo-like models. It is defined as-

$$FCF = \frac{\langle B_r^4 \rangle - \langle B_r^2 \rangle^2}{\langle B_r^2 \rangle^2} \tag{5.9}$$

The flux concentration is considered low when flux exits one hemisphere and enters through the other uniformly (Equation (5.9)). Conversely, it is large when it exits from a concentrated spot and enters the rest of the sphere uniformly. The flux concentration for a purely dipole field is 0.8. For Earth, the current value is 1.33 while the standard value is 1.50. The concentration value for our model is 4.22. This very large value reflects the dominance of the large intense positive flux patch in the northern hemisphere.

5.2.2 Radial Field and Secular Variation

More information about the field can be derived from maps estimated using the model. To understand the field change over time, it is important to look at the field and its variation immediately above its source which is the dynamo. Since the radial field is a continuous function, it is best to observe it and its maps at the top of the dynamo (Bloxham and Gubbins 1985; Jackson et al. 2000). Figure 5.7 shows the radial magnetic field and SV maps calculated using the model at R_{sf}. Comparing it to the radial map at the surface (Figure 4.13), we see that the large positive radial field patch in the northern

Table 5.2: The four quantitative criteria defined for Earth-like models using field morphology at the CMB (Christensen et al. 2010). For Earth, CHAOS-7.11 is used while for Jupiter, the model calculated in this study is used.

Criteria	Earth (standard)	Earth (n=8)	Jupiter (n=8)	Earth (n=13)	Jupiter (n=16)
AD/NAD	1.40	0.93	0.85	0.61	0.46
O/E	1.00	0.84	0.52	0.69	0.64
Z/NZ	0.15	0.33	0.20	0.22	0.19
FCF	1.50	1.33	4.22	1.67	7.37

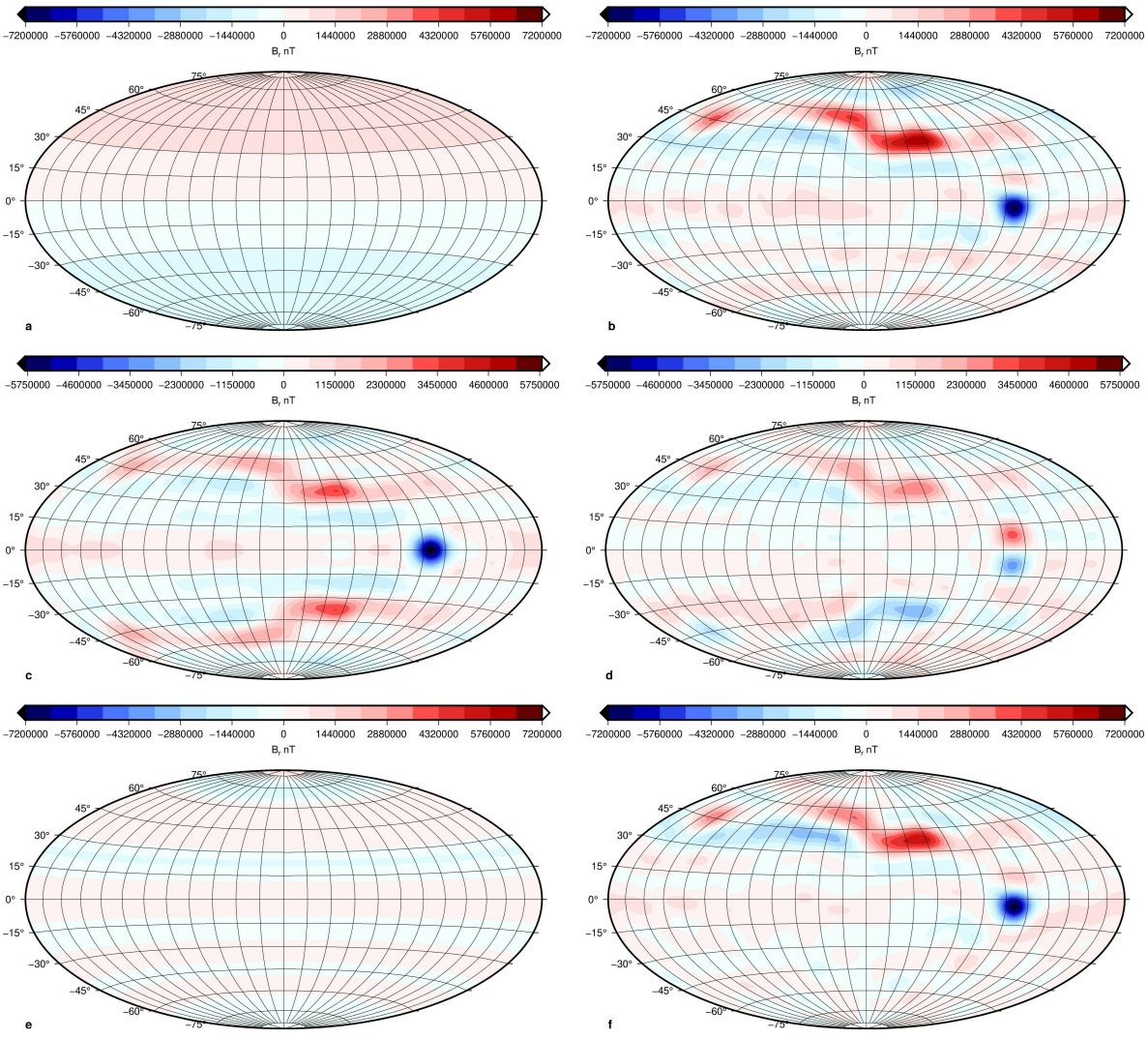

Figure 5.6: The radial field at R_{sf}. (**a**) Axial dipole field. (**b**) Non-axial dipole field. (**c**) Non-dipole symmetric field. (**d**) Non-dipole anti-symmetric field. (**e**) Non-dipole zonal field. (**f**) Non-dipole non-zonal field. The maps are centered at 180° longitude and the field is calculated up to degree 16.

hemisphere and the intense negative patch near the equator become more concentrated with depth.

The spatial pattern of temporal variation of the field brings further dynamical constraints (Figures 4.13b and 5.7b). The SV reveals intense small scale structures as also noted in the power spectra. The strong negative radial field patch immediately south of the equator coincides with a pair of SV structures suggesting eastward drift (Amit 2014; Livermore et al. 2017). This eastward drift could relate to the zonal winds observed at the surface or until 0.95 R_J (Moore et al. 2019). However, the model presents also other prominent SV structures which cannot be explained by zonal winds. There is some suggestion for a weak eastward drift near 45°N latitude, which is the centre of the large positive radial field patch. But, it is not associated with particularly strong SV for most of its structure, possibly indicating a region with weak flow or dominantly field-aligned flow (Finlay and Amit 2011; Livermore et al. 2017). The southern hemisphere has many alternating sign SV patches which are not correlated with particularly strong field structures. Keeping in mind that the model is less constrained at the south pole, the opposite signs of B_r and $\dot{B}_r$ (Figure 5.8) might suggest local fluid upwelling (Amit 2014), similar to the field and SV below Earth's poles and in agreement with a classic meridional circulation inside the tangent cylinder (Olson and Aurnou 1999; Cao et al. 2018). Finally, we note that the radial field and its SV from R_{sf} to the surface are weakly sensitive to depth, making these kinematic interpretations robust and independent of our results regarding the depth of the dynamo region.

5.3 Discussion

Using the results discussed above, we now have a more detailed view on the internal structure of Jupiter. Starting from the surface and moving towards the interior, it can be redefined as in Table 5.3.

Table 5.3: The interior of Jupiter as characterised using recent and this study.

0.95 R_J	Maximum penetration depth of surface zonal winds (Kaspi et al. 2018)
0.84 R_J	Upper bound of H-He demixing layer (Brygoo et al. 2021)
0.83 R_J	Dynamo Radius
0.68 R_J	Lower bound of H-He demixing layer (Brygoo et al. 2021)
0.5-0.6 R_J	Dilute core limit (Wahl et al. 2017; Militzer et al. 2022)

Observational studies and numerical simulations provide very different results for the dynamo of Jupiter. The dynamo radius estimates based on magnetic field models

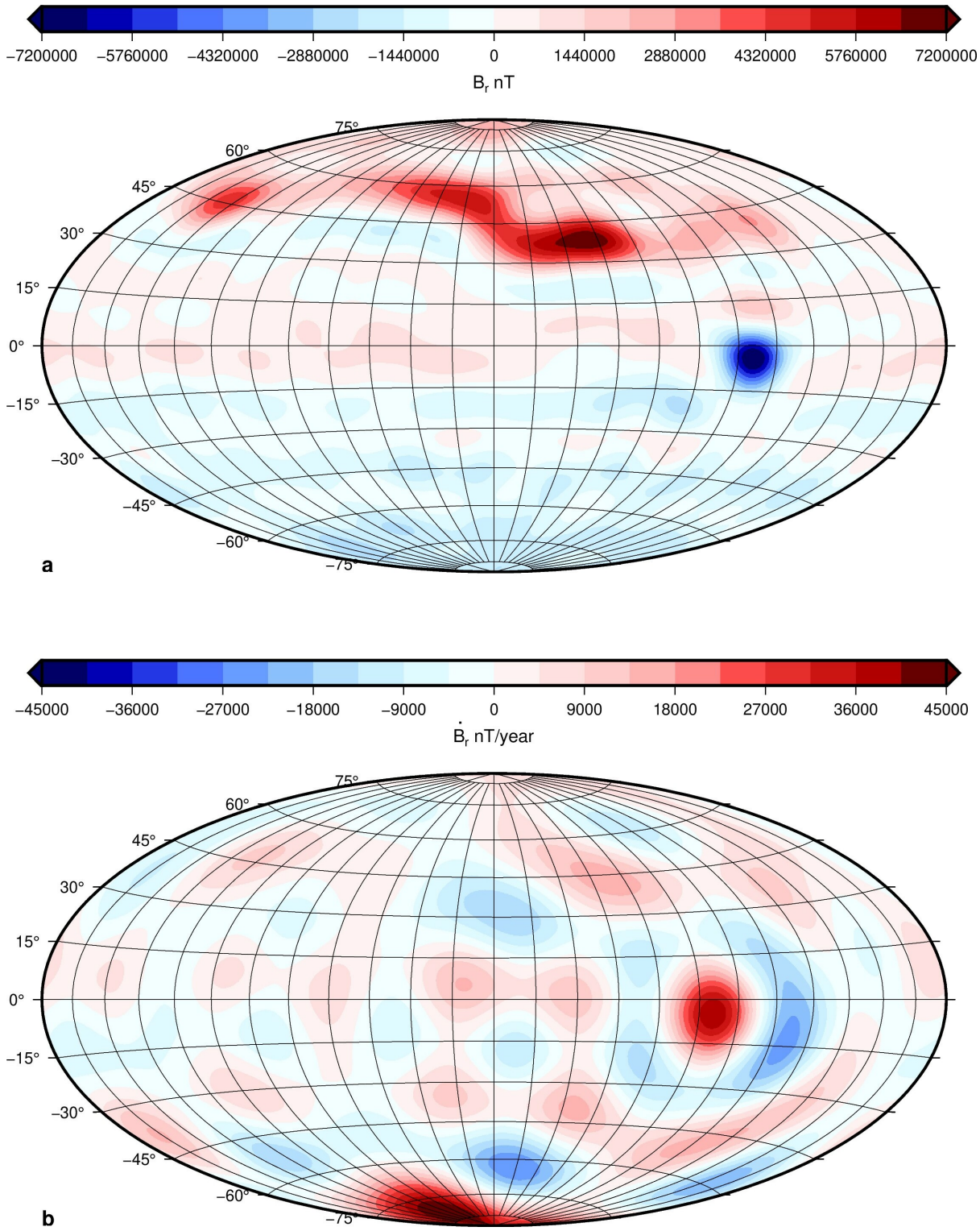

Figure 5.7: The (**a**) radial field and (**b**) its SV at R_{sf}. The maps are centered at 180° longitude.

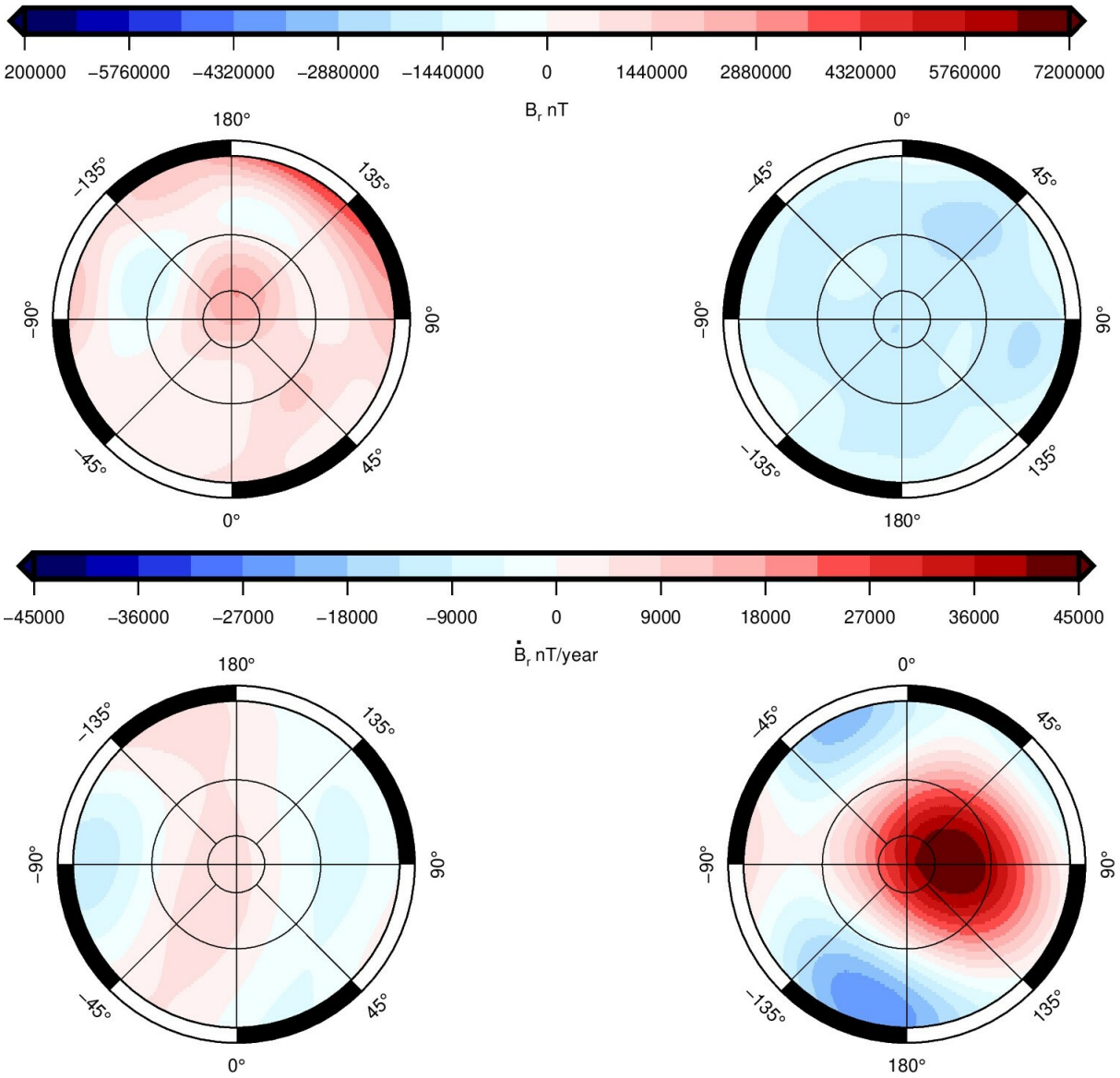

Figure 5.8: The (top) radial field and (bottom) radial SV at R_{sf} for the (left) North Pole and (right) South Pole. The inner to outer circles represent latitudes 85°, 75° and 60° respectively.

derived from Juno data result in a deep dynamo with no evidence of a stratified layer (e.g., Connerney et al. 2018, 2022) above it. Numerical simulations suggest the possibility of two distinct dynamo regions inside Jupiter (Wicht and Gastine 2020). The primary region would be at depth, and is responsible for the dipole dominated field geometry. The secondary one would be shallower, and operates where the equatorial jets encounter conductive material in the transition layer. However, surface jets motion decays rapidly with depth and are unlikely to extend at depths larger than about 3,000-3,500 km or $\sim$0.95 R_J (Guillot et al. 2018; Kaspi et al. 2018). Christensen et al. (2020) suggested that a stratified layer, close to the surface, could quench the jets at depth and play a role in the secondary dynamo. The recent interior model by Militzer et al. (2022) using

gravity models suggest a five layer interior- a dilute core producing the dynamo followed by a stably stratified transition layer. A convective layer of metallic hydrogen follows which could generate a secondary dynamo. The helium rain stably stratified layer and a final convective molecular hydrogen envelop is placed at the top.

We use the analogy of the geomagnetic field and the resulting dynamo radius from the spectra to infer similar results for Jupiter. Our study points towards a source free region extending up to a radius of 0.830 R_J. It matches well the radius of the transition layer in between the metallic and molecular hydrogen (Brygoo et al. 2021), suggesting that this layer is part of the dynamo region. The results do not provide constraints on the bottom radius of the dynamo and do not indicate a shallower secondary dynamo (Gastine and Wicht 2021) above 0.830 R_J. A model that was previously built using the first 28 orbits (see Appendix A) displays similar results.

SV has only been described robustly for Earth till now. This is the first time a satellite observes SV and a model is developed for a global SV of high resolution for any other planet. There have been other studies using either numerical models or field differences over time between models generated for different epochs. The results for the SV due to the flow in the interior are also not consistent between different studies. Numerical simulations constrain the magnetic Reynolds number to be 10 while our similarity of the SV timescales between Earth and Jupiter renders a Reynolds number of about 1000. Bloxham et al. (2022) stated that the zonal winds cause the SV of the Great Blue Spot while Dietrich et al. (2021) stated that the zonal winds are not the only driving force of the time variations. Wicht et al. (2019) concluded that diffusive effects might govern the dynamo in the transition layer. Though their transition region starts above R_{sf}, the SV timescales we compute are independent of radii, hence challenging the importance of diffusion. It thus remains an interesting question as to what phenomenon drives the observed SV of Jupiter. One result that can be evaluated using our model is to infer the flow at the dynamo radius, similar to what was done by Ridley and Holme (2016) using their model. This flow model can constrain the movement and velocity of the fluid present in the interior.

5.4 Concluding Remarks

For the Jovian case, we made use of 5 years of Juno data close to the surface to model the internal main field and its SV. We corroborated our results with synthetic tests performed with the help of a well known and understood geomagnetic field model. Our model is available till degree 16 for the main field and degree 8 for the SV. We use our model to decipher the depth of generation of the dynamo field and the morphology of the flow in the interior.

Figure 5.9 sums up the information we have on Jupiter's interior from other and this study. From the main field model, we know that the upper limit of the dynamo radius is 0.830 R_J, which corresponds to about 59338 km. This is represented by the dark blue line in the figure. Above this layer, there is probably absence of the conducting

metallic hydrogen and presence of only non-conducting molecular hydrogen. The blue arrows represent convection in the conducting fluid occurring at some unknown depth in the deep interior. Combining the main field and the SV, we interpret that the dominant flow at the interior is due to advection with some movement due to diffusion always taking place. The maximum depth of zonal winds is displayed with a black line at depth 0.95 R_J. The hydrogen-helium phase separation result of Brygoo et al. (2021) is shown in red between depths 0.84 and 0.68 R_J. Finally, the metallic hydrogen extends down to somewhere between 0.6-0.5 R_J where the dilute core boundary is (Wahl et al. 2017; Militzer et al. 2022), beyond which is the dense core at the center.

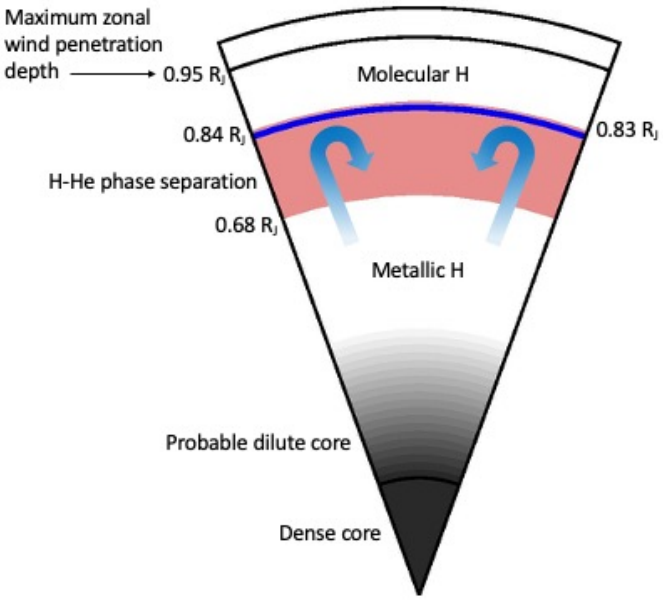

Figure 5.9: A schematic view of the interior of Jupiter as characterised after this study. The bold blue line depicts our result R_{sf}. The grey area depicts the core (0.2 R_J) and the possible dilute core region (Wahl et al. 2017; Wicht and Gastine 2020). The red area between 0.68 and 0.84 R_J depicts the H-He phase separated layer (Brygoo et al. 2021). The top black line at 0.95 R_J depicts the depth where the jets decay down to the minimum (Kaspi et al. 2018). The arrows represent possible convection area with unknown origin depth.

The Martian Case

6. Martian Interior and Field

Mars is the fourth planet from the Sun at a distance of about 1.52 AU with an equatorial radius of 3,393.5 km (1 R_M). This chapter presents a brief overview on the interior structure and composition of the planet, including the most recent results from the lander mission InSight. We then discuss the magnetic exploration by satellites, in particular MGS and MAVEN, and the different magnetic results obtained from them.

6.1 Current Knowledge of the Interior

The most studied planet other than Earth is Mars. It is relatively easier to send scientific instruments to Mars due to its distance from Earth and its thin atmosphere, as compared to the other planets. The earliest theories surrounding the interior of the terrestrial planets stemmed from their astronomical data combined with information available about Earth (e.g., Urey 1951; MacDonald 1962). These described Mars as a cold body that might be nearly homogeneous chemically. Some models assumed there was no core while others estimated a core of mass comparatively much lighter than that of Earth. This indicated high contents of light elements in the Martian interior. Over time, data from missions consisting of orbiters around the planet and landers on the surface came, although abundant data became available only starting at the end of the 20^{th} century.

The first successful flyby and orbiter missions were the Mariner 4 and Mariner 9 in 1964 and 1971 respectively. Subsequently, many other missions provided useful observations. The first successful lander mission was Viking 1, shortly followed by Viking 2, both of which landed on the surface in 1976. Using constraints from the observations, our knowledge gradually increased. No significant magnetic field was observed which questioned the status of the core. It was concluded that the interior was not homogeneous, although not as differentiated as Earth either (Anderson 1972). The core is probably smaller and less dense than the Earth's, with a relatively higher sulphur content. In contrast, the mantle is denser while the crustal thickness is highly variable. From images and remote sensing, it was known that the surface of Mars shows a clear dichotomy. The northern hemisphere consists of plains while the southern hemisphere is full of craters (e.g., Soderblom et al. 1974; Bills and Ferrari 1978). Although the seismometer onboard the Viking missions did not provide much information about the interior, it showed that Mars was seismically not very active (Anderson et al. 1977). But other results from the Viking missions proved very significant like the estimation of the mean density and mo-

ment of inertia, as well as the identification of the SNC meteorites' origin (e.g., Bills and Ferrari 1978; Arvidson et al. 1980).

A very important source of information about the interior comes from the Martian meteorites called the SNC (Shergotty, Nakhla, Chassigny) meteorites (McSween Jr 1984; Treiman et al. 2000). Their composition resembles that of basaltic and ultramafic rocks found on Earth. Many options, especially asteroids, were discussed for their origin. Arguments in favor of their Martian origin are the small size of the planet, its distance from Earth, and its surface geology coinciding with the rocks' ages. But, the most important reason came from the Viking mission results which confirmed the presence of trace gases in the rocks that are similar to the Martian atmosphere (e.g., Bogard and Johnson 1983; Smith et al. 1984). Using information obtained from the meteorites, many new implications for the Martian interior appeared. The Martian mantle was concluded to be more iron rich than that of Earth (McSween Jr 1994). The dominantly silicate mantle and crust has comparatively more volatile elements. The core was still debated to be either partially solid or totally fluid. If the core was large and sulphur rich, it would be largely liquid while if it was small and poor in sulphur, it would be solid (Schubert and Spohn 1990).

On combining these with results from new satellite missions, especially MGS, more about the interior could be estimated. A global topography map with the elevation data ranging between ± 8 km was created (Smith et al. 1999). There is a very apparent elevation difference of about 5 km between the northern and southern hemisphere. The southern hemisphere is considered old while the northern hemisphere is young due to volcanic activities and visible absence of large impact structures. The crust had been assumed to be at least 50 km thick on average, which coincided with geological data, especially with the rate of volcanic generation, while there could be a stagnant and thick mantle layer near the surface (Spohn et al. 2001). By the end of the 20th century, the structure of Mars could be described by the Figure 6.1 from Stevenson (2001). There is a thin crust of variable thickness, a convecting silicate mantle, an iron rich liquid outer core and possibly a solid inner core.

From all these wealth of information, we have been able to start to understand the interior of the planet. We could derive estimates of the mass, moment of inertia and knowledge about the composition. But important information regarding the internal structure were still missing such as a direct measurement of the crust thickness and the size of the core. The seismometer of the InSight mission was designed to answer these important questions. It is the first seismometer that is located on the surface of Mars. The instrument records seismic events which can be classified as low (< 1 Hz) and high (> 1 Hz) frequency (Clinton et al. 2021). The source for the low frequency marsquakes is attributed to the deep interior, mainly in the deep crust or mantle while the high frequency events arise from shallower depths. Nearly 500 marsquakes were recorded from the first 400 Martian days of observations.

Initial results showed that Mars does not have very large intensity quakes, although the spectral characteristics are similar to an earthquake. Most marsquakes observed are

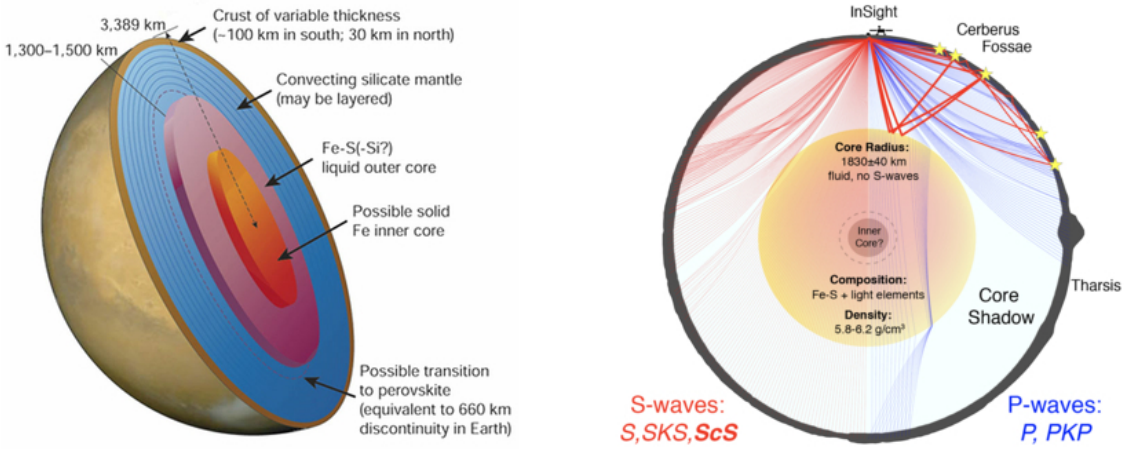

Figure 6.1: Internal structure models of Mars as constrained by Stevenson (2001) and Stähler et al. (2021).

high frequency (Giardini et al. 2020). In particular, results from 3 large events hinted that the crust is either altered or damaged and contains small amounts of volatiles, with the uppermost layer being composed of basaltic rocks (Lognonné et al. 2020). The thickness of the crust can be explained by two models showing either a thin or thick crust of maximum values 25 and 47 km respectively at the landing site. On average, the thickness is estimated between 24 and 72 km (Knapmeyer-Endrun et al. 2021). A study using 8 low frequency events investigated the interior to a depth of 800 km in the upper mantle and found a structure compatible with a low-velocity zone associated with a thermal lithosphere much thicker than on Earth (Khan et al. 2021). The most important result however was the estimation of the size of the liquid metal outer core (Stähler et al. 2021). The large value of 1830 km suggests light elements in the core and an absence of a thermally insulating dense lower mantle (Figure 6.1). More recently, Huang et al. (2022) studied five marsquakes located 3400 to 4400 km away from the lander and found a seismic discontinuity in the mantle at depths of 1000 km, possibly related to a postolivine transition. Their study also confirmed that the Martian mantle is richer in iron than Earth.

InSight also contains a heat probe which could not be deployed properly inside the surface due to the insufficient knowledge about the physical and thermal properties of the regolith present (Spohn et al. 2022). The knowledge of this mission is nevertheless useful for future missions. After InSight, three more landers- Perseverance and Tianwen-1 lander with its rover Zhurong, have been deployed on Mars and many more are in development. Perseverance rover has been designed to collect samples from different locations on the surface as a first step towards the ambitious plan to return Mars samples to Earth (Moeller et al. 2021). Our knowledge about the surface as well as the interior of Mars would expand immensely after the analysis of the returned samples.

6.2 Magnetic Exploration

The magnetic field measurements for Mars were first observed in-situ from the Mariner 4 mission through a flyby in 1965. The periapsis was about 4 R_M and the observed fields very weak in comparison with the measurements observed above Earth at similar distances and in similar regions of solar interactions (Smith et al. 1965). This was used to establish a limit for the dipole moment at about 3x10^{-4} times that of Earth, which corresponds to a surface field intensity of around 100 nT. In the 1970s, three orbiter satellites visited Mars. The Mars 2, 3 and 5 missions observed data from day and night sides with an altitude of over 1000 km above the surface. The presence of an internal field was debated with no clear conclusion. Based on the measurements, Dolginov (1978) tried to estimate the magnetic moment. However, it was observed that the SH degree 1 terms were constantly changing which made it difficult to estimate the dipole moment accurately. Next, Phobos 2 provided measurements from elliptical and circular orbits with closest approach at 850 km above the surface (Riedler et al. 1989). No evidence of an intrinsic magnetic field was found. But there was presence of remanent magnetisation on the meteorites which was attributed to either shock or a past dynamo.

Data from all of the above satellites were useful for understanding the bowshock and the solar wind interactions. The models developed for the bowshock estimated it to be at distances of 1.56 and 2.66 R_M at solar and dark sides respectively (Slavin et al. 1991). But to understand further the magnetic field and its sources, a global coverage at low altitudes was needed. This came with the MGS orbiter.

6.2.1 MGS

A better understanding of the Martian magnetic field came from the data of the Mars Global Surveyor (MGS). The spacecraft carried 5 scientific instruments focusing on surface features as well as on the weather and atmosphere. One of the aims of the mission was to characterise, model and understand the magnetic field. Another important purpose was to study the interaction of the field and the solar winds. The two fluxgate magnetometers were attached at the end of the two solar panels (Figure 6.2). The spacecraft was launched in November 1996 and reached the Martian orbit in September 1997 with an elliptical orbit (Albee et al. 1998). The circular orbit was supposed to start in early 1998, but due to structural damage, it was delayed by a year. The initial elliptical orbits gave low altitude measurements with the periapsis ranging from 80 to 170 km above surface. The final circular orbits observed data from a near constant polar orbit of 350-450 km altitude (Acuña et al. 2001). MGS crossed the day side equator at the same local time of 2 pm travelling from the south to the north.

The initial results from the satellite showed no significant global fields (Acuna et al. 1998). However, localised fields were observed that could have been the result of a past dynamo. The first encounter with the bowshock occurred at a distance of 2.33 R_M. As more data were made available, many magnetic field models were developed using MGS

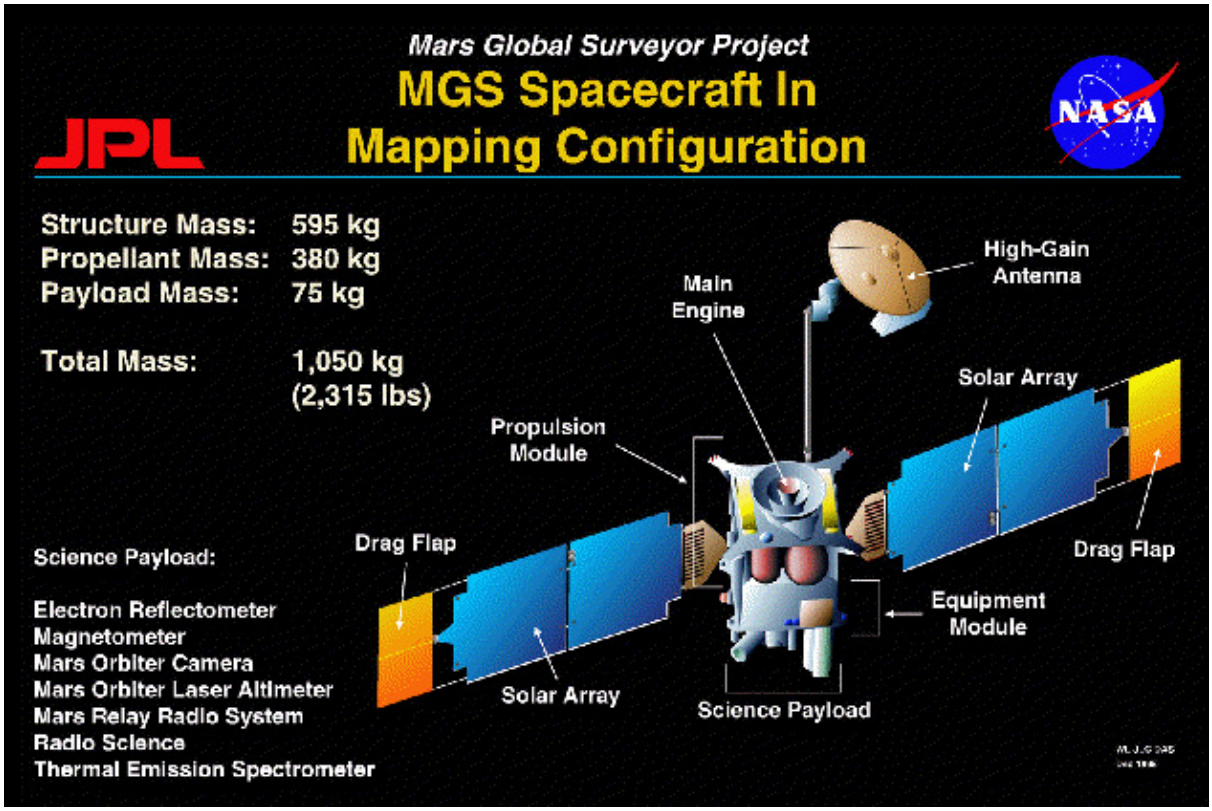

Figure 6.2: The instruments onboard the MGS spacecraft. The two magnetometers are located at the end of the two solar panels. Source: NASA

data (e.g., Purucker et al. 2000; Arkani-Hamed 2002). These models allowed for the first time to obtain global magnetic maps which displayed strong crustal fields of the order of 10^2-10^3 nT at satellite altitudes.

6.2.2 MAVEN

The Mars Atmosphere and Volatile EvolutioN (MAVEN) spacecraft was launched in November 2013 and reached Mars in September 2014 in an elliptical orbit of 6200 km by 150 km above the planet's surface. It carries 8 scientific instruments focusing on the evolution of the climate. Its main objective is to study the Martian upper atmosphere and ionosphere and the processes governing atmospheric loss to space (Jakosky et al. 2015). Additionally, its objective is to analyse the magnetic field as well as its interaction with the solar winds. It carries two vector magnetometers that are attached at the end of the solar array panels (Figure 6.3). The orbital period was around 4.5 hours till early 2019 with apoapsis reaching above 6000 km, after which it underwent a course change in orbit, bringing the orbital period down to around 3.6 hours and the apoapsis to altitudes near 4500 km. On the other hand, the periapsis of MAVEN reach near 100 km allowing it to measure near surface field values.

The high resolution data of MAVEN helped to develop detailed maps of the crustal fields (Langlais et al. 2019). It is easier to understand the external fields around Mars

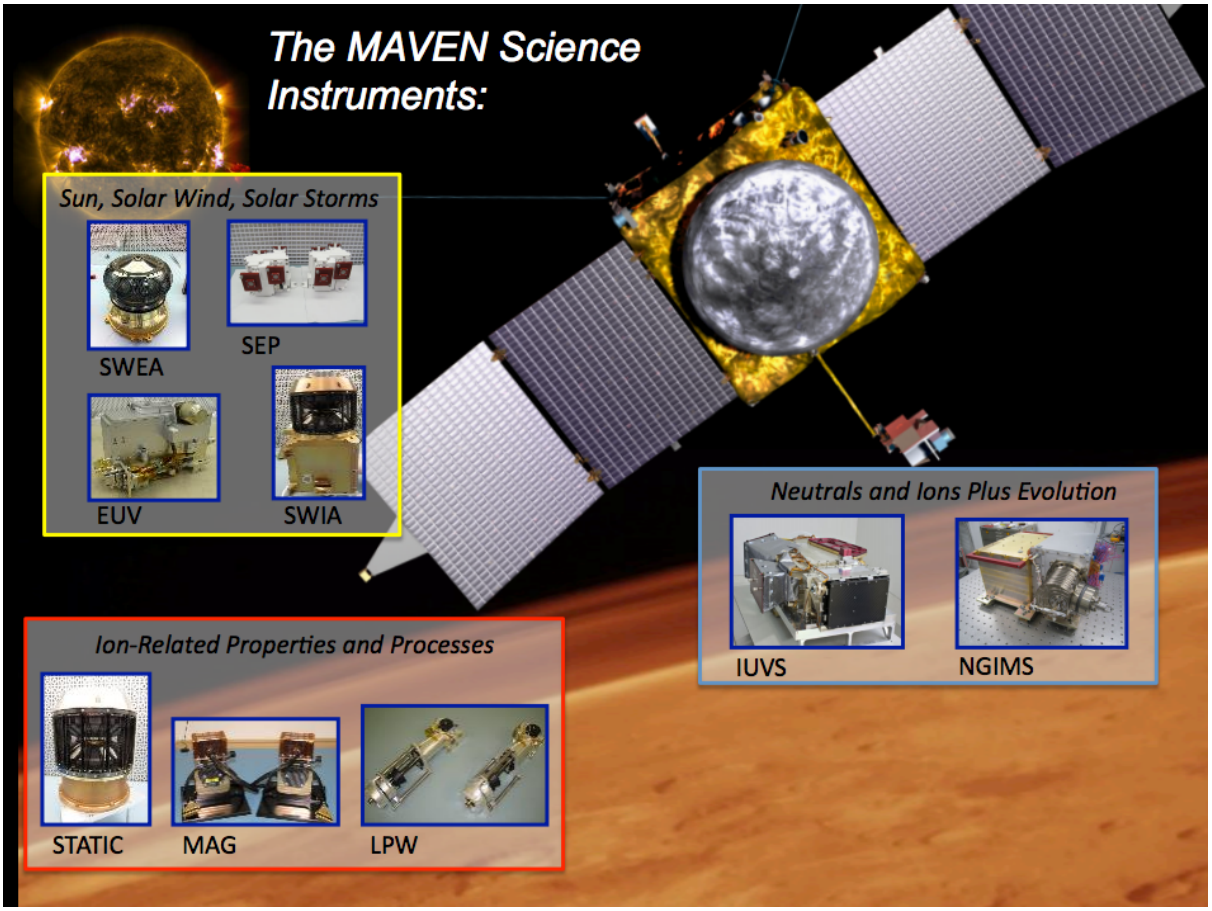

Figure 6.3: The instruments onboard the MAVEN spacecraft. The two magnetometers are located at the end of the two solar panels. Source: MAVEN

using this satellite since it measures the field interaction with the solar winds at several different altitudes. The magnetic results from both MGS and MAVEN are discussed in detail in the next section.

6.2.3 InSight

The only lander on Mars that contains a magnetometer is Interior exploration using Seismic Investigations, Geodesy and Heat Transport (InSight). The InSight mission was launched in May 2018 and landed in November 2018 about 4° north of the equator near longitude of about 135° in a volcanic plain Elysium Planitia (Banerdt et al. 2020). Its main objective is to understand the formation and evolution of the planet. It has 3 major scientific instruments that measure the planet's vibration and temperature. It is powered by two solar array panels and lithium-ion batteries. The magnetometer is part of the auxiliary payload located below one of the solar panels. The magnetic data observed shows that the field is ten times larger at the surface as compared with the field predicted by satellite based models at the same location (Johnson et al. 2020).

6.3 Overview of the Magnetic Field

Many magnetic field models have been developed using different datasets of MGS and MAVEN. For instance, Purucker et al. (2000) used all data below 200 km to model an altitude-normalised radial field map. The model predicts radial fields up to about 200 nT near the satellite altitude of 400 km. Comparing the results with the geomagnetic crustal fields, the Martian fields are about 1 to 2 orders of magnitude larger. Arkani-Hamed (2002) developed a crustal field model up to SH degree 50. Two models using high and low altitude data respectively were merged to form a single model. Langlais et al. (2004) used elliptical orbits data below 350 km and circular orbits data below 440 km altitudes to model the crustal fields. They considered dipole sources located 20 km beneath the surface and suggested magnetisation to be at least one order of magnitude larger compared to Earth. The most common aspect of the results from all these models is the localisation of the remanent crustal fields more in the southern hemisphere than in the northern. They are strong enough to interact and modify the plasma around them (Brain 2006). The bowshock however remains unaffected by the crustal fields. The interaction is highly variable due to the pressure created from the fields as well as the planet's rotation. MGS data was also used to understand external magnetic fields. Langlais et al. (2017) divided the data into day and night sides and computed daily averages which showed a periodicity of 26-27 days and an annual cycle related to Mars revolution. They studied the fields in an effort to use them to separate quiet and noisy data. Since there are no magnetic indices available for Mars, this would help in quiet data selection for future crustal field modelling. A similar study by Mittelholz et al. (2017) was performed on MGS data between 50° and 60° north latitudes which exhibited the same periodicity. No SV has been observed for Mars, which re-confirms that there is no active dynamo field (Purucker et al. 2003).

Since MAVEN has a highly elliptical orbit, it allows for the observations at different altitudes. Both external and internal fields can and have been investigated using them. Mittelholz et al. (2018) proposed magnetic index proxies could be derived using MAVEN data. They examined the correlations between the external fields at 150 to 600 km altitudes and the interplanetary magnetic fields embedded in the solar winds. Their suggested proxy was using the interplanetary magnetic fields that are upstream of the bowshock. For the internal fields, Langlais et al. (2019) combined the MGS and MAVEN observations to build an updated crustal field model. They used low altitude data from the two spacecrafts accumulated over 13 years to estimate a model up to SH degree 134. The predicted magnetic field maps of the different components from their model at the surface are shown in Figure 6.4. Two areas in the mid southern hemisphere called the Terra Sirenum and Terra Cimmeria near 180° longitude show maximum crustal anomalies.

The model by Langlais et al. (2019) was used by Gong and Wieczorek (2021) to constrain magnetization depths using power spectrum analyses. They suggested that the stronger magnetic anomalies in the southern hemisphere are related to deeper depths. Their preferred interpretation reason for this was the formation of deeper sources in early

history while the shallower sources were newly formed probably after an impact event. The argument of impact craters removing magnetisation is also used to infer the timing of the Martian dynamo (Lillis et al. 2013; Vervelidou et al. 2017). Most estimates study the presence or absence of magnetic field over the large Martian basins to present a dynamo cessation time. In a recent study, Mittelholz et al. (2020) suggested the presence of dynamo at two epochs. The study used MAVEN data to show low intensity fields in the northern hemisphere, especially near the rims of basins to conclude that the dynamo was present 4.5 million years ago. However, they also interpreted the signal above another region to be a result of a dynamo operating 3.7 million years ago. Based on their results, the Martian dynamo is thought to have been operating early in Martian history and at least at 3.7 Gyrs.

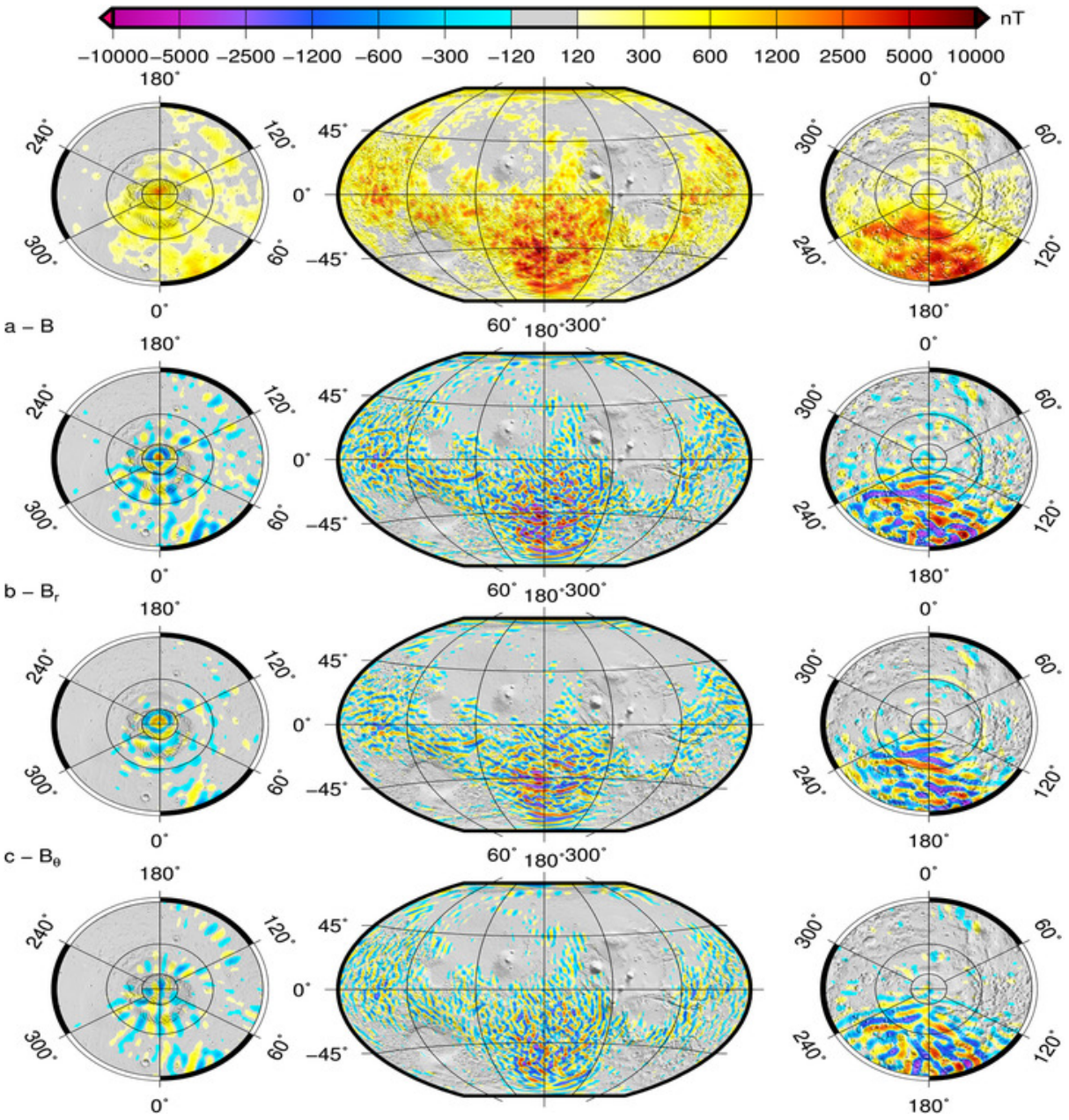

Figure 6.4: The predicted crustal field maps of Mars from the model of Langlais et al. (2019) at the surface using MGS and MAVEN data. The different components from top to bottom are the field intensity, radial, latitudinal and longitudinal fields respectively.

7. Time Variable Fields and Models

This chapter starts with information about the data used in this study. Our aim is to choose data suitable for modelling the transient fields that would provide information about the interior conductivity. For this, we need to first separate the internal from the external fields. After the removal of static fields from the observations of MGS and MAVEN, we analyse and model the transient fields. The SH modelling techniques follow those defined in Chapter 2.

7.1 Description of the Data

Both MGS and MAVEN have been very beneficial in understanding the nature of magnetic field around Mars. This is mainly because of the long time series measurements that were available from them. The MGS mission operated between 1997 and 2006 while MAVEN, providing data from 2014, is still in orbit. The satellites provide magnetic field measurements in Planetocentric, Payload and Sun-State coordinate systems with a high sampling rate along their orbits. The MGS data are available for different samplings depending on the telemetry while MAVEN data are available from 1 sample to up to 32 samples per second. The MGS data used in this study range in sampling from 0.75 sec to 3 sec while the MAVEN data are selected every 0.5 sec.

The orbit configurations of the two satellites are very different. While MGS travelled in a circular polar orbit, favorable for SH analyses and internal/external field separation, the elliptical orbit of MAVEN introduces more ambiguities. The two different orbit configurations create a lot of differences in the measurements picked up by both above the same location due to the different altitudes. The variation of the periapsis with altitude and latitude for MGS and MAVEN are shown in Figures 7.1 and 7.2 respectively. It clearly shows the difference between the two satellites. While the periapsis altitude was constant around 350 km for MGS, the altitude goes as low as 110 km for MAVEN. The periapsis latitude of MGS is fixed near the south pole while for MAVEN, the latitude keeps varying with time. For this study, we select MGS data obtained between February 1999 and November 2006, corresponding to the orbital phase along a quasi-circular orbit. We select MAVEN measurements from October 2014 to January 2022 below an altitude of 1000 km. This threshold is considered to be a good compromise between data coverage and data sensitivity to the global internal induced field in the Mars' mantle.

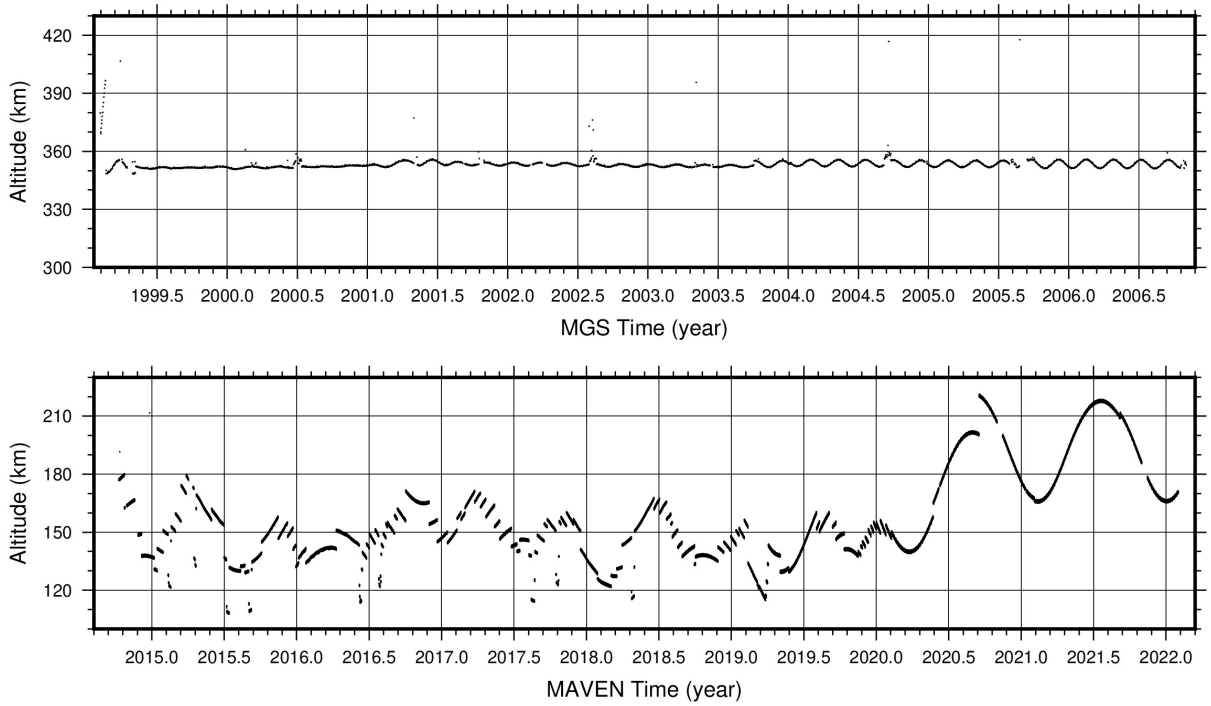

Figure 7.1: The periapsis variation of the satellite orbits for MGS and MAVEN with respect to altitude.

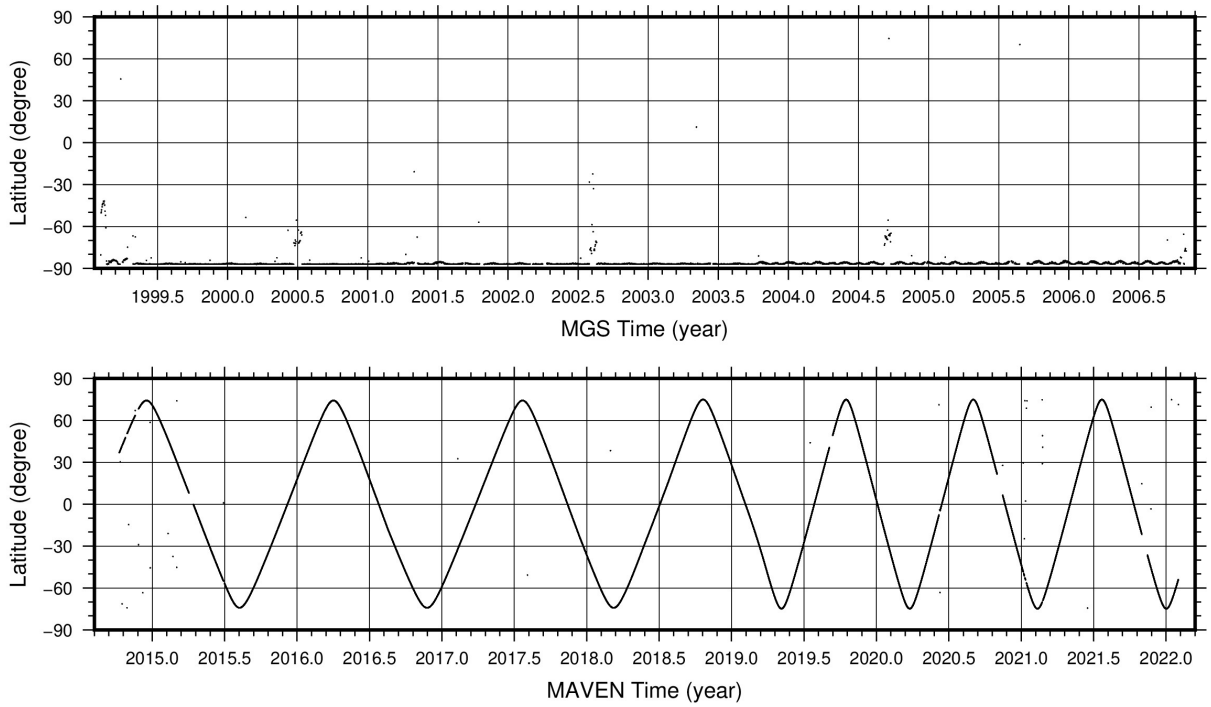

Figure 7.2: The periapsis variation of the satellite orbits for MGS and MAVEN with respect to latitude.

In the following, MGS and MAVEN data refer to the selected data set described above. Out of the 2829 days of MGS measurements, data is available for 2731 days. This corresponds to a little more than 7 Earth years or about 4 Martian years. For MAVEN,

out of the 2671 days, we have data for 2613 days, which corresponds to 7 Earth years or a little less than 4 Martian years. We convert the data from Cartesian coordinates to Spherical using the equations defined in Chapter 4.

7.2 Removal of the Static Fields

The Martian magnetic field has both static and time-varying components. The static contribution comes from the crustal fields while the time-varying part is a result of the interaction with solar phenomena. Our focus is on the internally generated transient fields. These induced fields depend on the electrical conductivity of the planet and hence allow to obtain some information about the interior. Since the induced response can be weak in magnitude and because the available measurements have an imperfect geographical coverage, a careful correction of the static measurements is required to minimize the leakage of the crustal field signals into the time series of the internal varying fields.

Crustal field models (e.g., Purucker et al. 2000; Langlais et al. 2004; Morschhauser et al. 2014) show that Mars has very localized magnetic field anomalies of magnitude one to two orders higher than that of Earth. However, InSight magnetometer results show even larger field values at the surface (Johnson et al. 2020). While the satellite models predicted intensities near 300 nT at the InSight location, the magnetometer onboard recorded intensities around 2000 nT. These high values suggest that Mars once had an active dynamo present that left this magnetized crust. Most of the magnetized terrain is found in the southern hemisphere where strong fields are observed. The northern hemisphere is associated with weaker fields and thinner crust as compared to the southern (Smith et al. 1999). They may have once been magnetized and could have de-magnetized due to heating events or it could be that they were never strongly magnetized (e.g., Nimmo et al. 2008; Quesnel et al. 2009). There is still much debate on this question and no final answer to it.

In this study, we use the model by Langlais et al. (2019) to predict the crustal fields at our selected data locations and to correct the measurements for it. The model relies on the measurements from both the MGS and MAVEN satellites. The MGS elliptical as well as circular orbit data between 1997 and 2006 were taken. For MAVEN, data up until mid-May 2017 were selected. The model was estimated using the modelling tool called the Equivalent Source Dipole (ESD). This approach works well for inhomogeneous geographical data distribution and does not require an explicit regularisation. ESD is based on the mechanism that there are dipoles present all over the surface of the planet and that their combination produces the observed magnetic field. Modelling the field at a source free location requires combining the contributions from all these dipoles at that location. The magnetic field at a given location produced by a given dipole decreases with the cube of the distance. A maximum distance of 1800 km was assumed beyond which the dipole contribution was not considered. The ESD model was then converted to a SH model of degree and order 134.

After the prediction of the static fields at the spacecraft positions using the above

discussed model, they are subtracted from the observed field to get the residual or time-varying fields. The intensities of the satellite observations, the predicted remanent fields at these locations and the final residual fields for both the satellites with respect to latitude are shown in Figure 7.3. The differences between the observations made by the two satellites are very evident here. Since MGS was in a constant circular orbit around the planet, the measurements picked up by it are of the same intensity throughout. The intensities for the measurements at altitudes ranging between 350-450 km are of the order of 10^2 nT. MAVEN on the other hand picks up signals whose intensity goes up to 10^3 nT due to its highly elliptical orbits which reach altitudes as low as 110 km. Since the remanent fields are the dominant fields, especially in the southern hemisphere, most of the high intensity measurements are reflected in the predicted crustal fields. Removing the crustal fields leave us with residual fields that do not show variations with respect to latitude. There is a significant difference of magnitudes between the observations and the residual transient fields for MAVEN while they are of the same order for MGS. Both MGS and MAVEN residual field intensities range between 0 to 250 nT, with a few reaching up to 500 nT.

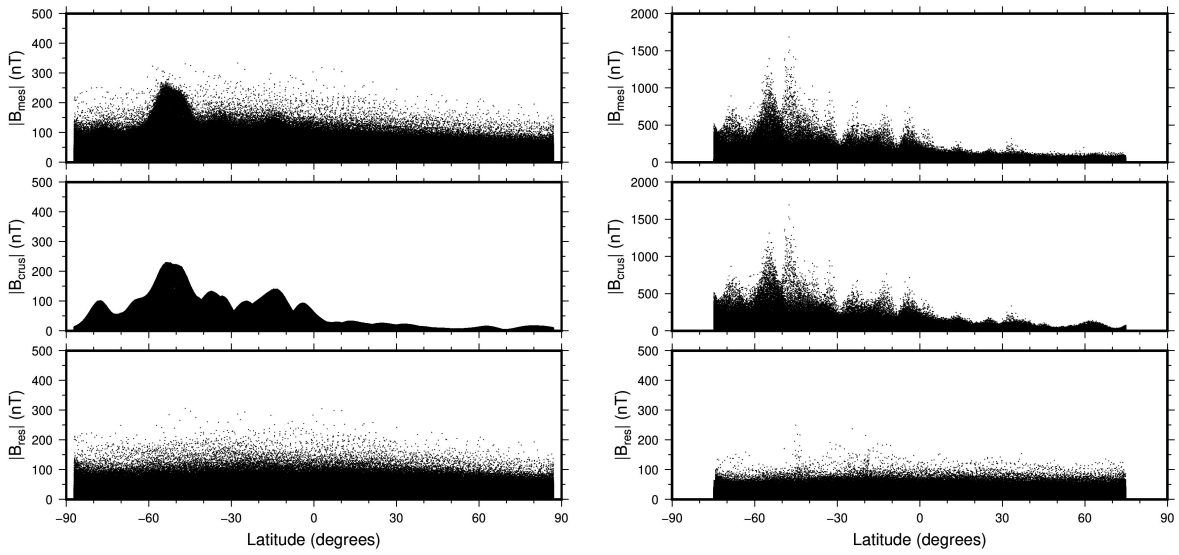

Figure 7.3: The field intensities of the observed data measurements (B_{mes}), predicted static crustal fields (B_{crus}) and the residual transient fields (B_{res}) for both MGS (left) and MAVEN (right) data. Note the different scales for both satellites.

In order to be sure that no leakage from the crustal fields seeped into the time-varying fields, we attempt to model the static fields again using the residual fields. We calculate an internal field model each for the two satellites with no external field contributions. Since the dominant fields have been removed from the measurements, we consider a model up to degree 10 to be sufficient enough to account for any remaining static signals. We use the residual data below 500 km for MAVEN and all residual data for MGS to estimate the models. Figure 7.4 shows the field intensity maps calculated using the two models. The magnitude is very low which indicates all the remanent fields have been removed from the observations at this scale ($N_{int} = 10$). Though not at the exact same locations,

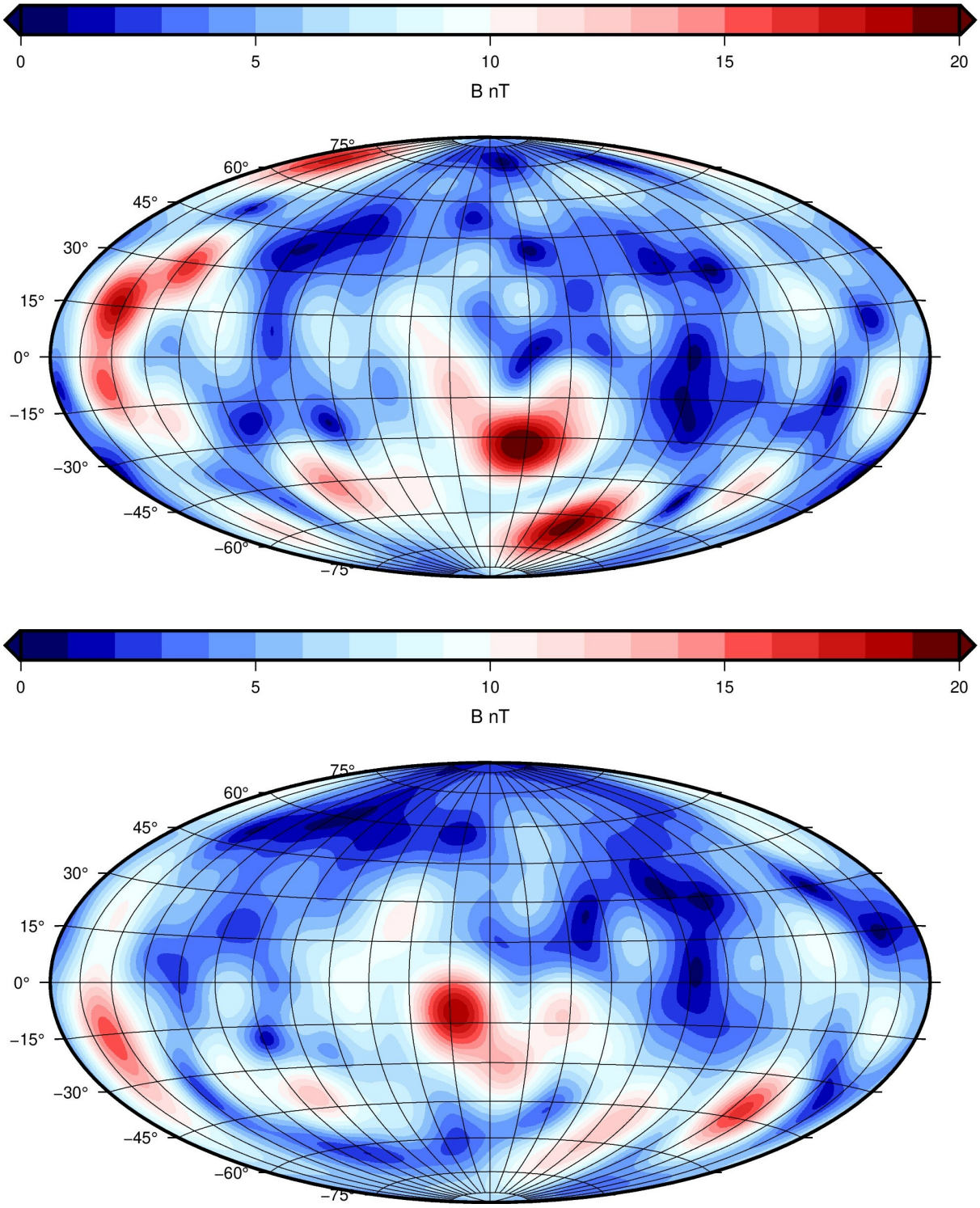

Figure 7.4: The crustal field intensity from a model calculated using residual MGS data (top) and residual MAVEN data below 500 km altitude (bottom).

we do see the maximum intensity features for both the models replicate themselves where the crustal fields were high before their removal. This could be due to the fact that the measurements are corrected with a model developed with a different data set and hence we observe some residual structures. Another reason could be the presence of transient fields where the crustal fields were present. The crustal fields can interact with the solar winds and form mini-magnetospheres at their locations. The geometry of the field is complex and thus it can create multiple current systems inside the mini-magnetospheres where field intensity is very high (Harnett and Winglee 2003). It could be that the intensities observed on the maps are related to this.

7.3 Analysis of the Transient Fields

After the removal of the static crustal fields, we are left with the time-varying fields. The constantly changing fields have two origins. The first is the interaction of the solar winds and the interplanetary magnetic fields with the planet. As the sources of the external fields are outside the planet, they induce currents inside the planet's conducting crust and mantle due to induction. This generates internally induced fields which are the other sources of the time-varying fields. The residual fields thus contain combined information from both the externally inducing and internally induced fields.

In order to analyse and understand the transient fields, it can be advantageous to view the observations in both the Planetocentric (PC) and the Sun-State (SS) Coordinate systems. As discussed before, the PC coordinate system is body fixed while the SS system is defined with respect to the Sun. The SS coordinate system is also known as the Mars-centered Solar Orbital (MSO) coordinate system. In this system, the x axis is positive in direction of the Sun from Mars, the y axis lies in the plane determined by the Mars-Sun vector and the Mars orbital velocity vector (anti-parallel to orbital velocity) and the z axis is perpendicular to x and y axes and is positive in direction of the northward normal of the orbit plane of Mars. We analyse the time series of the residuals in both the PC and SS system. The transient field components averaged over per day in the SS coordinate system gives interesting results for both the satellites.

7.3.1 For MGS data

For MGS, we look at the average over all local times and the day and night sides separately. This allows us to distinguish between the quieter (night) and noisier (day) data. In the day side, the contamination from the particle interaction with solar winds introduces a lot of scatter in the measurements. This can be partly avoided by observing only the dark or night side data. The opposite polarity of day and night sides cancel out in the Bx component of the daily average (Figure 7.5). On the other hand, the By component displays almost zero magnitudes in the night side but displays maximum activity on the day side. The Bz component is low in the day side and daily average. It is particularly low in the night side, similar to the By component. Figures 7.6 and 7.7

show the averaged residual fields for MGS day and night sides data respectively.

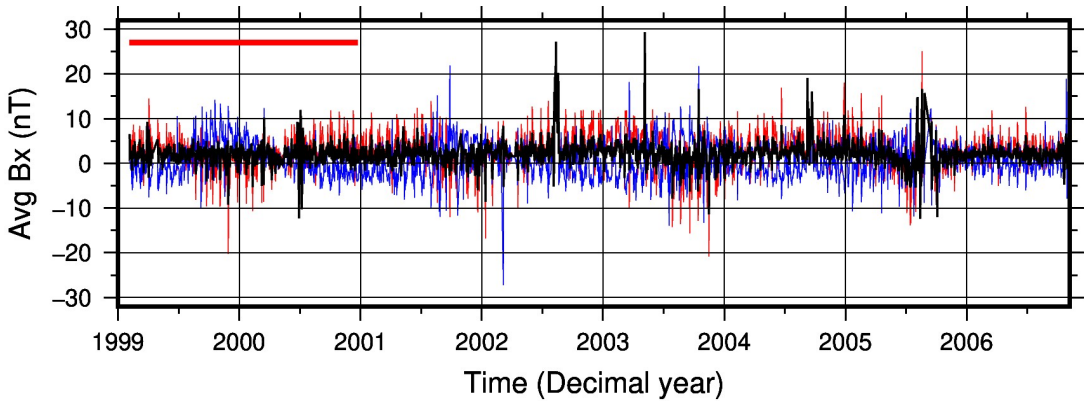

Figure 7.5: The average Bx component per day for MGS data (black) in SS coordinates. The separate daily day and night sides averages are shown in red and blue colours respectively. The red horizontal bar represents one Martian year.

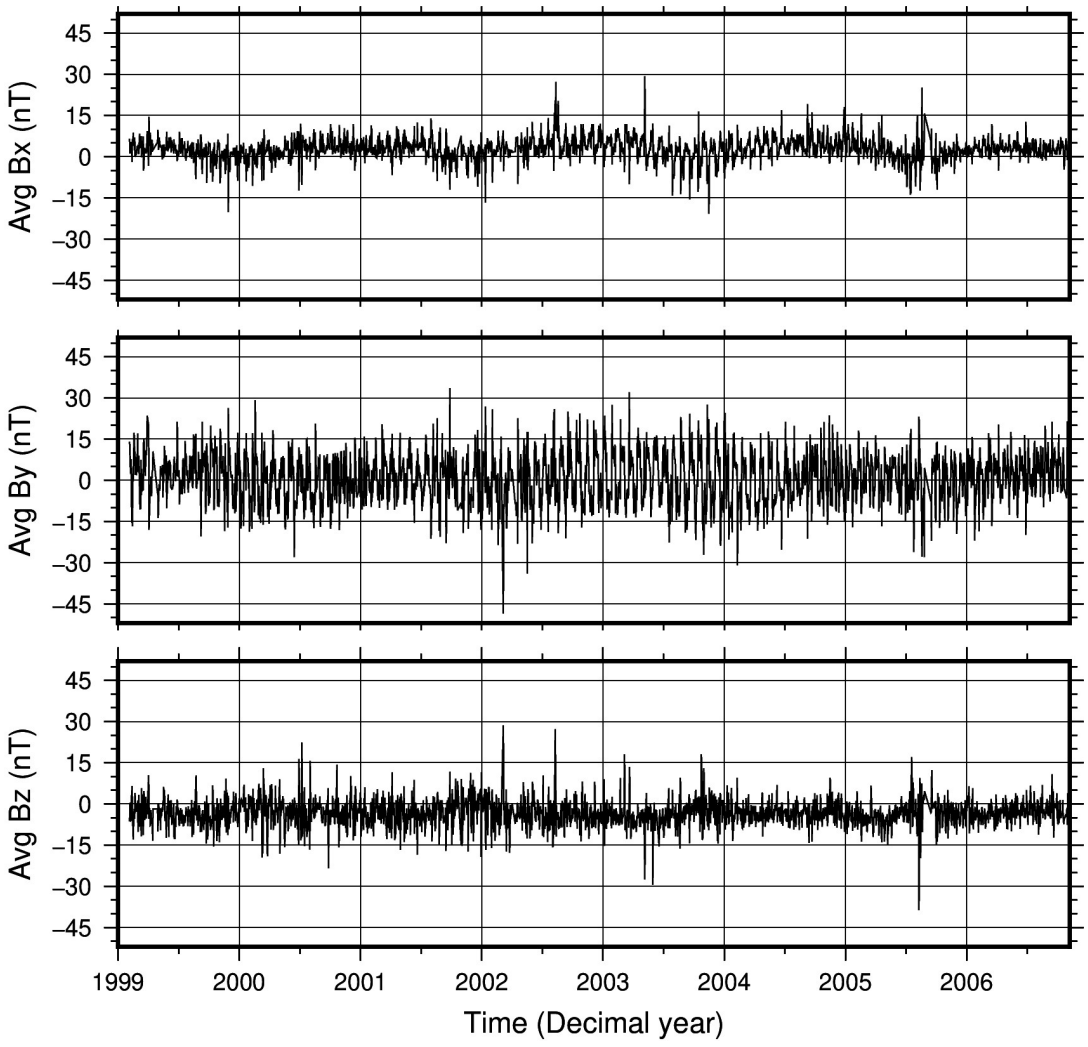

Figure 7.6: The average field per day for day side MGS data in SS coordinates.

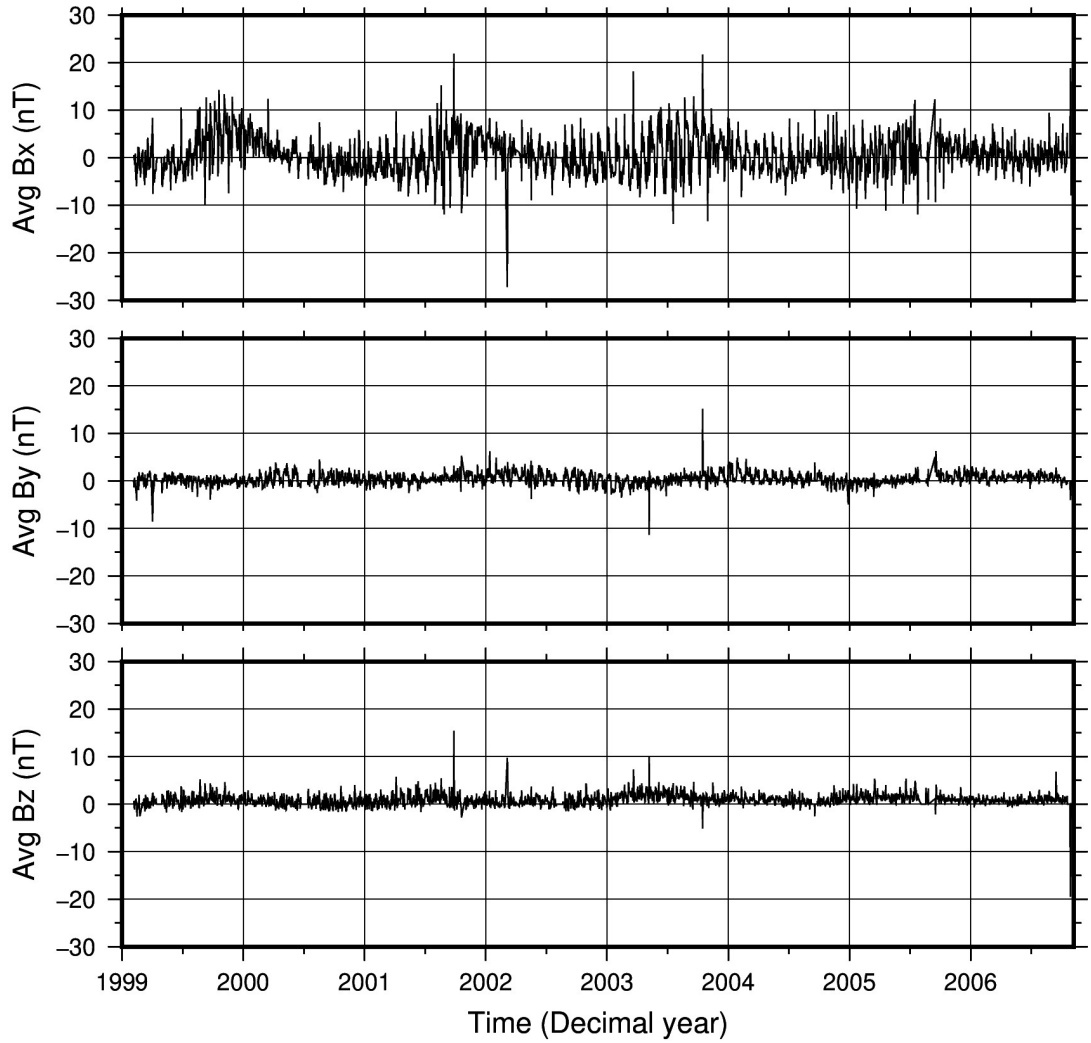

Figure 7.7: The average field per day for night side MGS data in SS coordinates.

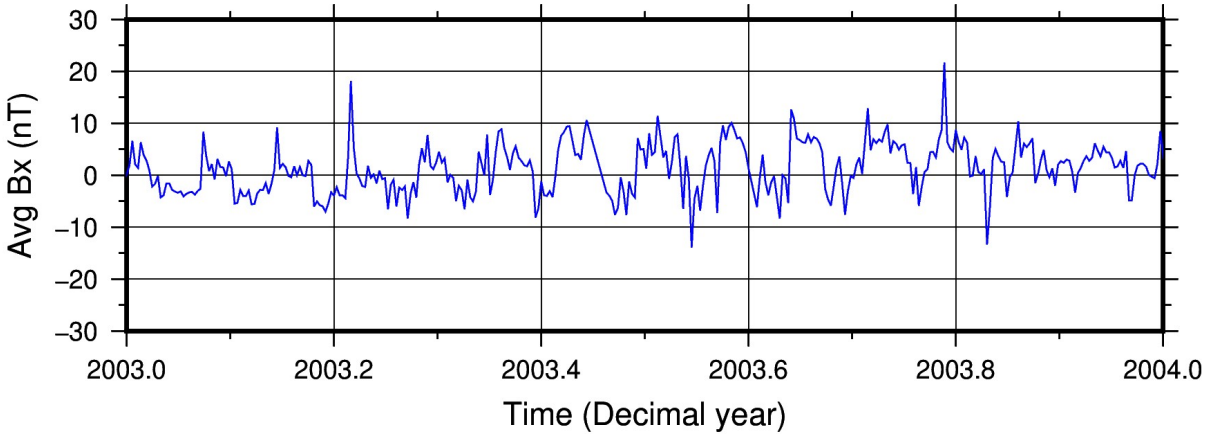

Figure 7.8: The average field per day for night side MGS data for the year 2003 in SS coordinates.

For better clarity, Figure 7.8 shows the daily night side average for one particular year, namely 2003. The year was part of solar cycle 23 where the solar peak occurred in

2000. Large solar flares occurred in late October 2003 which could be related to the peak value observed in the figure near the same time (Crider et al. 2005). The perihelion for this particular Martian year occurred in August 2003.

7.3.2 For MAVEN data

For MAVEN, Figure 7.9 displays the averaged field for each component. The By and Bz components appear to follow a pattern though the Bz component is a little lower in magnitude. The Bx component appears to be noisier than the other two, i.e., it contains more short term variations. The signal around 2019 especially is a lot lower in amplitude for all the three components. The MAVEN data we use is below 1000 km. However, on averaging data by using measurements below other different altitudes as well, the pattern observed remains the same.

Putting constraints with respect to local time in addition to altitude for MAVEN results in sparse time series, or no data for some days, thereby ruling out the possibility to accurately assess any continuous time series. But the partial time series thus obtained does show some large amplitudes in the Bx component for the night side that could follow some time period. Similar to MGS, the By component in the day side has maximum amplitudes and the Bz component for both day and night has the lowest amplitudes.

Figure 7.10 shows the daily average for the year 2016. It was part of solar cycle 24 and the solar peak occurred in 2014. Solar activity in this cycle was comparatively very weak which could be the reason of some low values seen in the figure. The Martian perihelion occurred in October 2016.

7.3.3 Comparison of the Results

A pattern is observed in the daily averaged Bx component for night side MGS data and the By component for MAVEN data across all local times. This temporal series pattern was also previously observed by Langlais et al. (2017) and Mittelholz et al. (2018). Their results and the latest observations discussed here coincide with a 26-27 days pattern for the variation of the field components with each day. This could correspond to the Carrington cycle, which is the rotation period of the Sun on its axis. This might give some information about the interplanetary magnetic fields and its correlation, if any, with the Martian magnetic field. Since there are no magnetic indices available for Mars, this can be used to design a proxy of the external time-variations which can in turn be used for crustal field modelling.

In addition, owing to the elliptical orbit of MAVEN, we observed its transient fields with respect to the seasons and local times as defined in Allison and McEwen (2000). The seasons are represented by solar longitude (L_S). For the northern hemisphere, L_S = 90° starts the summer while L_S = 270° is the onset of winter. The opposite is true for the southern hemisphere. Mars is farthest from the Sun near L_S = 70° where the northern hemisphere is tilted towards the Sun and the planet moves slowly. On the other

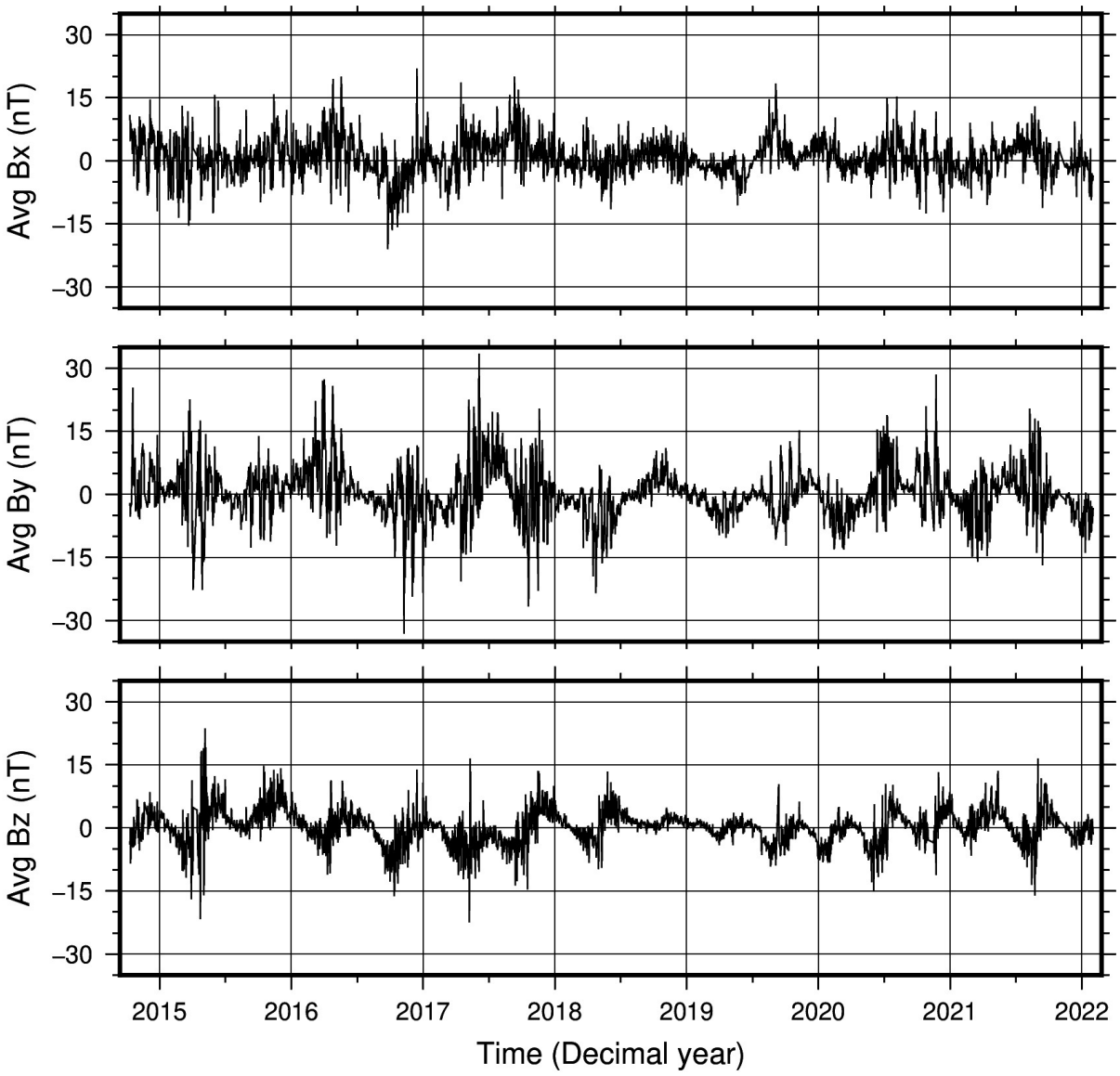

Figure 7.9: The average field per day for MAVEN data in SS coordinates.

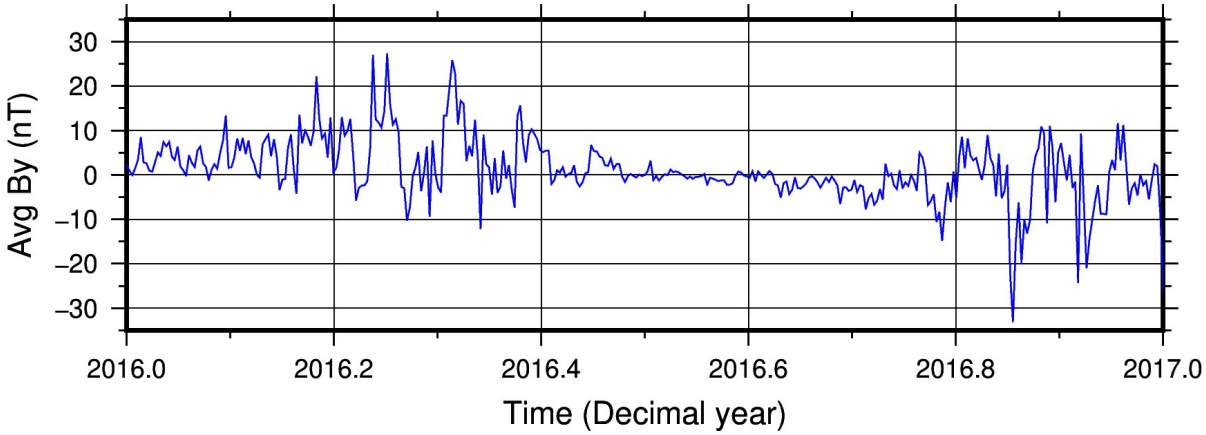

Figure 7.10: The average field per day for MAVEN data for the year 2016 in SS coordinates.

hand, the perihelion takes place near $L_S = 250°$, when the planet moves fastest and the southern hemisphere is tilted towards the Sun. The dust storm season starts near $L_S = 260°$. Since the orbit of Mars is much more elliptical, more energy from the Sun reaches it during perihelion and hence summer in the southern hemisphere would have more solar interactions. No particular pattern with respect to the season is observed except some data that shows comparatively higher magnitudes near $L_S = 350°$, which is expected since the southern summer is more intense (Figure 7.11). For field variation with respect to local time, the average peak is observed at 10 am for some data but there is no overall specific pattern observed.

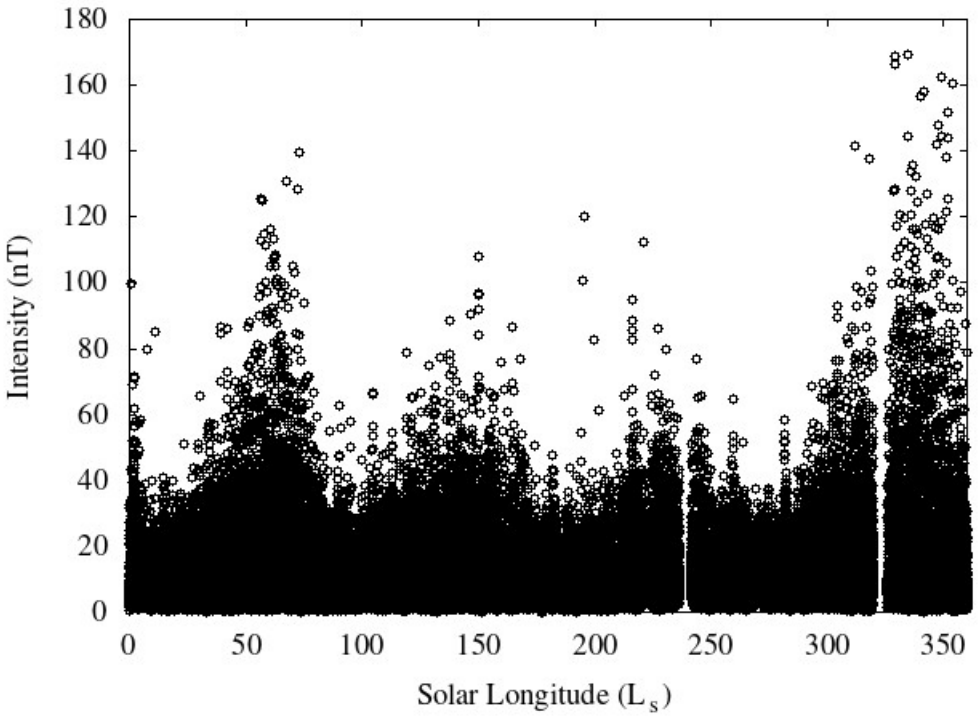

Figure 7.11: The field intensity with respect to the solar longitude for one Martian year MAVEN data.

7.4 Modelling of the Transient Fields

The residual measurements contain the internal and external field signals. Their separation can be performed in SH provided the measurements cover sufficiently the whole planet. We use the same equation for potential for modelling the internal and external fields as defined in Equation (2.6) with the residual measurements in the PC reference frame. After a successful separation, the internal field coefficients depict the secondary signal generated in the planet's interior due to the external time-varying fields.

7.4.1 Synthetic Tests

A perfect internal/external field separation would be achieved to high spatial resolution if perfect measurements are available over the whole closed surface within our desired 1-day time window. However, this is not the case for either MGS or MAVEN. MGS provides around 10 orbits per 24 hours and an even lower coverage after selection of night side data, whereas MAVEN provides about 6 to 7 orbits per day. In order to test the robustness of the field separation, we perform synthetic tests using predicted field measurements at the real data locations. This analysis is also a mean to define the optimum time window when inverting for real data and to assess the maximum SH degree expansion. We use the geomagnetic magnetospheric model, `MMA_SHA_2C` obtained from the Swarm mission website (Olsen et al. 2013). The models are available for different degrees depending on the day, but they are defined up to at least degree 1 and 5 for magnetospheric fields and its induced parts respectively. The model provides the degree 1 and order 0 terms for every 90 minutes and other terms for every 6 hours. The coefficients are calculated using all quiet time data available during the Swarm mission.

We first predict the magnetic data using the Gauss coefficients of the magnetospheric model at the locations of MGS and MAVEN. The measurements obtained have combined externally inducing and internally induced fields data. The next step is to invert this data to recover the external and internal time-varying coefficients and to compare them with the input model coefficients. We estimate several models using different truncation degrees and time windows. Ideally, the resulting models would match exactly the input model coefficients. But the geomagnetic model used and the data predicted are time and space dependent. Since the inversion is performed using different data sets as compared to the initial model, we do not expect a complete correlation. We still find good correlations, especially when using MGS locations. The models are calculated for truncation degrees 1, 2 and 3 and using time windows varying between 1 and 30 days. For all these models, the magnitude of the inducing fields are much higher than their induced counterparts and the correlation between them is positive. The correlation coefficient between the initial and the predicted models is highest for the degree 1 and order 0 terms for daily models (0.92 and 0.95 using MGS while 0.89 and 0.90 using MAVEN for internal and external coefficients respectively) and decreases with increasing time windows. It is expected that the MAVEN measurements do not allow a perfect recovery of the coefficients because of the ellipticity of its orbit. Figure 7.12 displays the synthetic coefficients obtained for the degree 1 order 0 terms for daily models using MAVEN data along with the original coefficients. The different truncation degrees for the model (N_{int}) does not affect much the correlation for the dipole terms.

Our synthetic results confirm that our inversion is sufficiently constrained. Similar to Mars, the 27 days peak is observed on Earth and it is represented by the dipole (Banks 1969). This geometry is reflected in the induced response obtained from the same term. The external field of Earth is dominated by the ring currents that originate in the magnetosphere. On the other hand, Mars does not have a clear magnetosphere

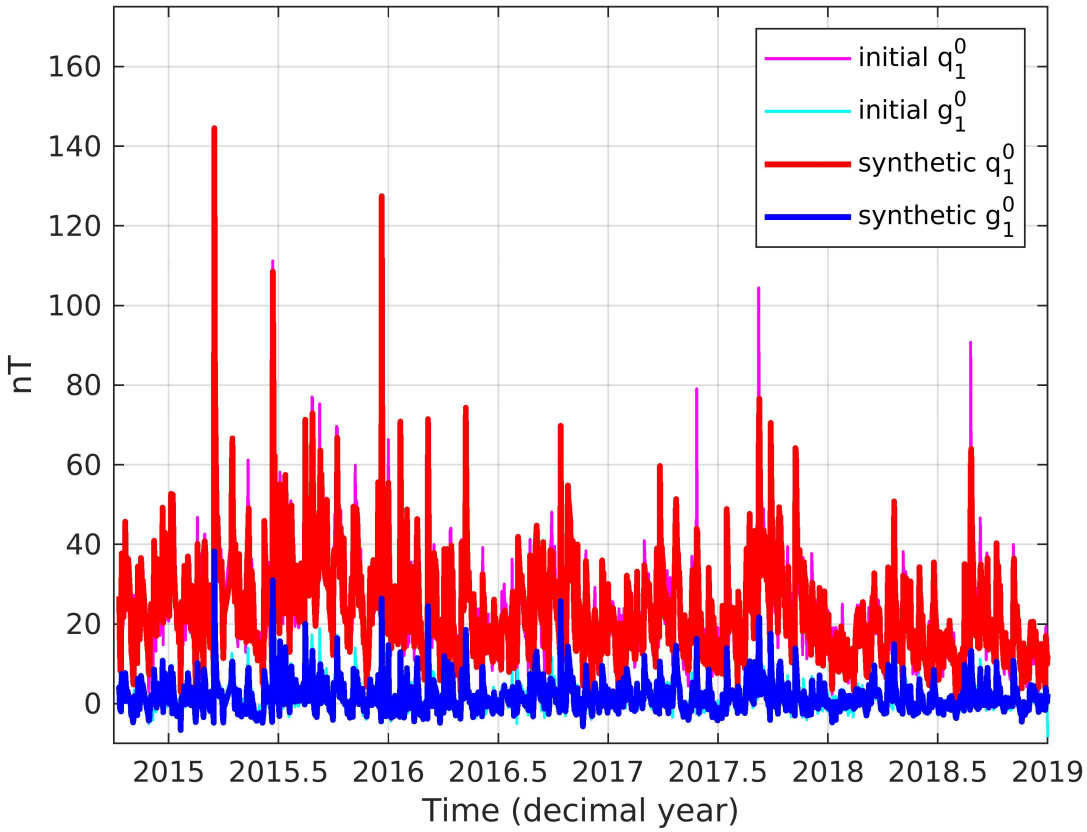

Figure 7.12: The degree 1 and order 0 coefficients estimated each day for the inducing and induced fields for the original geomagnetic external (magenta) and internal (cyan) models with the synthetic external (red) and internal (blue) models for MAVEN data.

which can generate such currents. Though the dipole term is dominant for the Earth's magnetospheric field, it might not be the case for Mars. Hence, we cannot rely solely on the geomagnetic results to understand or compare the external field models of Earth and Mars. But, we can at least start our analysis using our synthetic test results and obtain Martian external field models calculated for a time window and maximum degree and order that are similar.

7.4.2 Application to Real Data

From our synthetic analysis, we see that the dipole term best represents the transient fields and that the truncation degree N_{int} does not change it much. Our data locations can model sufficiently the field up to $N_{int} = 3$. Hence, for the inversion of real data, the residual fields obtained from the MGS and MAVEN data are modelled up to SH degree 3 for both the internal and external parts. This allows us to examine not only the dipole terms but also the time variation of the quadrupole and octupole terms. The models are initially calculated for each day. Due to lack of sufficient amount of data for some days, the SH inverse problem becomes ill-conditioned and we get outliers in the model which

correspond to extremely high magnitudes of the coefficients ($> 10^4$) as compared to other values that are of orders 10^1. While displaying and discussing the models in the figures and text below, we choose to remove these outliers and consider only the coefficients that lie between ± 50 nT for each degree and order.

MGS

Figure 7.13 displays the internal (blue) and external (red) field models calculated for each day for MGS data. Among all degrees and orders displayed on these figures, the magnitude for the degree 1 and order 0 term is dominant for both the internal and external fields. Figure 7.14 shows this term in detail. The external fields are higher in magnitude than the internal fields but the correlation coefficient is below 0.5. This is probably due to presence of noise in the data. We also estimate the models using night (or, quiet) and day sides data separately. The correlation for the day side models for the dipole term is 0.89 while the correlation for the night side models for the same term is -0.78 (Figure 7.15). The zonal term for degree 2 displays amplitudes similar to the zonal degree 1 term but the correlation is -0.54 between the external and internal night side coefficients (Figure 7.16). Even if the correlation values are a bit larger for the day side data, we will focus on the night side data since day side data of Mars possibly contains geometries distorted due to the mini-magnetospheres.

MAVEN

Figure 7.17 displays the internal (blue) and external (red) field models calculated for each day for MAVEN data. The graphs display high magnitudes for many terms. However, we concentrate on the degree 1 and order 0 term which shows the highest correlation as well as maximum amplitude and variability with time. Figure 7.18 shows this term in detail. The external fields are comparable in magnitude with the internal fields and the correlation coefficient is 0.88 between them.

In order to better compare with MGS, we opt for MAVEN data that are lower in altitude for modelling the field. We estimate daily models by choosing data available for different combinations of the altitudes ranging between 300 to 2000 km. This involves modelling data available between 300 to 400 km only or modelling all data below 600 km, among many other different criteria used by altitude selection. But all the results are similar to the time series obtained for the models discussed above using data below 1000 km. If we go even lower in altitude, we lose coverage over a day and the inverse problem becomes ill-conditioned. For the same reason, it is difficult to separate and model the night and day sides data for MAVEN.

7.4.3 Comparison of the Results

The orbit configuration and its effects can be seen in the results obtained from the two satellites. The external fields are larger than the internal for the constant orbit configu-

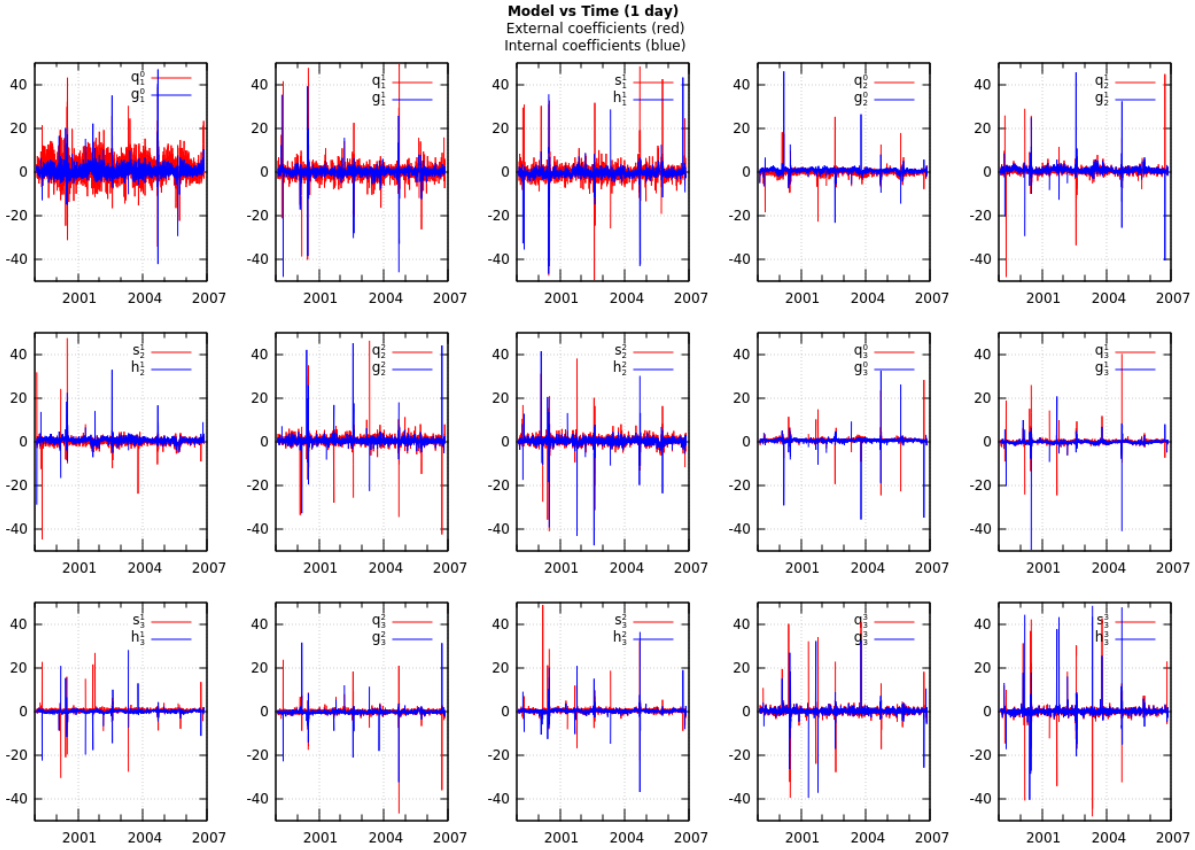

Figure 7.13: The internal (blue) and external (red) magnetic field models for each day estimated up to degree and order 3 for MGS data. The x-axis for each plot is time in decimal years while the y-axis is the coefficient magnitude in nT.

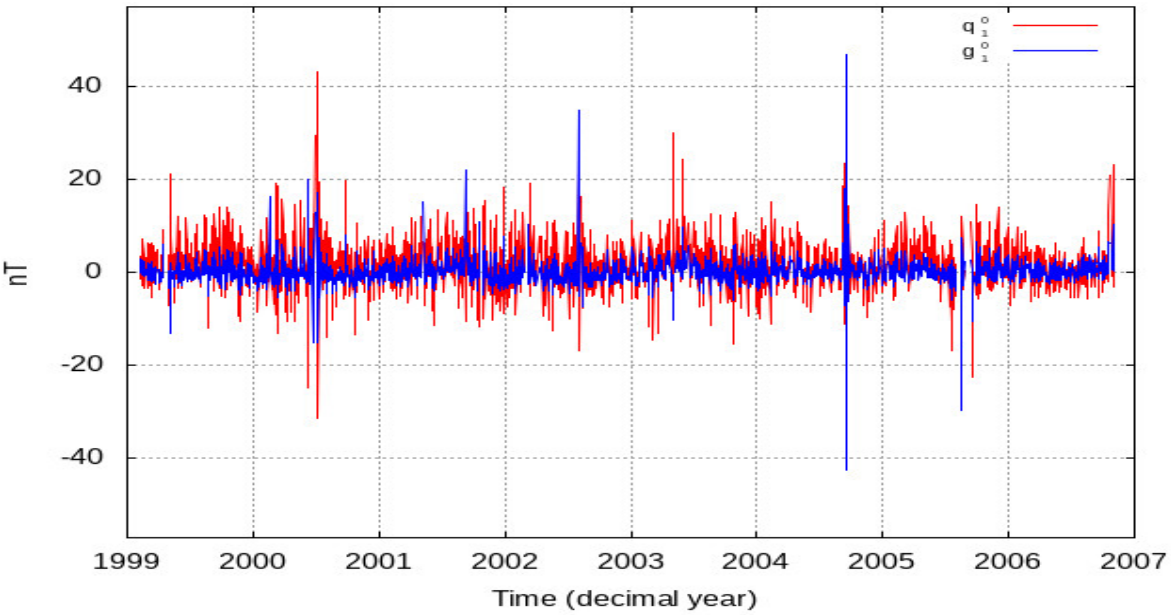

Figure 7.14: The internal (blue) and external (red) magnetic field models for each day for the degree 1 and order 0 coefficient for MGS data.

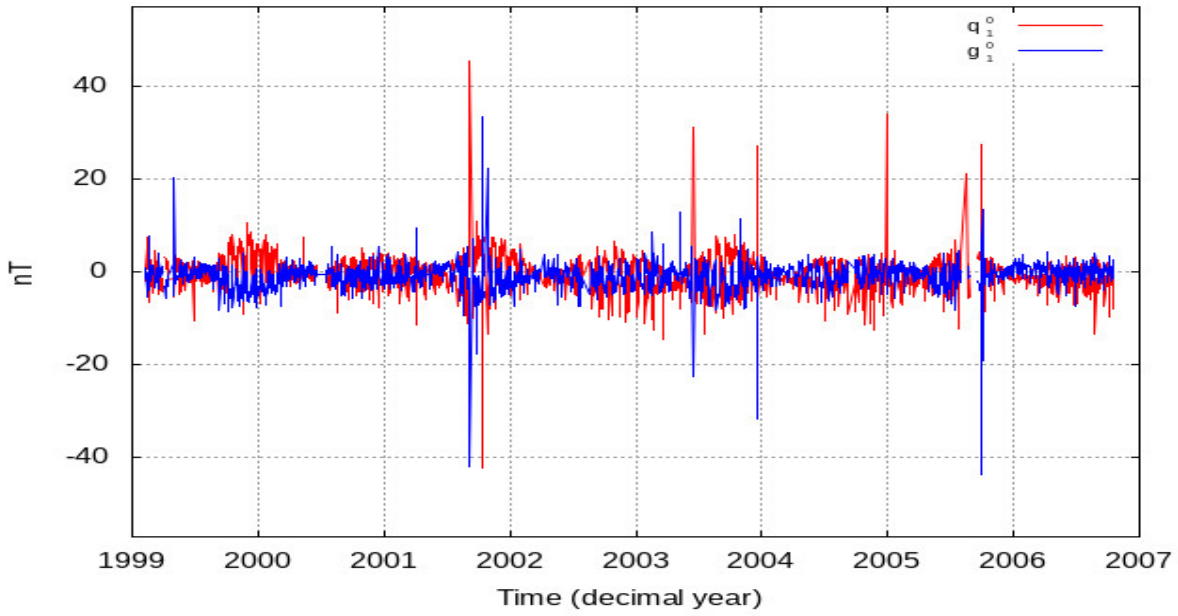

Figure 7.15: The internal (blue) and external (red) magnetic field models for each day for the degree 1 and order 0 coefficient for MGS night side data.

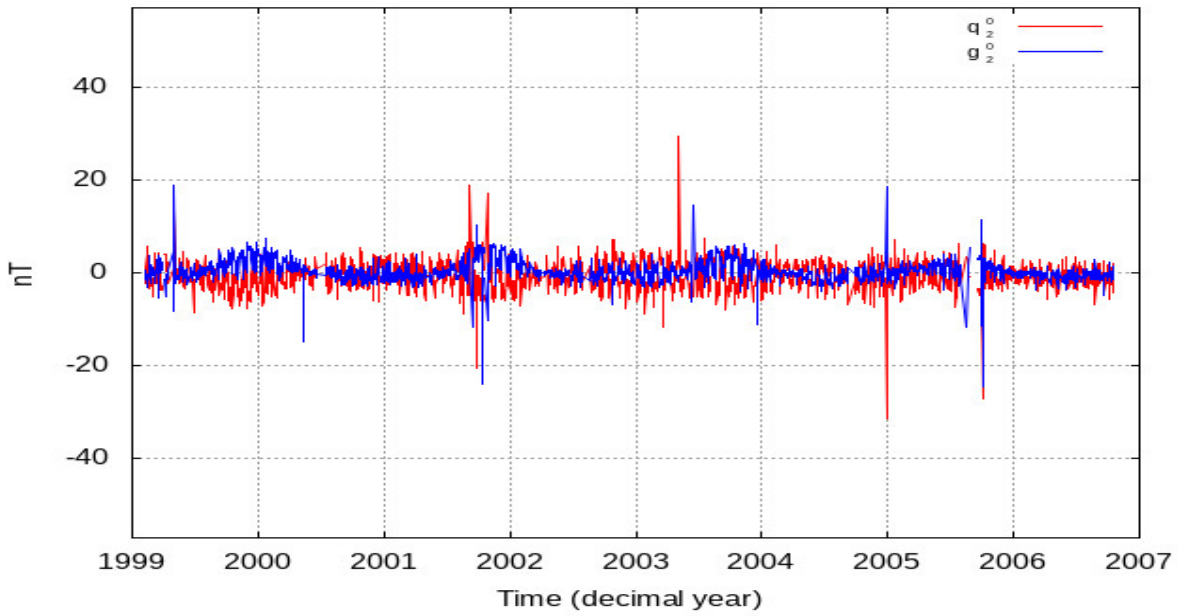

Figure 7.16: The internal (blue) and external (red) magnetic field models for each day for the degree 2 and order 0 coefficient for MGS night side data.

ration while they are comparable to the internal fields in the elliptical orbit configuration when considering data over the whole day. But separating the constant orbit data into night and day sides give different results. The night side data of MGS is quieter and hence much lower in magnitude, and similar to the results of MAVEN. Both show comparable internal and external signals for the time series. A comparison between the MGS and MAVEN results can also be done using the correlation coefficients. MGS internal and

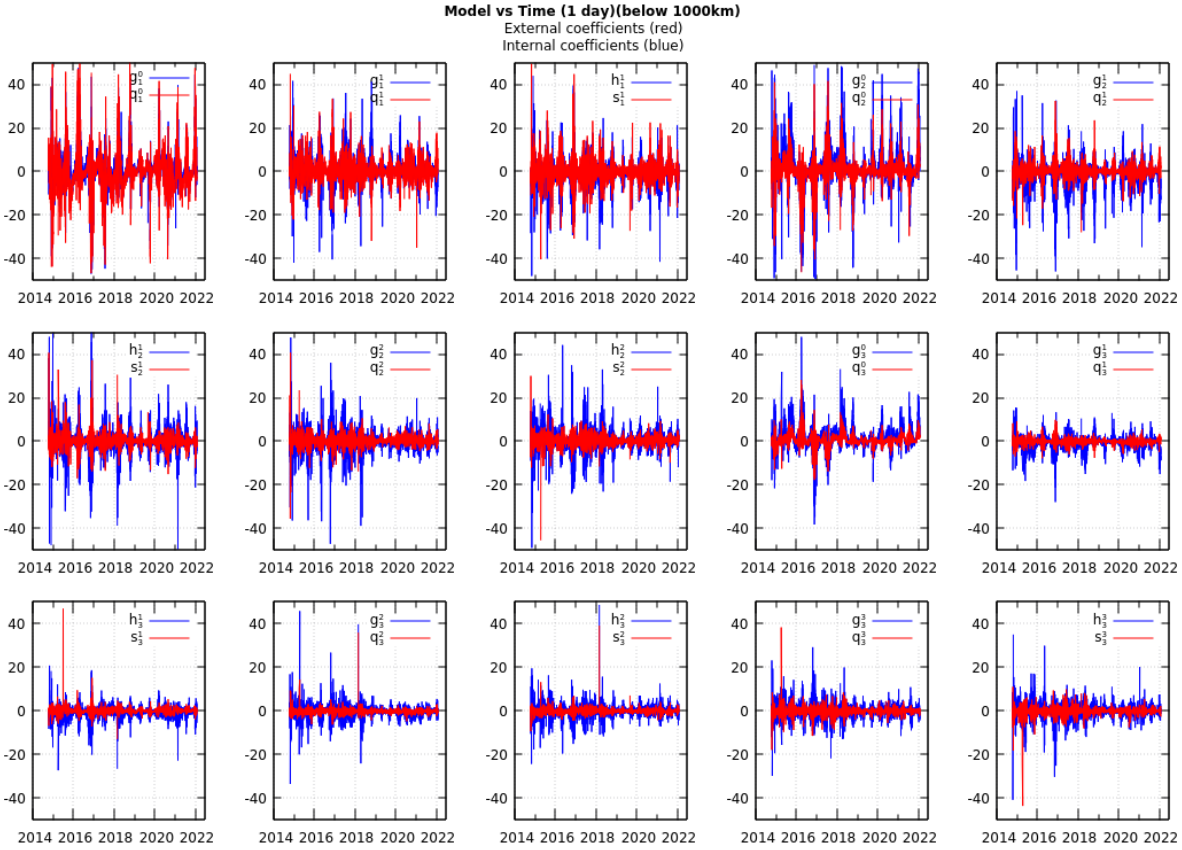

Figure 7.17: The internal (blue) and external (red) magnetic field models for each day estimated up to degree and order 3 for MAVEN data. The x-axis for each plot is time in decimal years while the y-axis is the coefficient magnitude in nT.

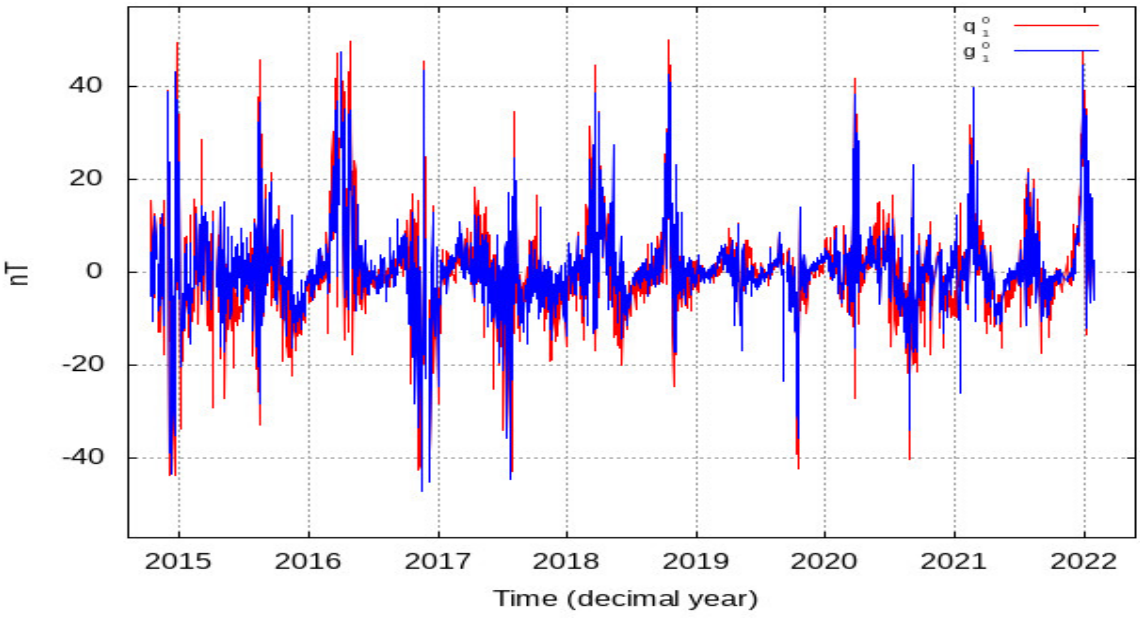

Figure 7.18: The internal (blue) and external (red) magnetic field models for each day for the degree 1 and order 0 coefficient for MAVEN data.

external models are negative in correlation for the night side data while MAVEN shows positive correlation.

What is puzzling in most of the results is the almost comparable magnitude of the inducing and induced fields. As observed for the geomagnetic field, the inducing fields should be visibly higher in magnitude. However, for more than half of our data, the induced fields are either comparable or higher than the inducing fields. But as discussed before, we cannot rely on our geomagnetic analysis alone to develop the Martian field models since their external environments are very different from each other. Following the 26-27 days pattern we observed for some components of the Martian magnetic data, we estimate models combining data for every 27 days for both MGS and MAVEN. We use models estimated independently using data from 27 days as well as models using data from 27 days with a sliding window of every 20 days. No outliers are observed in these models since there is sufficient data needed for a robust SH inversion. For the models with overlapping data, the correlation coefficient for the internal and external degree 1 and order 0 terms for MAVEN is 0.91. For MGS the correlation is lower at 0.73 while it is -0.83 when using only night side data. The correlation for MGS is highest at 0.90 for the day side models. Figure 7.19 shows the time series of the coefficients for a sliding 27 day model using night side MGS data. The interesting result in these models is the higher inducing fields for the MGS coefficients for the dipole term. In stark contrast, the degree 2 coefficients, especially the zonal term exhibits much higher internal values.

From the results of this chapter, we observe that the induced field signals are much higher than we anticipated. To sound the interior, our next step is to invert the transient internal field models to get some probability distributions. We can estimate the conductivity up to certain depths since the internally induced fields depend on the electrical conductivity of the planet. From Faraday's law, we know that the magnetic field at the surface of a pure conductor cannot have a normal component. This implies that $Br = Br_{int} + Br_{ext}$ should be zero. For the dipole term-

$$2g_1^0 cos(\theta) = q_1^0 cos(\theta) \tag{7.1}$$

and hence $g_1^0/q_1^0 = 1/2$ for a perfect conductor. Values larger than this limit are physically meaningless. But both the MGS and MAVEN coefficients correspond to values above 0.5 for half of the time series.

One reason for this could be the leakage of crustal fields into the transient signals. Though we already ruled this out after we removed the crustal fields and modelled the residual fields for only internal sources, there might still be some large scale contributions. The spectra of the two models obtained using residual data and modelling for internal field only (estimated for $N_{int} = 10$) display some energy for the quadrupole and octupole terms (around 7-8 nT^2). This could be the result of assuming dipole contributions only up to 1800 km for the ESD model by Langlais et al. (2019). To clarify this, we estimated an 'in-house' crustal field model using our original measurements from the satellites. But, the residuals and spectrum resemble those of the model by Langlais et al. (2019). Thus, no static crustal contributions appear to have leaked in the residuals, although some kind

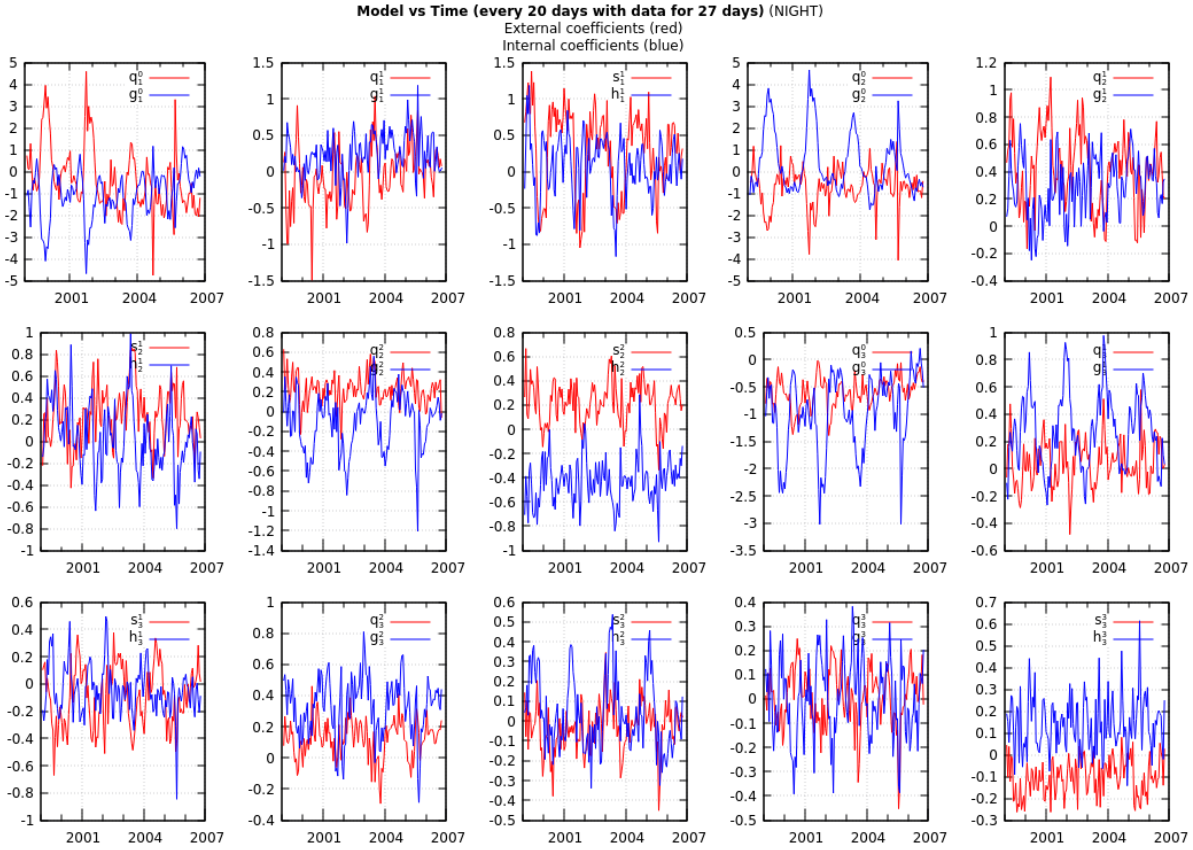

Figure 7.19: The internal (blue) and external (red) coefficients for sliding 27 day models estimated up to degree and order 3 using MGS night side data. The x-axis for each plot is time in decimal years while the y-axis is the coefficient magnitude in nT.

of internal contribution from unknown sources at low degrees might be present.

The other possibility for the source of this issue might be the separation between the internal and external fields. Mars does not have a distinct ionosphere or magnetosphere. This means that we do not have a particular altitude below or above which we can be sure that the separation can take place properly. We might be performing the inversion at satellite altitudes that might not properly separate the sources, especially for MAVEN. Since MAVEN is in an elliptical orbit, the satellite might be treating both the external and internal fields as internal sources. However, we try modelling the fields at different altitudes and it does not resolve the problem. In addition, MGS is at a constant altitude which should not affect the separation. Since we obtain similar results for both the satellites, we conclude that this issue cannot be resolved by simple changes in altitude. Similarly, local time selections do not show significantly different results other than lower signal to noise ratio.

We anticipate that the time series we have will not work perfectly for our Bayesian inversion to estimate the interior conductivity due to the comparable magnitudes of the internal and external coefficients. We nevertheless attempt the inversion in order to observe what our results would show.

8. Electrical Conductivity Profiles

Our aim is to obtain some probabilities of conductivity profiles using the transient magnetic fields. Probability distributions can be estimated using different analyses. We use one such technique called the Bayesian approach using the Markov Chain Monte Carlo method. The first section presents how the inverse problem is solved using the Metropolis Hastings sampler. The second section details how the forward problem is computed using transfer functions. We then discuss the results obtained for the Martian mantle conductivity, assuming a 1D structure, after the application of the described method to synthetic as well as real data.

8.1 Bayesian Approach

Probability, in simple words, is defined as the certainty of the occurrence of an event. A function that represents the probability of an event within a certain range is a probability density function (pdf) (Smith 1991; Tarantola 2005).

The Bayesian approach allows to compute probabilities for given parameter values and some prior knowledge. It uses Bayes' theorem (Bayes 1763) that gives probability distributions and is defined in terms of prior and conditional probabilities. Assuming m is the model parameter and d is the observed data, we have the theorem-

$$\mathbf{p}(\mathrm{m}|\mathrm{d}) = \frac{\mathbf{p}(\mathrm{d}|\mathrm{m})\,\mathbf{p}(\mathrm{m})}{\mathbf{p}(\mathrm{d})} \tag{8.1}$$

where, $\mathbf{p}(\mathrm{m})$ is the a priori knowledge of the model. The prior distribution is defined as the knowledge of a model before any data observations. $\mathbf{p}(\mathrm{d}|\mathrm{m})$ is the likelihood of data given the model. $\mathbf{p}(\mathrm{d})$ is the observed data distribution, used as a normalization factor. The posterior distribution $\mathbf{p}(\mathrm{m}|\mathrm{d})$ is the model probability density given the data. Our aim is to get the posterior distribution, where the data d is the 1 day time-varying models and the model m is the conductivity at different depths of the Martian interior.

From the law of total probability that relates marginal and conditional probabilities, we can express the total probability of an event as the sum of all distinct events -

$$\mathbf{p}(\mathrm{m}|\mathrm{d}) = \frac{\mathbf{p}(\mathrm{d}|\mathrm{m})\,\mathbf{p}(\mathrm{m})}{\int \mathbf{p}(\mathrm{d}|\mathrm{m})\,\mathbf{p}(\mathrm{m})} \tag{8.2}$$

If we take a simple case, we can try to get the probability of someone having covid given that they have a particular symptom, say cough. We can then test 1000 people for

covid and note the results along with the possibility of whether they are experiencing a cough. Then, our posterior distribution is-

$$\begin{aligned}\mathbf{p}(\text{covid}|\text{cough}) &= \frac{\mathbf{p}(\text{cough}|\text{covid})\,\mathbf{p}(\text{covid})}{\mathbf{p}(\text{cough})} \\ &= \frac{\mathbf{p}(\text{cough}|\text{covid})\,\mathbf{p}(\text{covid})}{\mathbf{p}(\text{cough}|\text{covid})\,\mathbf{p}(\text{covid}) + \mathbf{p}(\text{cough}|\text{no covid})\,\mathbf{p}(\text{no covid})}\end{aligned} \tag{8.3}$$

This can be easily calculated. But, if we increase the number of symptoms or parameters to breathlessness, fever and loss of taste, our solution will become a little more complicated.

Generally, most inverse problems involve a lot of different parameters and hence are much more exhaustive than the example discussed (e.g., Tarits et al. 1994; Grandis and Tarits 2019). Due to the difficulty of computing the denominator in Equation (8.2) which requires a computation over all the parameter space, the posterior distribution cannot be estimated directly from its definition. To overcome this problem, specific sampling techniques of the parameter spaces have been developed that allow to estimate the posterior distribution. In particular, the Markov Chain Monte Carlo (MCMC) method creates random samples to estimate a pdf. The MCMC provides a good compromise between the computational time and probability result. A routine is required now that either accepts or rejects the sequence of random values proposed for the parameters. Here, we use the Metropolis-Hastings algorithm (Metropolis et al. 1953; Hastings 1970) as sampler.

This sampling technique requires a few parameters to be tuned. First, there are a number of iterations called cold runs. The intention is for the inversion process to forget the initial conditions. The sampler then randomly chooses and updates one parameter to another with a Gaussian probability. At each step a random probability value is proposed within our specified ranges for the posterior distribution which relies on the last step. In order for the values to not be similar in successive steps, one value every n number of iterations is chosen.

This results in the generation of a candidate model. The next step is to either accept or reject this model, for which we estimate the likelihood $\mathbf{p}(\text{d}|\text{m})$ from the forward problem. At the same time, a prior pdf for the candidate model is computed and added to the misfit. A smoothing or damping parameter value can be multiplied to the prior to smooth out the pdf between the different parameter values. Similar to the SH inversion in Chapter 2, the Bayesian inversion minimises the misfit, which is here a balance between the likelihood and the prior, to get a model that best describes the data. If the new model is accepted, this is used for the next iteration. On the other hand, if it is rejected, the old accepted model is retained. An acceptance rate is computed that evaluates the convergence of the MCMC. The iterations performed are called the main runs. We need a high main run number in order to sample adequately the posterior probability.

In our problem, the different parameters are the conductivity values of l layers, chosen to model the deep interior. The conductivity values are defined in $\log_{10}$ for each depth. The input data are the Gauss coefficients $g_1^0(t)$ and $q_1^0(t)$. They are made to undergo

Fourier transformation, which defines the models from the time (t) domain to the frequency (ω) domain. We define the coefficients in the frequency domain as $g_1^0(\omega)$ and $q_1^0(\omega)$ for the induced and inducing parts respectively for the zonal dipole terms. The inversion which either rejects or accepts the candidate model generated is based on the function-

$$\sum_w [log_{10}(|g_1^0(\omega)|) - log_{10}(|g_{1,syn}^0(\omega)|)]^2 + \lambda_\sigma \sum_l |log_{10}(\sigma_l) - log_{10}(\sigma_{l+1})| \tag{8.4}$$

where, λ_σ is the damping parameter and σ_l is the conductivity value for layer l. The $g_{1,syn}^0(\omega)$ is the synthetic induced response calculated from the candidate model of the Bayesian inversion. The next section describes how this value is calculated by making use of transfer functions.

8.2 Transfer Function

The induced magnetic fields, dominantly generated by the currents in the crust and mantle, are dependent on the electrical conductivity of the materials present. Electromagnetic induction provides a good estimate of the conductivity of these conducting layers in the interior (Saur et al. 2010). Assuming that the conductivity distribution is radially symmetric, the inducing and induced field would be of the same geometry. Our aim to obtain the conductivity profile of the different layers depends on the time series of our data. The depth up to which the model can penetrate is given by the penetration or skin depth. It is defined as -

$$\delta(\omega) = \sqrt{\frac{T}{\pi \mu_0 \sigma}} \tag{8.5}$$

where, T is the time period, equal to $\frac{2\pi}{\omega}$, μ_0 is the magnetic permeability of free space equal to 4 π x 10^{-7} H/m and σ is the electrical conductivity. The penetration depth is proportional to the square root of time or inversely proportional to the square root of frequency of the data. The longer our time series, or the lower is the frequency of the data, the deeper we can estimate the conductivity. Hence, studying different periods of the time-varying magnetic fields allows us to sound different depths. Assuming a constant conductivity of 1 S/m, the minimum period needed to sound the mantle up to depths of 1830 km (assumed CMB of Mars) is 153 days.

Since the internal magnetic response provides an estimate of the conductivity, different functions of the Gauss coefficients g, h, q, s of the internal and external fields can be used to estimate it. These functions are called transfer functions. Q functions are one example of such transfer functions that are used for induction studies. They are related to the internal and external coefficients as the ratio of the induced to the inducing parts (e.g., Olsen 1999; Püthe and Kuvshinov 2013)-

$$Q_n(\omega) = \frac{\iota_n^m(\omega)}{\epsilon_n^m(\omega)} \tag{8.6}$$

where, the complex coefficients $\iota_n^m(\omega)$ and $\epsilon_n^m(\omega)$ are defined as (Olsen et al. 2010)-

$$\iota_n^m = g_n^m - ih_n^m \tag{8.7}$$

$$\epsilon_n^m = q_n^m - is_n^m \tag{8.8}$$

The Q-response is dependent on the frequency and the degree of the coefficients. Given that we now have the models in the frequency ranges, we remove the static signal or the zero frequency signal that contains no information. To obtain the Q transfer functions, we make use of Bessel and Hankel functions.

The different layers, or spherical shells, each with a constant conductivity can be defined using a radial function $f(r)$ and a constant k by the equation (Srivastava 1966)-

$$r^2\frac{d^2f(r)}{dr^2} + 2r\frac{df(r)}{dr} + (k^2r^2 - n(n+1))f(r) = 0 \tag{8.9}$$

where,

$$k^2 = -4\pi\sigma iw \tag{8.10}$$

The solution of the equation, for each l, is given by j_n and η_n that are spherical Bessel functions of first and second kind of order n-

$$f(r) = Aj_n(kr) + B\eta_n(kr) \tag{8.11}$$

The impedence Z for each shell can be given by-

$$Z = -\frac{iw}{k} \cdot \frac{Akr\,.\,j_n(kr) + B\,.\,kr\,.\,\eta_n(kr)}{A(d/dkr)(kr\,.\,j_n(kr)) + B\,.\,(d/dkr)(kr\,.\,\eta_n(kr))} \tag{8.12}$$

where, B is zero when r tends to zero, i.e., for the last shell near the centre of the planet-

$$Z = -\frac{iw}{k} \cdot \frac{kr\,.\,j_n(kr)}{(d/dkr)(kr\,.\,j_n(kr))} \tag{8.13}$$

Using the transfer functions, synthetic data from the candidate model can be derived from the degree 1 zonal geometry as-

$$g^0_{1,syn}(\omega) = Q_1(\omega)\; q^0_1(\omega) \tag{8.14}$$

8.3 1-D Conductivity Profile

There are various results available for the electrical conductivity profiles from laboratory based or magnetic measurements of many different bodies in the Solar System. Specifically for Earth, results from the inversion of induced magnetic fields data provide a good estimate of the mantle conductivity (e.g., Püthe and Kuvshinov 2013; Civet et al. 2015; Verhoeven et al. 2021). There are some recent studies available for the conductivity of Mercury and the Moon as well (e.g., Wardinski et al. 2019; Mittelholz et al. 2021). One of the major implications of induced fields and electromagnetic induction has been

the discovery of conductive layers in the moons of the gas giants (e.g., Jia et al. 2010; Saur et al. 2010). However, when it comes to Mars, conductivity results using magnetic data from spacecrafts are very limited. Previously, only one study provided the electrical conductivity distribution of the Martian mantle with respect to depth based on satellite data (Civet and Tarits 2014). There have been a few other studies that provide the mantle conductivity profile using laboratory based measurements constraints (Mocquet and Menvielle 2000; Vacher and Verhoeven 2007; Verhoeven and Vacher 2016). The inversion process for most of the conductivity profiles involve the use of Bayesian inversion to estimate the pdf.

8.3.1 Previous Results

In a study highlighting the complementarity between seismological and electromagnetic sounding methods, Mocquet and Menvielle (2000) developed models of the Martian mantle by adjusting seismological model and conductivity profiles from Earth to Martian conditions. Using physical parameters of five minerals- olivine, spinelle (wadsleyite and ringwoodite), pyroxene and garnet- the minimum and maximum conductivity values of the minerals present in the Martian mantle were estimated. These values differ according to the assumed composition and temperature of the Martian mantle. If the mantle was cold and rich in olivine, the conductivity would be low. On the other hand, if it was hot and rich in garnet, the conductivity would be higher. On average, the conductivity in the depth range of 400 to 800 km would be about 1 S/m and increase by one order of magnitude for higher depths. The variation in conductivity could be dependent on either the temperature or the composition of the mantle.

Vacher and Verhoeven (2007) studied the effect of iron content on the electrical conductivity using 9 mantle minerals or phases, namely olivine, wadsleyite, ringwoodite, orthopyroxene, clinopyroxene, akimotoite+garnet, Al-free perovskite, Al-perovskite and magnesiowüstite. They extrapolated the results from low iron content minerals measured in laboratory to iron rich minerals and estimated a synthetic conductivity profile for the Martian mantle. From analysis of the SNC meteorites, iron content in the mantle of Mars is placed at 25% as opposed to the 10% on Earth. They calculated the conductivity for individual minerals and averaged them using the Hashin-Shtrikman scheme. They concluded that the Martian mantle conductivity is higher than that of Earth by magnitudes of orders 1 to 1.5 and, combined with the uncertainties associated with their results, falls within the previous limits of Mocquet and Menvielle (2000). Two sharp jumps between the depths of 1000 and 1200 km occurs in the profile that relate to the transition of the olivine phases to ringwoodite and wadsleyite respectively.

Civet and Tarits (2014) was the first and only study until now that used observations of magnetic field to compute an estimate of the mantle conductivity profile. They removed the static fields using the lithospheric model of Langlais et al. (2004) to obtain the time-varying fields. Only night side MGS data was used to estimate the induced response of the mantle. Since this created a lot of gaps in the data set, they interpolated the data

using two proxies. One was defined by averaging every half orbit data resulting in six and two time series of 125 and 210 days respectively while the other proxy was defined using solar wind data of the Advanced Composition Explorer (ACE) satellite. Since the ACE satellite is located at the L1 Lagrange point of the Earth-Sun system, the data can only be used for locations where Mars and Earth were close together on the same Parker spiral arm (Parker 1958). After extrapolating the ACE Earth measurements to Mars, four time series of 200 days were developed. These three types of time series were used to obtain the Gauss coefficients in the frequency domain using degree and order 3. The coefficients exhibiting values larger than the standard values of a perfect conductor for different degrees were removed. These non-physical values were present due to the low signal-to-noise ratio. The energy of the coefficients were observed to be intense for periods larger than 2 days, in particular for degree 2. Inversion was performed on all the order 0 terms from degree 1 to 3 for all three data sets but the two time series of 210 days were selected for the final inversion. An electrical conductivity profile using 9 layers of 180 km thickness each was defined. Their results showed that the conductivity increases gradually up to 1000 km followed by a sharp increase. The results lie between the ranges of the previous two studies. Civet and Tarits (2014) discussed the limitations of the data gaps and the importance of using continuous time series for induction studies.

Verhoeven and Vacher (2016) updated the results of Vacher and Verhoeven (2007) using new laboratory measurements and a new modelling scheme. Similar to the previous study, their study focused on the effect of iron content on the conductivity of the minerals. The effects of pressure, temperature, oxygen fugacity and composition of the mantle were discussed. They determined that the temperature and iron content play the most important role in conductivity. Due to the presence of large iron content, the small polaron conduction mechanism is dominant in the mantle of Mars, compared to proton or ionic conduction. This overcame the difficulty of estimating water content for proton conduction. Their results were calculated for iron content at both 25% and the reference 10%. This study showed that iron content increased the conductivity of all the phases. In addition to the Hashin-Shtrikman averaging scheme used previously, they used an effective medium averaging scheme to compute the electrical conductivity of the mantle from the individual conductivity of mineral phases. They obtained slightly larger conductivity profiles than Vacher and Verhoeven (2007) for the first 1000 km. The results match well with the conductivity results obtained from satellite data up to 1000 km. Beyond this depth, the olivine transition was probably difficult to detect due to the assumed layer thickness in the satellite study.

Figure 8.1 displays the results of the previously estimated conductivity profiles from Vacher and Verhoeven (2007), Verhoeven and Vacher (2016) and Civet and Tarits (2014). On average, the results from the latter two studies agree for the upper mantle up to depths of around 1000 km. The conductivity near the surface can be assumed to be between 0.01 and 0.1 S/m while at depth it varies from 1 to 10 S/m. The conductivity increases with depth up until about 1000-1200 km where it encounters a sharp increase due to change in mineral phase. It is constant or insensitive to depth up to about 1800

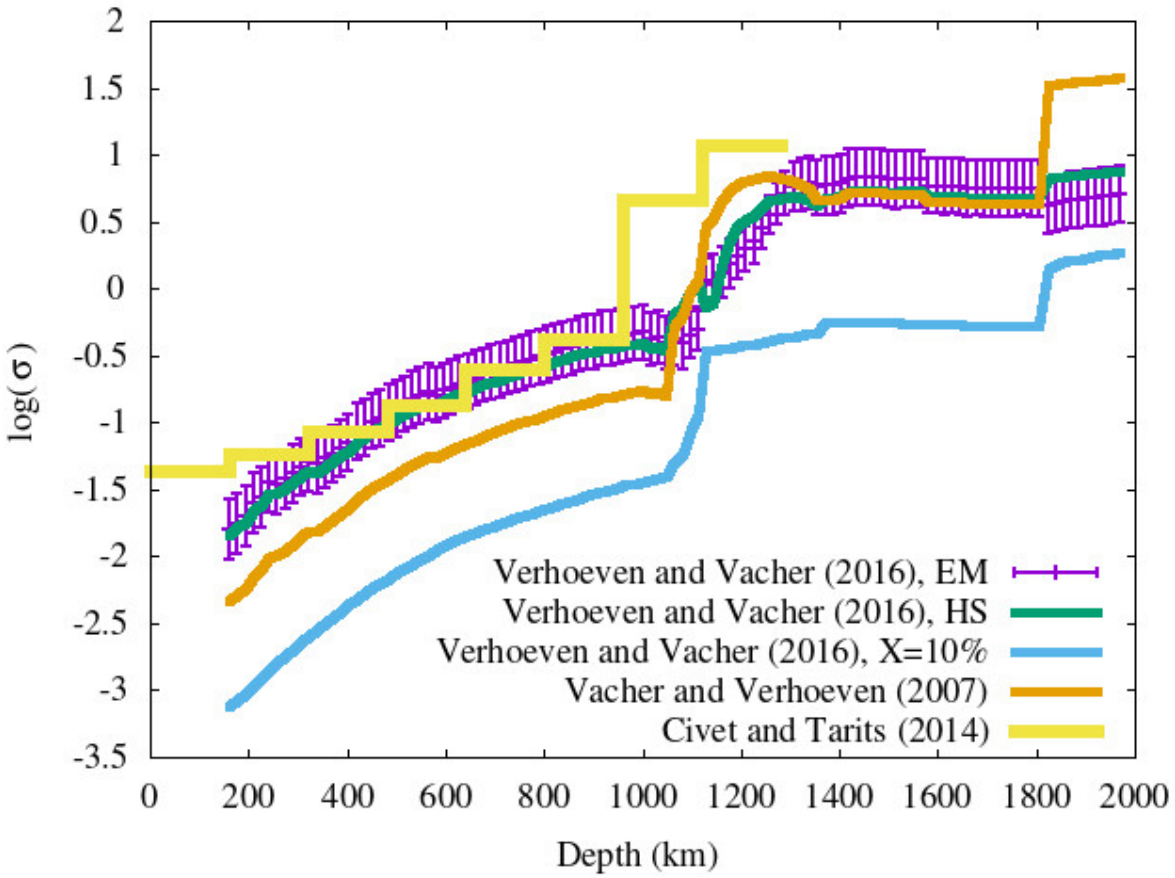

Figure 8.1: The electrical conductivity profile estimates from Verhoeven and Vacher (2016). They display their laboratory based profiles using two different averaging schemes- Hashin-Shtrikman (HS) and effective medium (EM). Standard deviation and mean is shown for the EM computations. The results for the reference 10% iron content as well as previous results of Vacher and Verhoeven (2007) and satellite based results of Civet and Tarits (2014) are also displayed for comparison. The units for conductivity is Sm^{-1}.

km where it probably encounters another phase transition. An independent study using seismic observations from InSight also indicates a discontinuity in the mantle near 1000 km depths (Huang et al. 2022).

8.3.2 Synthetic Data Results

Before estimating the conductivity pdf by the Bayesian inversion of magnetic field data, we test the reliability and robustness of our inversion process on synthetic data. For our inversion, the input data are the daily transient field internal coefficients for degree 1 and order 0 and the parameters are the electrical conductivity values for the different layers. To compute synthetic data, we start from a reference conductivity profile, compute synthetic data through the forward problem, add some noise and then invert these synthetic data. The comparison between the conductivity profiles computed from

the Bayesian inversion and the reference profile will allow us to test our procedure, study the evolution of resolution with depth and adopt the best strategy for the inversion. It allows also to have some estimates of the inversion parameters that will govern the convergence of the MCMC process such as the smoothing parameter λ or the number of runs.

In our case, the reference profile is established after combining the values obtained from the results of laboratory measurements of Verhoeven and Vacher (2016) and satellite measurements of Civet and Tarits (2014) (Figure 8.1). We work in log conductivity values and set the range of probabilities between 4 and -3, i.e., a parameter ranging from 10^{-4} S/m to 10^3 S/m. We opt for a simple uniform discretization that consists of 11 layers with a thickness of 200 km each starting from the surface up to a depth of 2000 km. The core radius is set to 1830 km. Synthetic data correspond to the internal response g_1^0 in accordance with the externally inducing coefficients q_1^0 of the real data and the transfer function Q_1 associated with our reference conductivity profile. We compute different sets of synthetic data using the models obtained in the previous chapter. This includes the daily MGS and MAVEN models as well as the separate night and day sides models using MGS. We use only the time series that lie in the ranges of $\pm$50 nT. However, this selection as well as the fact that we do not have measurements for all continuous days creates some gaps in the series. To overcome this, we linearly interpolate the model for the missing days to obtain a continuous time series. The probabilities for all the different inputs using synthetic analyses display similar profiles.

In order to tune the different parameters that govern the inversion, we focus on the synthetic data associated with MGS night side models. To find the optimum value for the number of main runs, we perform our inversion for 50,000 iterations and observe the evolution of the misfit (Figure 8.2). After some cold runs needed to obtain results independent of the initial values of the parameters, the iterations do not change significantly the misfit values. Hence, we choose the final number of main runs to sample adequately the parameter space to be 10,000 while the number of cold runs used to obtain a pdf independent of the initial state is chosen as 1000. The damping parameter value is chosen such that there is optimal balance between misfit and prior in Equation (8.4). High values of λ lead to strong smoothing coefficients which prevent the increase of conductivity with depth, and very small values of λ lead to slow convergence of the Markov chain. Figure 8.3 displays the mean and minimum misfit and prior values corresponding to different smoothing parameters. It shows that a λ value less than 5 should be sufficient for smoothing the prior. A value above 5 will lead to a prior becoming equal to or greater than the misfit, thereby biasing the inversion towards the prior. Though the misfit remains almost constant below 5, the least mean value is observed for $\lambda = 2$. This corresponds to a minimum and maximum prior equal to 3.8 and 41.4 respectively of the total misfit value obtained during the inversion. Overall, all our synthetic analysis display a good acceptance rate of 20-30% and low misfit values.

Figures 8.4 and 8.5 show the results we get for the transient field models of MGS night side data and MAVEN daily data for the degree 1 and order 0 terms. Figure 8.4 focuses

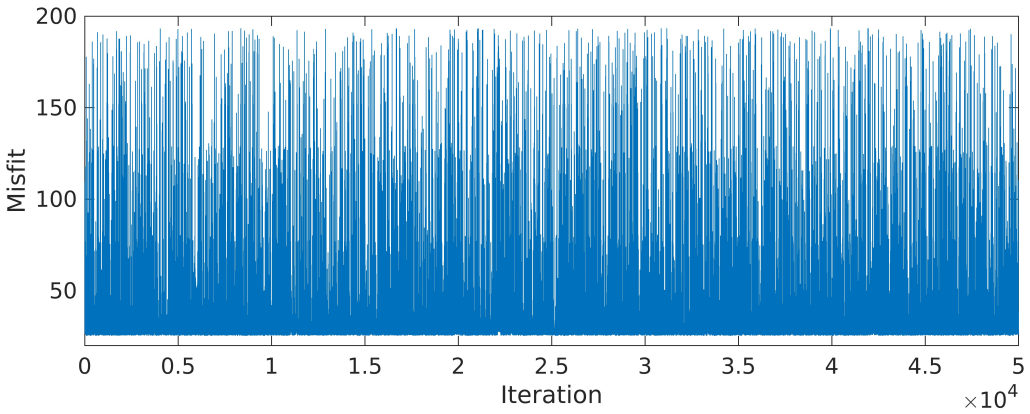

Figure 8.2: The evolution of the misfit with respect to the number of iterations during the main runs inversion of synthetic data using MGS night side models.

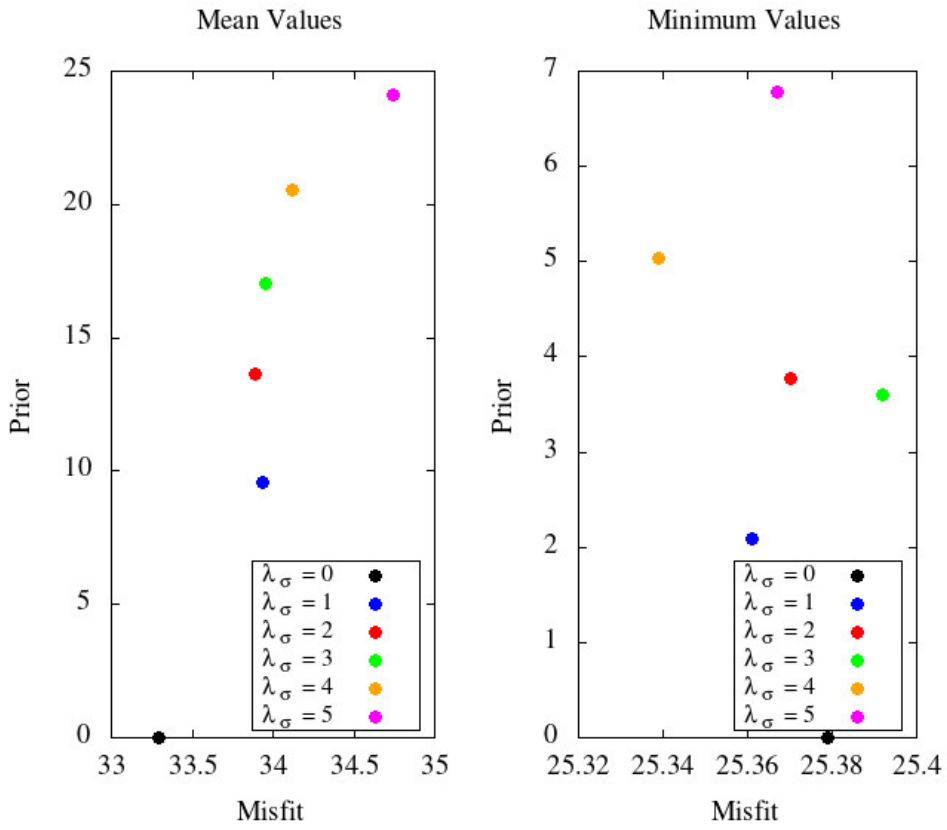

Figure 8.3: The mean and minimum values for the misfit vs prior obtained with respect to the different smoothing parameter values during the inversion of synthetic data using MGS night side models.

on the posterior probabilities we get after the inversion while Figure 8.5 displays the mean and maximum likelihood conductivity values. It also displays the 68% confidence bound levels and the reference profile for comparison. The figures show good correlation of the computed profiles with the reference profile until depths of about 1000-1200 km. After this depth, the increase in the difference between them is possibly related to the smaller

number of Gauss coefficients at large periods. Overall, our synthetic results show that our time series have the ability to sound well the mantle until a depth of about 1000-1200 km.

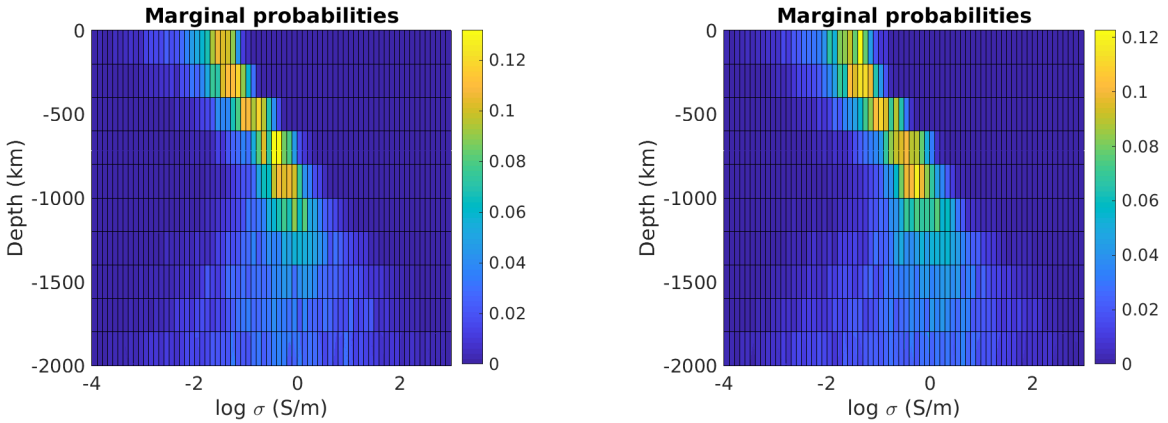

(a) MGS night side data

(b) MAVEN daily data

Figure 8.4: The marginal probabilities obtained for the electrical conductivity profile of the Martian mantle from the inversion of synthetic data.

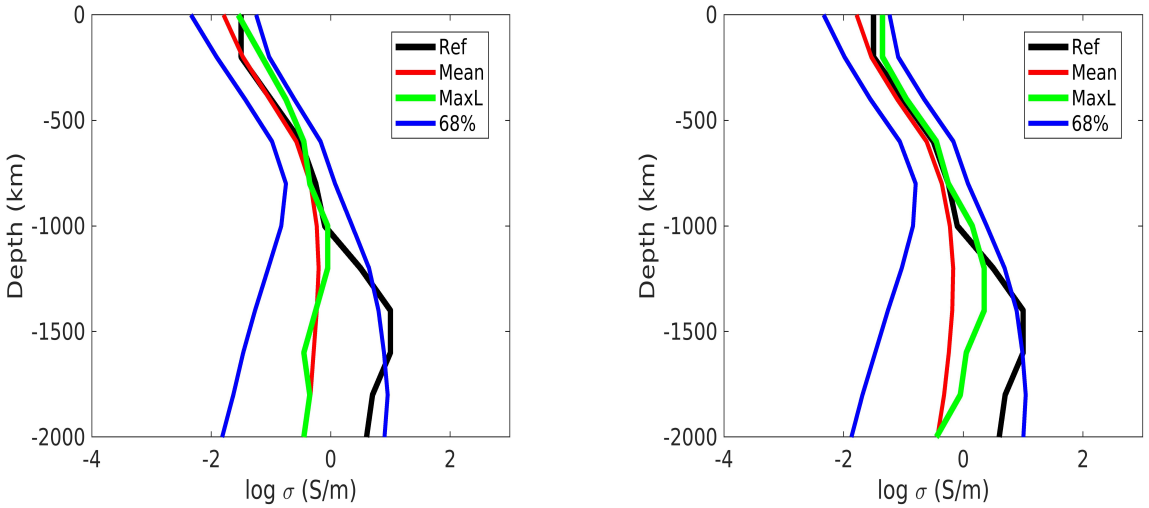

(a) MGS night side data

(b) MAVEN daily data

Figure 8.5: The mean, maximum likelihood and 68% confidence curves for the electrical conductivity profile of the Martian mantle obtained from the inversion of synthetic data along with the reference profile.

8.3.3 Real Data Results

Results form our inversion of synthetic data has allowed to obtain some estimates of the values of the parameters governing the inversion scheme and has highlighted a decrease

of resolution with depth. For our inversion of real data, we use the same constant values for the core radius and λ as well as the number of runs, as for the synthetic analysis.

The inversion results for the real data are very different from the synthetic results. Figures 8.6 and 8.7 show the results we get for MGS night side data and MAVEN daily data after removal of the abnormal values and interpolating for the missing days for the degree 1 and order 0 terms. The profiles start from a very high conductivity and continue to decrease slightly with depth. This is expected since most of our values exhibit or exceed the maximum induced to inducing ratio limit. The maximum value of the Q_n response for a pure conductor using degree 1 is 0.5. Reaching this value equates to inverting for a pure conductor. This would mean that the conductivity profile will be very biased towards positive values which is what we observe.

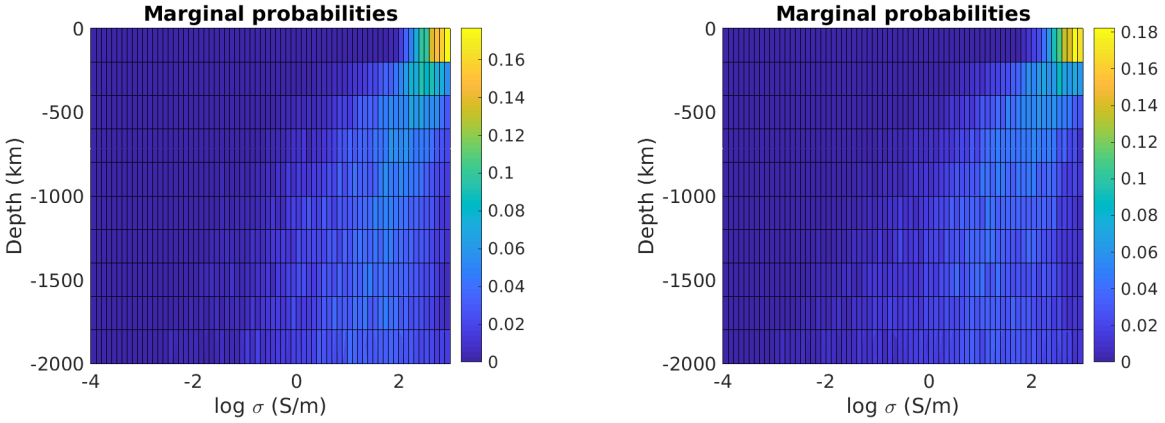

(a) MGS night side data

(b) MAVEN daily data

Figure 8.6: The marginal probabilities obtained for the electrical conductivity profile of the Martian mantle from the inversion of real data.

Civet and Tarits (2014) found maximum amplitude for the zonal quadrupole terms. We hence attempt the inversion assuming this term as the dominant geometry driving the external fields on Mars. However, the results are similar to the zonal dipole geometry inversion. Figure 8.8 shows the probabilities and profiles for the inversion performed using the degree 2 order 0 terms.

Since we know that the external coefficients are not always larger than the internal coefficients, we attempt a different interpolation as well. This includes first the removal of values where the ratio between the induced to the inducing parts is non-physical for degree 1 and order 0 terms ($g_1^0/q_1^0 > 0.5$). The next step within this scheme is to linearly interpolate separately for the internal and external coefficients for the missing days using the remaining physical values (i.e., interpolate separately g_1^0 and q_1^0 using their values which satisfy the condition $g_1^0/q_1^0 < 0.5$). However, even after interpolating in this way, we get some values for g_1^0 and q_1^0 that correspond to ratios that are above 0.5 and the conductivity profile obtained is similar to the previous cases.

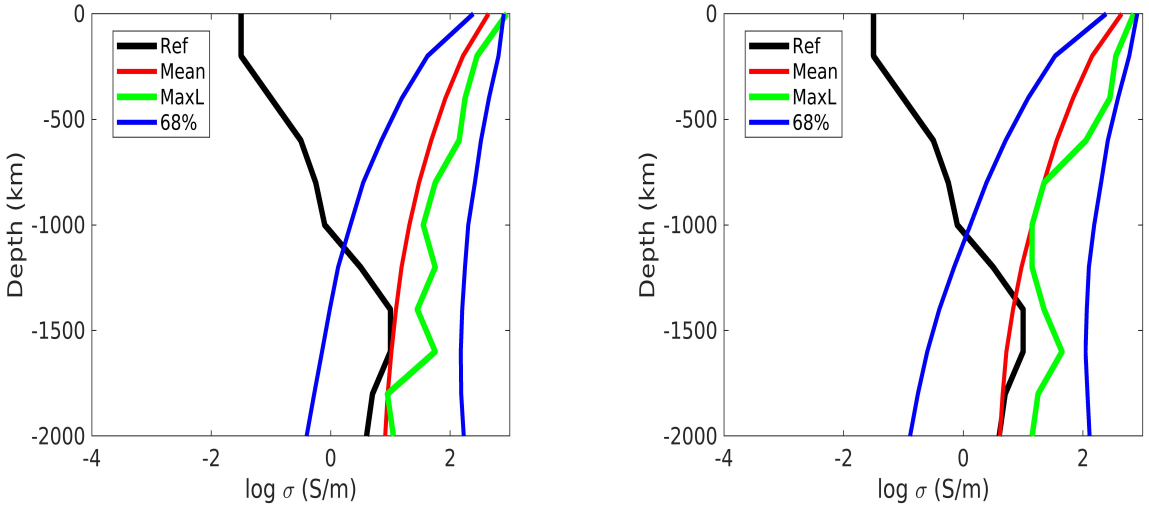

(a) MGS night side data

(b) MAVEN daily data

Figure 8.7: The mean, maximum likelihood and 68% confidence curves for the electrical conductivity profile of the Martian mantle obtained from the inversion of real data along with the reference profile.

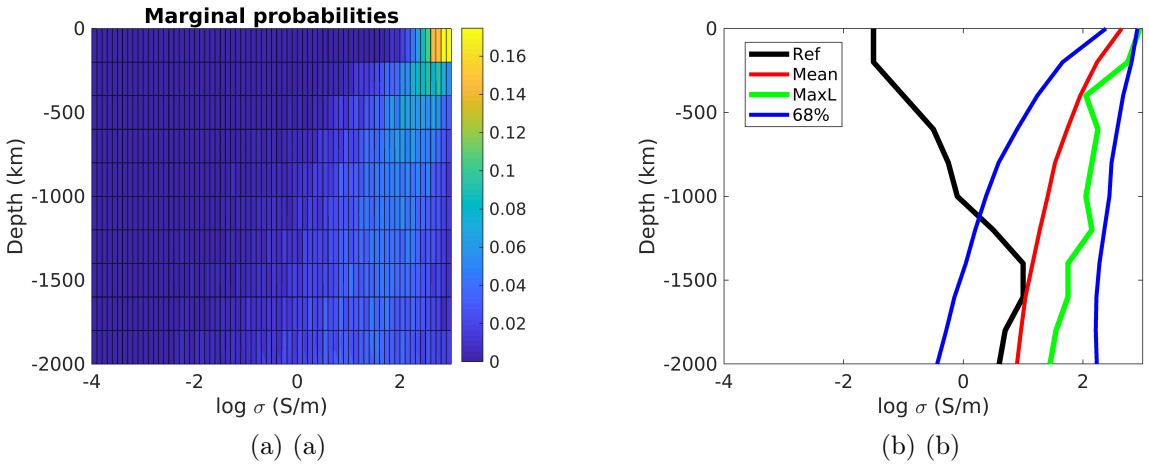

(a) (a)

(b) (b)

Figure 8.8: (a) The marginal probabilities obtained for the electrical conductivity profile of the Martian mantle from the inversion of real data using degree 2 order 0 terms. (b) The mean, maximum likelihood and 68% confidence curves for the electrical conductivity profile of the Martian mantle obtained from the inversion of real data using degree 2 order 0 terms along with the reference profile.

8.4 Discussion and Concluding Remarks

The only other study using satellite data to derive the Martian mantle conductivity (Civet and Tarits 2014) calculated their probability profile using MGS data and estimated the models in frequency domains. Their inversion was performed using a combination of coefficients. However, they did not use a continuous time series. They instead used

binned data in a short time window. Hence, a direct comparison with their study is difficult.

Our inversion provides very different estimates of the conductivity for the synthetic and real cases. The conductivity values are biased towards higher values, indicating we are probably approaching the highly conductive material in the interior very swiftly. This was anticipated since we obtain the g_1^0/q_1^0 ratios larger than 1/2. Our protocol was carefully developed starting from the external/internal field separation to the inversion for conductivity as demonstrated by all the synthetic analyses but, indeed, the real data analysis failed. Since the results are not similar to results previously obtained, different approaches need to be tested in order to look for discrepancies, if any. This can be done in various ways. Since the synthetic results show that the inversion is performed properly, it would be worth to concentrate more on the separation between the internal and external field contributions before looking for alternate inversion techniques. The separation of the internal and external fields is much more complicated than we anticipated on Mars. There might be presence of strong 3D asymmetric electrical structures or a highly conductive layer in the crust. Mars dichotomy is also an important feature to be considered in the sense that it affects global properties of the crust and the mantle beyond the crust-mantle boundary. The assumption of a purely radial electrical conductivity also has to be questioned. The original plan of the thesis was also to adapt new inversion techniques to the solution of the global induction problem, such as the use of the multi-dimensional Bayesian inversion but even if these techniques appear very efficient, they cannot compensate the difficulties in the time series.

An estimate of the conductivity values along with seismological values would be valuable since it provides a way to distinguish between the thermal and compositional effects. We calculate the probability of the electrical conductivity for varying depths. Figure 8.9 presents a summary of our results along with the profiles obtained by Civet and Tarits (2014) and Verhoeven and Vacher (2016). The inversion of synthetic data has shown a decrease of the resolution with depth, in relation to a smaller number of periods relevant to constrain this depth. On the other hand, an unrealistic profile has been obtained from inversion of real data which shows very high conductivity values for all depths. From the results of this work, it seems that an estimate of the electrical conductivity of Mars may require to go beyond the standard one-dimensional induction problem along with recognising and resolving the issue in the transient time series.

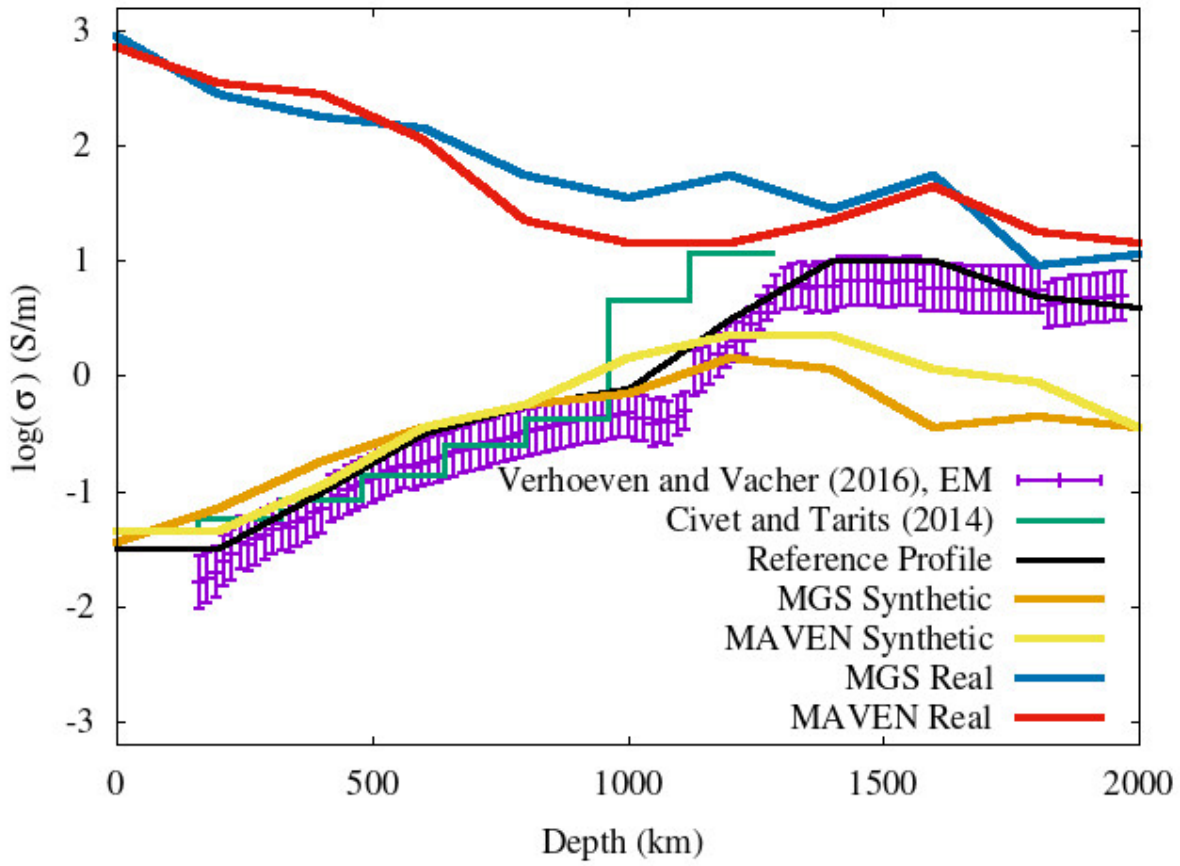

Figure 8.9: The electrical conductivity profile estimates of Verhoeven and Vacher (2016) for the effective medium (EM) and the satellite based results of Civet and Tarits (2014). Our reference profile is a compromise between the two models. The conductivity profile we obtain for MGS and MAVEN synthetic as well as real cases are also displayed.

Conclusion

9. General Conclusion and Perspectives

The work detailed in the previous chapters has highlighted the ability of using planetary magnetic field to derive important information about the internal structure of planets. According to the sources of the field, different parameters can be estimated. For Jupiter, the study of the internal field has allowed us to estimate the upper boundary of the dynamo convective region and detect as well as understand the SV. On the other hand, for Mars, the study of the time-varying induced magnetic fields provided us the opportunity to sound the mantle and obtain an estimate of its conductivity. In this final chapter, we conclude the work described in this thesis and discuss what future projects could be pursued as a follow up.

9.1 Jupiter

The data from Juno's 5 years of observations allowed us to model the internal magnetic field along with the time variations in it. The model was used to estimate the depth of the dynamo and understand the strength, pattern and flow of the SV. The dynamo radius is about 0.83 R_J calculated using the power spectra of the non-zonal and quadrupole families. The strength of the SV is of the order of 10^4 nT and its spatial pattern displays eastwards drifts as well as weak or field aligned flows. The combined main field and SV spectra show that the field change is dominantly advective. This answers the three main questions we asked in the first chapter
- How deep is the magnetic field of Jupiter generated?
- Are there any time variations in the field?
- What is the morphology of the time variations of this field?

There are however many new questions that can be further asked. Since SV has not been robustly determined for a planet other than Earth, questions about it and the flow in the interior would be evident. Some of them might be
- Does Juno efficiently observe the SV?
- Does there exist a stratified layer in Jupiter that controls the field and its changes?
- Does diffusion also play a major role in the flow deep inside the planet?
- What are the dominant dynamo processes?

For the first question, we can wait for more data from the Juno extended mission and update our results. The JUICE mission which will provide data from the late years of this decade can also be used to confirm the field predictions by the model at large

distances. However, from modelling the SV using different Juno data, we do not see any significant evolution of the field temporal variation, i.e, no higher derivative of the field. The data spanning across different time intervals also allowed the use of more knots for the calculation of the time derivation using B-Splines. The robust inversion outputs confirm the reliability of the models. Moreover, other studies constraining the SV match our results (e.g., Moore et al. 2019; Bloxham et al. 2022) though rapid variations such as jerks remain to be observed (Mandea et al. 2010).

The multi-layer dynamo with a stable stratification layer is a dominant feature found in Saturn (Stanley 2010). The numerical simulations for the Jovian dynamo match the results of the observations with this layer intact. However, it is assumed to be shallower which our results do not show (e.g., Gastine and Wicht 2021; Militzer et al. 2022). The diffusion dominant dynamo action also plays a role in the shallower regions (Wicht et al. 2019). It would be interesting to investigate a way which allows for the reconciliation of simulation and observation results. One possibility could be the consideration of induced fields in Jupiter. However, if these are present, they would probably be extremely low that would allow them to go undetected. The molecular hydrogen has comparatively lower conductivity than the metallic hydrogen (French et al. 2012). It could be a possibility that very low currents might be generated due to the external fields in the molecular region. For instance, Cao and Stevenson (2017) discussed wind induced magnetic fields in the semi-conducting regions of the planet. Their results indicated poloidal magnetic perturbations due to the zonal winds.

The dominant dynamo processes and the resulting sources of SV is a difficult question to answer. While Bloxham et al. (2022) stated that the pair of SV patches near the equator is due to zonal winds, Dietrich et al. (2021) suggested that the winds alone cannot explain the generation of the variations. Our results also present both zonal and non-zonal features in the SV maps. While the interplay between advection and diffusion in our study shows that the former is more dominant, Wicht et al. (2019) performed simulations that displayed dominant diffusion, especially near the surface. It would be beneficial to understand the flow at the top of the dynamo using our model before trying to answer these questions.

The knowledge we gained from this work is of importance for future missions' preparation and data interpretation. The JUICE and Europa Clipper missions will reach Jupiter and its moons by the end of this decade (Grasset et al. 2013; Phillips and Pappalardo 2014). The results from this work can provide the information on what data to expect from them. The magnetic field models of Jupiter can be used to extrapolate the Jovian field at the location of its moons. This will provide some important insights on their magnetic field environments that will allow to better understand measurements from the upcoming missions.

9.2 Mars

For Mars, we focused on the time-varying fields obtained after removing the crustal remanent fields from the data observations. The study of time-varying induced magnetic fields allows us to estimate the electrical conductivity of the mantle, providing some insight on the temperature and composition. This conductivity estimate relies on a proper identification of both externally inducing and internally induced magnetic fields. This separation is however challenging for Mars (e.g., Civet and Tarits 2014). To try to overcome this issue, we considered in this work two sets of data, from two different space missions, MGS and MAVEN, that have different orbital characteristics.

The main questions we started with were about the characterisation of external fields and their effect on the interior. This was intensively studied in this work. As observed on other planetary bodies, the external fields are generally greater than the internal fields (e.g., Püthe and Kuvshinov 2013; Wardinski et al. 2019; Mittelholz et al. 2021). However, for Mars, it is not always true. Our estimates of the externally inducing fields are more intense than the internally induced fields for the circular orbit data of MGS when considering data over all time periods while they are comparable for night side data. On the other hand, for the elliptical orbit of MAVEN, they are always comparable to each other. This results in obtaining highly positive conductivities in the interior due to the physically meaningless transfer function values. For both the satellites, there is a monthly trend observed in the MSO coordinates which can be useful for developing magnetic indices proxy. Although it is not easy to do so since the magnetic environment of Mars is different than the Earth's, the results can be used as a starting step. Obtaining a proxy magnetic field index for Mars in the future might help in removing noisy data for crustal field models as well as in separating the time-varying fields for transient field models.

The new questions we get from this study for the Martian magnetic field can be focused mainly on the accurate separation of the induced and inducing contributions in the temporal series, and the future development of different inversion techniques for conductivity models. From the observations and results, we believe the best methods would be

- Analysis of transient sources and mini-magnetospheres.
- Relation between the geometry of the mini-magnetospheres and transient fields.
- Alternate modelling techniques for conductivity profiles.

The reason why the time-varying models of the externally inducing and the internally induced fields are in comparable magnitude ranges is a complicated question which can have many answers. It is possible that there is a additional source on Mars that has not been accounted for or that the existing solar wind interaction is complex. Olsen et al. (2010) tried modelling the internal and external sources along with toroidal sources using MGS data. But their results are similar to ours in the sense that the internal fields are higher than the external fields, even on the night side. An alternative could be the use of surface values. But at the moment, we only have surface magnetic measurements

from one location. If we are able to obtain more data from different locations, it might prove helpful for both conductivity studies and external fields comprehension. The mini-magnetospheres and the interaction of the solar wind near and on the surface could be investigated in detail. However, using the satellite measurements available now, near as well as far to the planet, can also provide a way to better understand them. But it would be difficult to concentrate on individual days and understand the interaction for each due to the abundance of data. Since an orbit by orbit analysis is not practical, we need to look for alternate techniques.

This leads us to look for different inversion methods. The method that we employed in this thesis looks for a 1D electrical conductivity profile of the mantle. But this can be questioned if we take into account the prominent Martian dichotomy (Soderblom et al. 1974). The dichotomy might be affecting our method to estimate the conductivity since the conductivity of the shallow depth northern and deeper southern hemispheres might vary differently. The assumption of a constant magnetic permeability can also be replaced with separate permeability values for each assumed conductivity layer or according to magnetisation depths. Additionally, considering only a radial conductivity might not be the correct way to interpret the interior. The only way to properly overcome this problem is to develop 3D modelling.

9.3 Comparison with Earth

Planetary magnetic field can have different sources and each source provides invaluable and complementary information on the internal structure of a planet (e.g., Stevenson 2003). Large global fields give insight into the current dynamics deep inside the planet, remanent fields are clues of an ancient global field and past dynamics and, induced fields allow to obtain some information on the temperature and composition of the mantle through electrical conductivity estimations. These contributions are known for many years on Earth and have largely contributed to increasing our understanding of its interior, in complement to other geophysical data such as geodesy or seismology. The work described in this thesis is an example of the way that the sources of magnetic field can be used to estimate parameters that govern the internal structure of planetary bodies.

The terrestrial and gaseous planets in our Solar System resemble and differ each other in their interior properties. A comparison between them, especially with Earth, would be helpful for future studies that can use Earth as a standard model to understand the other planets. As expected, there is no significant similarity between Jupiter and Mars. Jupiter is dominated by its internal dynamo field while Mars is dominated by its internal crustal field. However, comparing them both to Earth is feasible since the geomagnetic field comprises both the internal sources. All the three planets have some kind of time-varying fields as well. The similarity between Earth and Jupiter is limited to their SV timescales and advection dominated SV. For Earth and Mars, the behaviour of externally inducing and internally induced models are expected to be similar but we do not see it in this study. Other techniques, like those discussed in the last section, which are also

used for Earth, might be more helpful for a better comparison.

Finally, for the other planetary bodies, their dynamo or induced fields can be modelled to understand some properties of their interior. Currently, with the exceptions of Venus and Mars, we can model the internal dynamo field for all planets as well as the moon Ganymede. Especially with the data from missions like BepiColombo and JUICE, the different sources of the field for Mercury and the moons of Jupiter can be investigated extensively.

Appendix A: Communications and Publications

IASPEI
International Association of Seismology and Physics of the Earth's Interior
IUGG
IAGA
International Association of Geomagnetism and Aeronomy

IAGA-IASPEI 2021
21-27 August 2021 | Hyderabad, India

Sr No: 146
SYMPOSIUM: D2 Planetary magnetic fields and geomagnetic secular variation

Time-varying magnetic fields around Mars

CORRESPONDING & PRESENTING AUTHOR:
Shivangi Sharan, University of Nantes, France
Benoit Langlais, University of Nantes, France
Erwan Thebault, University of Nantes, France
Olivier Verhoeven, University of Nantes, France

Although a large part of the observed Martian magnetic field is constituted by crustal fields that are static and invariant in time, there is also a time-varying, transient field formed from the interaction between the static field and the solar wind. Its behavior is driven by both internal and external sources, and can thus be used for investigations of ionosphere as well as internal structure.

For this study, data from two satellites are used. The Mars Global Surveyor (MGS) and Mars Atmospheric and Volatile Evolution (MAVEN) have very different orbit configurations, resulting in different magnetic field observations with respect to local time and altitude. MGS stayed in a polar orbit around Mars providing vector measurements from 1999 to 2006. Currently orbiting Mars in a highly elliptical orbit and providing data from 2014, MAVEN changed its orbit course in early 2019. For each of these datasets, a priori crustal field models are used to subtract the static field from the data to obtain the time varying fields. The resulting residuals are analyzed in both planetocentric and sun-state coordinates and significant differences in field with respect to latitude and altitude are noticed. These results are useful for modelling the external field to study the internal structure and composition of Mars. It is also useful in removing external variations when modelling the static crustal field.

KEYWORDS: Mars, transient magnetic fields, MGS and MAVEN

Time-varying magnetic fields around Mars from MGS and MAVEN

S. Sharan [1] B. Langlais [1] E. Thébault [1] O. Verhoeven [1]

[1]Laboratory of Planetology and Geodynamics, University of Nantes

Introduction

The first magnetic field measurements around Mars from satellites like the Mariners gave a good initial estimate but were still insufficient to study it deeply. The Mars Global Surveyor (MGS) was the first satellite to provide useful details of the field at a constant altitude. The current orbiting spacecraft Mars Atmosphere and Volatile Evolution (MAVEN) provides high resolution data at both high and low altitudes.

The field around Mars is driven by both internal and external sources. The internal sources are the magnetized rocks in the crust. And the external sources are the currents produced due to the planet's interaction with the solar wind and the induced currents in the crust and mantle due to this.

Many crustal field models are available using data from MGS and MAVEN that show the field to be dominant in the southern hemisphere with magnitudes higher than that observed on Earth. However, very few studies focus on the external fields observed around Mars and its implications.

Time-varying fields

At the satellite data locations -

- B_{mes} : The observed magnetic field measurements
- B_{pred} : The predicted crustal magnetic field using a priori model
- B_{res} : The residual transient magnetic field

$$B_{res} = B_{mes} - B_{pred}$$

MGS

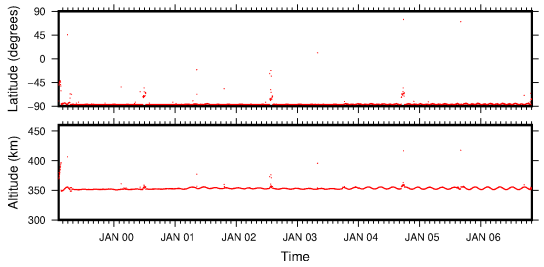

Figure 1: Orbit periapsis - 10 orbits per day

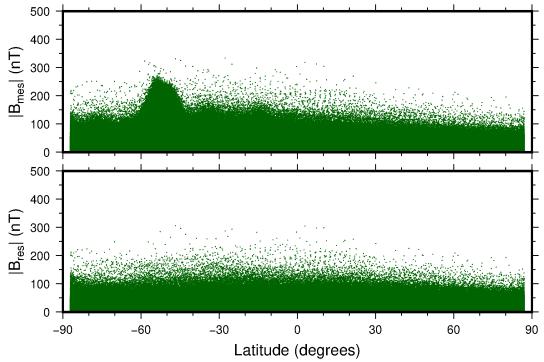

Figure 2: Total field intensity with respect to latitude for all data

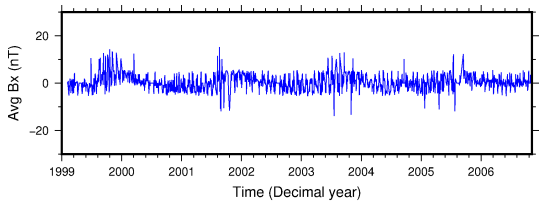

Figure 3: Daily average of Bx component in sun state coordinates for nightside data

MAVEN

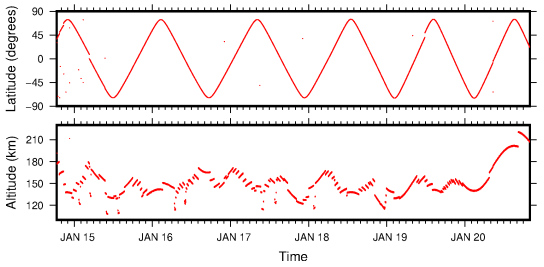

Figure 4: Orbit periapsis - 5 to 7 orbits per day

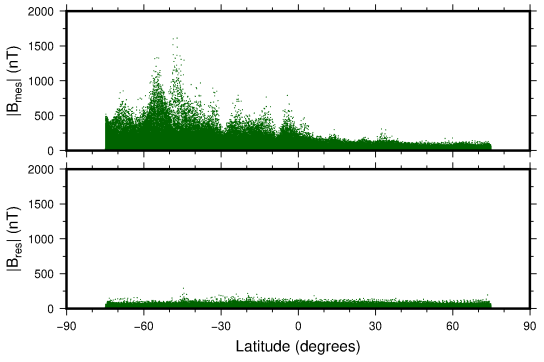

Figure 5: Total field intensity with respect to latitude for data below 1000 km

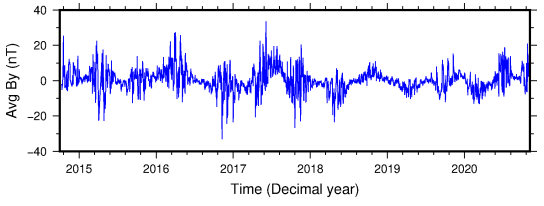

Figure 6: Daily average of By component in sun state coordinates for data below 1000 km

26-day cycle in SS coordinates

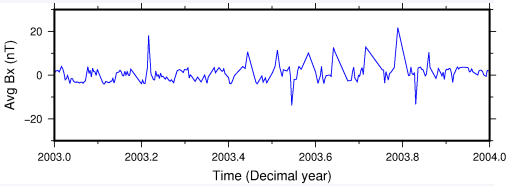

Figure 7: MGS : Daily average of Bx component in sun state coordinates for nightside data for 2003

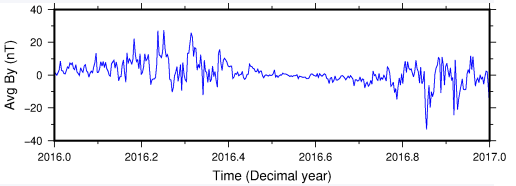

Figure 8: MAVEN : Daily average of By component in sun state coordinates for data below 1000 km for 2016

Conclusion

Importance of the external field study and its modelling-

- Proxy for interplanetary magnetic fields (IMF)
- Correction for external fields when modelling crustal anomalies
- Estimating electrical conductivity of the mantle

References

[1] Langlais et al. A new model of the crustal magnetic field of mars using mgs and maven. *JGR: Planets*, 124(6):1542--1569, 2019.

[2] Morschhauser et al. A spherical harmonic model of the lithospheric magnetic field of mars. *JGR: Planets*, 119(6):1162--1188, 2014.

EGU22-2981, updated on 09 Nov 2022
https://doi.org/10.5194/egusphere-egu22-2981
EGU General Assembly 2022

Jupiter's internal structure and dynamics inferred from a high resolution magnetic field and secular variation model

Shivangi Sharan[1], Benoit Langlais[1], Hagay Amit[1], Mathis Pinceloup[1], Erwan Thébault[2], and Olivier Verhoeven[1]

[1]Laboratoire de Planétologie et Géosciences, CNRS UMR 6112, Nantes Université, Université d'Angers, Le Mans Université, Nantes, France

[2]Laboratoire Magma et Volcans, Université Clermont Auvergne, UMR 6524, CNRS, IRD, OPGC, Clermont-Ferrand, France

The interior of Jupiter can be described broadly as a dense core surrounded by fluids, dominantly hydrogen and helium. The hydrogen rich metallic fluid generates the strongest planetary magnetic field in the Solar System. Modelling and interpreting this field give essential information about the dynamo process inside Jupiter. However, the depth of the dynamo region and the temporal variation of the magnetic field are still debatable. Here we use the Juno mission data across four years to derive an internal magnetic field model using spherical harmonic functions. We take the fluxgate magnetometer measurements acquired during the first 28 perijoves to compute a main field model to degree 13, and a secular variation model to degree 8. The power spectrum of the main field model is used to investigate the radius of the dynamo region. We use the properties of the non-zonal and quadrupole family spectra to infer that the convective region has an upper boundary at 0.843 ± 0.015 Jupiter radius. The slope of the secular variation timescales indicate that the dynamo is dominated by advective effects. The secular variation (SV) displays a maximum near the equator with a dipole structure in agreement with zonal drift of the Great Blue Spot. However, numerous small scale SV structures at mid and high latitudes suggest that the flow at the interior is complex involving both zonal and non-zonal features.

AGU FALL MEETING
Chicago, IL & Online Everywhere
12–16 December 2022

P013
Giant Planet Interiors
Session ID#: 161075

P32D 1856
Jupiter's Internal Structure and Dynamics inferred from a High Resolution Magnetic Field and Secular Variation Model (1050133)

Shivangi Sharan[1], **Benoit Langlais**[2], Hagay Amit[3], Erwan Thébault[4], Mathis Pinceloup[5] and Olivier Verhoeven[3]

(1)FRANCE, (2)Lab Planetologie Geodynamique, Nantes, France, (3)LPGN Laboratoire de Planétologie et Géodynamique de Nantes, Nantes Cedex 03, France, (4)Université Clermont Auvergne, Laboratoire Magmas et Volcans, Clermont-Ferrand, France, (5)Nantes University, Nantes, France

The interior of Jupiter can be described broadly as a dense core surrounded by fluids, dominantly hydrogen and helium. The hydrogen rich metallic fluid generates the strongest planetary magnetic field in the Solar System. Modelling and interpreting this field gives essential information about the dynamo process inside Jupiter. However, the depth of the dynamo region and the temporal variation of the magnetic field are still debatable. Here we use the Juno mission data across 5 years to derive an internal magnetic field model using spherical harmonic functions. We take the fluxgate magnetometer measurements acquired during the first 38 perijoves to compute a main field model to degree 16, and a secular variation (SV) model to degree 8. The power spectrum of the main field model is used to investigate the radius of the dynamo region. We use the properties of the non-zonal and quadrupole families' spectra to infer that the convective region has an upper boundary at 0.830 ± 0.022 Jupiter radius. The slope of the SV timescales indicate that the dynamo is dominated by advective effects. The SV displays a maximum near the equator with a dipole structure in agreement with zonal drift of the Great Blue Spot. However, numerous small scale SV structures at mid and high latitudes suggest that the flow at the interior is complex involving both zonal and non-zonal features.

Jupiter's Internal Structure and Dynamics inferred from a High Resolution Magnetic Field and Secular Variation Model

S. Sharan[1], B. Langlais[1], H. Amit[1], E. Thébault[2], M. Pinceloup[1] and O. Verhoeven[1]

[1]Laboratoire de Planétologie et Géosciences, CNRS UMR 6112, Nantes Université, Université d'Angers, Le Mans Université, Nantes, France
[2]Laboratoire Magmas et Volcans, Université Clermont Auvergne, UMR 6524, CNRS, IRD, OPGC, Clermont-Ferrand, France

AGU FALL MEETING
Chicago, IL & Online Everywhere
12– 16 December 2022
P32D 1856

Overview

In this study we use the magnetic field measurements made by the Juno spacecraft around Jupiter. Our goal is to model the Jovian magnetic field of internal origin. This model describes simultaneously the main field (MF) and its secular variation (SV) using spherical harmonics functions. This model extends the work published by Sharan et al. (2022) and uses more than 5 years of measurements.

The model is used to infer several important properties of the Jovian internal structure and dynamics. The field spectrum indicates the dynamo upper bound is 0.83 Jovian radii. The observed SV timescales show that the dynamo is dominated by advective effects as on Earth. The SV map above the dynamo region displays a maximum near the equator, with a dipolar structure in agreement with an eastward drift of the Great Blue Spot. However, numerous small-scale SV structures at mid and high latitudes suggest that the flow is complex, with both zonal and non-zonal features.

Data and model derivation

Juno is the first spacecraft that orbits Jupiter at low altitudes on a polar trajectory. Here we use the 1-second magnetic field measurements across 5 years (38 orbits) to derive an internal magnetic field model using spherical harmonic functions. Only measurements acquired during the perijove are considered, below 300,000 km altitude (Figs. 1 and 2), such that fields associated with magnetodisk can be ignored (Connerney et al., 2020).

Synthetic tests are made with a scaled geomagnetic field model and with real data location. Sensitivity matrix and correlation analyses show that the field is resolvable up to SH degree 16 and 8 for MF and SV, respectively.

Fig. 1 – altitude vs. latitude distribution of Juno measurements around Jupiter, below 300,000 km

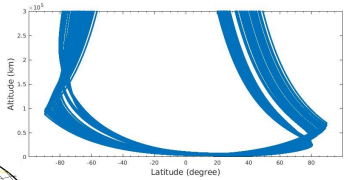

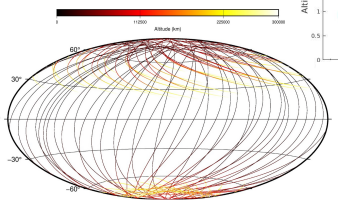

Fig. 2 – geographical distribution of Juno measurements around Jupiter, below 300,000 km

Results: Field model and maps

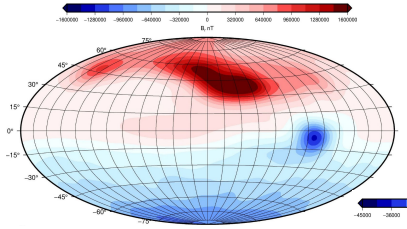

Fig. 3 – Radial MF predicted at Jupiter's surface

MF is computed to n =20, but only terms ≤16 are kept. SV is computed to n =8, using temporal splines with a 2.6-yr spacing. Rms misfit to data is about 850 nT.

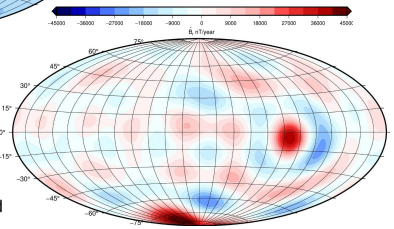

Fig. 4 – Radial SV component at Jupiter's dynamo radius

Fig. 5 – Lowes-Mauersberger magnetic energy spectrum (Jupiter's surface) compared to Ridley and Holme (2016) and Connerney et al. (2022)

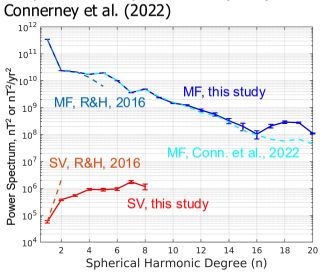

The field is dipole-dominated as on Earth but the non-dipole field is relatively stronger (Figs. 3 & 5).

The SV feature close to the equator (Fig. 4) shows eastward drift, or azimuthal flow. Weak SV at mid and northern latitudes suggests weak flow or field-aligned flow, and eastward drift. SV close to the South pole is not well constrained by data.

Results: SV timescales

The ratio of the MF to SV spectra gives the SV timescales (Fig. 6). Dipole one is 2500 yrs, the shortest one is 40 yrs.

The linear slope (log-log) is -1.11 ± 0.23

This is consistent with an advection dominated secular variation (purely adv. slope is -1, Christensen et al., 2012).

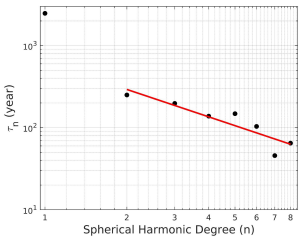

Fig. 6 – SV timescales of the Jovian field

Results: Jovian internal structure

Two sub-families of the magnetic spectrum can be used to estimate the radius of the dynamo. On Earth, error with respect to the seismological radius of the core is below 0.3% (Langlais et al., 2014).

Immediately above the magnetic sources, the non-zonal (ie., $m \neq 0$) and quadrupole (ie., $n+m$ even) spectra should be flat.

Fig. 7 – Sub-family spectra above dynamo region

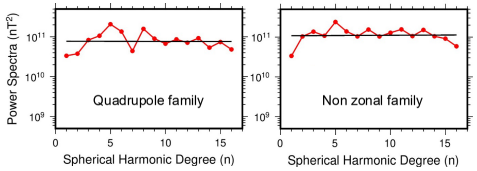

The radius of the dynamo is computed to be 0.830 ± 0.022 R_J (Fig. 7).

This coincides (Fig. 8) with the radius of the H-He demixing layer at 0.84 R_J (Brygoo et al., 2021).

No proof of a shallower secondary dynamo, no indication regarding the bottom of the dynamo.

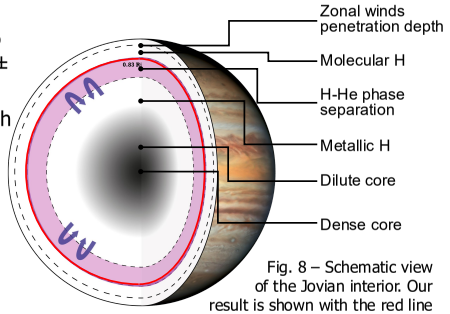

Fig. 8 – Schematic view of the Jovian interior. Our result is shown with the red line

Conclusions and more

- 1st high resolution model of the SV for another planet than Earth;
- Total field change over 5 years reaches almost 3% (twice the Earth's);
- Dynamo radius estimated at 0.830 R_J;
- Dynamo dominated by advection;
- Jovian field is dipole-dominated, SV shows zonal and non zonal patterns.

References. Brygoo et al., Nature, 593, 2021; Christensen et al., GJI, 190, 2012; Connerney et al., JGR, 125, 2020; Connerney et al., JGR, 127, 2022; Langlais et al. EPSL 401, 2014; Ridley and Holme, JGR, 121, 2016; Sharan et al., GRL, 49, 2022.

Contact: Shivangi Sharan, shivangi.sharan@univ-nantes.fr

AGU ADVANCING EARTH AND SPACE SCIENCE

Geophysical Research Letters

RESEARCH LETTER
10.1029/2022GL098839

The Internal Structure and Dynamics of Jupiter Unveiled by a High-Resolution Magnetic Field and Secular Variation Model

S. Sharan[1], B. Langlais[1], H. Amit[1], E. Thébault[2], M. Pinceloup[1], and O. Verhoeven[1]

[1]Laboratoire de Planétologie et Géosciences, CNRS UMR 6112, Nantes Université, Université d'Angers, Le Mans Université, Nantes, France, [2]Laboratoire Magma et Volcans, Université Clermont Auvergne, UMR 6524, CNRS, IRD, OPGC, Clermont-Ferrand, France

Key Points:

- Magnetic field of Jupiter is modeled from Juno's first 4 years of observations
- A degree 16 magnetic field model and degree 8 secular variation model are derived
- The model indicates a dynamo not far from the surface and complex motions deep inside Jupiter

Supporting Information:

Supporting Information may be found in the online version of this article.

Correspondence to:

S. Sharan and B. Langlais,
shivangi.sharan@univ-nantes.fr;
benoit.langlais@univ-nantes.fr

Citation:

Sharan, S., Langlais, B., Amit, H., Thébault, E., Pinceloup, M., & Verhoeven, O. (2022). The internal structure and dynamics of Jupiter unveiled by a high-resolution magnetic field and secular variation model. *Geophysical Research Letters*, *49*, e2022GL098839. https://doi.org/10.1029/2022GL098839

Received 28 MAR 2022
Accepted 21 JUL 2022

Abstract Unique information about the dynamo process acting at Jupiter can be inferred by modeling and interpreting its magnetic field. Using the fluxgate magnetometer measurements acquired during the 4 years of the Juno mission, we derive a magnetic field model which describes simultaneously the main field and the secular variation (SV) up to spherical harmonic degrees 16 and 8, respectively. Apart from the Earth's, this is the first time another planetary magnetic field along with its time variation is described to such a high degree. We use properties of the power spectrum of the static field to infer the upper boundary of the dynamo convective region at 0.830 ± 0.022 Jupiter radius. The SV and correlation times are relatively comparable to the Earth's and indicate that the field is dominated by advection. The field and SV morphologies suggest zonal as well as non-zonal deep fluid motions.

Plain Language Summary The interior of Jupiter can be described broadly as a dense core surrounded by fluids, dominantly hydrogen and helium. The hydrogen-rich metallic fluid generates the strongest planetary magnetic field in the Solar System. Modeling and interpreting this field gives essential information about the dynamo process inside Jupiter. We use the Juno mission data throughout 4 years (or, 28 orbits) to derive an internal magnetic field and secular variation (SV) model using spherical harmonic functions. We compute a magnetic field model to degree 16 for its static part, and model its temporal variation to degree 8. The power spectrum of the magnetic field model is used to investigate the radius of the dynamo region. We infer that the convective region has an upper boundary at 0.830 ± 0.022 Jupiter radius. The strength of the annual change of field is relatively comparable to the Earth's. The slope of the SV timescales indicates that the dynamo is dominated by advective effects. The SV displays a maximum near the equator with a bi-polar structure in agreement with zonal drift of the Great Blue Spot. However, numerous small scale SV structures suggest that the flow at the interior is complex involving both zonal and non-zonal features.

1. Introduction

The interior of the giant planets of our Solar System can be described in simple terms as consisting of a core of unknown composition surrounded by fluid envelopes (Guillot, 2005). For Jupiter, the core could be small and dense, but also large and dilute (Wahl et al., 2017). The overlying envelopes consist of an inner layer of metallic hydrogen and an outer layer of molecular hydrogen. Recent experimental results describe a transition H-He demixing layer, suggesting Helium rain between depths 0.68 and 0.84 R_J (Jupiter's equatorial radius, 1 R_J = 71,492 km) (Brygoo et al., 2021). The high temperature and pressure inside the planet renders it electrically conducting. Convection in the electrically conductive metallic hydrogen generates the strong Jovian magnetic field (Jones, 2011, 2014). In contrast to rocky bodies, Jupiter does not have an abrupt change between its metallic hydrogen (magnetic source) and molecular hydrogen (source free) regions. The change is expected to be gradual. The electrical conductivity profile of the different hydrogen layers at different depths from an ab-initio simulation (French et al., 2012) does not indicate a clear value of the dynamo region radius. Previous attempts to constrain this radius using the magnetic energy spectrum place it somewhere between 0.80 and 0.90 R_J (Connerney et al., 2022; Langlais et al., 2014; Tsang & Jones, 2020).

Jupiter's magnetic field has been measured by various flybys and orbiting satellites. The observations made by the flybys of Pioneer 10 and 11, Voyager 1 and 2 (during the seventies), and the Ulysses probe (early nineties) gave some initial information about the planet (Balogh et al., 1992; Ness et al., 1979; Smith et al., 1974). The first orbiting satellite, Galileo, was launched in 1989. It provided measurements from Jupiter and its moons from

1995 to 2003. Although these magnetic observations are spread over long periods of time, there have been only a few attempts to constrain or estimate the temporal variation of the field (Connerney et al., 1982; Ridley & Holme, 2016; Yu et al., 2010). Out of these studies, only Ridley and Holme (2016) co-estimated the secular variation (SV) with the main field (MF) using magnetic field measurements made between 1973 and 2003. However, due to the inhomogeneous temporal and geographical data distribution, most of the selected observations were from the Galileo mission at low latitudes. Ridley and Holme (2016) computed two models, one with only MF time averaged Gauss coefficients and one with time dependent MF and SV coefficients. The latter model was considered better because of its lower residuals and greater smoothness. Nevertheless, they considered their SV model to be reliable only up to degree 2.

None of these spacecrafts provided data near the poles. This was overcome by the recent Juno measurements. Juno space probe was launched on August 5, 2011 and entered Jupiter's orbit in July 2016. Its magnetic measurements have already been used to propose recent models of the Jovian field. Connerney et al. (2018) provided a spherical harmonic (SH) internal field model up to degree 10 using the first nine orbits. This initial model was improved by Connerney et al. (2022) who calculated a static model up to degree 30 for internal and degree 1 for external, from the first 33 orbits, using a generalized inversion technique to damp the unresolved parameters. They state that the Gauss coefficients are well resolved until degree 13 though useful information can be retained until degree 18 for some coefficients. Jupiter's internal field is characterized by a very high magnitude, showing both dipole and non-dipole parts. The non-dipole field is dominantly observed in the northern hemisphere. Field change over a 45-year time span was observed and zonal drift was invoked to explain the temporal change of an intense magnetic flux patch near the equator (Moore et al., 2018, 2019). An updated external magnetodisk field model for Juno is also available (Connerney et al., 2020). None of the existing models based on Juno data attempt to model explicitly the current global temporal variation of the field.

In this study, we use the high quality Juno measurements to derive a SH model of the Jovian field, simultaneously describing its MF and SV up to SH degrees 16 and 8, respectively. Section 2 details the data and the selection criteria we use for this study. Section 3 describes the method used to derive the models and their spectra that was assessed with a thorough synthetic analysis (Text S1 in Supporting Information S1). In Section 4 we analyze the model and discuss our results. We first determine the dynamo radius assuming white spectrum of specific parts of the field. We also calculate the SV correlation times of the Jovian field. We finally downward continue the field into Jupiter's interior to the estimated dynamo radius and infer kinematic properties. We conclude in Section 5.

2. Data

Juno has a near polar, highly elliptical orbit with apojove exceeding over 100 times Jupiter's radius. The prime mission lasted 5 years and provided data for 33 orbits with one complete orbit taking about 53 days. The space probe was initially planned to undergo a reduction maneuver for achieving 14-day science orbits but Juno entered safe mode for its second orbit, thereby remaining in its initial 53-day capture orbit for the entire mission. The spacecraft aims to obtain a global coverage of the planet. For the first eight orbits, the shift between successive orbits was 45° in longitude. The subsequent shifts reduce the longitudinal spacing by half to obtain data from the gaps left previously.

Juno uses two fluxgate magnetometers, located on one of the three solar arrays to measure the vector magnetic field. Magnetic field measurements acquired by Juno are available under two versions. The version 1 data provides measurements across the entire orbit, whereas the version 2 data gives only near planet measurements from the orbit, denoted as perijove hereafter. Both version 1 and 2 data are provided in three Cartesian coordinate systems—planetocentric, sun-state, and payload. Since planetocentric system is body-fixed, it is the most appropriate to study the internal field. We use the version 2 one-second data in planetocentric coordinates from the first 28 perijoves (data available for only 27 perijoves, excluding the second one). As discussed later, synthetic tests inversion including the latest perijoves from 29 to 33 leads to an increase in polar gaps that degrades some model coefficients. Perijove 19 was also dismissed because spurious oscillations were later observed.

The periapsis reaches altitude as low as 2,500 km, or radius 1.03 R_J, and precesses about 1° in latitude northward, starting from the equator, after each orbit. In order to minimize external field contributions and to increase the signal-to-noise ratio of high internal magnetic field harmonics, we select measurements near the planet's surface, that is, the vector data below an arbitrarily chosen altitude of 300,000 km (or radius $\sim 5.2R_J$). Moreover, due to

geometric attenuation with the altitude, high-altitude measurements are less sensitive to small spatial scales than the ones at comparatively lower altitudes. The vector data range from August 2016 to July 2020 giving 628,828 data locations, that are plotted in Figure S1 in Supporting Information S1. Minimum measured field intensity is of the order of 3,000 nT at maximum altitude while the maximum intensity reaches above 10^6 nT.

3. Methodology

The magnetic field in a source free location can be expressed as the gradient of a scalar potential V that satisfies the Laplace equation:

$$\nabla^2 V = 0 \tag{1}$$

The potential for internal and external sources can be written as an expansion of SH functions:

$$\begin{aligned} V(r,\theta,\phi,t) = R_J \sum_{n=1}^{n_i^{\max}} \sum_{m=0}^{n} \left\{ \left(\frac{R_J}{r}\right)^{n+1} \left(g_n^m(t)\cos m\phi + h_n^m(t)\sin m\phi\right) P_n^m(\cos\theta) \right\} \\ + R_J \sum_{n=1}^{n_e^{\max}} \sum_{m=0}^{n} \left\{ \left(\frac{r}{R_J}\right)^{n} \left(q_n^m(t)\cos m\phi + s_n^m(t)\sin m\phi\right) P_n^m(\cos\theta) \right\} \end{aligned} \tag{2}$$

where (r, θ, ϕ, t) are the planetocentric spherical coordinates (radius, co-latitude, and longitude) and time, respectively. R_J is the reference radius equal to Jupiter's equatorial radius (71,492 km). $g_n^m(t)$ and $h_n^m(t)$ are the time-dependent internal field Gauss coefficients of degree n and order m while $q_n^m(t)$ and $s_n^m(t)$ are the external field coefficients. P_n^m are the Schmidt quasi-normalized associated Legendre functions. $n_i^{\max}$ and $n_e^{\max}$ are the maximum degree for the internal and external field coefficients, respectively.

To calculate the SH coefficients, we apply a weighted least-squares inversion approach based on a singular value decomposition algorithm. The weights are defined in nT by the instrument error and intrinsic noise for each Juno data location (Connerney et al., 2017). The temporal variation of the internal field is calculated using B-splines of order 2, which are piece-wise polynomials describing the time derivatives between defined knots. We use three knots, at the beginning, middle, and final epoch of the measurements (spacing is about 1.95 years). This parameterization was extensively tested on the selected set of Juno's data location with a synthetic time-varying internal magnetic field mimicking the strength and the power spectrum of the actual internal field of Jupiter. The inversion on synthetic measurements does not require regularization with this parameterization and it is stable with random noise (Details of the method, tests, and assessments are provided in Text S1 in Supporting Information S1).

Once the Gauss coefficients and their time variation are estimated, several statistical quantities can be computed. The Lowes-Mauersberger spectrum represents the magnetic field power spectrum per SH degree (Lowes, 2007; Mauersberger, 1956). For a given time, and at a given radius r, it can be defined as

$$\mathcal{R}_n = (n+1)\left(\frac{R_J}{r}\right)^{(2n+4)} \sum_{m=0}^{n} \left[(g_n^m)^2 + (h_n^m)^2\right] \tag{3}$$

at SH degree n. Similarly, for the SV, it can be defined as

$$\mathcal{S}_n = (n+1)\left(\frac{R_J}{r}\right)^{(2n+4)} \sum_{m=0}^{n} \left[(\dot{g}_n^m)^2 + (\dot{h}_n^m)^2\right] \tag{4}$$

where $\dot{g}_n^m$ and $\dot{h}_n^m$ are the Gauss coefficients of the SV.

The MF and its spectrum $\mathcal{R}_n$ can be upward or downward continued, provided there are no magnetic field sources present in between. This property has been used to derive estimates of the radius of the dynamo region, or of the liquid core, in the case of the Earth. This is also known as the white noise hypothesis: immediately outside the dynamo region, the part of the magnetic spectrum associated with the dynamo is assumed flat, and the depth to the dynamo can thus be grossly estimated (Lowes, 1974). However some terms ($n = 1$ and $n = 2$) have to be ignored in order for this approximation to match the radius of the Earth's core (Cain et al., 1989; Voorhies, 2004). Langlais et al. (2014) found that certain parts of the spectrum $\mathcal{R}_n$, namely the non-zonal and quadrupole families, are independent of n at some radius r (see Text S2 in Supporting Information S1, for details). On Earth, these

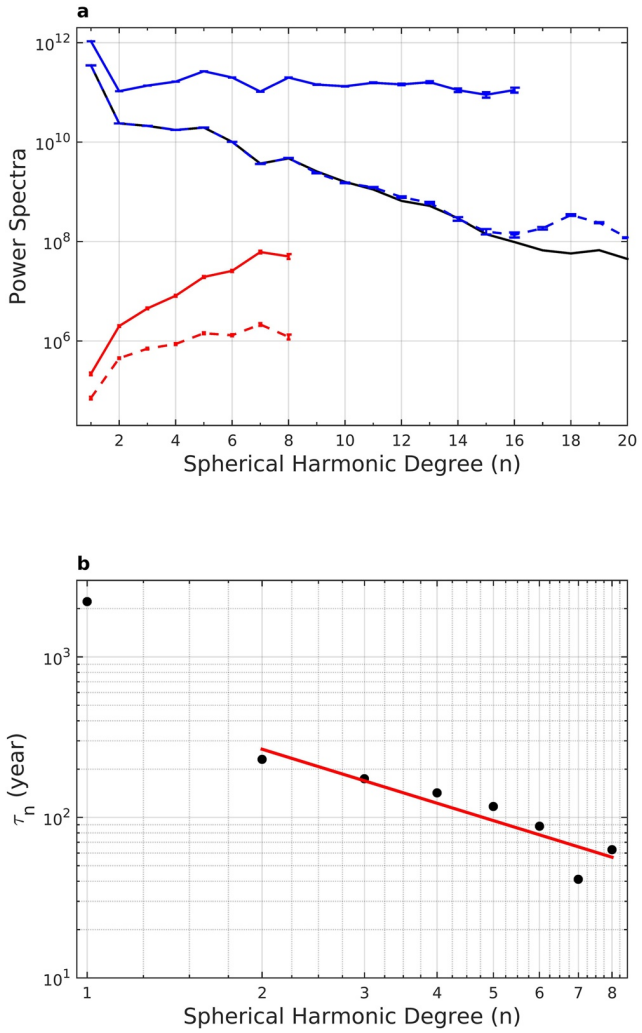

Figure 1. (a) The power spectra with error bars for the main field (shown in blue, units - nT^2) and secular variation (shown in red, units - (nT/year)^2) of the model at the surface (dashed line) and at $\mathbf{R}_{sf}$ (solid line). The main field terms for $n > 16$ are not downward continued to $\mathbf{R}_{sf}$. The black line is the main field power spectrum of the model of Connerney et al. (2022), which lies within the 99% bound of our model. (b) The secular variation timescales of the model. The red line is the linear best fit to the non-dipole part.

approaches return the value of the core or dynamo radius with a combined relative error lower than 0.3%. In the following, we refer to the dynamo radius at Jupiter, estimated from the non-zonal and quadrupole families of coefficients, as $\mathbf{R}_{sf}$. It can be interpreted as the radius of the top of the source region, or the bottom of the source free region.

The correlation times as a function of degree n can also be defined combining the quantities $\mathcal{R}_n$ and $\mathcal{S}_n$. The correlation times, also referred to as the SV timescales, give a measure of how long it takes for the field of a particular degree to get reorganized, or become uncorrelated to its former state at that degree (Amit et al., 2018; Christensen & Tilgner, 2004; Hulot & Le Mouël, 1994). It is expressed as

$$\tau_n = \sqrt{\frac{\mathcal{R}_n}{\mathcal{S}_n}} \tag{5}$$

4. Results and Discussion

We calculate the MF model up to degree 20 and the SV to degree 8. The external field is estimated up to degree 2. Suspicion of power leakage from unresolved small and rapid spatial scales leads us to reject 29 out of the 608 eigenvalues in the weighted least-squares inversion. As a consequence, the terms beyond SH degree 16 are damped, and the final model is truncated to $n_i^{\max} = 16$. We estimate a posteriori standard error on the coefficients from the covariance matrix and the inversion misfit for the three vector components. The misfits for each vector component are given in Table S1 in Supporting Information S1. This table also shows the statistics for a model to SH degree 20 derived without SV. The misfit difference between these two cases supports the fact that a statistically significant and global SV is present in the measurements. The SV improves data fit better than increasing field complexity (see Ridley and Holme (2016) for a similar conclusion). Note that Connerney et al. (2022) also indicates strong evidences for local SV in the vicinity of Jupiter's Great Blue Spot between Juno perijoves 9 and 33. Figure 1a displays the MF (and the SV) power spectra with the 99% error bars. For comparison, the power spectrum of the model of Connerney et al. (2022) is also shown, which falls within the error bars down to SH degree 15–16. The increase of the power between $n = 16$ and 18 of our model probably arises because of the spectral aliasing of remaining signal in the measurements. We also note that with increasing orbits the satellite goes lower in altitude near the north pole while increasing the size of a gap at similar latitude ranges over the south pole area. This results in high degree, low order terms being less resolved (i.e., zonal and near zonal terms). Figure S2 in Supporting Information S1 shows the root mean square differences between Juno's dataset and predictions by our model, a model calculated without SV, and the model by Connerney et al. (2022), considering different truncation degrees for each model. At SH degree 16, our model and the model by Connerney et al. (2022) have a root mean square misfit to data equal to about 800 nT.

4.1. Inferences on the Internal Structure

We estimate the dynamo radius $\mathbf{R}_{sf}$ for varying truncation degrees of the MF model $n_i^{\max}$ seeking in a minimum least-squares sense the depth at which the power spectra from the non-zonal ($m \neq 0$) and quadrupole ($n + m$ even) families of coefficients are statistically flat (Langlais et al., 2014). The error bars on the estimated dynamo radius decrease up to truncation degree $n_i^{\max} = 16$ for both families (Figure S8 in Supporting Information S1). It is also the truncation degree for which the maximum likelihood estimates from the non-zonal and quadrupole families of power spectra coincide. This again supports the choice of truncating the present model to the maximum

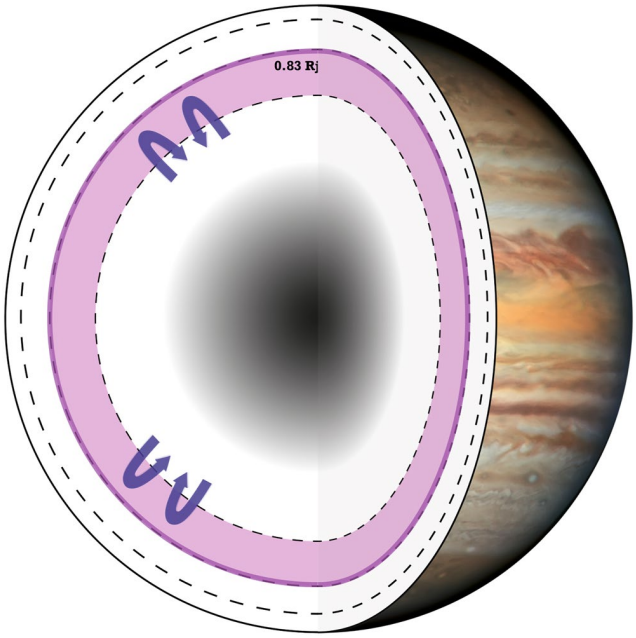

Figure 2. Schematic view of the interior of Jupiter. The bold violet line depicts our result $\mathbf{R}_{sf}$. The gray area depicts the core (0.2 R_J) and the possible dilute core region (Wahl et al., 2017; Wicht & Gastine, 2020). The violet area between the dotted lines (0.68 and 0.84 R_J) depicts the H-He phase separated layer (Brygoo et al., 2021). The top dotted line at 0.95 R_J depicts the depth where the jets decay down to the minimum (Kaspi et al., 2018). The arrows represent possible convection area with unknown origin depth.

degree 16. The maximum likelihood value from the non-zonal field is equal to 0.831 R_J and that from the quadrupole family is equal to 0.829 R_J. We use their mean and combine their standard errors to provide a single estimate for $R_{sf} = 0.830 \pm 0.022$ R_J. Previous studies such as the one by Connerney et al. (2018) estimate the dynamo radius "near 0.85 R_J" while Connerney et al. (2022) estimate it to $0.81R_J$ and Tsang and Jones (2020) between 0.82 and $0.87R_J$ using a numerical model. However, all these studies use the white noise hypothesis as discussed above, which ignores the $n = 1$ and even $n = 2$ terms.

For a dynamo to exist in a planet, two main criteria are required: an electrically conducting fluid and an energy source, which is often convection within a spherical shell in rotation. For Jupiter, the metallic hydrogen is the fluid, and its convective motion drives the dynamo. Convection can also take place in the source free region, without contributing to the dynamo. Wicht and Gastine (2020), through numerical simulations, suggested the possibility of two distinct dynamo regions inside Jupiter. The primary region would be at depth, and is responsible for the dipole dominated field geometry. The secondary one would be shallower, and operates where the equatorial jets encounter conductive material in the transition layer. However, surface jets motion decays rapidly with depth and are unlikely to extend at depths larger than about 3,000–3,500 km or ∼0.95 R_J (Guillot et al., 2018; Kaspi et al., 2018). Christensen et al. (2020) suggested that a stratified layer, close to the surface, could quench the jets at depth and play a role in the secondary dynamo. Our study points toward a source free region extending deeper, with a radius placed at 0.830 R_J. This radius could correspond to the upper limit of the dynamo region. We note that it also matches well the radius of the transition layer in between the metallic and molecular hydrogen (Brygoo et al., 2021), rendering this layer part of the dynamo region (Figure 2). Our results do not provide constraints on the bottom radius of the dynamo and do not indicate a shallower secondary dynamo (Gastine & Wicht, 2021) above 0.830 R_J.

4.2. SV Timescales

The SV timescales are shown in Figure 1b. For Earth, the correlation time for the dipole is around 1,000 years and the lowest value at $\sim n_i^{\max} = 13$ is of the order of 10 years. Field models and numerical dynamo simulations indicate that the non-dipole SV timescales are inversely proportional to the SH degree (e.g., Bouligand et al., 2016; Lhuillier et al., 2011). For Jupiter, the correlation time for the dipole (τ_1) is 2,210 years while the lowest value we obtain is 40 years for degree 7. We observe similar inverse proportionality for the Jovian SV timescales. The best fit slope for $n = 2 - 8$ is -1.12 with a standard deviation of 0.21. According to the scaling theory of the magnetic induction equation, a slope of -1 corresponds to advective SV, whereas -2 indicates diffusive SV (Christensen et al., 2012; Holme & Olsen, 2006). A -2 slope for our model is well outside 2 standard deviations and can be excluded. Therefore, our best fit value -1.12 ± 0.21 suggests that the field change is dominated by advective effects, as is the case for Earth (Christensen et al., 2012; Lhuillier et al., 2011). In addition, the overall similarity between the non-dipole SV timescales of Jupiter and Earth suggests a similar magnetic Reynolds number (Christensen & Tilgner, 2004), that is, $Rm_J \sim 1{,}000$. In contrast, Wicht et al. (2019) concluded that diffusive effects might govern the dynamo in the transition layer. Though their transition region starts above $\mathbf{R}_{sf}$, the SV timescales we compute are independent of the radius, hence challenging the importance of diffusion. It thus remains an open question as to what phenomenon drives the observed SV of Jupiter.

4.3. Implications to Jupiter's Dynamo

Using the four morphological criteria defined in Christensen et al. (2010) for Earth-like dynamo models at the core-mantle boundary, we compare our results with the geodynamo. For comparison purposes, we set $n_i^{\max} = 8$ to calculate the different criteria, that is, smaller than that shown in Figures 3a–3f. The relative axial dipole power

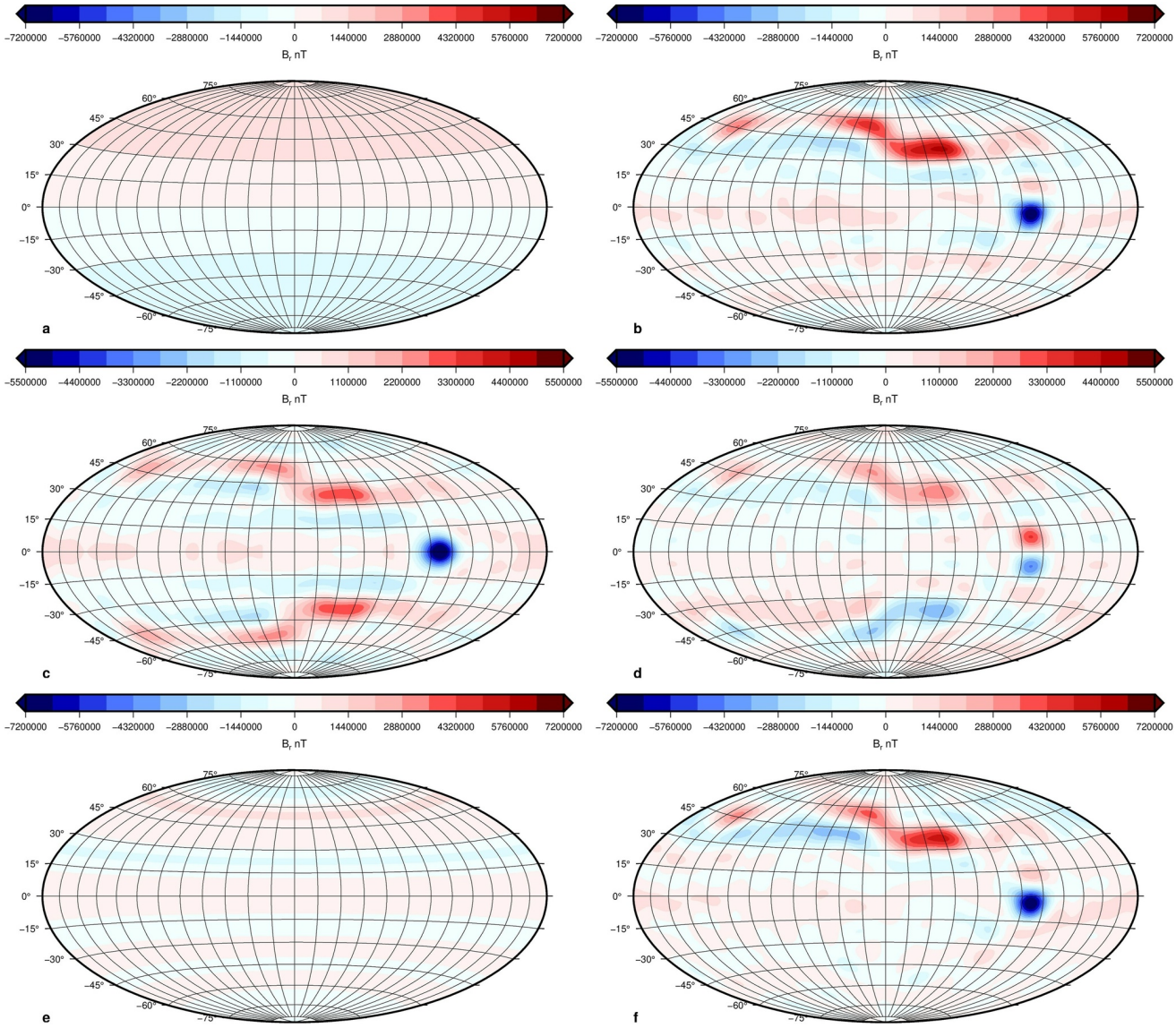

Figure 3. The radial field at $\mathbf{R}_{sf}$. (a) Axial dipole field. (b) Non-axial dipole field. (c) Non-dipole symmetric field. (d) Non-dipole anti-symmetric field. (e) Non-dipole zonal field. (f) Non-dipole non-zonal field. The maps are centered at 180° longitude.

for our model is 0.86 at $\mathbf{R}_{sf}$ while the standard value for Earth is 1.4, though the present-day value is about 1. This indicates that Jupiter's dynamo is either less dipolar or comparable to Earth's (Figures 3a and 3b). The equatorial anti-symmetry for Earth is 1.0, whereas our model provides a value of 0.52. A random equipartitioned non-dipole field ratio would give an equatorial anti-symmetry of 0.83 (Christensen et al., 2010). Thus, Jupiter's non-dipole field is more symmetric with respect to the equator than Earth's (Figures 3c and 3d). The zonal to non-zonal ratio for a random equipartitioned field is 0.10 (Christensen et al., 2010). For Earth, the value is 0.15, while for our model the value is 0.20, which indicates a stronger zonal contribution (Figures 3e and 3f). Lastly, the flux concentration for a purely dipole field is 0.8 and that for the geomagnetic field is 1.50 (Christensen et al., 2010). The flux concentration is considered low when flux exits one hemisphere and enters through the other uniformly. Conversely, it is large when it exits from a concentrated spot and enters the rest of the sphere uniformly. The concentration value for our model is 4.23. This very large value reflects the dominance of the large intense flux patch in the northern hemisphere.

Figure 4 shows the radial magnetic field and SV maps calculated using the model at Jupiter's surface and at $\mathbf{R}_{sf}$. The large positive radial field patch in the northern hemisphere and the intense negative patch near the equator

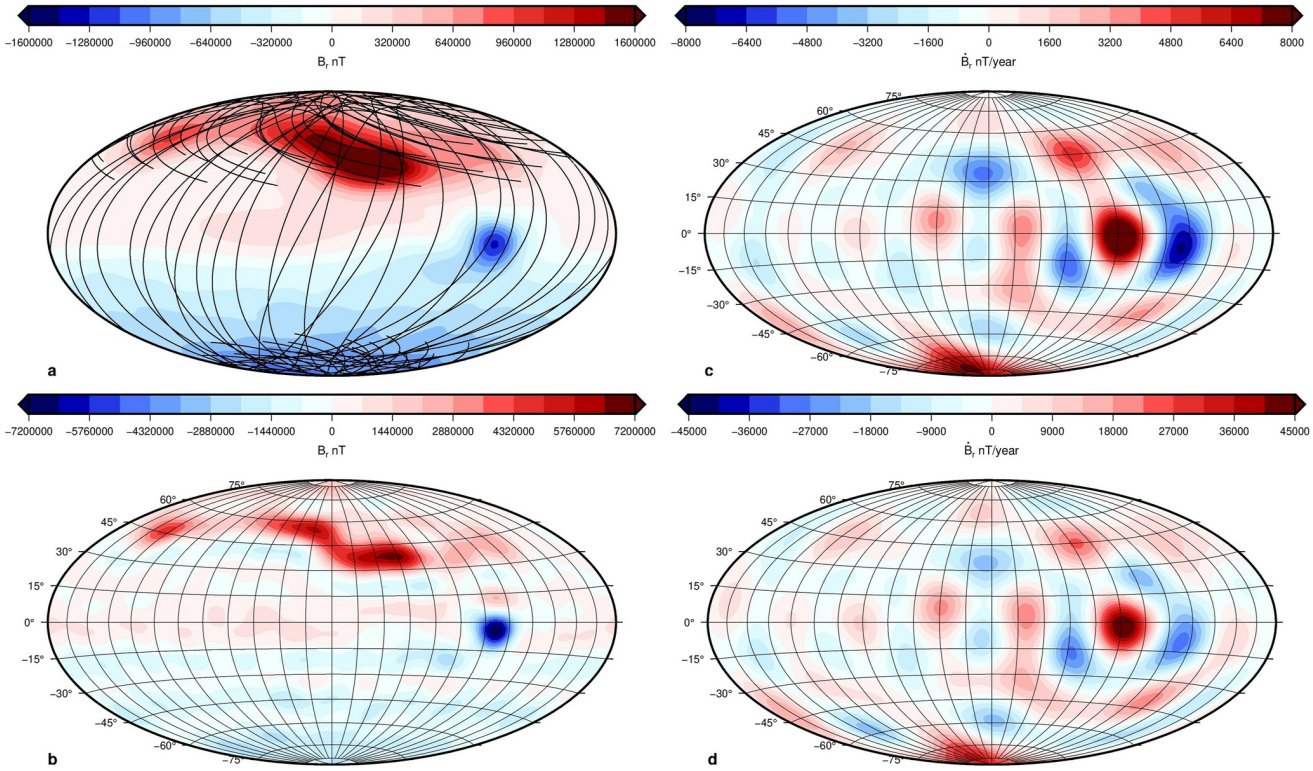

Figure 4. The (a, b) radial field and (c, d) its secular variation at (top) Jupiter's surface and (bottom) $\mathbf{R}_{sf}$. The maps are centered at 180° longitude. The lines in (a) show the orbit paths of the used data set.

(the Great Blue Spot) become more concentrated with depth. SV is of the order of 10^4 nT/year at the surface. This corresponds to a 2.3% change over the course of 4 years of the dataset used, compared to the 1.4% change over a similar duration for the Earth's magnetic field. As for Earth's, it should not be ignored when modeling the magnetic field over periods exceeding a few years.

The spatial pattern of temporal variation of the field brings further dynamical constraints. The power spectrum of the SV calculated at $\mathbf{R}_{sf}$ increases with degree (Figure 1a). Indeed, the SV reveals intense small scale structures (Figure 4). The strong negative radial field patch immediately south of the equator (Figure 4b) coincides with a pair of SV structures (Figure 4d), suggesting eastward drift (Amit, 2014; Livermore et al., 2017). This is opposite to the westward drifting low- and mid-latitude patches observed with Earth's SV (Aubert & Finlay, 2019; Bullard et al., 1950; Finlay & Jackson, 2003). This eastward drift could relate to the zonal winds observed at the surface or until 0.95 R_J (Moore et al., 2019). However, our model presents also other prominent SV structures which cannot be explained by zonal winds. There is some suggestion for a weak eastward drift near 45°N latitude, which is the center of the large positive radial field patch (Figure 4b). But, it is not associated with particularly strong SV for most of its structure, possibly indicating a region with dominantly field-aligned flow (Finlay & Amit, 2011). Livermore et al. (2017) gave similar explanation for the absence of strong SV at southern high latitudes of Earth. The southern hemisphere has many alternating sign SV patches up to 60°S latitude (Figure 4d) which are not correlated with particularly strong field structures (Figure 4b). Bearing in mind that the model is less constrained at the south pole, the opposite signs of B_r and $\dot{B}_r$ (Figure S3 in Supporting Information S1) suggest local fluid upwelling (Amit, 2014), similar to the field and SV below Earth's poles and in agreement with a classic meridional circulation inside the tangent cylinder (Cao et al., 2018; Olson & Aurnou, 1999). We note that the radial field and its SV from $\mathbf{R}_{sf}$ to the surface are weakly sensitive to depth (Figure 4), making these kinematic interpretations robust.

5. Concluding Remarks

We present a co-estimated magnetic field and SV model robust up to degree 16 and degree 8, respectively. The model uses Juno measurements made during the first 28 orbits. As expected, our static field resembles previously published field models (e.g., Connerney et al., 2022). However, we also present here for the first time a small-scale SV model for Jupiter. Our innovative Jovian magnetic SV model provides crucial insight into its deep interior and dynamics. We use two different families of the magnetic spectra and derive a consistent dynamo radius at 0.830 R_J. This confirms that the transition region is part of the dynamo generation. The SV allows to calculate SV timescales and leads to kinematic interpretations of inductive effects (Amit, 2014). The dominance of advective SV and the dipole SV timescale of Jupiter exhibit similarities with the geodynamo. The SV is consistent with zonal as well as non-zonal motions deep inside Jupiter. We further conclude that the global SV is significant and cannot be neglected over the course of 1 year or so.

More insights into the dynamo regime could be gleaned by inferring the flow at Jupiter's deep interior. Our field and SV model can be inverted for the flow at $\mathbf{R}_{sf}$. Such an inversion, which is commonly performed for the flow at the top of Earth's core (Holme, 2015), was performed for Jupiter by Ridley and Holme (2016), but using a very low resolution SV model. More data are also needed to increase the resolution of the field model and to confirm the temporal variation observed during the last 4 years. This will come from Juno during the upcoming extended mission, but also when the ESA's JUICE mission enters Jupiter's orbit at the end of this decade.

Data Availability Statement

All Juno magnetometer data used here are publicly available on NASA's Planetary Data System (PDS) at Planetary Plasma Interactions (PPI) node at https://pds-ppi.igpp.ucla.edu/search/?sc=Juno%26t=Jupiter%26i=FGM. The model coefficients and their standard deviation for the static field to degree 16 and its SV to degree 8 are available at: https://doi.org/10.5281/zenodo.6564162.

Acknowledgments
This work was financially supported by the Centre National D'Études Spatiales (CNES). The authors would like to thank the Editor, Andrew Dombard, and two anonymous reviewers for their useful comments which contributed to improving the manuscript. We thank Stéphanie Beaunay for graphical assistance. We acknowledge AGU's data policy.

References

Amit, H. (2014). Can downwelling at the top of the earth's core be detected in the geomagnetic secular variation? *Physics of the Earth and Planetary Interiors*, *229*, 110–121. https://doi.org/10.1016/j.pepi.2014.01.012

Amit, H., Coutelier, M., & Christensen, U. R. (2018). On equatorially symmetric and antisymmetric geomagnetic secular variation timescales. *Physics of the Earth and Planetary Interiors*, *276*, 190–201. (Special Issue:15th SEDI conference). https://doi.org/10.1016/j.pepi.2017.04.009

Aubert, J., Finlay, C. C., & Fournier, A. (2013). Bottom-up control of geomagnetic secular variation by the earth's inner core. *Nature*, *502*(7470), 219–223. https://doi.org/10.1038/nature12574

Balogh, A., Dougherty, M. K., Forsyth, R. J., Southwood, D. J., Smith, E. J., Tsurutani, B. T., et al. (1992). Magnetic field observations during the Ulysses flyby of Jupiter. *Science*, *257*(5076), 1515–1518. https://doi.org/10.1126/science.257.5076.1515

Bouligand, C., Gillet, N., Jault, D., Schaeffer, N., Fournier, A., & Aubert, J. (2016). Frequency spectrum of the geomagnetic field harmonic coefficients from dynamo simulations. *Geophysical Journal International*, *207*(2), 1142–1157. https://doi.org/10.1093/gji/ggw326

Brygoo, S., Loubeyre, P., Millot, M., Rygg, J. R., Celliers, P. M., Eggert, J. H., et al. (2021). Evidence of hydrogen-helium immiscibility at Jupiter-interior conditions. *Nature*, *593*(7860), 517–521. https://doi.org/10.1038/s41586-021-03516-0

Bullard, E. C., Freedman, C., Gellman, H., & Nixon, J. (1950). The westward drift of the earth's magnetic field. *Philosophical Transactions of the Royal Society of London - Series A: Mathematical and Physical Sciences*, *243*(859), 67–92. https://doi.org/10.1098/rsta.1950.0014

Cain, J. C., Wang, Z., Schmitz, D. R., & Meyer, J. (1989). The geomagnetic spectrum for 1980 and core-crustal separation. *Geophysical Journal International*, *97*(3), 443–447. https://doi.org/10.1111/j.1365-246X.1989.tb00514.x

Cao, H., Yadav, R. K., & Aurnou, J. M. (2018). Geomagnetic polar minima do not arise from steady meridional circulation. *Proceedings of the National Academy of Sciences*, *115*(44), 11186–11191. https://doi.org/10.1073/pnas.1717454115

Christensen, U. R., Aubert, J., & Hulot, G. (2010). Conditions for earth-like geodynamo models. *Earth and Planetary Science Letters*, *296*(3), 487–496. https://doi.org/10.1016/j.epsl.2010.06.009

Christensen, U. R., & Tilgner, A. (2004). Power requirement of the geodynamo from ohmic losses in numerical and laboratory dynamos. *Nature*, *429*(6988), 169–171. https://doi.org/10.1038/nature02508

Christensen, U. R., Wardinski, I., & Lesur, V. (2012). Timescales of geomagnetic secular acceleration in satellite field models and geodynamo models. *Geophysical Journal International*, *190*(1), 243–254. https://doi.org/10.1111/j.1365-246X.2012.05508.x

Christensen, U. R., Wicht, J., & Dietrich, W. (2020). Mechanisms for limiting the depth of zonal winds in the gas giant planets. *The Astrophysical Journal*, *890*(1), 61. https://doi.org/10.3847/1538-4357/ab698c

Connerney, J. E. P., Acuña, M. H., & Ness, N. F. (1982). Voyager 1 assessment of Jupiter's planetary magnetic field. *Journal of Geophysical Research*, *87*(A5), 3623–3627. https://doi.org/10.1029/JA087iA05p03623

Connerney, J. E. P., Benn, M., Bjarno, J. B., Denver, T., Espley, J., Jorgensen, J. L., et al. (2017). The juno magnetic field investigation. *Space Science Reviews*, *213*(1), 39–138. https://doi.org/10.1007/s11214-017-0334-z

Connerney, J. E. P., Kotsiaros, S., Oliversen, R. J., Espley, J. R., Joergensen, J. L., Joergensen, P. S., et al. (2018). A new model of Jupiter's magnetic field from juno's first nine orbits. *Geophysical Research Letters*, *45*(6), 2590–2596. https://doi.org/10.1002/2018GL077312

Connerney, J. E. P., Timmins, S., Herceg, M., & Joergensen, J. L. (2020). A Jovian magnetodisc model for the juno era. *Journal of Geophysical Research: Space Physics*, *125*(10), e2020JA028138. https://doi.org/10.1029/2020JA028138

Connerney, J. E. P., Timmins, S., Oliversen, R. J., Espley, J. R., Joergensen, J. L., Kotsiaros, S., et al. (2022). A new model of Jupiter's magnetic field at the completion of Juno's prime mission. *Journal of Geophysical Research: Planets*, *127*(2), e2021JE007055. https://doi.org/10.1029/2021JE007055

Finlay, C. C., & Amit, H. (2011). On flow magnitude and field-flow alignment at Earth's core surface. *Geophysical Journal International*, *186*(1), 175–192. https://doi.org/10.1111/j.1365-246X.2011.05032.x

Finlay, C. C., & Jackson, A. (2003). Equatorially dominated magnetic field change at the surface of earth's core. *Science*, *300*(5628), 2084–2086. Retrieved from https://science.sciencemag.org/content/300/5628/2084. https://doi.org/10.1126/science.1083324

French, M., Becker, A., Lorenzen, W., Nettelmann, N., Bethkenhagen, M., Wicht, J., & Redmer, R. (2012). Ab initio simulations for material properties along the Jupiter adiabat. *The Astrophysical Journal - Supplement Series*, *202*(1), 5. https://doi.org/10.1088/0067-0049/202/1/5

Gastine, T., & Wicht, J. (2021). Stable stratification promotes multiple zonal jets in a turbulent Jovian dynamo model. *Icarus*, *368*, 114514. Retrieved from https://www.sciencedirect.com/science/article/pii/S0019103521001895. https://doi.org/10.1016/j.icarus.2021.114514

Guillot, T. (2005). The interiors of giant planets: Models and outstanding questions. *Annual Review of Earth and Planetary Sciences*, *33*(1), 493–530. https://doi.org/10.1146/annurev.earth.32.101802.120325

Guillot, T., Miguel, Y., Militzer, B., Hubbard, W. B., Kaspi, Y., Galanti, E., et al. (2018). A suppression of differential rotation in Jupiter's deep interior. *Nature*, *555*(7695), 227–230. https://doi.org/10.1038/nature25775

Holme, R. (2015). Large-scale flow in the core. In *Treatise on geophysics* (pp. 91–113). https://doi.org/10.1016/B978-0-444-53802-4.00138-X

Holme, R., & Olsen, N. (2006). Core surface flow modelling from high-resolution secular variation. *Geophysical Journal International*, *166*(2), 518–528. https://doi.org/10.1111/j.1365-246X.2006.03033.x

Hulot, G., & Le Mouël, J. (1994). A statistical approach to the earth's main magnetic field. *Physics of the Earth and Planetary Interiors*, *82*(3), 167–183. Retrieved from https://www.sciencedirect.com/science/article/pii/0031920194900701. https://doi.org/10.1016/0031-9201(94)90070-1

Jones, C. A. (2011). Planetary magnetic fields and fluid dynamos. *Annual Review of Fluid Mechanics*, *43*(1), 583–614. https://doi.org/10.1146/annurev-fluid-122109-160727

Jones, C. A. (2014). A dynamo model of Jupiter's magnetic field. *Icarus*, *241*, 148–159. Retrieved from https://www.sciencedirect.com/science/article/pii/S0019103514003315. https://doi.org/10.1016/j.icarus.2014.06.020

Kaspi, Y., Galanti, E., Hubbard, W. B., Stevenson, D. J., Bolton, S. J., Iess, L., et al. (2018). Jupiter's atmospheric jet streams extend thousands of kilometres deep. *Nature*, *555*(7695), 223–226. https://doi.org/10.1038/nature25793

Langlais, B., Amit, H., Larnier, H., Thébault, E., & Mocquet, A. (2014). A new model for the (geo)magnetic power spectrum, with application to planetary dynamo radii. *Earth and Planetary Science Letters*, *401* , 347–358. https://doi.org/10.1016/j.epsl.2014.05.013

Lhuillier, F., Fournier, A., Hulot, G., & Aubert, J. (2011). The geomagnetic secular-variation timescale in observations and numerical dynamo models. *Geophysical Research Letters*, *38*(9). Retrieved from https://agupubs.onlinelibrary.wiley.com/doi/abs/10.1029/2011GL047356. https://doi.org/10.1029/2011GL047356

Livermore, P. W., Hollerbach, R., & Finlay, C. C. (2017). An accelerating high-latitude jet in earth's core. *Nature Geoscience*, *10*(1), 62–68. https://doi.org/10.1038/ngeo2859

Lowes, F. J. (1974). Spatial power spectrum of the main geomagnetic field, and extrapolation to the core. *Geophysical Journal International*, *36*(3), 717–730. https://doi.org/10.1111/j.1365-246X.1974.tb00622.x

Lowes, F. J. (2007). Geomagnetic spectrum, spatial. In D. Gubbins & E. Herrero-Bervera (Eds.), *Encyclopedia of geomagnetism and paleomagnetism* (pp. 350–353). Dordrecht: Springer Netherlands. https://doi.org/10.1007/978-1-4020-4423-6_126

Mauersberger, P. (1956). Das mittel der energiedichte des geomagnetischen hauptfeldes an der erdoberflache und seine saulare anderung. *Gerlands Beitr. Geophys.*, *65*, 207–215. Retrieved from https://ci.nii.ac.jp/naid/10006217427/en/

Moore, K. M., Cao, H., Bloxham, J., Stevenson, D. J., Connerney, J. E. P., & Bolton, S. J. (2019). Time variation of Jupiter's internal magnetic field consistent with zonal wind advection. *Nature Astronomy*, *3*(8), 730–735. https://doi.org/10.1038/s41550-019-0772-5

Moore, K. M., Yadav, R. K., Kulowski, L., Cao, H., Bloxham, J., Connerney, J. E. P., et al. (2018). A complex dynamo inferred from the hemispheric dichotomy of Jupiter's magnetic field. *Nature*, *561*(7721), 76–78. https://doi.org/10.1038/s41586-018-0468-5

Ness, N. F., Acuna, M. H., Lepping, R. P., Burlaga, L. F., Behannon, K. W., & Neubauer, F. M. (1979). Magnetic field studies at Jupiter by voyager 1: Preliminary results. *Science*, *204*(4396), 982–987. https://doi.org/10.1126/science.204.4396.982

Olson, P., & Aurnou, J. (1999). A polar vortex in the earth's core. *Nature*, *402*(6758), 170–173. https://doi.org/10.1038/46017

Ridley, V. A., & Holme, R. (2016a). Modeling the Jovian magnetic field and its secular variation using all available magnetic field observations. *Journal of Geophysical Research: Planets*, *121*(3), 309–337. Retrieved from https://agupubs.onlinelibrary.wiley.com/doi/abs/10.1002/2015JE004951. https://doi.org/10.1002/2015je004951

Smith, E. J., Davis, L., Jr., Jones, D. E., Coleman, P. J., Jr., Colburn, D. S., Dyal, P., et al. (1974). The planetary magnetic field and magnetosphere of Jupiter: Pioneer 10. *Journal of Geophysical Research*, *79*(25), 3501–3513. Retrieved from https://agupubs.onlinelibrary.wiley.com/doi/abs/10.1029/JA079i025p03501. https://doi.org/10.1029/ja079i025p03501

Tsang, Y.-K., & Jones, C. A. (2020). Characterising Jupiter's dynamo radius using its magnetic energy spectrum. *Earth and Planetary Science Letters*, *530*, 115879. Retrieved from https://www.sciencedirect.com/science/article/pii/S0012821X19305710. https://doi.org/10.1016/j.epsl.2019.115879

Voorhies, C. V. (2004). Narrow-scale flow and a weak field by the top of earth's core: Evidence from Ørsted, Magsat, and secular variation. *Journal of Geophysical Research*, *109*(B3). Retrieved from https://agupubs.onlinelibrary.wiley.com/doi/abs/10.1029/2003JB002833. https://doi.org/10.1029/2004jb003289

Wahl, S. M., Hubbard, W. B., Militzer, B., Guillot, T., Miguel, Y., Movshovitz, N., et al. (2017). Comparing Jupiter interior structure models to *Juno* gravity measurements and the role of a dilute core. *Geophysical Research Letters*, *44*(10), 4649–4659. https://doi.org/10.1002/2017gl073160

Wicht, J., & Gastine, T. (2020). Numerical simulations help revealing the dynamics underneath the clouds of Jupiter. *Nature Communications*, *11*(1), 2886. https://doi.org/10.1038/s41467-020-16680-

Wicht, J., Gastine, T., & Duarte, L. D. V. (2019). Dynamo action in the steeply decaying conductivity region of Jupiter-like dynamo models. *Journal of Geophysical Research: Planets*, *124*(3), 837–863. Retrieved from https://agupubs.onlinelibrary.wiley.com/doi/abs/10.1029/2018JE005759. https://doi.org/10.1029/2018je005759

Yu, Z. J., Leinweber, H. K., & Russell, C. T. (2010). Galileo constraints on the secular variation of the Jovian magnetic field. *Journal of Geophysical Research*, *115*(E3). https://doi.org/10.1029/2009JE003492

References From the Supporting Information

Alken, P., Thebault, E., Beggan, C. D., Aubert, J., Baerenzung, J., Brown, W. J., …Wardinski, I. (2021). Evaluation of candidate models for the 13th generation international geomagnetic reference field. *Earth Planets and Space*, *73*(1), 48. Retrieved from https://doi.org/10.1186/s40623-020-01281-4

Aubert, J., & Finlay, C. C. (2019). Geomagnetic jerks and rapid hydromagnetic waves focusing at earth's core surface. *Nature Geoscience*, *12*(5), 393–398. Retrieved from https://doi.org/10.1038/s41561-019-0355-1

Connerney, J. E. P., Benn, M., Bjarno, J. B., Denver, T., Espley, J., Jorgensen, J. L., et al. (2017). The juno magnetic field investigation. *Space Science Reviews*, *213* (1), 39–138. Retrieved from https://doi.org/10.1007/s11214-017-0334-z

Connerney, J. E. P., Timmins, S., Oliversen, R. J., Espley, J. R., Joergensen, J. L., Kotsiaros, S., et al. (2022). A new model of Jupiter's magnetic field at the completion of juno's prime mission. *Journal of Geophysical Research: Planets*, *127*(2), e2021JE007055. https://doi.org/10.1029/2021JE007055

de Boor, C. (2001). Calculation of the smoothing spline with weighted roughness measure. *Mathematical Models and Methods in Applied Sciences*, *11* (01), 33–41. https://doi.org/10.1142/S0218202501000726

Finlay, C. C., Kloss, C., Olsen, N., Hammer, M. D., Tøffner-Clausen, L., Grayver, A., & Kuvshinov, A. (2020). The chaos-7 geomagnetic field model and observed changes in the south atlantic anomaly. *Earth Planets and Space*, *72*(1), 156. https://doi.org/10.1186/s40623-020-01252-9

Langel, R. A., & Estes, R. H. (1982). A geomagnetic field spectrum. *Geophysical Research Letters*, *9*(4), 250–253. https://doi.org/10.1029/GL009i004p00250

Langlais, B., Amit, H., Larnier, H., Thébault, E., & Mocquet, A. (2014). A new model for the (geo)magnetic power spectrum, with application to planetary dynamo radii. *Earth and Planetary Science Letters*, *401*, 347–358. https://doi.org/10.1016/j.epsl.2014.05.013

Lowes, F. J. (1966). Mean-square values on sphere of spherical harmonic vec-tor fields. *Journal of Geophysical Research*, *71* (8), 2179. https://doi.org/10.1029/JZ071i008p02179

McLeod, M. G. (1996). Spatial and temporal power spectra of the geomagnetic field. *Journal of Geophysical Research*, *101*(B2), 2745–2763. https://doi.org/10.1029/95JB03042

Ridley, V. A., & Holme, R. (2016). Modeling the Jovian magnetic field and its secular variation using all available magnetic field observations. *Journal of Geophysical Research: Planets*, *121* (3), 309–337. https://doi.org/10.1002/2015JE004951

Supporting Information for "The internal structure and dynamics of Jupiter unveiled by a high-resolution magnetic field and secular variation model"

S. Sharan[1], B. Langlais[1], H. Amit[1], E. Thébault[2], M. Pinceloup[1], and O. Verhoeven[1]

[1]Laboratoire de Planétologie et Géosciences, CNRS UMR 6112, Nantes Université, Université d'Angers, Le Mans Université, Nantes, France

[2]Laboratoire Magma et Volcans, Université Clermont Auvergne, UMR 6524, CNRS, IRD, OPGC, Clermont-Ferrand, France

Contents of this file

1. Text S1 and S2
2. Figures S1 to S8
3. Table S1

Text S1. Synthetic simulation

Corresponding authors: S. Sharan, Laboratoire de Planétologie et Géosciences, CNRS UMR 6112, Nantes Université, Nantes, France (shivangi.sharan@univ-nantes.fr)

Corresponding authors: B. Langlais, Laboratoire de Planétologie et Géosciences, CNRS UMR 6112, Nantes Université, Nantes, France (benoit.langlais@univ-nantes.fr)

The internal Jovian magnetic field and its temporal rate of change (secular variation, SV) is expanded in terms of Spherical Harmonics (SH). Above the magnetic sources, the magnetic field $\mathbf{B}$ derives from the expression of a magnetic scalar potential V by $\mathbf{B} = -\nabla V$ and where in spherical coordinates it is approximated by the finite series

$$\begin{aligned} V(r,\theta,\phi,t) \;=\; & R_J \sum_{n=1}^{n_i^{max}} \sum_{m=0}^{n} \left\{ \left(\frac{R_J}{r} \right)^{n+1} (g_n^m(t)\cos m\phi + h_n^m(t)\sin m\phi) P_n^m(\cos\theta) \right\} \\ & + R_J \sum_{n=1}^{n_e^{max}} \sum_{m=0}^{n} \left\{ \left(\frac{r}{R_J} \right)^{n} (q_n^m(t)\cos m\phi + s_n^m(t)\sin m\phi) P_n^m(\cos\theta) \right\} \end{aligned} \tag{1}$$

where r denotes the radial distance from the center of Jupiter, R_J is Jupiter's equatorial radius equal to 71,492 km, θ the co-latitude, and ϕ the longitude. The functions $P_n^m(\cos\theta)$ are the Schmidt quasi-normalized associated Legendre functions of degree n and order m. The Gauss coefficients $g_n^m(t)$, $h_n^m(t)$ are the time-varying parameters to be estimated by inversion of the measurements conventionally given in the units of nano-Tesla (nT). The mathematical series in Eq.(1) is truncated to n_i^{max} and n_e^{max}, which are the maximum degrees for the internal and external field coefficients.

The three vector components of Jupiter's magnetic field in the radial, southward and eastward horizontal directions (B_r, B_θ and B_ϕ) are calculated from the negative gradient of Eq.(1) in the spherical coordinate system

$$B_r = -\frac{\partial V}{\partial r}, \quad B_\theta = -\frac{1}{r}\frac{\partial V}{\partial \theta}, \quad B_\phi = -\frac{1}{r\sin\theta}\frac{\partial V}{\partial \phi}. \tag{2}$$

In order to test the data distribution and its adequacy with model determination, we compute a set of synthetic vector magnetic field predictions at the actual Juno locations

and epochs using the CHAOS-7.8 Earth's magnetic field model (Finlay et al., 2020). This time-dependent model is based on magnetic field observations collected by the low-Earth orbiting satellites between years 1999 and 2021. It is expanded to SH degree $n_i^{max} = 20$ for the time varying internal field with order 6 B-splines (de Boor, 2001) with a 6-month knot separation. The synthetic data we build therefore contains a significant amount of rapid secular variation, secular acceleration, and contributions of higher time derivatives, including some geomagnetic jerks or core pulses, which are sudden changes in the second time derivative of the Earth's magnetic field (e.g., Aubert & Finlay, 2019).

Before predicting the field over the four years of available Juno data, we note that the strength and shape of Earth's and Jupiter's magnetic fields are different. Figure S4 shows the power spectra of Earth's main field CHAOS model, its secular variation, and the power spectrum of Jupiter's magnetic field model derived by Connerney et al. (2022), both at the reference radius of each planet.

In a first step towards building a realistic synthetic data set, we estimate by standard least-squares the power law of Jupiter's magnetic field model. For the CHAOS model, we estimate two power laws in order to account for the different internal field sources contributing to the model. Indeed, a distinct change of slope occurs around SH degree 13 that indicates that the field from the core dominates from SH degree 1 to 13, while the field from the crust dominates from SH degree 15 (Langel & Estes, 1982). For each part of the power spectrum we use the power law difference with Jupiter's model to rescale the CHAOS internal field model to SH degree 20. In addition, we impose that the power spectrum of the rescaled secular variation keeps the same slope as the original CHAOS

model. Without this precaution, the synthetic secular variation power spectrum diverges at the dynamo radius of Jupiter. The power spectra of the rescaled CHAOS main field model, following now the general trend of the model by Connerney et al. (2022), and its secular variation are displayed in Figure S4.

The rescaling of the CHAOS model allows us to incorporate the a priori information provided with Juno data. In the database, each measurement is given with a precision index corresponding to the magnetometer operating range and an instrumental noise less than 1 nT. The uncertainties are defined for six different operating ranges and vary with the strength of the ambient magnetic field (Connerney et al., 2017). Each synthetic observation we build is therefore associated with a weight (with a minimum weight of 1 nT) and we further add a Gaussian random noise of 25 nT to each vector measurement. This Gaussian noise is the upper bound of the instrument error of Juno measurements.

We then set up the parameterization of the inverse problem. The internal static field is derived up to SH degree $n_i^{max} = 20$ and a static external field to SH degree 2. The maximum resolution of the internal time variation of the model is imposed by the time difference and the spatial coverage between Juno's polar orbits. We choose to parameterize the time variation with splines of order 2 with a knot spacing of 2 years and for SH degrees 1 to 10 only. The examination of the covariance matrix indicates that we are not dealing with an ill-conditioned inverse problem that would require an explicit regularization. The 608 coefficients are then estimated by weighted least-squares and the inversion is performed with a singular value decomposition (SVD) algorithm, thus offering

the possibility at a later stage to solve the problem with the generalized truncated SVD technique.

The results of the synthetic inversion is assessed in the spatial and spectral domains using several criteria (see Alken et al. (2021) for a list of possible criteria). We show in Figure S5 the power spectrum of the estimated model with the power spectrum of the input rescaled CHAOS model for the main field and its secular variation. These are accompanied with the results of the spherical harmonic correlation analysis. Both power spectra for the main field agree in strength and correlate better than 0.99 over the full degree range. For the SV the correlation is better than 0.75. However, we observe an increase in the estimated power spectrum starting from SH degree 8. This overestimated energy compared to the rescaled CHAOS benchmark model is the sign of power leakage from the time-varying structures that are not accounted for in the estimated model. Figure S6 shows the input and output radial field and its difference at $\mathbf{R}_{sf}$ (0.83 times Jupiter's radius) to SH degree 20 for the static part and to SH degree 8 for the SV part. We observe no significant residuals for the static field while the SV residuals follow the SV structures. The residuals are one order of magnitude smaller than the input SV model indicating the presence of a small power leakage that is amplified at the dynamo radius.

Text S2. Dynamo Radius Estimate

For Earth, the geomagnetic field spectrum (Lowes, 1966) can be steadily interpreted in terms of magnetic source location. There is an apparent slope break near degrees 13-14 that distinguishes between the energy from the core and crustal field components, respectively. Ignoring the dipole term, the spectrum becomes almost flat when downward

extrapolated to the CMB for the core part, while it shows an almost null slope at the surface for higher degrees. This property has been observed for a long time (Lowes, 1974) and has been suggested to provide a crude estimate of the core radius on other planets where seismological measurements are not available.

This crude estimate can be refined by using alternative expressions to the power spectrum. McLeod (1996) defined an expression using magnetic monopoles to estimate core radius. Langlais, Amit, Larnier, Thébault, and Mocquet (2014) defined two additional expressions, first using the non-zonal terms ($m \neq 0$) and the second using the quadrupole terms ($n+m$ even). These two sub-families show flat spectra independent of degree n at a radius r, interpreted as the CMB for Earth (Figure S7). The non-zonal spectrum has a null slope immediately above the dynamo area. This is expected because the geomagnetic field is axisymmetric on the long term, and the non-axisymmetric part is thought to be random. The flatness of the quadrupole family spectrum is explained by the dominance of rotational effects in the dynamo process. They can be defined as

$$\mathcal{R}_n^{nz}(r) = (n+1)\left(\frac{a}{r}\right)^{(2n+4)} \sum_{m=1}^{n} [(g_n^m)^2 + (h_n^m)^2] \tag{3}$$

$$\mathcal{R}_n^{qf}(r) = (n+1)\left(\frac{a}{r}\right)^{(2n+4)} \sum_{m=0,\ n+m\ even}^{n} [(g_n^m)^2 + (h_n^m)^2] \tag{4}$$

where a is the reference radius, equal to the planet's radius.

The $\mathcal{R}_n^{nz}$ and $\mathcal{R}_n^{qf}$ provide a close estimate of the core radius as was verified using four different geomagnetic models (Langlais et al., 2014). For CHAOS-4 field model at epoch 2005 and $n = 13$, the estimated core radius R_{nz} estimated from Eq.(3) is 3,486.6 km and the R_{qf} estimated from Eq.(4) is 3,496.7 km, which are similar to the accepted

seismic value of 3,481.7 km. The maximum likelihood value using the approach of Lowes (1974) gives R_{lowes}=3,294.5 km and the one using the approach of McLeod (1996) provides R_{mcleod}=3,586.5 km, both deviating significantly from the accepted seismic value. The core (or dynamo) radii for other planets were also estimated. Using the JSV model of Ridley and Holme (2016) for Jupiter up to $n = 5$, Langlais et al. (2014) provided the values 0.86 and 0.87 R_J for R_{nz} and R_{qf} respectively. For our model, we estimate the dynamo radius for both the non-zonal and quadrupole families (Figure S8) by varying the truncation degree between 10 and 20, and observe that the slope is the most flat at $n = 16$. The radius starts to increase beyond it. The non-zonal spectrum gives a value of 0.831 R_J with a standard deviation of 0.021 R_J, while the quadrupole family spectrum returns 0.829 R_J with a standard deviation of 0.024 R_J. Both independent estimates therefore fall within each other's error bars. The mean of the radii estimated using $n_i^{max} = 16$ corresponds to 0.830±0.022 R_J.

References

Alken, P., Thébault, E., Beggan, C. D., Aubert, J., Baerenzung, J., Brown, W. J., ... Wardinski, I. (2021). Evaluation of candidate models for the 13th generation international geomagnetic reference field. *Earth, Planets and Space*, *73*(1), 48. Retrieved from https://doi.org/10.1186/s40623-020-01281-4 doi: 10.1186/s40623-020-01281-4

Aubert, J., & Finlay, C. C. (2019). Geomagnetic jerks and rapid hydromagnetic waves focusing at earth's core surface. *Nature Geoscience*, *12*(5), 393–398. Retrieved from https://doi.org/10.1038/s41561-019-0355-1 doi: 10.1038/s41561-019-0355-1

Connerney, J. E. P., Benn, M., Bjarno, J. B., Denver, T., Espley, J., Jorgensen, J. L., ... Smith, E. J. (2017). The juno magnetic field investigation. *Space Science Reviews*, *213*(1), 39–138. Retrieved from https://doi.org/10.1007/s11214-017-0334-z doi: 10.1007/s11214-017-0334-z

Connerney, J. E. P., Timmins, S., Oliversen, R. J., Espley, J. R., Joergensen, J. L., Kotsiaros, S., ... Levin, S. M. (2022). A new model of jupiter's magnetic field at the completion of juno's prime mission. *Journal of Geophysical Research: Planets*, *127*(2), e2021JE007055. Retrieved from https://agupubs.onlinelibrary.wiley.com/doi/abs/10.1029/2021JE007055 (e2021JE007055 2021JE007055) doi: https://doi.org/10.1029/2021JE007055

de Boor, C. (2001). Calculation of the smoothing spline with weighted roughness measure. *Mathematical Models and Methods in Applied Sciences*, *11*(01), 33-41. Retrieved from https://doi.org/10.1142/S0218202501000726 doi: 10.1142/S0218202501000726

Finlay, C. C., Kloss, C., Olsen, N., Hammer, M. D., Tøffner-Clausen, L., Grayver, A., & Kuvshinov, A. (2020). The chaos-7 geomagnetic field model and observed changes in the south atlantic anomaly. *Earth, Planets and Space*, *72*(1), 156. Retrieved from https://doi.org/10.1186/s40623-020-01252-9 doi: 10.1186/s40623-020-01252-9

Langel, R. A., & Estes, R. H. (1982). A geomagnetic field spectrum. *Geophysical Research Letters*, *9*(4), 250-253. Retrieved from https://agupubs.onlinelibrary.wiley.com/doi/abs/10.1029/GL009i004p00250 doi: https://doi.org/10.1029/

GL009i004p00250

Langlais, B., Amit, H., Larnier, H., Thébault, E., & Mocquet, A. (2014). A new model for the (geo)magnetic power spectrum, with application to planetary dynamo radii. *Earth and Planetary Science Letters*, *401*, 347-358. Retrieved from https://www.sciencedirect.com/science/article/pii/S0012821X14003070 doi: https://doi.org/10.1016/j.epsl.2014.05.013

Lowes, F. J. (1966). Mean-square values on sphere of spherical harmonic vector fields. *Journal of Geophysical Research (1896-1977)*, *71*(8), 2179-2179. Retrieved from https://agupubs.onlinelibrary.wiley.com/doi/abs/10.1029/JZ071i008p02179 doi: https://doi.org/10.1029/JZ071i008p02179

Lowes, F. J. (1974, 03). Spatial power spectrum of the main geomagnetic field, and extrapolation to the core. *Geophysical Journal International*, *36*(3), 717-730. Retrieved from https://doi.org/10.1111/j.1365-246X.1974.tb00622.x doi: 10.1111/j.1365-246X.1974.tb00622.x

McLeod, M. G. (1996). Spatial and temporal power spectra of the geomagnetic field. *Journal of Geophysical Research: Solid Earth*, *101*(B2), 2745-2763. Retrieved from https://agupubs.onlinelibrary.wiley.com/doi/abs/10.1029/95JB03042 doi: https://doi.org/10.1029/95JB03042

Ridley, V. A., & Holme, R. (2016). Modeling the jovian magnetic field and its secular variation using all available magnetic field observations. *Journal of Geophysical Research: Planets*, *121*(3), 309-337. Retrieved from https://agupubs.onlinelibrary.wiley.com/doi/abs/10.1002/2015JE004951 doi: https://doi

.org/10.1002/2015JE004951

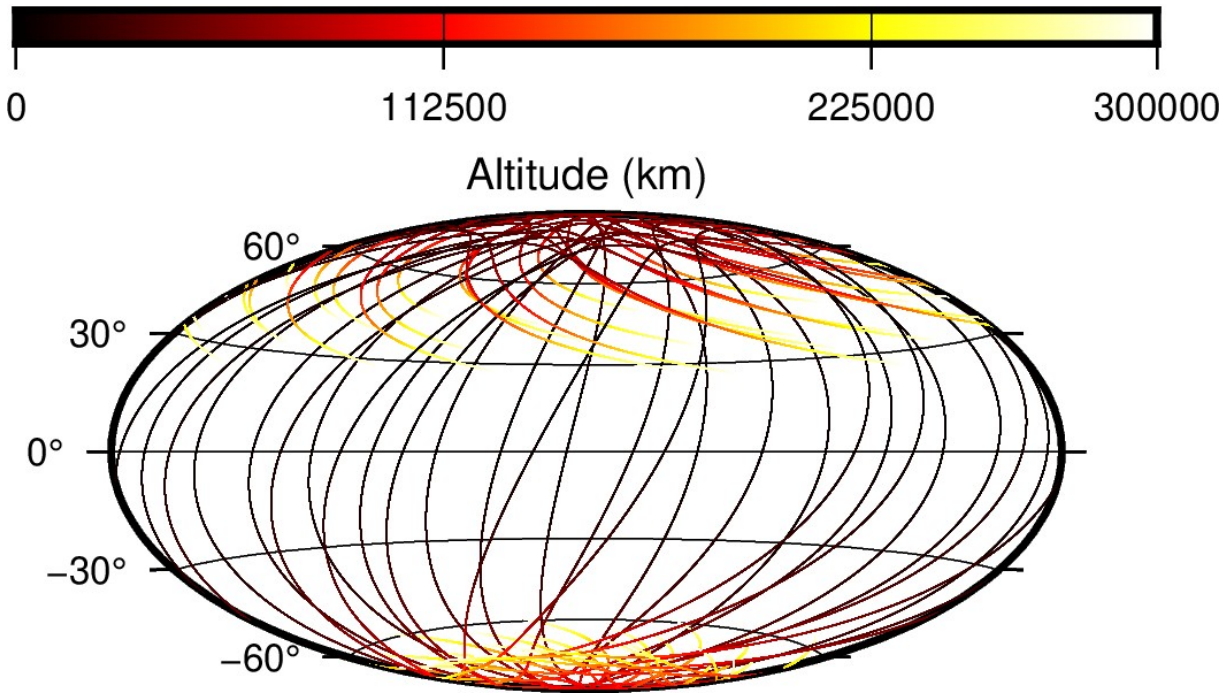

Figure S1. The data locations of Juno satellite below 300,000 km for the first 28 (without orbit 2 and 19) perijoves. The colour scale represents the altitude above the mean radius. The map is centered at 180° longitude.

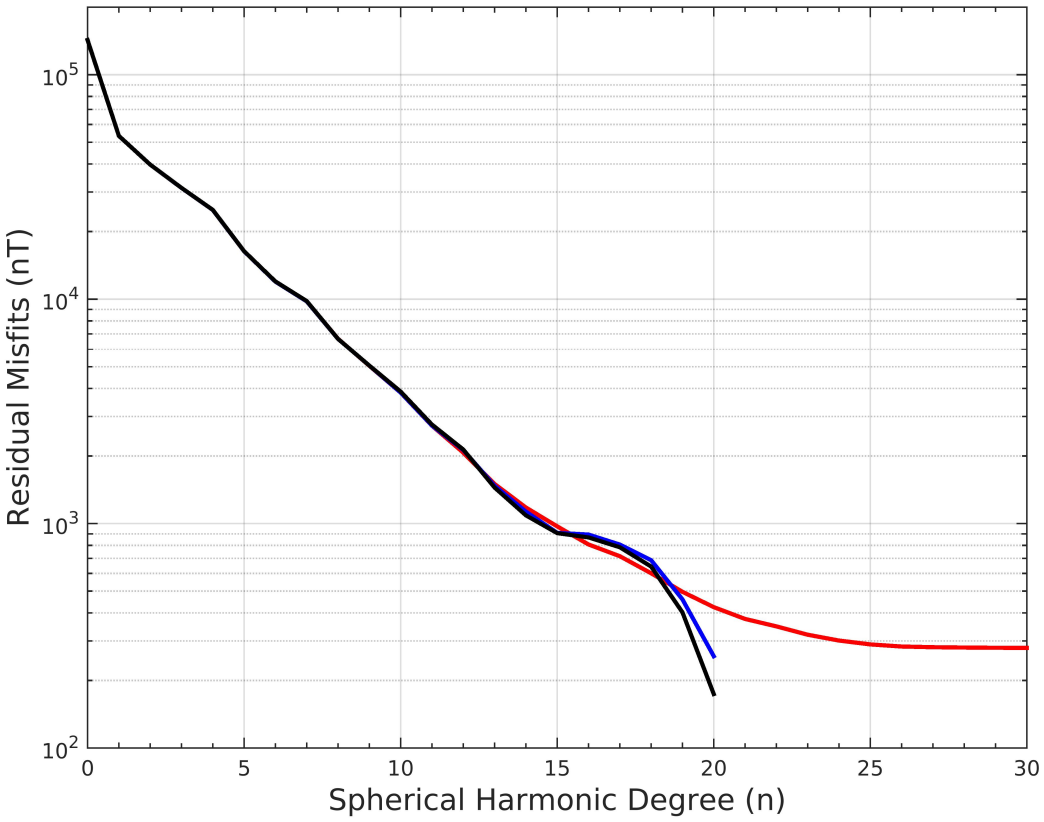

Figure S2. The residual misfits plotted as a function of the SH degree for the model by Connerney et al. (2022) (red), a model without SV (blue) and our model (black).

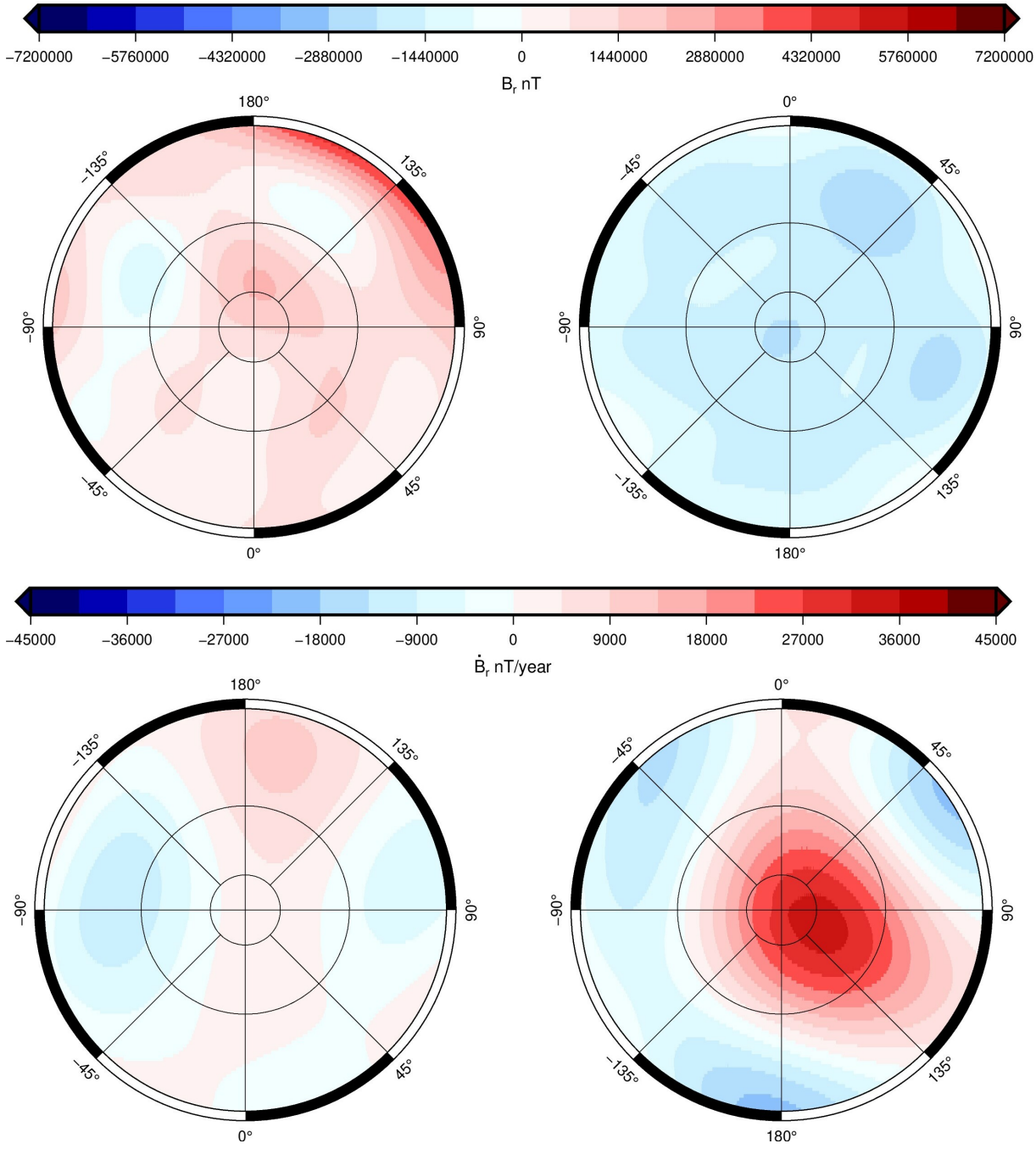

Figure S3. The (top) radial field and (bottom) radial secular variation at the estimated dynamo radius $\mathbf{R}_{sf}$ for the (left) North Pole and (right) South Pole. The inner to outer circles represent latitudes 85°, 75° and 60° respectively.

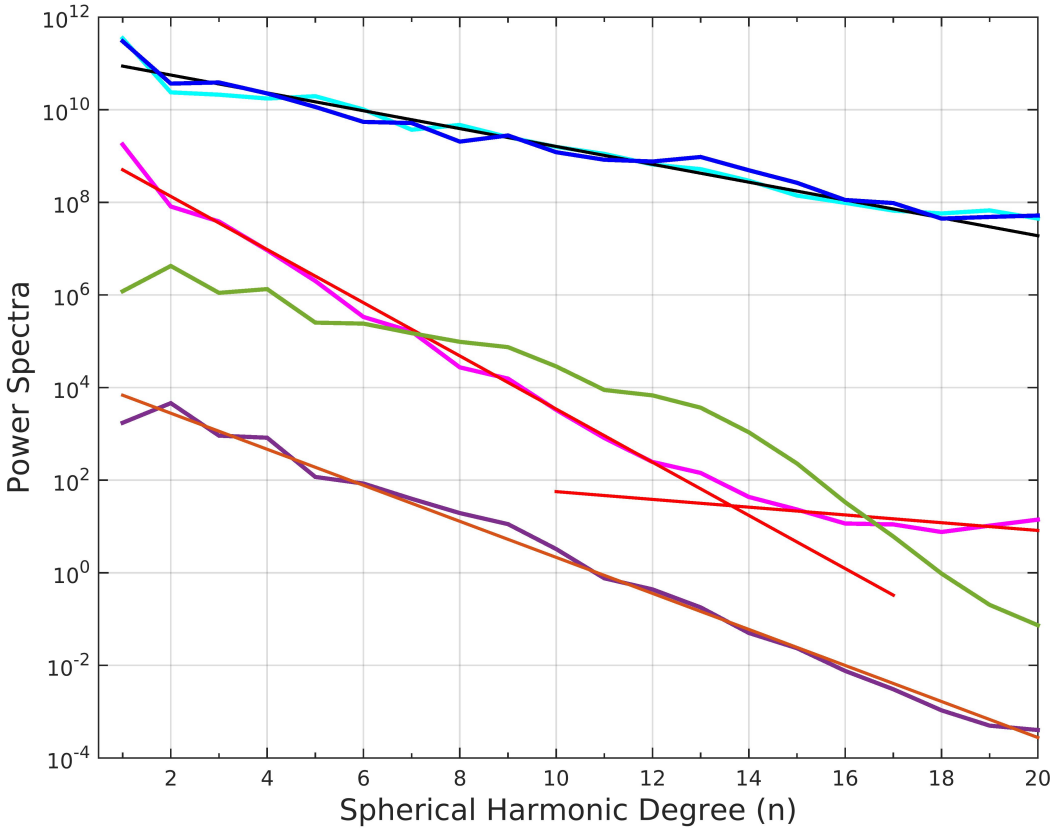

Figure S4. (**a**) The initial power spectrum of the CHAOS-7.8 main field model (magenta), its SV (purple) and the spectrum of Connerney et al. (2022) main field (cyan). The red, orange and black straight lines are the power law rules estimated by least-squares fits for these models respectively. The power laws for the CHAOS main field model (red lines) are different from degrees 1 to 13 and from degrees 14 to 20 (Text S1 for details). The new rescaled CHAOS-7.8 main field and SV models are shown in blue and green respectively. The units for main field are nT^2 and $(nT/year)^2$ for SV spectra.

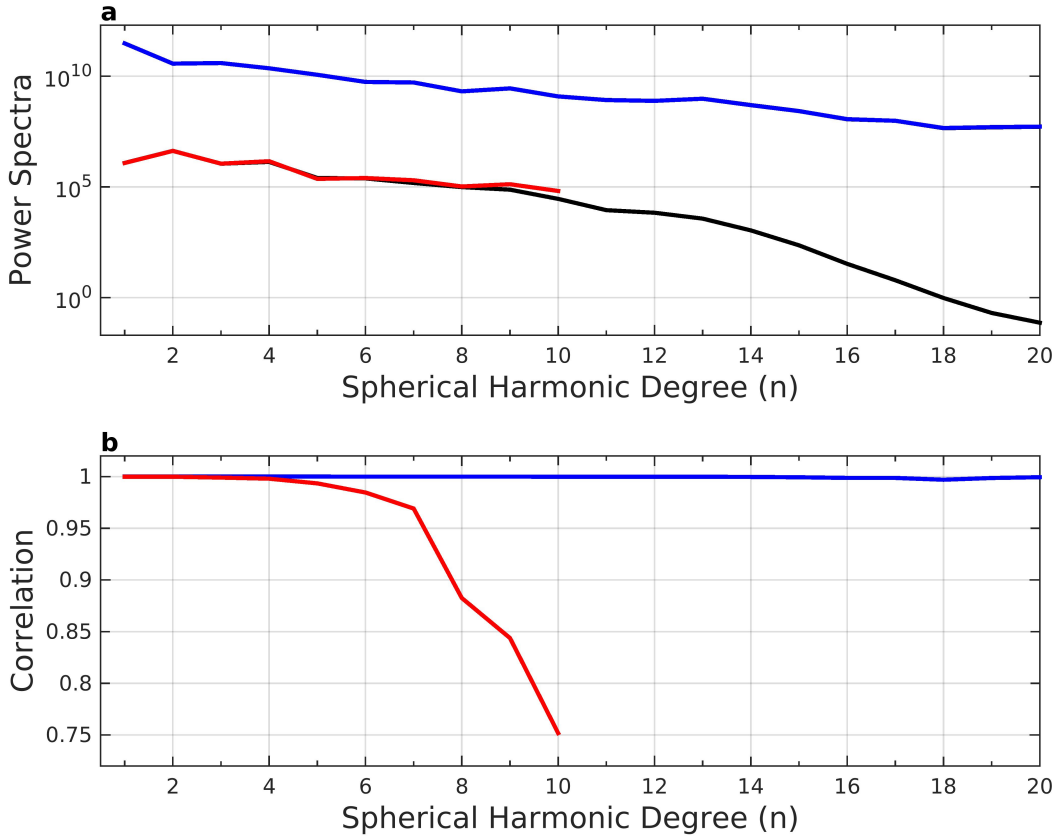

Figure S5. (**a**) The power spectrum of the main field (in blue with units of nT^2) and secular variation (in red with units of $(nT/year)^2$) of the estimated and input (black) magnetic field models at the Jovian surface. (**b**) The spherical harmonic correlation between the estimated and the input models for the main field (blue) and the SV (red).

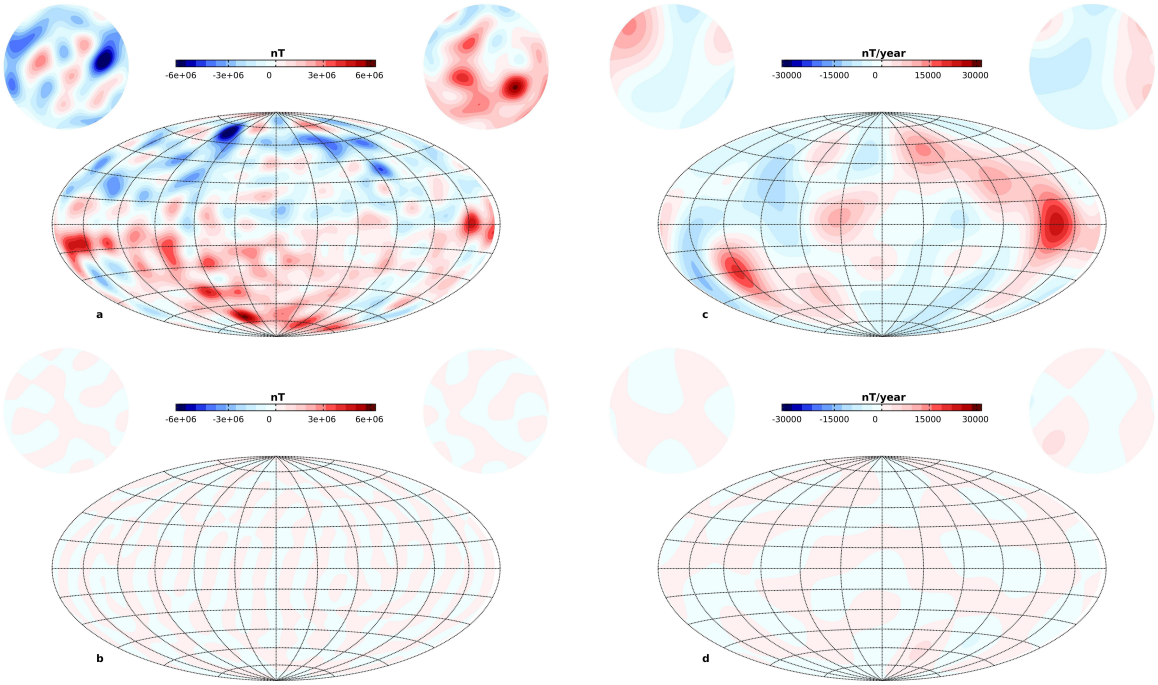

Figure S6. The (**a**) radial field of the estimated model and the (**b**) difference of the radial field between the input and estimated model in the synthetic analysis. The (**c**) radial SV of the estimated model and the (**d**) difference of the radial SV between the input and estimated model in the synthetic analysis. The maps are centered at 180° longitude and plotted at $\mathbf{R}_{sf}$.

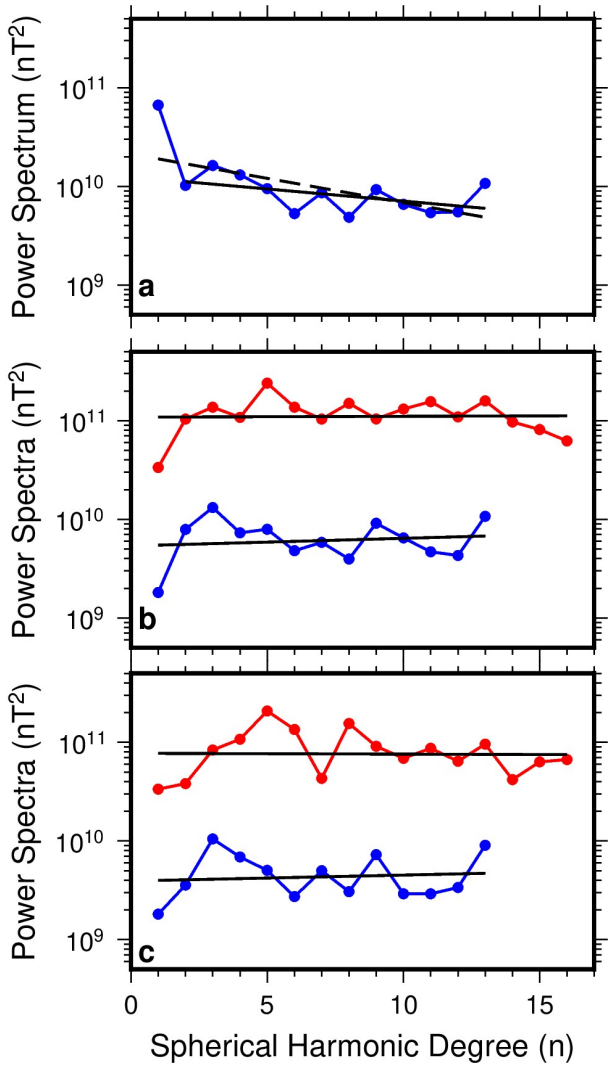

Figure S7. (**a**) Geomagnetic power spectrum of CHAOS-7.8 model at the CMB with linear regression from n=1-13 (black dashed line, slope = -0.0493) and 2-13 (black line, slope = -0.0245). (**b**) The non-zonal spectra with linear regression (black line) for the geomagnetic model (blue, slope = 0.0077) at CMB and for our model (red, slope = 0.0008) at the estimated dynamo radius $\mathbf{R}_{sf}$. (**c**) The quadrupole family spectra with linear regression (black line) for the geomagnetic field (blue, slope = 0.0060) at CMB and for our model (red, slope = 0.0008) at the estimated dynamo radius $\mathbf{R}_{sf}$.

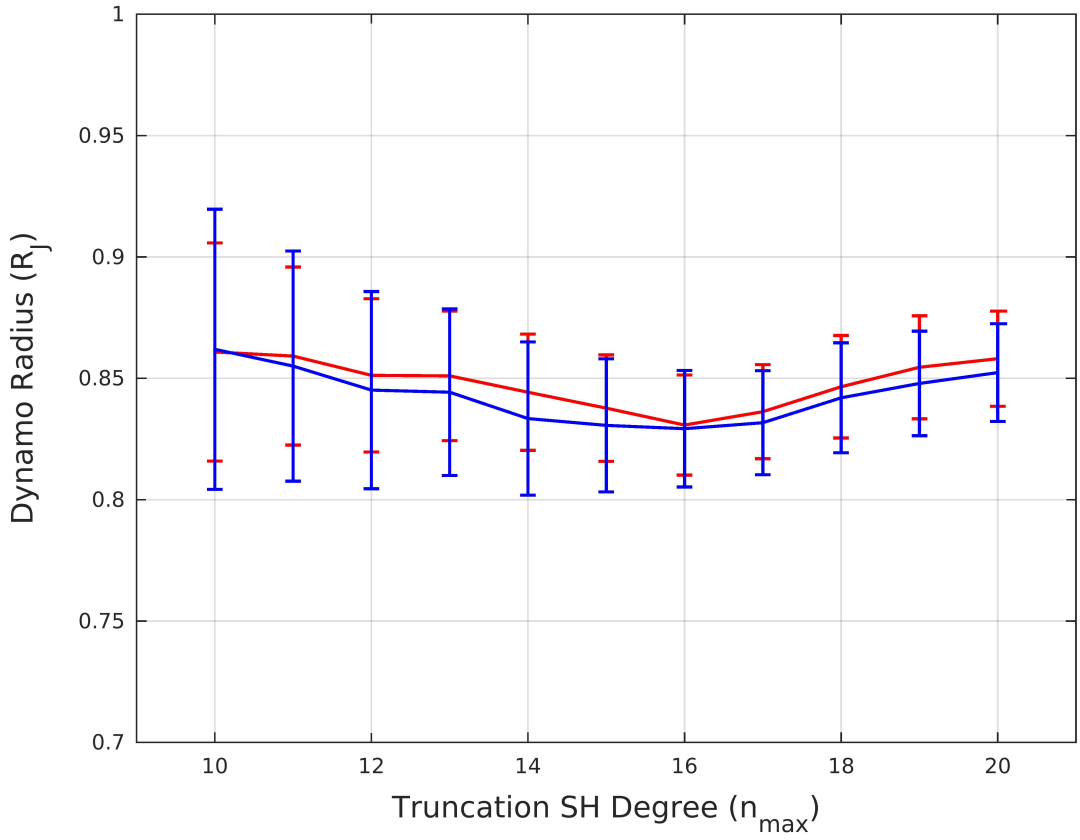

Figure S8. The dynamo radius estimates with the error bounds calculated using the non-zonal (red) and quadrupole (blue) terms at different truncation degrees using the estimated Jovian magnetic field model.

Table S1. Inversion misfits (in nT) for models without and with secular variation ($n_i^{max} = 20$ and 8 for the main field and SV respectively).

	B_r	B_θ	B_ϕ	**B**
model without SV	286	264	357	305
model with SV	176	203	176	186

Appendix B: Jovian Field Model

Jupiter's spherical harmonic magnetic field and secular variation model coefficients using data from the first 28 orbits (Sharan et al. 2022) and the first 38 orbits (this work) at data central epoch 2016.65 and 2019.40 respectively. No data from orbits 2 and 19. Main field degree 16, secular variation degree 8, external field degree 2 and reference radius of Jupiter 71,492 km.

Table B.1: Jovian Internal Field Model

		Sharan et al. (2022)				**This work**			
n	m	g_n^m	h_n^m	$\dot{g}_n^m$	$\dot{h}_n^m$	g_n^m	h_n^m	$\dot{g}_n^m$	$\dot{h}_n^m$
1	0	411153.53	0.00	-97.25	0.00	411024.90	0.00	-115.05	0.00
1	1	-71063.01	20940.18	-113.01	-115.83	-71010.70	20804.22	-92.99	-81.71
2	0	11537.93	0.00	276.99	0.00	11692.29	0.00	291.74	0.00
2	1	-57037.75	-42536.46	80.32	-130.39	-56860.62	-42644.88	59.15	-78.93
2	2	48227.17	20099.65	-88.23	204.19	47949.08	20067.74	-74.10	159.73
3	0	3092.27	0.00	-170.68	0.00	2974.62	0.00	-187.59	0.00
3	1	-37626.04	-32740.77	188.94	-71.96	-37578.54	-32864.73	173.63	-49.96
3	2	15602.98	42617.43	-182.98	31.62	15357.05	42601.33	-89.68	24.25
3	3	-1700.39	-27446.04	263.62	31.17	-1475.94	-27172.47	242.91	26.69
4	0	-34707.64	0.00	135.11	0.00	-34483.55	0.00	232.81	0.00
4	1	-8046.11	32191.31	-32.80	-66.66	-7928.04	32240.16	-124.64	-114.32
4	2	-2383.10	27597.69	-151.52	-39.17	-2472.41	27583.55	-190.73	-33.43
4	3	-10718.53	-662.97	114.08	-79.50	-10712.20	-662.58	35.19	-89.37
4	4	-18089.89	-944.44	173.84	-275.30	-17749.35	-1580.82	89.75	-214.41
5	0	-17856.80	0.00	-140.37	0.00	-18023.07	0.00	-213.12	0.00
5	1	4362.86	45523.13	-187.56	116.94	4210.10	45500.67	-87.50	123.75
5	2	16649.31	-714.88	-5.06	43.58	16564.49	-904.71	96.55	78.00
5	3	-17211.91	6031.78	-63.65	-128.94	-17214.35	5895.26	-48.31	-107.58
5	4	-2883.56	10394.59	-208.39	-162.35	-2609.80	10471.02	-113.31	-27.49
5	5	-4678.60	10203.50	-201.55	-190.71	-5298.38	9956.86	-163.85	-105.30
6	0	-21231.56	0.00	-1.79	0.00	-21176.57	0.00	119.54	0.00
6	1	9714.60	13996.60	-72.40	-15.39	9714.06	13791.28	-44.31	-91.45
6	2	11942.85	-10225.15	-65.68	37.71	11805.13	-10159.33	-88.12	52.26
6	3	-12622.24	-271.76	-77.67	-75.41	-12744.70	-259.32	-9.36	-140.49
6	4	2672.75	13824.29	-128.32	133.64	2676.63	14044.99	-202.09	77.52
6	5	1748.66	-3602.24	31.42	58.61	1477.30	-3802.35	25.02	-14.40
6	6	7848.26	4539.45	-154.27	317.46	7998.19	5233.75	-108.33	144.53
7	0	-61.47	0.00	-200.51	0.00	-69.33	0.00	-189.35	0.00
7	1	5597.20	-7263.70	19.82	190.66	5398.87	-7277.93	92.65	189.17
7	2	-6832.54	-11467.06	137.94	18.03	-6716.27	-11278.70	233.60	-0.50
7	3	-1344.27	2568.40	158.07	88.71	-1177.07	2419.96	48.85	52.00
7	4	-6911.37	5288.77	-20.51	-174.99	-7033.88	5223.52	-72.31	-102.33
7	5	2734.69	-6312.53	126.99	129.17	3264.05	-6408.06	112.94	109.23
7	6	-2574.12	-2044.66	39.62	-46.45	-2669.19	-2012.43	70.50	-51.59

Continued on next page

Table B.1 – Continued from previous page

		Sharan et al. (2022)				This work			
n	m	g_n^m	h_n^m	$\dot{g}_n^m$	$\dot{h}_n^m$	g_n^m	h_n^m	$\dot{g}_n^m$	$\dot{h}_n^m$
7	7	3936.91	-5781.51	267.57	-7.58	4150.80	-5936.35	123.77	121.03
8	0	11453.24	0.00	212.32	0.00	11480.07	0.00	209.33	0.00
8	1	983.01	-2610.78	46.89	-51.05	1178.28	-2687.25	0.41	-168.95
8	2	-7146.85	-12863.53	132.39	-77.25	-7253.82	-12944.48	1.22	-66.00
8	3	-306.49	9857.06	-136.72	22.89	-444.33	9951.04	-65.77	-84.50
8	4	-4636.44	-1717.37	42.05	-31.47	-4762.16	-1917.15	29.66	24.94
8	5	-1412.15	2341.37	-79.85	-92.32	-1511.14	2388.01	-55.11	-85.16
8	6	-3970.48	-3105.74	82.92	-20.31	-4140.63	-3234.17	24.09	-20.47
8	7	-1690.24	1105.01	-31.01	-43.37	-1721.54	1094.36	-20.78	-73.65
8	8	-2996.16	-2880.33	-102.36	58.83	-3117.97	-2941.74	15.54	-149.78
9	0	8076.54	0.00	0.00	0.00	8126.90	0.00	0.00	0.00
9	1	-3220.81	-7642.35	0.00	0.00	-3311.26	-7416.23	0.00	0.00
9	2	873.72	-1223.09	0.00	0.00	852.85	-1258.05	0.00	0.00
9	3	1135.56	6572.41	0.00	0.00	1255.60	6685.52	0.00	0.00
9	4	3641.94	-1228.88	0.00	0.00	3653.30	-1208.15	0.00	0.00
9	5	-3110.86	3573.32	0.00	0.00	-3034.54	3581.76	0.00	0.00
9	6	1244.46	-251.42	0.00	0.00	1267.65	-199.29	0.00	0.00
9	7	-1469.37	1967.77	0.00	0.00	-1471.63	1939.54	0.00	0.00
9	8	1358.28	1023.33	0.00	0.00	1440.62	1001.75	0.00	0.00
9	9	-2296.38	2019.93	0.00	0.00	-2330.85	1941.57	0.00	0.00
10	0	-1308.44	0.00	0.00	0.00	-1038.41	0.00	0.00	0.00
10	1	1391.82	-6086.98	0.00	0.00	1425.74	-6098.71	0.00	0.00
10	2	2176.27	5524.15	0.00	0.00	2182.58	5542.54	0.00	0.00
10	3	3923.74	-2669.47	0.00	0.00	3690.24	-2534.99	0.00	0.00
10	4	3947.41	-1923.03	0.00	0.00	3811.55	-1853.30	0.00	0.00
10	5	481.53	-184.22	0.00	0.00	401.15	-219.24	0.00	0.00
10	6	2336.46	-579.87	0.00	0.00	2355.61	-520.12	0.00	0.00
10	7	732.70	-1514.01	0.00	0.00	740.86	-1605.71	0.00	0.00
10	8	2273.50	151.39	0.00	0.00	2285.73	330.32	0.00	0.00
10	9	889.19	-983.52	0.00	0.00	857.86	-908.80	0.00	0.00
10	10	1280.61	1591.60	0.00	0.00	1234.11	1674.89	0.00	0.00
11	0	-389.83	0.00	0.00	0.00	-92.92	0.00	0.00	0.00
11	1	3609.87	880.92	0.00	0.00	3589.11	1091.92	0.00	0.00
11	2	-1290.11	4730.76	0.00	0.00	-1219.85	4708.17	0.00	0.00
11	3	4083.11	-4469.26	0.00	0.00	4256.91	-4158.95	0.00	0.00
11	4	535.12	-2422.30	0.00	0.00	632.48	-2507.14	0.00	0.00
11	5	598.53	-444.96	0.00	0.00	746.97	-368.47	0.00	0.00
11	6	-1673.23	-2896.61	0.00	0.00	-1599.13	-2927.95	0.00	0.00
11	7	-501.45	-1375.26	0.00	0.00	-387.31	-1414.43	0.00	0.00
11	8	1074.29	-1445.50	0.00	0.00	1028.33	-1476.48	0.00	0.00

Continued on next page

Table B.1 – Continued from previous page

		Sharan et al. (2022)				This work			
n	m	g_n^m	h_n^m	$\dot{g}_n^m$	$\dot{h}_n^m$	g_n^m	h_n^m	$\dot{g}_n^m$	$\dot{h}_n^m$
11	9	366.02	-1393.24	0.00	0.00	384.72	-1502.28	0.00	0.00
11	10	-424.09	-540.02	0.00	0.00	-395.10	-612.43	0.00	0.00
11	11	1202.85	-641.95	0.00	0.00	1277.93	-656.97	0.00	0.00
12	0	3845.75	0.00	0.00	0.00	4287.60	0.00	0.00	0.00
12	1	1148.29	3956.28	0.00	0.00	1081.20	3961.96	0.00	0.00
12	2	-1040.61	1949.28	0.00	0.00	-838.17	1923.58	0.00	0.00
12	3	144.54	-1993.78	0.00	0.00	-80.08	-1920.78	0.00	0.00
12	4	-561.10	-1563.93	0.00	0.00	-809.02	-1521.57	0.00	0.00
12	5	-1469.03	1204.92	0.00	0.00	-1602.81	950.01	0.00	0.00
12	6	-409.87	-981.42	0.00	0.00	-332.70	-869.77	0.00	0.00
12	7	-2035.35	1166.38	0.00	0.00	-2083.95	976.67	0.00	0.00
12	8	215.54	-1376.96	0.00	0.00	175.11	-1281.22	0.00	0.00
12	9	-1543.90	-715.80	0.00	0.00	-1509.78	-583.48	0.00	0.00
12	10	-648.59	-146.77	0.00	0.00	-614.45	-117.25	0.00	0.00
12	11	-757.67	22.72	0.00	0.00	-784.47	178.42	0.00	0.00
12	12	-108.02	-917.50	0.00	0.00	-305.69	-1012.82	0.00	0.00
13	0	-667.02	0.00	0.00	0.00	-130.67	0.00	0.00	0.00
13	1	7.59	4191.62	0.00	0.00	88.83	4111.49	0.00	0.00
13	2	1601.02	313.22	0.00	0.00	1748.10	318.53	0.00	0.00
13	3	-2038.56	-829.09	0.00	0.00	-2028.07	-535.14	0.00	0.00
13	4	65.11	2721.00	0.00	0.00	21.30	2501.61	0.00	0.00
13	5	644.44	354.21	0.00	0.00	757.04	464.87	0.00	0.00
13	6	-227.77	814.01	0.00	0.00	-257.12	842.65	0.00	0.00
13	7	-924.56	1052.06	0.00	0.00	-901.19	1046.95	0.00	0.00
13	8	1562.39	691.23	0.00	0.00	1545.02	659.29	0.00	0.00
13	9	-417.77	-45.40	0.00	0.00	-533.83	-97.64	0.00	0.00
13	10	-150.47	1414.51	0.00	0.00	-163.78	1343.03	0.00	0.00
13	11	-140.86	502.26	0.00	0.00	-189.79	386.59	0.00	0.00
13	12	-277.74	1004.80	0.00	0.00	28.44	824.72	0.00	0.00
13	13	-448.22	-115.18	0.00	0.00	-527.13	77.62	0.00	0.00
14	0	1550.00	0.00	0.00	0.00	1953.53	0.00	0.00	0.00
14	1	-2602.93	-507.60	0.00	0.00	-2684.25	-512.06	0.00	0.00
14	2	826.10	-356.65	0.00	0.00	896.79	-511.77	0.00	0.00
14	3	-1271.56	47.31	0.00	0.00	-1312.89	188.56	0.00	0.00
14	4	173.93	1367.07	0.00	0.00	-212.59	1401.05	0.00	0.00
14	5	655.15	-1087.67	0.00	0.00	713.80	-1302.52	0.00	0.00
14	6	588.09	922.96	0.00	0.00	641.62	1037.68	0.00	0.00
14	7	766.74	377.32	0.00	0.00	693.69	168.91	0.00	0.00
14	8	562.32	-280.61	0.00	0.00	458.10	-214.56	0.00	0.00
14	9	243.13	-508.61	0.00	0.00	173.80	-260.74	0.00	0.00

Continued on next page

Table B.1 – Continued from previous page

		Sharan et al. (2022)				This work			
n	m	g_n^m	h_n^m	$\dot{g}_n^m$	$\dot{h}_n^m$	g_n^m	h_n^m	$\dot{g}_n^m$	$\dot{h}_n^m$
14	10	111.95	523.49	0.00	0.00	308.03	579.32	0.00	0.00
14	11	274.80	240.59	0.00	0.00	285.82	475.24	0.00	0.00
14	12	134.15	-156.08	0.00	0.00	203.69	128.85	0.00	0.00
14	13	595.85	159.87	0.00	0.00	413.67	88.74	0.00	0.00
14	14	-162.62	368.71	0.00	0.00	52.95	303.04	0.00	0.00
15	0	956.25	0.00	0.00	0.00	1571.86	0.00	0.00	0.00
15	1	-1868.93	-1463.29	0.00	0.00	-1941.22	-1679.01	0.00	0.00
15	2	-237.35	-509.38	0.00	0.00	-65.00	-533.10	0.00	0.00
15	3	-885.37	87.11	0.00	0.00	-966.82	374.36	0.00	0.00
15	4	-441.63	236.08	0.00	0.00	-647.00	86.20	0.00	0.00
15	5	119.42	-320.16	0.00	0.00	180.02	-404.46	0.00	0.00
15	6	-511.26	40.79	0.00	0.00	-467.02	148.69	0.00	0.00
15	7	409.21	125.79	0.00	0.00	285.50	1.18	0.00	0.00
15	8	-458.86	-778.36	0.00	0.00	-198.47	-831.52	0.00	0.00
15	9	259.56	108.42	0.00	0.00	1.74	-26.55	0.00	0.00
15	10	-310.41	-8.06	0.00	0.00	-85.69	-26.99	0.00	0.00
15	11	372.88	71.32	0.00	0.00	126.05	-331.78	0.00	0.00
15	12	32.13	330.48	0.00	0.00	111.46	353.11	0.00	0.00
15	13	149.77	28.35	0.00	0.00	72.95	-338.87	0.00	0.00
15	14	-20.96	-369.30	0.00	0.00	-24.25	-203.56	0.00	0.00
15	15	199.32	43.45	0.00	0.00	179.64	-7.00	0.00	0.00
16	0	-1884.59	0.00	0.00	0.00	-1370.26	0.00	0.00	0.00
16	1	-347.36	-244.83	0.00	0.00	-350.67	-283.20	0.00	0.00
16	2	-144.01	-726.33	0.00	0.00	-109.11	-866.18	0.00	0.00
16	3	-392.03	241.94	0.00	0.00	-216.22	661.56	0.00	0.00
16	4	-145.70	289.05	0.00	0.00	-407.23	41.39	0.00	0.00
16	5	-844.38	181.70	0.00	0.00	-398.54	212.77	0.00	0.00
16	6	-303.68	-12.75	0.00	0.00	-398.99	121.06	0.00	0.00
16	7	319.15	317.18	0.00	0.00	348.71	109.87	0.00	0.00
16	8	-160.39	191.13	0.00	0.00	-205.86	421.54	0.00	0.00
16	9	-391.54	519.95	0.00	0.00	-415.40	469.13	0.00	0.00
16	10	158.01	-134.12	0.00	0.00	138.27	309.07	0.00	0.00
16	11	-941.17	621.16	0.00	0.00	-669.48	758.10	0.00	0.00
16	12	-12.14	-524.61	0.00	0.00	-106.35	-335.70	0.00	0.00
16	13	-362.43	116.72	0.00	0.00	-92.12	334.33	0.00	0.00
16	14	120.19	-222.17	0.00	0.00	30.46	-153.85	0.00	0.00
16	15	-144.94	112.48	0.00	0.00	-213.98	0.13	0.00	0.00
16	16	259.00	21.71	0.00	0.00	110.66	-14.26	0.00	0.00

Table B.2: Jovian External Field Model

		Sharan et al. (2022)		**This work**	
n	m	q_n^m	s_n^m	q_n^m	s_n^m
1	0	-120.15	0.00	-133.50	0.00
1	1	10.65	0.52	10.64	-0.07
2	0	0.55	0.00	0.68	0.00
2	1	-0.23	-0.39	-0.14	-0.16
2	2	-0.21	-0.13	-0.25	0.21

Bibliography

Acuña, M. H., Connerney, J. E. P., Wasilewski, P., Lin, R. P., Mitchell, D., Anderson, K. A., Carlson, C. W., McFadden, J., Rème, H., Mazelle, C., Vignes, D., Bauer, S. J., Cloutier, P., and Ness, N. F. (2001). Magnetic field of Mars: Summary of results from the aerobraking and mapping orbits. *Journal of geophysical research: planets* 106.E10, 23403–23417. ISSN: 01480227.

Acuna, M. H., Connerney, J. E. P., Wasilewski, P., Lin, R. P., Anderson, K. A., Carlson, C. W., McFadden, J., Curtis, D. W., Mitchell, D., Reme, H., et al. (1998). Magnetic field and plasma observations at Mars: initial results of the Mars Global Surveyor mission. *Science* 279.5357, 1676–1680.

Acuña, M. H., Connerney, J. E. P., Ness, N. F., Lin, R. P., Mitchell, D., Carlson, C. W., McFadden, J., Anderson, K. A., Reme, H., Mazelle, C., et al. (1999). Global distribution of crustal magnetization discovered by the Mars Global Surveyor MAG/ER experiment. *Science* 284.5415, 790–793.

Albee, A. L., Palluconi, F. D., and Arvidson, R. E. (1998). Mars global surveyor mission: overview and status. *Science* 279.5357, 1671–1672.

Alken, P., Thébault, E., Beggan, C. D., Aubert, J., Baerenzung, J., Brown, W. J., Califf, S., Chulliat, A., Cox, G. A., Finlay, C. C., Fournier, A., Gillet, N., Hammer, M. D., Holschneider, M., Hulot, G., Korte, M., Lesur, V., Livermore, P. W., Lowes, F. J., Macmillan, S., Nair, M., Olsen, N., Ropp, G., Rother, M., Schnepf, N. R., Stolle, C., Toh, H., Vervelidou, F., Vigneron, P., and Wardinski, I. (2021). Evaluation of candidate models for the 13th generation international geomagnetic reference field. *Earth, planets and space* 73.1, 48.

Allison, M. and McEwen, M. (2000). A post-Pathfinder evaluation of areocentric solar coordinates with improved timing recipes for Mars seasonal/diurnal climate studies. *Planetary and space science*, 21.

Amit, H. and Olson, P. (2010). A dynamo cascade interpretation of the geomagnetic dipole decrease. *Geophysical journal international* 181.3, 1411–1427.

Amit, H., Coutelier, M., and Christensen, U. R. (2018). On equatorially symmetric and antisymmetric geomagnetic secular variation timescales. *Physics of the earth and planetary interiors* 276. Special Issue:15th SEDI conference, 190–201. ISSN: 0031-9201.

Amit, H. (2014). Can downwelling at the top of the Earth's core be detected in the geomagnetic secular variation? *Physics of the earth and planetary interiors* 229, 110–121. ISSN: 0031-9201.

Anderson, B. J., Johnson, C. L., Korth, H., Purucker, M. E., Winslow, R. M., Slavin, J. A., Solomon, S. C., McNutt Jr, R. L., Raines, J. M., and Zurbuchen, T. H. (2011). The global magnetic field of Mercury from messenger orbital observations. *Science* 333.6051, 1859–1862.

Anderson, D. L., Miller, W. F., Latham, G. V., Nakamura, Y., Toksöz, M. N., Dainty, A. M., Duennebier, F. K., Lazarewicz, A. R., Kovach, R. L., and Knight, T. C. D. (1977). Seismology on mars. *Journal of geophysical research* 82.28, 4524–4546.

Anderson, D. L. (1972). Internal constitution of mars. *Journal of geophysical research* 77.5, 789–795.

Arkani-Hamed, J. (2002). An improved 50-degree spherical harmonic model of the magnetic field of mars derived from both high-altitude and low-altitude data. *Journal of geophysical research: planets* 107.E10, 13-1-13–8.

Arvidson, R. E., Goettel, K. A., and Hohenberg, C. M. (1980). A post-viking view of Martian geologic evolution. *Reviews of geophysics* 18.3, 565–603.

Aubert, J. and Finlay, C. C. (2019). Geomagnetic jerks and rapid hydromagnetic waves focusing at Earth's core surface. *Nature geoscience* 12.5, 393–398.

Backus, G., Parker, R. L., and Constable, C. (1996). Foundations of geomagnetism. Cambridge University Press.

Backus, G. E. (1970). Non-uniqueness of the external geomagnetic field determined by surface intensity measurements. *Journal of geophysical research* 75.31, 6339–6341.

Balogh, A., Dougherty, M. K., Forsyth, R. J., Southwood, D. J., Smith, E. J., Tsurutani, B. T., Murphy, N., and Burton, M. E. (1992). Magnetic field observations during the ulysses flyby of Jupiter. 257.5076, 1515–1518.

Banerdt, W. B., Smrekar, S. E., Banfield, D., Giardini, D., Golombek, M., Johnson, C. L., Lognonné, P., Spiga, A., Spohn, T., Perrin, C., et al. (2020). Initial results from the insight mission on mars. *Nature geoscience* 13.3, 183–189.

Banks, R. J. (1969). Geomagnetic variations and the electrical conductivity of the upper mantle. *Geophysical journal international* 17.5, 457–487.

Baumjohann, W. and Nakamura, R. (2007). 5.03 - magnetospheric contributions to the terrestrial magnetic field. *Treatise on geophysics (second edition)*. Ed. by G. Schubert. Second Edition. Oxford: Elsevier, 79–90.

Bayes, T. (1763). Lii. an essay towards solving a problem in the doctrine of chances. *Philosophical transactions of the royal society of london* 53, 370–418.

Bills, B. G. and Ferrari, A. J. (1978). Mars topography harmonics and geophysical implications. *Journal of geophysical research: solid earth* 83.B7, 3497–3508.

Bloxham, J., Moore, K. M., Kulowski, L., Cao, H., Yadav, R. K., Stevenson, D. J., Connerney, J. E. P., and Bolton, S. J. (2022). Differential rotation in Jupiter's interior revealed by simultaneous inversion for the magnetic field and zonal flux velocity. *Journal of geophysical research: planets*, e2021JE007138.

Bloxham, J. and Gubbins, D. (1985). The secular variation of Earth's magnetic field. *Nature* 317.6040, 777–781.

Bogard, D. D. and Johnson, P. (1983). Martian gases in an Antarctic meteorite? *Science* 221.4611, 651–654.

Bolton, S. J., Lunine, J., Stevenson, D., Connerney, J. E. P., Levin, S., Owen, T. C., Bagenal, F., Gautier, D., Ingersoll, A. P., Orton, G. S., et al. (2017). The Juno mission. *Space science reviews* 213.1, 5–37.

Brain, D. A. (2006). Mars Global Surveyor measurements of the martian solar wind interaction. *The mars plasma environment*, 77–112.

Breuer, D., Hauck, S. A., Buske, M., Pauer, M., and Spohn, T. (2007). Interior evolution of Mercury. *Space science reviews* 132.2, 229–260.

Brygoo, S., Loubeyre, P., Millot, M., Rygg, J. R., Celliers, P. M., Eggert, J. H., Jeanloz, R., and Collins, G. W. (2021). Evidence of hydrogen-helium immiscibility at jupiter-interior conditions. *Nature* 593.7860, 517–521.

Burton, M. E., Dougherty, M. K., and Russell, C. T. (2009). Model of Saturn's internal planetary magnetic field based on Cassini observations. *Planetary and space science* 57.14-15, 1706–1713.

Burke, B. F. and Franklin, K. L. (1955). Observations of a variable radio source associated with the planet jupiter. *Journal of geophysical research* 60.2, 213–217.

Cain, J. C., Wang, Z., Schmitz, D. R., and Meyer, J. (June 1989). The geomagnetic spectrum for 1980 and core-crustal separation. *Geophysical journal international* 97.3, 443–447.

Campbell, J. K. and Synnott, S. P. (1985). Gravity field of the jovian system from pioneer and voyager tracking data. *The astronomical journal* 90, 364–372.

Cao, H. and Stevenson, D. J. (2017). Zonal flow magnetic field interaction in the semi-conducting region of giant planets. *Icarus* 296, 59–72.

Cao, H., Yadav, R. K., and Aurnou, J. M. (2018). Geomagnetic polar minima do not arise from steady meridional circulation. *Proceedings of the national academy of sciences* 115.44, 11186–11191. ISSN: 0027-8424.

Chapman, S. and Bartels, J. (1940). Geomagnetism, Vol. II: Analysis of the Data, and Physical Theories.

Christensen, U. R. and Tilgner, A. (2004). Power requirement of the geodynamo from ohmic losses in numerical and laboratory dynamos. *Nature* 429.6988, 169–171.

Christensen, U. R., Aubert, J., and Hulot, G. (2010). Conditions for Earth-like geodynamo models. *Earth and planetary science letters* 296.3, 487–496. ISSN: 0012-821X.

Christensen, U. R., Wardinski, I., and Lesur, V. (2012). Timescales of geomagnetic secular acceleration in satellite field models and geodynamo models. *Geophysical journal international* 190.1, 243–254. ISSN: 0956-540X.

Christensen, U. R., Wicht, J., and Dietrich, W. (2020). Mechanisms for limiting the depth of zonal winds in the gas giant planets. *The astrophysical journal* 890.1, 61.

Civet, F. and Tarits, P. (2014). Electrical conductivity of the mantle of Mars from MGS magnetic observations. *Earth, planets and space* 66.1, 85.

Civet, F., Thébault, E., Verhoeven, O., Langlais, B., and Saturnino, D. (2015). Electrical conductivity of the Earth's mantle from the first Swarm magnetic field measure-

ments: mantle electrical conductivity. *Geophysical research letters* 42.9, 3338–3346. ISSN: 00948276.

Clinton, J. F., Ceylan, S., Driel, M. van, Giardini, D., Stähler, S. C., Böse, M., Charalambous, C., Dahmen, N. L., Horleston, A., Kawamura, T., et al. (2021). The marsquake catalogue from InSight, sols 0–478. *Physics of the earth and planetary interiors* 310, 106595.

Constable, C. and Korte, M. (2006). Is earth's magnetic field reversing? *Earth and planetary science letters* 246.1-2, 1–16.

Connerney, J. E. P., Benn, M., Bjarno, J. B., Denver, T., Espley, J., Jorgensen, J. L., Jorgensen, P. S., Lawton, P., Malinnikova, A., Merayo, J. M., Murphy, S., Odom, J., Oliversen, R., Schnurr, R., Sheppard, D., and Smith, E. J. (2017). The juno magnetic field investigation. *Space science reviews* 213.1, 39–138.

Connerney, J. E. P., Kotsiaros, S., Oliversen, R. J., Espley, J. R., Joergensen, J. L., Joergensen, P. S., Merayo, J. M. G., Herceg, M., Bloxham, J., Moore, K. M., Bolton, S. J., and Levin, S. M. (2018). A new model of Jupiter's magnetic field from juno's first nine orbits. *Geophysical research letters* 45.6, 2590–2596.

Connerney, J. E. P., Timmins, S., Herceg, M., and Joergensen, J. L. (2020). A jovian magnetodisc model for the juno era. *Journal of geophysical research: space physics* 125.10. e2020JA028138 2020JA028138, e2020JA028138.

Connerney, J. E. P., Timmins, S., Oliversen, R. J., Espley, J. R., Joergensen, J. L., Kotsiaros, S., Joergensen, P. S., Merayo, J. M. G., Herceg, M., Bloxham, J., Moore, K. M., Mura, A., Moirano, A., Bolton, S. J., and Levin, S. M. (2022). A new model of Jupiter's magnetic field at the completion of juno's prime mission. *Journal of geophysical research: planets* 127.2, e2021JE007055.

Connerney, J. E. P., Acuña, M. H., and Ness, N. F. (1981). Modeling the jovian current sheet and inner magnetosphere. *Journal of geophysical research: space physics* 86.A10, 8370–8384.

Connerney, J. E. P., Acuna, M. H., and Ness, N. F. (1982). Voyager 1 assessment of jupiter's planetary magnetic field. *Journal of geophysical research: space physics* 87.A5, 3623–3627.

Connerney, J. E. P., Acuña, M. H., and Ness, N. F. (1996). Octupole model of Jupiter's magnetic field from Ulysses observations. *Journal of geophysical research: space physics* 101.A12, 27453–27458.

Crider, D. H., Espley, J., Brain, D. A., Mitchell, D. L., Connerney, J. E. P., and Acuña, M. H. (2005). Mars global surveyor observations of the halloween 2003 solar superstorm's encounter with mars. *Journal of geophysical research: space physics* 110.A9.

De Boor, C. (2001). Calculation of the smoothing spline with weighted roughness measure. *Mathematical models and methods in applied sciences* 11.01, 33–41.

Demarcus, W. C. (1958). The constitution of jupiter and saturn. *The astronomical journal* 63, 2.

Dietrich, W., Wulff, P., Wicht, J., and Christensen, U. R. (2021). Linking zonal winds and gravity–ii. Explaining the equatorially antisymmetric gravity moments of Jupiter. *Monthly notices of the royal astronomical society* 505.3, 3177–3191.

Dolginov, S. S. (1978). On the magnetic field of mars: mars 2 and 3 evidence. *Geophysical research letters* 5.1, 89–92.

Dougherty, M. K., Khurana, K. K., Neubauer, F. M., Russell, C. T., Saur, J., Leisner, J. S., and Burton, M. E. (2006). Identification of a dynamic atmosphere at enceladus with the cassini magnetometer. *Science* 311.5766, 1406–1409.

Dougherty, M. K., Cao, H., Khurana, K. K., Hunt, G. J., Provan, G., Kellock, S., Burton, M. E., Burk, T. A., Bunce, E. J., Cowley, S. W. H., Kivelson, M. G., Russell, C. T., and Southwood, D. J. (2018). Saturn's magnetic field revealed by the Cassini Grand Finale. *Science* 362.6410, eaat5434.

Douglas, J. N. and Smith, H. J. (1963). Change in rotation period of Jupiter's decameter radio sources. *Nature* 199.4898, 1080–1081.

Dougherty, M. K., Balogh, A., Southwood, D. J., and Smith, E. J. (1996). Ulysses assessment of the Jovian planetary field. *Journal of geophysical research: space physics* 101.A11, 24929–24941.

Duarte, L. D. V., Wicht, J., and Gastine, T. (2018). Physical conditions for jupiter-like dynamo models. *Icarus* 299, 206–221. ISSN: 0019-1035.

Dyal, P., Parkin, C. W., and Daily, W. D. (1974). Magnetism and the interior of the moon. *Reviews of geophysics* 12.4, 568–591.

Ferrers, N. M. (1877). An elementary treatise on spherical harmonics and subjects connected with them. Macmillan and Company.

Finlay, C. C. and Amit, H. (2011). On flow magnitude and field-flow alignment at Earth's core surface. *Geophysical journal international* 186.1, 175–192. ISSN: 0956-540X.

Finlay, C. C., Kloss, C., Olsen, N., Hammer, M. D., Tøffner-Clausen, L., Grayver, A., and Kuvshinov, A. (2020). The chaos-7 geomagnetic field model and observed changes in the south atlantic anomaly. *Earth, planets and space* 72.1, 156.

French, M., Becker, A., Lorenzen, W., Nettelmann, N., Bethkenhagen, M., Wicht, J., and Redmer, R. (2012). Ab initio simulations for material properties along the Jupiter adiabat. *The astrophysical journal supplement series* 202.1, 5.

Friis-Christensen, E., Lühr, H., and Hulot, G. (2006). Swarm: a constellation to study the Earth's magnetic field. *Earth, planets and space* 58.4, 351–358.

Gastine, T. and Wicht, J. (2021). Stable stratification promotes multiple zonal jets in a turbulent jovian dynamo model. *Icarus* 368, 114514. ISSN: 0019-1035.

Gauss, C. F. (1839). Allgemeine Theorie des Erdmagnetismus, Leipzig.

Giardini, D., Lognonné, P., Banerdt, W. B., Pike, W. T., Christensen, U., Ceylan, S., Clinton, J. F., Driel, M. van, Stähler, S. C., Böse, M., et al. (2020). The seismicity of mars. *Nature geoscience* 13.3, 205–212.

Gong, S. and Wieczorek, M. (2021). Depth of Martian Magnetization From Localized Power Spectrum Analysis. *Journal of geophysical research: planets* 126.8.

Grasset, O., Dougherty, M. K., Coustenis, A., Bunce, E. J., Erd, C., Titov, D., Blanc, M., Coates, A., Drossart, P., Fletcher, L. N., et al. (2013). JUpiter ICy moons Explorer (JUICE): an ESA mission to orbit Ganymede and to characterise the Jupiter system. *Planetary and space science* 78, 1–21.

Grandis, H. and Tarits, P. (2019). Bayesian inversion for layered spherical symmetric Earth conductivity model from global magnetic data. *Iop conference series: earth and environmental science* 318.1, 012003.

Gubbins, D. (June 1983). Geomagnetic field analysis — I. Stochastic inversion. *Geophysical journal international* 73.3, 641–652.

Guillot, T., Miguel, Y., Militzer, B., Hubbard, W. B., Kaspi, Y., Galanti, E., Cao, H., Helled, R., Wahl, S. M., Iess, L., Folkner, W. M., Stevenson, D. J., Lunine, J. I., Reese, D. R., Biekman, A., Parisi, M., Durante, D., Connerney, J. E. P., Levin, S. M., and Bolton, S. J. (2018). A suppression of differential rotation in jupiter's deep interior. *Nature* 555.7695, 227–230.

Guillot, T., Gautier, D., and Hubbard, W. B. (1997). New constraints on the composition of jupiter from galileo measurements and interior models. *Icarus* 130.2, 534–539.

Guillot, T. (2005). The interiors of giant planets: models and outstanding questions. *Annual review of earth and planetary sciences* 33.1, 493–530.

Guillot, T. (1999). Interior of giant planets inside and outside the solar system. *Science* 286, 72–77.

Gutenberg, B. (2016). Physics of the earth's interior. Elsevier.

Harnett, E. M. and Winglee, R. M. (2003). The influence of a mini-magnetopause on the magnetic pileup boundary at mars. *Geophysical research letters* 30.20.

Hastings, W. K. (1970). Monte Carlo sampling methods using Markov chains and their applications, 13.

Heiskanen, W. A. and Meinesz, F. A. V. (1958). The earth and its gravity field. McGraw-Hill.

Holme, R. and Olsen, N. (2006). Core surface flow modelling from high-resolution secular variation. *Geophysical journal international* 166.2, 518–528. ISSN: 0956-540X.

Holme, R. and Bloxham, J. (1996). The magnetic fields of uranus and neptune: methods and models. *Journal of geophysical research: planets* 101.E1, 2177–2200.

Huang, Q., Schmerr, N. C., King, S. D., Kim, D., Rivoldini, A., Plesa, A., Samuel, H., Maguire, R. R., Karakostas, F., Lekić, V., et al. (2022). Seismic detection of a deep mantle discontinuity within Mars by InSight. *Proceedings of the national academy of sciences* 119.42, e2204474119.

Hubbard, W. B. and Marley, M. S. (1989). Optimized jupiter, saturn, and uranus interior models. *Icarus* 78.1, 102–118.

Hubbard, W. B. (1982). Effects of differential rotation on the gravitational figures of jupiter and saturn. *Icarus* 52.3, 509–515.

Huber, P. J. (1996). Robust statistical procedures. SIAM.

Hulot, G., Finlay, C. C., Constable, C. G., Olsen, N., and Mandea, M. (2010). The magnetic field of planet earth. *Space science reviews* 152.1, 159–222.

Hulot, G. and Le Mouël, J. L. (1994). A statistical approach to the Earth's main magnetic field. *Physics of the earth and planetary interiors* 82.3, 167–183. ISSN: 0031-9201.

Iess, L., Folkner, W. M., Durante, D., Parisi, M., Kaspi, Y., Galanti, E., Guillot, T., Hubbard, W. B., Stevenson, D. J., Anderson, J. D., et al. (2018). Measurement of Jupiter's asymmetric gravity field. *Nature* 555.7695, 220–222.

Jackson, A., Jonkers, A. R. T., and Walker, M. R. (2000). Four centuries of geomagnetic secular variation from historical records. *Philosophical transactions of the royal society of london. series a: mathematical, physical and engineering sciences* 358.1768, 957–990.

Jakosky, B. M., Lin, R. P., Grebowsky, J. M., Luhmann, J. G., Mitchell, D. F., Beutelschies, G., Priser, T., Acuna, M., Andersson, L., Baird, D., et al. (2015). The Mars atmosphere and volatile evolution (MAVEN) mission. *Space science reviews* 195.1, 3–48.

Jia, X., Kivelson, M. G., Khurana, K. K., and Walker, R. J. (2010). Magnetic fields of the satellites of Jupiter and Saturn. *Space science reviews* 152.1, 271–305.

Johnson, C. L., Mittelholz, A., Langlais, B., Russell, C. T., Ansan, V., Banfield, D., Chi, P. J., Fillingim, M. O., Forget, F., Haviland, H. F., Golombek, M., Joy, S., Lognonné, P., Liu, X., Michaut, C., Pan, L., Quantin-Nataf, C., Spiga, A., Stanley, S., Thorne, S. N., Wieczorek, M. A., Yu, Y., Smrekar, S. E., and Banerdt, W. B. (2020). Crustal and time-varying magnetic fields at the InSight landing site on Mars. *Nature geoscience* 13.3, 199–204. ISSN: 1752-0894, 1752-0908.

Jones, C. A. (2011). Planetary magnetic fields and fluid dynamos. *Annual review of fluid mechanics* 43.1, 583–614.

Jones, C. A. (2014). A dynamo model of Jupiter's magnetic field. *Icarus* 241, 148–159. ISSN: 0019-1035.

Kaspi, Y., Galanti, E., Hubbard, W. B., Stevenson, D. J., Bolton, S. J., Iess, L., Guillot, T., Bloxham, J., Connerney, J. E. P., Cao, H., Durante, D., Folkner, W. M., Helled, R., Ingersoll, A. P., Levin, S. M., Lunine, J. I., Miguel, Y., Militzer, B., Parisi, M., and Wahl, S. M. (2018). Jupiter's atmospheric jet streams extend thousands of kilometres deep. *Nature* 555.7695, 223–226.

Khan, A., Ceylan, S., Van Driel, M., Giardini, D., Lognonné, P., Samuel, H., Schmerr, N. C., Stähler, S. C., Duran, A. C., Huang, Q., Kim, D., Broquet, A., Charalambous, C., Clinton, J. F., Davis, P. M., Drilleau, M., Karakostas, F., Lekic, V., McLennan, S. M., Maguire, R. R., Michaut, C., Panning, M. P., Pike, W. T., Pinot, B., Plasman, M., Scholz, J. R., Widmer-Schnidrig, R., Spohn, T., Smrekar, S. E., and Banerdt, W. B. (2021). Upper mantle structure of Mars from InSight seismic data. en. *Science* 373.6553, 434–438.

Khurana, K. K., Kivelson, M. G., Stevenson, D. J., Schubert, G., Russell, C. T., Walker, R. J., and Polanskey, C. (1998). Induced magnetic fields as evidence for subsurface oceans in europa and callisto. *Nature* 395.6704, 777–780.

Khurana, K. K. (1992). A generalized hinged-magnetodisc model of jupiter's nightside current sheet. *Journal of geophysical research: space physics* 97.A5, 6269–6276.

Kivelson, M. G., Khurana, K. K., Russell, C. T., Walker, R. J., Warnecke, J., Coroniti, F. V., Polanskey, C., Southwood, D. J., and Schubert, G. (1996). Discovery of Ganymede's magnetic field by the Galileo spacecraft. *Nature* 384.6609, 537–541.

Knapmeyer-Endrun, B., Panning, M. P., Bissig, F., Joshi, R., Khan, A., Kim, D., Lekić, V., Tauzin, B., Tharimena, S., Plasman, M., et al. (2021). Thickness and structure of the martian crust from insight seismic data. *Science* 373.6553, 438–443.

Langlais, B., Purucker, M. E., and Mandea, M. (2004). Crustal magnetic field of Mars: crustal magnetic field of Mars. *Journal of geophysical research: planets* 109.E2, n/a–n/a. ISSN: 01480227.

Langlais, B., Amit, H., Larnier, H., Thébault, E., and Mocquet, A. (2014). A new model for the (geo)magnetic power spectrum, with application to planetary dynamo radii. *Earth and planetary science letters* 401, 347–358. ISSN: 0012-821X.

Langlais, B., Civet, F., and Thébault, E. (2017). In situ and remote characterization of the external field temporal variations at Mars: MARTIAN EXTERNAL FIELD TIME VARIABILITY. *Journal of geophysical research: planets* 122.1, 110–123. ISSN: 21699097.

Langlais, B., Thébault, E., Houliez, A., Purucker, M. E., and Lillis, R. J. (2019). A New Model of the Crustal Magnetic Field of Mars Using MGS and MAVEN. *Journal of geophysical research: planets* 124.6, 1542–1569.

Langel, R. A., Estes, R. H., Mead, G. D., Fabiano, E. B., and Lancaster, E. R. (1980). Initial geomagnetic field model from Magsat vector data. *Geophysical research letters* 7.10, 793–796.

Langel, R. A. and Estes, R. H. (1982). A geomagnetic field spectrum. *Geophysical research letters* 9.4, 250–253.

Langel, R. A. and Hinze, W. J. (1998). The magnetic field of the earth's lithosphere: the satellite perspective. Cambridge University Press.

Lanczos, C. (1950). An iteration method for the solution of the eigenvalue problem of linear differential and integral operators. *Journal of research of the national bureau of standards* 45, 255–282.

Lillis, R. J., Robbins, S., Manga, M., Halekas, J. S., and Frey, H. V. (2013). Time history of the Martian dynamo from crater magnetic field analysis. *Journal of geophysical research: planets* 118.7, 1488–1511.

Livermore, P. W., Hollerbach, R., and Finlay, C. C. (2017). An accelerating high-latitude jet in Earth's core. *Nature geoscience* 10.1, 62–68.

Lognonné, P., Banerdt, W. B., Pike, W. T., Giardini, D., Christensen, U., Garcia, R. F., Kawamura, T., Kedar, S., Knapmeyer-Endrun, B., Margerin, L., et al. (2020). Constraints on the shallow elastic and anelastic structure of mars from insight seismic data. *Nature geoscience* 13.3, 213–220.

Lowes, F. J. (1966). Mean-square values on sphere of spherical harmonic vector fields. *Journal of geophysical research (1896-1977)* 71.8, 2179–2179.

Lowes, F. J. (1974). Spatial Power Spectrum of the Main Geomagnetic Field, and Extrapolation to the Core. *Geophysical journal international* 36.3, 717–730. ISSN: 0956-540X.

MacDonald, G. J. F. (1962). On the internal constitution of the inner planets. *Journal of geophysical research* 67.7, 2945–2974.

Mandea, M. and Purucker, M. (2005). Observing, modeling, and interpreting magnetic fields of the solid earth. *Surveys in geophysics* 26.4, 415–459.

Mandea, M., Holme, R., Pais, A., Pinheiro, K., Jackson, A., and Verbanac, G. (2010). Geomagnetic jerks: rapid core field variations and core dynamics. *Space science reviews* 155.1, 147–175.

Mandea, M. and Korte, M. (2010). Geomagnetic observations and models. Vol. 5. Springer.

Marcus, P. S. (1993). Jupiter's Great Red Spot and other vortices. *Annual review of astronomy and astrophysics* 31, 523–573.

Maus, S., Rother, M., Hemant, K., Stolle, C., Lühr, H., Kuvshinov, A., and Olsen, N. (2006). Earth's lithospheric magnetic field determined to spherical harmonic degree 90 from CHAMP satellite measurements. *Geophysical journal international* 164.2, 319–330.

Mauersberger, P. (1956). Das mittel der energiedichte des geomagnetischen hauptfeldes an der erdoberflache und seine saulare anderung. 65, 207–215.

McFadden, P. L., Merrill, R. T., and McElhinny, M. W. (1988). Dipole/quadrupole family modeling of paleosecular variation. *Journal of geophysical research: solid earth* 93.B10, 11583–11588.

McSween Jr, H. Y. (Jan. 1984). SNC meteorites: Are they Martian rocks? *Geology* 12.1, 3–6.

McSween Jr, H. Y. (1994). What we have learned about Mars from SNC meteorites. *Meteoritics* 29.6, 757–779.

Metropolis, N., Rosenbluth, A. W., Rosenbluth, M. N., Teller, A. H., and Teller, E. (1953). Equation of state calculations by fast computing machines. *The journal of chemical physics* 21.6, 1087–1092.

Militzer, B., Hubbard, W. B., Wahl, S., Lunine, J. I., Galanti, E., Kaspi, Y., Miguel, Y., Guillot, T., Moore, K. M., Parisi, M., et al. (2022). Juno spacecraft measurements of Jupiter's gravity imply a dilute core. *The planetary science journal* 3.8, 185.

Mittelholz, A., Johnson, C. L., and Lillis, R. J. (2017). Global-scale external magnetic fields at Mars measured at satellite altitude: GLOBAL-SCALE EXTERNAL MAGNETIC FIELDS. *Journal of geophysical research: planets* 122.6, 1243–1257. ISSN: 21699097.

Mittelholz, A., Johnson, C. L., and Morschhauser, A. (2018). A New Magnetic Field Activity Proxy for Mars From MAVEN Data. *Geophysical research letters*.

Mittelholz, A., Johnson, C. L., Feinberg, J. M., Langlais, B., and Phillips, R. J. (2020). Timing of the martian dynamo: New constraints for a core field 4.5 and 3.7 Ga ago. *Science advances* 6.18, eaba0513. ISSN: 2375-2548.

Mittelholz, A., Grayver, A., Khan, A., and Kuvshinov, A. (2021). The Global Conductivity Structure of the Lunar Upper and Midmantle. *Journal of geophysical research: planets* 126.11.

Mocquet, A. and Menvielle, M. (2000). Complementarity of seismological and electromagnetic sounding methods for constraining the structure of the martian mantle. *Planetary and space science* 48.12-14, 1249–1260.

Moeller, R. C., Jandura, L., Rosette, K., Robinson, M., Samuels, J., Silverman, M., Brown, K., Duffy, E., Yazzie, A., Jens, E., et al. (2021). The Sampling and Caching Subsystem (SCS) for the scientific exploration of Jezero crater by the Mars 2020 Perseverance rover. *Space science reviews* 217.1, 1–43.

Moore, K. M., Yadav, R. K., Kulowski, L., Cao, H., Bloxham, J., Connerney, J. E. P., Kotsiaros, S., Jørgensen, J. L., Merayo, J. M. G., Stevenson, D. J., Bolton, S. J., and Levin, S. M. (2018). A complex dynamo inferred from the hemispheric dichotomy of Jupiter's magnetic field. *Nature* 561.7721, 76–78.

Moore, K. M., Cao, H., Bloxham, J., Stevenson, D. J., Connerney, J. E. P., and Bolton, S. J. (2019). Time variation of Jupiter's internal magnetic field consistent with zonal wind advection. *Nature astronomy* 3.8, 730–735.

Morales, M. A., McMahon, J. M., Pierleoni, C., and Ceperley, D. M. (2013). Nuclear quantum effects and nonlocal exchange-correlation functionals applied to liquid hydrogen at high pressure. *Physical review letters* 110.6, 065702.

Morschhauser, A., Lesur, V., and Grott, M. (2014). A spherical harmonic model of the lithospheric magnetic field of Mars. *Journal of geophysical research: planets* 119.6, 1162–1188.

Morris, D. and Berge, G. L. (1962). Measurements of the polarization and angular extent of the decimetric radiation of Jupiter. *The astrophysical journal* 136, 276–282.

Ness, N. F., Behannon, K. W., Lepping, R. P., and Whang, Y. C. (1975). Magnetic field of mercury confirmed. *Nature* 255.5505, 204–205.

Ness, N. F., Acuña, M. H., Lepping, R. P., Burlaga, L. F., Behannon, K. W., and Neubauer, F. M. (1979a). Magnetic field studies at Jupiter by Voyager 1: Preliminary results. *Science* 204.4396, 982–987.

Ness, N. F., Acuña, M. H., Lepping, R. P., Burlaga, L. F., Behannon, K. W., and Neubauer, F. M. (1979b). Magnetic field studies at Jupiter by Voyager 2: Preliminary results. *Science* 206.4421, 966–972.

Nimmo, F., Hart, S. D., Korycansky, D. G., and Agnor, C. B. (2008). Implications of an impact origin for the martian hemispheric dichotomy. *Nature* 453.7199, 1220–1223.

Olsen, N., Glassmeier, K. H., and Jia, X. (2010). Separation of the magnetic field into external and internal parts. *Space science reviews* 152.1, 135–157.

Olsen, N., Friis-Christensen, E., Floberghagen, R., Alken, P., Beggan, C. D., Chulliat, A., Doornbos, E., Da Encarnação, J. T., Hamilton, B., Hulot, G., et al. (2013). The swarm satellite constellation application and research facility (scarf) and swarm data products. *Earth, planets and space* 65.11, 1189–1200.

Olsen, N., Albini, G., Bouffard, J., Parrinello, T., and Tøffner-Clausen, L. (2020). Magnetic observations from CryoSat-2: calibration and processing of satellite platform magnetometer data. *Earth, planets and space* 72.1, 1–18.

Olson, P. and Aurnou, J. (1999). A polar vortex in the Earth's core. *Nature* 402.6758, 170–173.

Olsen, N. (May 2002). A model of the geomagnetic field and its secular variation for epoch 2000 estimated from Ørsted data. *Geophysical journal international* 149.2, 454–462.

Olsen, N. (1999). Induction studies with satellite data. *Surveys in geophysics* 20.3, 309–340.

Parker, E. N. (1958). Dynamics of the interplanetary gas and magnetic fields. *The astrophysical journal* 128, 664.

Pfaffenzeller, O., Hohl, D., and Ballone, P. (1995). Miscibility of hydrogen and helium under astrophysical conditions. *Physical review letters* 74.13, 2599.

Phillips, C. B. and Pappalardo, R. T. (2014). Europa Clipper mission concept: exploring Jupiter's ocean moon. *Eos, transactions american geophysical union* 95.20, 165–167.

Purucker, M., Ravat, D., Frey, H., Voorhies, C., Sabaka, T., and Acuña, M. (2000). An altitude-normalized magnetic map of Mars and its interpretation. *Geophysical research letters* 27.16, 2449–2452.

Purucker, M., Connerney, J., Mandea, M., and Hulot, G. (2003). A test for secular variation of the Martian magnetic field. *Egs-agu-eug joint assembly*, 7394.

Purucker, M. E. (2008). A global model of the internal magnetic field of the moon based on lunar prospector magnetometer observations. *Icarus* 197.1, 19–23.

Püthe, C. and Kuvshinov, A. (2013). Determination of the 1-d distribution of electrical conductivity in earth's mantle from swarm satellite data. *Earth, planets and space* 65.11, 1233–1237.

Quesnel, Y., Sotin, C., Langlais, B., Costin, S., Mandea, M., Gottschalk, M., and Dyment, J. (2009). Serpentinization of the martian crust during Noachian. *Earth and planetary science letters* 277.1-2, 184–193.

Ravat, D., Purucker, M. E., and Olsen, N. (2020). Lunar magnetic field models from lunar prospector and selene/kaguya along-track magnetic field gradients. *Journal of geophysical research: planets* 125.7, e2019JE006187.

Ridley, V. A. and Holme, R. (2016). Modeling the jovian magnetic field and its secular variation using all available magnetic field observations. *Journal of geophysical research: planets* 121.3, 309–337.

Riedler, W., Möhlmann, D., Oraevsky, V. N., Schwingenschuh, K., Yeroshenko, Ye., Rustenbach, J., Aydogar, Oe., Berghofer, G., Lichtenegger, H., Delva, M., et al. (1989). Magnetic fields near Mars: first results. *Nature* 341.6243, 604–607.

Russell, C. T., Elphic, R. C., and Slavin, J. A. (1979). Initial pioneer venus magnetic field results: dayside observations. *Science* 203.4382, 745–748.

Russell, C. T. (2012). The galileo mission. Springer Science & Business Media.

Ruzmaikin, A. A. and Starchenko, S. V. (1991). On the origin of Uranus and Neptune magnetic fields. *Icarus* 93.1, 82–87.

Sabaka, T. J., Olsen, N., Tyler, R. H., and Kuvshinov, A. (2015). CM5, a pre-swarm comprehensive geomagnetic field model derived from over 12 yr of CHAMP, Ørsted, SAC-C and observatory data. *Geophysical journal international* 200.3, 1596–1626.

Saur, J., Neubauer, F. M., and Glassmeier, K. H. (2010). Induced magnetic fields in Solar System bodies. *Space science reviews* 152.1-4, 391–421.

Schubert, G. and Spohn, T. (1990). Thermal history of mars and the sulfur content of its core. *Journal of geophysical research: solid earth* 95.B9, 14095–14104.

Schmidt, A. F. K. (1917). Erdmagnetismus. Enzyklopädie der mathematischen Wissenschaften.

Sharan, S., Langlais, B., Amit, H., Thébault, E., Pinceloup, M., and Verhoeven, O. (2022). The internal structure and dynamics of Jupiter unveiled by a high-resolution magnetic field and secular variation model. *Geophysical research letters* 49.15, e2022GL098839.

Slavin, J. A., Schwingenschuh, K., Riedler, W., and Yeroshenko, Y. (1991). The solar wind interaction with mars: mariner 4, mars 2, mars 3, mars 5, and phobos 2 observations of bow shock position and shape. *Journal of geophysical research: space physics* 96.A7, 11235–11241.

Smith, E. J., Davis Jr, L., Coleman Jr, P. J., and Jones, D. E. (1965). Magnetic field measurements near Mars. *Science* 149.3689, 1241–1242.

Smith, E. J., Davis Jr., L., Jones, D. E., Coleman Jr., P. J., Colburn, D. S., Dyal, P., Sonett, C. P., and Frandsen, A. M. A. (1974). The planetary magnetic field and magnetosphere of Jupiter: Pioneer 10. *Journal of geophysical research (1896-1977)* 79.25, 3501–3513.

Smith, E. J., Davis Jr., L., Jones, D. E., Coleman Jr., P. J., Colburn, D. S., Dyal, P., and Sonett, C. P. (1975). Jupiter's magnetic field. magnetosphere, and interaction with the solar wind: Pioneer 11. *Science* 188.4187, 451–455.

Smith, M. R., Laul, J. C., Ma, M. S., Huston, T., Verkouteren, R. M., Lipschutz, M. E., and Schmitt, R. A. (1984). Petrogenesis of the SNC (shergottites, nakhlites, chassignites) meteorites: Implications for their origin from a large dynamic planet, possibly Mars. *Journal of geophysical research: solid earth* 89.S02, B612–B630.

Smith, D. E., Zuber, M. T., Solomon, S. C., Phillips, R. J., Head, J. W., Garvin, J. B., Banerdt, W. B., Muhleman, D. O., Pettengill, G. H., Neumann, G. A., Lemoine, F. G., Abshire, J. B., Aharonson, O., David, C., Brown, Hauck, S. A., Ivanov, A. B., McGovern, P. J., Zwally, H. J., and Duxbury, T. C. (1999). The global topography of Mars and implications for surface evolution. *Science* 284.5419, 1495–1503.

Smith, A. F. M. (1991). Bayesian computational methods. *Philosophical transactions of the royal society of london. series a: physical and engineering sciences* 337.1647, 369–386.

Soderblom, L. A., Condit, C. D., West, R. A., Herman, B. M., and Kreidler, T. J. (1974). Martian planetwide crater distributions: implications for geologic history and surface processes. *Icarus* 22.3, 239–263.

Spohn, T., Acuña, M. H., Breuer, D., Golombek, M., Greeley, R., Halliday, A., Hauber, E., Jaumann, R., and Sohl, F. (2001). Geophysical constraints on the evolution of mars. *Chronology and evolution of mars*, 231–262.

Spohn, T., Hudson, T. L., Witte, L., Wippermann, T., Wisniewski, L., Kedziora, B., Vrettos, C., Lorenz, R. D., Golombek, M., Lichtenheldt, R., et al. (2022). The InSight-

HP3 mole on Mars: lessons learned from attempts to penetrate to depth in the Martian soil. *Advances in space research* 69.8, 3140–3163.

Srivastava, S. P. (1966). Theory of the magnetotelluric method for a spherical conductor. *Geophysical journal international* 11.4, 373–387.

Stähler, S. C., Khan, A., Banerdt, W. B., Lognonné, P., Giardini, D., Ceylan, S., Drilleau, M., Duran, A. C., Garcia, R. F., Huang, Q., Kim, D., Lekic, V., Samuel, H., Schimmel, M., Schmerr, N., Sollberger, D., Stutzmann, É., Xu, Z., Antonangeli, D., Charalambous, C., Davis, P. M., Irving, J. C. E., Kawamura, T., Knapmeyer, M., Maguire, R., Marusiak, A. G., Panning, M. P., Perrin, C., Plesa, A. C., Rivoldini, A., Schmelzbach, C., Zenhäusern, G., Beucler, E., Clinton, J., Dahmen, N., Van Driel, M., Gudkova, T., Horleston, A., Pike, W. T., Plasman, M., and Smrekar, S. E. (2021). Seismic detection of the martian core. *Science* 373.6553, 443–448.

Stanley, S. (2010). A dynamo model for axisymmetrizing Saturn's magnetic field. *Geophysical research letters* 37.5.

Stevenson, D. J., Spohn, T., and Schubert, G. (1983). Magnetism and thermal evolution of the terrestrial planets. *Icarus* 54.3, 466–489.

Stevenson, D. J. (2001). Mars' core and magnetism. *Nature* 412.6843, 214–219.

Stevenson, D. J. (2003). Planetary magnetic fields. *Earth and planetary science letters* 208.1-2, 1–11.

Stevenson, D. J. (1983). Planetary magnetic fields. *Reports on progress in physics* 46.5, 555.

Svedhem, H., Titov, D. V., Taylor, F. W., and Witasse, O. (2007). Venus as a more Earth-like planet. *Nature* 450.7170, 629–632.

Tarits, P., Jouanne, V., Menvielle, M., and Roussignol, M. (1994). Bayesian statistics of non-linear inverse problems: example of the magnetotelluric 1-d inverse problem. *Geophysical journal international* 119.2, 353–368.

Tarantola, A. (2005). Inverse problem theory and methods for model parameter estimation. SIAM.

Thébault, E., Finlay, C. C., Alken, P., Beggan, C. D., Canet, E., Chulliat, A., Langlais, B., Lesur, V., Lowes, F. J., Manoj, C., et al. (2015). Evaluation of candidate geomagnetic field models for igrf-12. *Earth, planets and space* 67.1, 1–23.

Thébault, E., Vigneron, P., Langlais, B., and Hulot, G. (2016). A Swarm lithospheric magnetic field model to SH degree 80. *Earth, planets and space* 68.1, 1–13.

Thébault, E., Langlais, B., Oliveira, J. S., Amit, H., and Leclercq, L. (2018). A time-averaged regional model of the Hermean magnetic field. *Physics of the earth and planetary interiors* 276, 93–105.

Treiman, A. H., Gleason, J. D., and Bogard, D. D. (2000). The snc meteorites are from Mars. *Planetary and space science* 48.12-14, 1213–1230.

Tsang, Y. K. and Jones, C. A. (2020). Characterising Jupiter's dynamo radius using its magnetic energy spectrum. *Earth and planetary science letters* 530, 115879. ISSN: 0012-821X.

Urey, H. C. (1951). The origin and development of the earth and other terrestrial planets. *Geochimica et cosmochimica acta* 1.4-6, 209–277.

Vacher, P. and Verhoeven, O. (2007). Modelling the electrical conductivity of iron-rich minerals for planetary applications. *Planetary and space science* 55.4, 455–466.

Van Allen, J. A., Baker, D. N., Randall, B. A., and Sentman, D. D. (1974). The magnetosphere of Jupiter as observed with pioneer 10: 1. instrument and principal findings. *Journal of geophysical research (1896-1977)* 79.25, 3559–3577.

Verhoeven, O. and Vacher, P. (2016). Laboratory-based electrical conductivity at Martian mantle conditions. *Planetary and space science* 134, 29–35. ISSN: 00320633.

Vervelidou, F., Lesur, V., Grott, M., Morschhauser, A., and Lillis, R. J. (2017). Constraining the date of the Martian dynamo shutdown by means of crater magnetization signatures. *Journal of geophysical research: planets* 122.11, 2294–2311.

Verhoeven, O., Thébault, E., Saturnino, D., Houliez, A., and Langlais, B. (2021). Electrical conductivity and temperature of the Earth's mantle inferred from Bayesian inversion of Swarm vector magnetic data. *Physics of the earth and planetary interiors* 314, 106702.

Voorhies, C. V. (2004). Narrow-scale flow and a weak field by the top of Earth's core: evidence from ørsted, magsat, and secular variation. *Journal of geophysical research: solid earth* 109.B3.

Wahl, S. M., Hubbard, W. B., Militzer, B., Guillot, T., Miguel, Y., Movshovitz, N., Kaspi, Y., Helled, R., Reese, D., Galanti, E., Levin, S., Connerney, J. E. P., and Bolton, S. J. (2017). Comparing Jupiter interior structure models to juno gravity measurements and the role of a dilute core. *Geophysical research letters* 44.10, 4649–4659.

Wang, J. Z., Huo, Z. X., and Zhang, L. (2021). A modular model of jupiter's magnetospheric magnetic field based on juno data. *Journal of geophysical research: space physics* 126.5, e2020JA029085.

Wardinski, I., Langlais, B., and Thébault, E. (2019). Correlated Time-Varying Magnetic Fields and the Core Size of Mercury. *Journal of geophysical research: planets* 124.8, 2178–2197.

Wardinski, I., Amit, H., Langlais, B., and Thébault, E. (2021). The internal structure of mercury's core inferred from magnetic observations. *Journal of geophysical research: planets* 126.12, e2020JE006792.

Warwick, J. W. (1964). Radio emission from jupiter. *Annual review of astronomy and astrophysics* 2, 1.

Warwick, J. W. (1967). Radiophysics of jupiter. *Space science reviews* 6.6, 841–891.

Wicht, J., Gastine, T., and Duarte, L. D. V. (2019). Dynamo action in the steeply decaying conductivity region of jupiter-like dynamo models. *Journal of geophysical research: planets* 124.3, 837–863.

Wicht, J. and Gastine, T. (2020). Numerical simulations help revealing the dynamics underneath the clouds of Jupiter. *Nature communications* 11.1, 2886.

Wildt, R. (1938). On the state of matter in the interior of the planets. *The astrophysical journal* 87, 508.

Winterhalter, D., Acuña, M., and Zakharov, A., eds. (2004). Mars' Magnetism and Its Interaction with the Solar Wind. Vol. 18. Space Sciences Series of ISSI. Dordrecht: Springer Netherlands.

Yu, Z. J., Leinweber, H. K., and Russell, C. T. (2010). Galileo constraints on the secular variation of the jovian magnetic field. *Journal of geophysical research: planets* 115.E3.

Zhang, T. L., Lu, Q. M., Baumjohann, W., Russell, C. T., Fedorov, A., Barabash, S., Coates, A. J., Du, A. M., Cao, J. B., Nakamura, R., et al. (2012). Magnetic reconnection in the near Venusian magnetotail. *Science* 336.6081, 567–570.

COLLEGE DOCTORAL PAYS DE LA LOIRE
ED MATIERE,MOLECULES MATERIAUX ET GEOSCIENCES

Nantes Université

Titre : Sur l'utilisation du champ magnétique pour caractériser l'intérieur des planètes : les cas de Jupiter et de Mars

Mots clés : champ magnétique, Jupiter, dynamo, variation séculaire, Mars, conductivité

Résumé : On étudie le champ magnétique de Mars et de Jupiter pour avoir des informations sur son intérieur. Il existe des sources internes et externes de champ magnétique autour d'une planète qui peuvent être modélisées à l'aide des harmoniques sphériques. Les sources internes sont la dynamo, la croûte et les champs induits, et les sources externes sont produites à l'extérieur de la planète. Pour Jupiter, le champ dynamo interne est étudié à l'aide des données du satellite Juno, et pour Mars, les champs induits sont étudiés à l'aide des données de deux satellites, MGS et MAVEN.

Le champ dynamo de Jupiter est généré par la convection de l'hydrogène liquide conducteur. Ce champ et ses variations séculaire (SV) sont modélisés jusqu'aux degrés 16 et 8 respectivement. On déduit la profondeur de génération du champ à 0,83 fois le rayon de la planète. La SV varie à un taux d'environ 0,6% par an et est principalement produite par les mouvements advectifs du fluide. Les cartes de champ montrent deux taches de flux proéminentes tandis que les cartes de SV montrent des caractéristiques zonales et non zonales.

Mars est gouvernée par des champs crustaux qui est au moins deux fois l'ordre de magnitude de celui observé sur Terre. Les champs résiduels obtenus après suppression des champs crustaux statiques sont de l'ordre de 10^2 nT. Les analyses donnent une tendance sur 27 jours qui peut être utilisée pour obtenir des indices magnétiques. Les champs résiduels est modélisé jusqu'au degré 3 pour ses deux composantes : le champ externe et le champ induit interne. A partir de celles-ci, on obtient des informations sur la conductivité électrique dans le manteau par inversion Bayésienne.

Title : The interior of planets as characterised by their magnetic fiels : the Jovian and Martian cases

Keywords : magnetic field, Jupiter, dynamo, secular variation, Mars, conductivity

Abstract : We study the magnetic field of Mars and Jupiter to obtain information about their interior from them. There are internal and external sources of magnetic field around a planet which can be modelled using Spherical Harmonics (SH). The internal sources are the dynamo, crust and induced fields while the external sources are produced outside the planet due to interaction with solar phenomena. For Jupiter, we work with the internal dynamo field using Juno satellite data while for Mars, we work with the induced fields using data of two satellites, MGS and MAVEN.

Jupiter's dynamo field is produced due to convection in the conducting liquid metallic hydrogen and undergoes changes with respect to time called secular variations (SV). We model the internal field and its changes up to SH degree 16 and 8 respectively. From them, we decipher the depths of field generation at 0.83 times the radius of the planet. The SV varies at a rate of about 0.6% per year and is dominantly produced by the advective movements of the fluid. The field maps display two prominent flux patches while the SV maps display zonal and non-zonal features.

Mars presently does not possess a dynamo but is governed by crustal fields that are at least twice the order of magnitude than that observed on Earth. The residual fields obtained after removal of the static crustal fields are of the order of 10^2 nT. Their analysis provides a 27 days trend that can be used to obtain magnetic indices. The residual fields are then modelled up to SH degree 3 for its two components- the externally inducing and the internally induced fields. From them, we get some information about the conductivity of the interior using Bayesian inversion.